Oleksiy Shulika
Igor Sukhoivanov *Editors*

Advanced Lasers

Laser Physics and Technology for
Applied and Fundamental Science

Springer Series in Optical Sciences

Volume 193

Springer Series in Optical Sciences is led by Editor-in-Chief William T. Rhodes, Georgia Institute of Technology, USA, and provides an expanding selection of research monographs in all major areas of optics:

– lasers and quantum optics
– ultrafast phenomena
– optical spectroscopy techniques
– optoelectronics
– information optics
– applied laser technology
– industrial applications and
– other topics of contemporary interest.

With this broad coverage of topics the series is useful to research scientists and engineers who need up-to-date reference books.

More information about this series at http://www.springer.com/series/624

Oleksiy Shulika • Igor Sukhoivanov
Editors

Advanced Lasers

Laser Physics and Technology for Applied
and Fundamental Science

Springer

Editors
Oleksiy Shulika
Universidad de Guanajuato
Salamanca
Mexico

Igor Sukhoivanov
Universidad de Guanajuato
Salamanca
Mexico

Printed on acid-free paper

Contents

Contributors

Alexander Alexandrov Adaptive Optics Lab, Moscow State Technical University (MAMI), Moscow, Russia

E. Alvarado-Méndez Departamento de Ingeniería Electrónica, División de Ingenierías Campus Irapuato Salamanca, Universidad de Guanajuato, Salamanca, GTO, México

Valerio Annovazzi-Lodi Department of Electrical, Computer and Biomedical Engineering, University of Pavia, Pavia, Italy

José E. Antonio-Lopez CREOL The College of Optics and Photonics, University of Central Florida, Orlando, FL, USA

A. A. Belyanin Department of Physics and Astronomy, Texas A & M University, College Station TX, USA

O. N. Bezkrovnaya Institute for Single Crystals, SSI "Institute for Single Crystals", National Academy of Sciences of Ukraine, Kharkiv, Ukraine

Vladimir L. Derbov Department of Physics, Saratov State University, Saratov, Russia

Silvano Donati Department of Electrical, Computer and Biomedical Engineering, University of Pavia, Pavia, Italy

Julián M. Estudillo-Ayala Cuerpo Académico de Optoelectrónica, DICIS Universidad de Guanajuato, Guanajuato, Mexico

F. Gómez-Aguilar Departmento de Materiales Solares, Instituto de Energías Renovables, Universidad Nacional Autónoma de México, Temixco, MOR, México

Cristina M. Gómez-Sarabia Digital Arts Department, Engineering Division, Campus Salamanca, University of Guanajuato, Guanajuato, Mexico

S. V. Gagarsky Mechanics and Optics, Saint Petersburg National Research University of Information Technologies, Saint-Petersburg, Russia

Chunlei Guo The Institute of Optics, University of Rochester, Rochester, NY, USA

Yu. A. Gurkalenko Institute for Single Crystals, SSI "Institute for Single Crystals", National Academy of Sciences of Ukraine, Kharkiv, Ukraine

Juan C. Hernandez Garcia Instituto Nacional de Astrofisica Optica y Electronica, Puebla, Mexico

Daniel Jauregui-Vazquez Cuerpo Académico de Optoelectrónica, DICIS Universidad de Guanajuato, Guanajuato, Mexico

Hitoshi Kawaguchi Graduate School of Materials Science, Nara Institute of Science and Technology, Ikoma, Nara, Japan

V. I. Kislov Prokhorov General Physics Institute, Russian Academy of Science, Moscow, Russia

V. V. Kiyko Prokhorov General Physics Institute, Russian Academy of Science, Moscow, Russia

E. R. Kocharovskaya IAP RAS, Nizhny Novgorod, Russia

V. V. Kocharovsky IAP RAS, Nizhny Novgorod, Russia

Department of Physics and Astronomy, Texas A & M University, College Station TX, USA

Vl. V. Kocharovsky IAP RAS, Nizhny Novgorod, Russia

V. A. Kondratyev Prokhorov General Physics Institute, Russian Academy of Science, Moscow, Russia

Alexis Kudryashov Adaptive Optics Lab, Moscow State Technical University (MAMI), Moscow, Russia

Sergio Ledesma Electronics Department, Engineering Division, Campus Salamanca, University of Guanajuato, Guanajuato, Mexico

P. LiKamWa CREOL The College of Optics and Photonics, University of Central Florida, Orlando, FL, USA

A. V. Lopin Institute for Single Crystals, SSI "Institute for Single Crystals", National Academy of Sciences of Ukraine, Kharkiv, Ukraine

V. V. Maslov O. Ya. Usikov Institute for Radiophysics and Electronics, National Academy of Sciences of Ukraine, Kharkiv, Ukraine

Daniel A. May-Arrioja Fiber and Integrated Optics Laboratory, UAMRR Universidad Autónoma de Tamaulipas, Reynosa, TAMPS, México

E. N. Ofitserov Prokhorov General Physics Institute, Russian Academy of Science, Moscow, Russia

Jorge Ojeda-Castañeda Electronics Department, Engineering Division, Campus Salamanca, University of Guanajuato, Guanajuato, Mexico

A. G. Plaksiy Institute for Single Crystals, SSI "Institute for Single Crystals", National Academy of Sciences of Ukraine, Kharkiv, Ukraine

S. V. Pogorelov National University of Pharmacy, Kharkov, Ukraine

I. M. Pritula Institute for Single Crystals, SSI "Institute for Single Crystals", National Academy of Sciences of Ukraine, Kharkiv, Ukraine

V. M. Puzikov Institute for Single Crystals, SSI "Institute for Single Crystals", National Academy of Sciences of Ukraine, Kharkiv, Ukraine

Roberto Rojas-Laguna Cuerpo Académico de Optoelectrónica, DICIS Universidad de Guanajuato, Guanajuato, Mexico

Alexey Rukosuev Adaptive Optics Lab, Moscow State Technical University (MAMI), Moscow, Russia

Nataliya Sakhnenko Kharkiv National University of Radio Electronics, Kharkiv, Ukraine

Institute of Radio Physics and Electronics NASU, Kharkiv, Ukraine

Vadim Samarkin Adaptive Optics Lab, Moscow State Technical University (MAMI), Moscow, Russia

José J. Sanchez-Mondragón Instituto Nacional de Astrofisica, Óptica y Electrónica, Tonantzintla, PUE, México

A. N. Sergeev Mechanics and Optics, Saint Petersburg National Research University of Information Technologies, Saint-Petersburg, Russia

Tatyana A. Sergeeva Department of Physics, Saratov State University, Saratov, Russia

Vladislav V. Serov Department of Physics, Saratov State University, Saratov, Russia

Juan M. Sierra Hernandez Cuerpo Académico de Optoelectrónica, DICIS Universidad de Guanajuato, Guanajuato, Mexico

A. G. Suzdaltsev Prokhorov General Physics Institute, Russian Academy of Science, Moscow, Russia

Miguel Torres-Cisneros Electronics Department, Engineering Division, Campus Salamanca, University of Guanajuato, Guanajuato, Mexico

A. Y. Vorobyev The Institute of Optics, University of Rochester, Rochester, NY, USA

Emmanuel Yépez-Vidal Electronics Department, Engineering Division, Campus Salamanca, University of Guanajuato, Guanajuato, Mexico

Chapter 1
Recent Progress in Polarization-Bistable VCSELs and Their Applications to All-Optical Signal Processing

Hitoshi Kawaguchi

Abstract In this chapter, we review recent progress in polarization-bistable vertical-cavity surface-emitting lasers (VCSELs) and their applications to all-optical signal processing. An all-optical flip-flop operation can be achieved at a very low bias current of 0.85 mA by using 980-nm polarization-bistable VCSELs built with an oxide current-confinement structure. All-optical retiming is then discussed as an example of signal processing. Retiming is performed using an AND gate function and a reset function. Next, memorization of an arbitrary bit of 20-Gb/s RZ and 40-Gb/s NRZ signals is demonstrated. A four-bit optical buffer memory can be constructed using four 1.55-μm polarization-bistable VCSELs. Two shift-register memories are connected in parallel in this memory. Finally, an optical header processing system is described. The system uses a 1.55-μm polarization-bistable VCSEL that operates as an all-optical AND gate and a holding element. Depending on the state ("0" or "1") of one bit in a four-bit header, the VCSEL holds one of two orthogonal polarization states. The output light of the VCSEL switches and holds the output state of an optical switch. This enables a payload to be sent to the destination determined by the header.

1.1 Introduction

Bistable laser diodes are expected to be key components in future optical communication and switching systems [1]. It is known that vertical-cavity surface-emitting lasers (VCSELs) preferentially emit linearly polarized light. In particular, VCSELs with a square mesa structure can emit in one of the two orthogonal linear polarization states which along the sides of the mesa and are bistable between these two polarization states. Polarization switching induced by optical injection is expected to be fast making it suitable for use in all-optical signal-processing systems. The main origin of the polarization bistability is considered to be gain saturation. Polarization-bistable VCSELs have functionalities of AND and OR gates and as memories. This means that the VCSELs can be used for all-optical retiming.

H. Kawaguchi (✉)
Graduate School of Materials Science, Nara Institute of Science and Technology,
8916-5 Takayama, Ikoma, Nara 630-0192, Japan
e-mail: khitoshi@ms.naist.jp
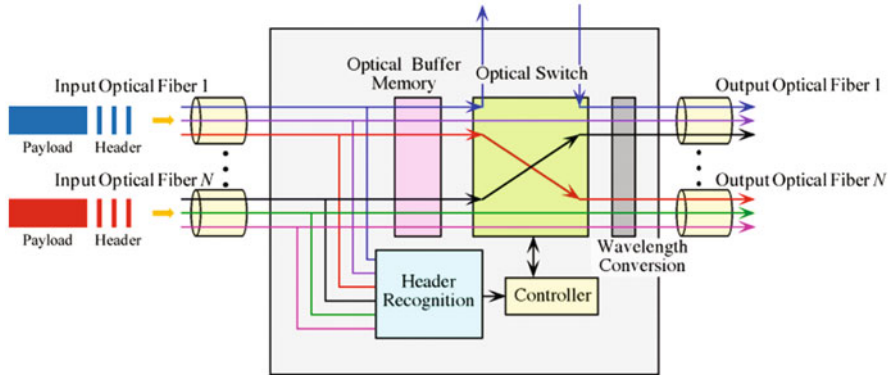
Fig. 1.1 Conceptual drawing of optical packet switch node

Optical packet switching is emerging as a potentially important technology in optical networks. Figure 1.1 shows a conceptual drawing of an optical-packet switch node. Such a node routes optical signals arriving at its N input ports to its N output ports. The input signals are in the form of packets, which consist of a payload containing data bits preceded by a header containing the destination address, priority, packet length, and error-check information. An optical packet switch node should perform the following functions:

1. Route optical packets from the input to the output by reading the address header and setting the switch permutation
2. Resolve contentions between packets at multiple ports for a single output port according to an established priority scheme, and in a manner that minimizes packet loss, e.g., by storing packets in a buffer

These two functions can be realized with bistable laser diodes. Optical buffer memories consisting of flip-flop devices have a great advantage in that the data stored can be read out at arbitrary timings. We previously developed an optical buffer memory with a shift register function consisting of a two-dimensional array of polarization-bistable VCSELs [2, 3]. The increasing speed of optical telecommunications has prompted research on high-speed optical header processing, and many types of non-linear optical signal processing have been investigated. All-optical packet switching based on wavelength labeling [4] has advantages in terms of bit-rate scalability and data format transparency of the payloads. The optical digital-to-analog converter [5] is also promising for high-speed operation. However, the scalability of the header length is limited in such a scheme. High-speed label switching using a multimode interference bistable laser diode has been demonstrated with a 1-bit header recognition [6]. The use of the optical AND gate functionality of optical-bistable devices may be able to overcome this limitation. VCSELs are promising bistable devices that are power efficient and easy to make into an array.

This chapter describes recent (mainly 2009 and after) progress in polarization-bistable VCSELs and their applications to all-optical signal processing. The following papers published before 2009 are referred to herein: [1, 3, 7].
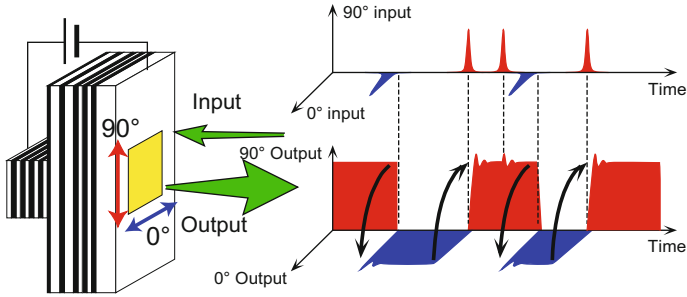
Fig. 1.2 Polarization-bistable switching of VCSEL by injection of optical pulses

1.2 Flip-Flop Operation with Low Power Consumption

A polarization-bistable VCSEL has a square mesa structure and two lasing modes with polarization directions orthogonal to each other (0° and 90°). When a control light with sufficient power and a polarization direction parallel to that of the suppressed mode is injected into it, the emitted laser light changes polarization to that of the suppressed mode, as shown in Fig. 1.2.

We achieved all-optical flip-flop operation at a very low bias current of 0.85 mA by using an oxide current-confinement structure [8]. Figure 1.3a shows the schematic diagram of a 980-nm VCSEL with such structure. The device consists of a three-quantum-well InGaAs active layer, a bottom 27-pair and a top 38-pair $Al_{0.16}Ga_{0.84}As/Al_{0.9}Ga_{0.1}As$ DBR mirrors on an n-type (001) GaAs substrate. The size of the rectangular mesa of the p-DBR is $5.5 \times 6.0\,\mu m$, and the sides are aligned to the $[1\bar{1}0]$ and $[110]$ crystal orientations. The 50-μm-square post mesa consists of the current confinement layer, active layer, and n-DBR. The 30-nm-thick current confinement layer is made of $Al_{0.98}Ga_{0.02}As$ that is oxidized from sides of the 50-μm-square mesa in high-temperature steam at 430 °C. When the oxidation was interrupted, the front edge of the oxidation $Al_{0.98}Ga_{0.02}As$ layer was able to be observed with an IR-CCD camera from the top of the device in the chamber. In our oxidation process, the depth of oxidation increased in proportion to the time exposed to high-temperature steam. After observation, oxidation was resumed at the same rate. We fabricated a current aperture of about 3 μm square at the center of the mesa, as shown in Fig. 1.3b.

Figure 1.4a plots the voltage and polarization-resolved light output versus current (V-I and L-I), as measured at 10 °C for the VCSEL. The threshold current was 0.22 mA, which is the lowest value of polarization-bistable VCSELs to the best of our knowledge. Hysteresises were observed at 0.71 ∼ 1.64 and 2.28 ∼ 3.53 mA. The VCSEL lases in a single longitudinal and transverse mode. The polarization-resolved near-field patterns match the Gaussian profiles in both polarizations. These results clearly demonstrate that the VCSEL with an oxide confinement mesa structure exhibits polarization bistability under a single frequency and lowest order transverse mode operation.
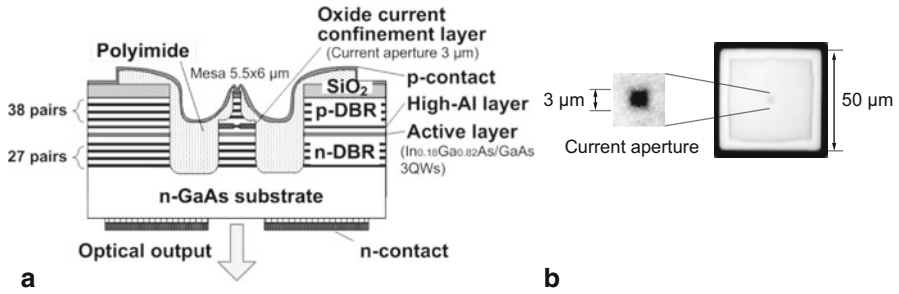
Fig. 1.3 a Schematic cross-section of polarization bistable VCSEL with oxide current-confinement layer and **b** infrared transparent image of confinement layer. (From [8])
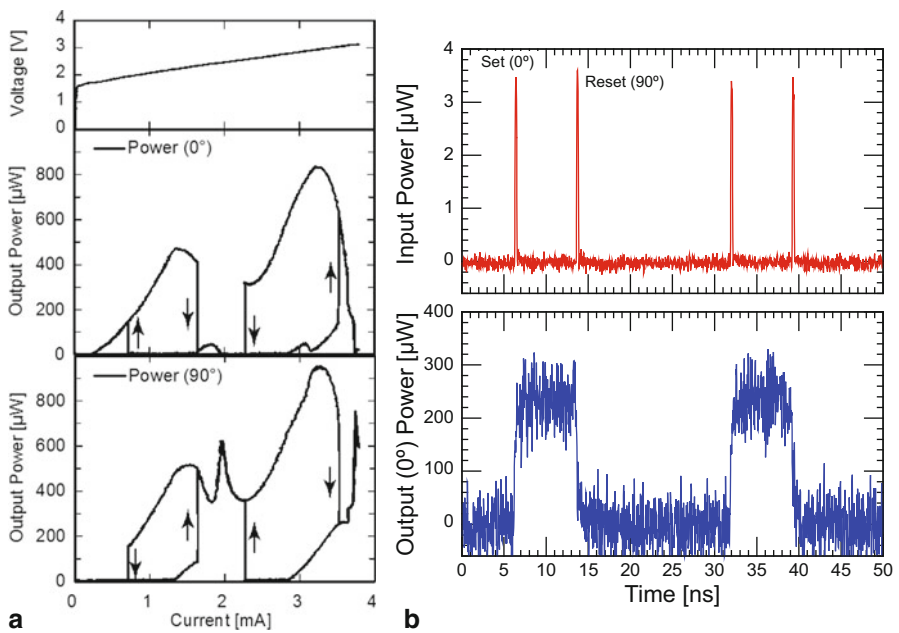
Fig. 1.4 a Measured V-I and polarization-resolved L-I curves of the VCSEL and **b** experimental demonstration of all-optical flip-flop operation at a bias current of 0.85 mA. (From [8])

The lasing polarization of the oxide current-confinement structure VCSEL we fabricated switched to the orthogonal polarization when an orthogonally polarized optical pulse was injected. As shown in Fig. 1.4b, we performed all-optical flip-flop operation using the polarization bistable VCSEL. The VCSEL was operated at 0.85 mA (power consumption was 1.7 mW) and 10 °C and its output power was 258 μW. The VCSEL initially oscillates with a 90° polarization. The polarization of the VCSEL switches to 0° when a 0° polarization trigger pulse with a 3.6 μW power and 200 ps duration is injected. The input power of the VCSEL is much smaller than

Fig. 1.5 Bias currents for
flip-flop operation in bistable
laser diodes
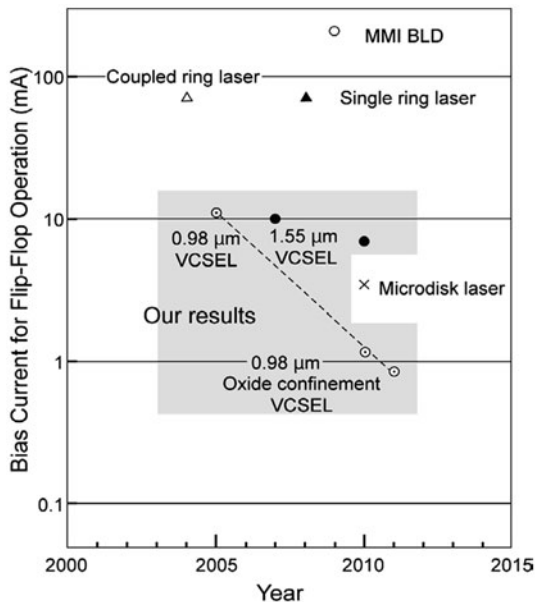
the output power. The lasing polarization remains at 0° for a holding time of 7.3 ns, which was determined by the input pulse period. When a 90° polarization trigger pulse is injected, the polarization of the VCSEL switches back to 90°.

Figure 1.5 shows the bias current needed for an all-optical flip-flop operation in various bistable laser diodes. In an all-optical signal processing application, the power consumed by the laser diode is mainly determined by the bias current, because the bias voltage is about 1–2 V and the power of the optical trigger pulses is very small compared with that of the electrical bias. It is apparent that polarization-bistable VCSELs have a great advantage over other types of bistable laser diodes as far as power consumption goes.

1.3   All-Optical Retiming

All-optical retiming can be performed with a polarization-bistable VCSEL by using an AND gate operation and a reset operation. An optical clock pulse and input data signal are used for the AND gate operation [9]. The timing jitter of the regenerated signal can be reduced by optimizing the injection power ratio of the clock pulse and the data signal. The principle of all-optical signal regeneration is shown in Fig. 1.6. The input data signal to be regenerated is shown at the top of the diagram. The set and reset pulses are clock pulses for the retiming operation. The data signal and the set pulse are polarized at 90°, and the reset pulse is polarized at 0°. These three signals are injected into the VCSEL. The injection powers of the data signal and the set pulse
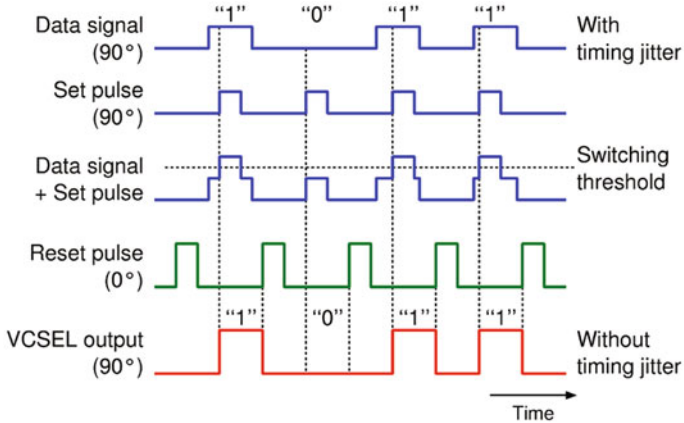
Fig. 1.6 Principle of all-optical retiming using polarization bistability

are both set to less than the polarization switching threshold of the VCSEL. When the data signal and set pulse are injected simultaneously, the injection power exceeds the polarization switching threshold and the lasing polarization of the VCSEL switches from 0 to 90°. When the reset pulse is injected, the lasing polarization returns to 0°. The regenerated signal is obtained by passing the output signal of the VCSEL through a polarizer with its polarization axis orientated at 90°; this regenerated signal has the same bit pattern as the data signal. The rise and fall timings of the output signal are mainly determined by the timings of the set pulse and the reset pulse, even when the data signal has timing jitter. Thus, the timing jitter of the data signal is reduced by the all-optical signal regeneration. In addition, all-optical signal regeneration can be used for signal reshaping, since the polarization switching has a threshold characteristic with respect to the injection power and a bistable memory effect.

Figure 1.7 shows the results of a timing jitter experiment. The peak powers of the data signal, set pulse, and reset pulse were 4.0, 4.4, and 16 μW, respectively. The waveforms were bandwidth-limited by a 2-GHz Gaussian digital filter to reduce the noise of the APD. The VCSEL described in reference [10] was used, and the figure shows that the peak-to-peak timing jitter in the data signal was 2 ns, but only 0.7 ns in the output signal. Therefore, successful retiming was achieved by performing all-optical signal regeneration. The amplitude noise of the VCSEL's output was mainly caused by the noise from the APD. The output power of the VCSEL was low (~ 28 μW), and the input power to the APD was attenuated by losses due to the optical components and coupling to the fiber. The reason why the amplitude noise of the VCSEL output was bigger than that of the data signal is that the APD-input optical power was much smaller than that for the data signal. If a higher-power VCSEL is used instead in a setup like this, the signal-to-noise ratio of the regenerated signal will be enhanced by a factor of 20 or more.

Furthermore, a calculation that includes random fluctuations in the polarization switching threshold and bandwidth limitation for the response to the injection light
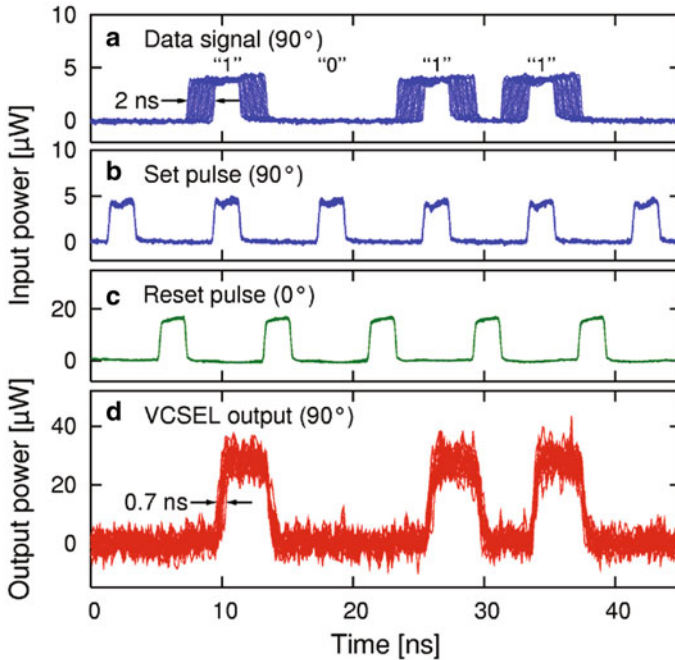
Fig. 1.7 Experimental results of all-optical retiming. The set pulse power was optimized so as to minimize the timing jitter. (From [9])

has shown that the timing jitter can be reduced to point that would enable retiming for a higher bit rate of 10 Gb/s at an operation current of 20 mA and a threshold current of 0.3 mA.

1.4 Use as a Memory

1.4.1 Principle of Operation

A novel optical buffer memory with a shift register function can be made from a two-dimensional (2D) array of polarization-bistable VCSELs in which the bit state of the optical signal, "0" or "1", is stored as a lasing linear polarization state of 0° or 90° (Fig. 1.8) [2]. One-bit optical buffering, which is an essential part of the memory, has been experimentally demonstrated using a 980-nm polarization-bistable VCSEL having a mesa structure.

The polarizations of the VCSELs in the first column ($M_{1 \times}$) are reset to 0° by injection of an optical reset pulse with 0° polarization. The ultrafast optical signal is converted into spatially parallel signals with a time-to-space converter, and the parallel signals are injected into the VCSELs together with optical set pulses. The
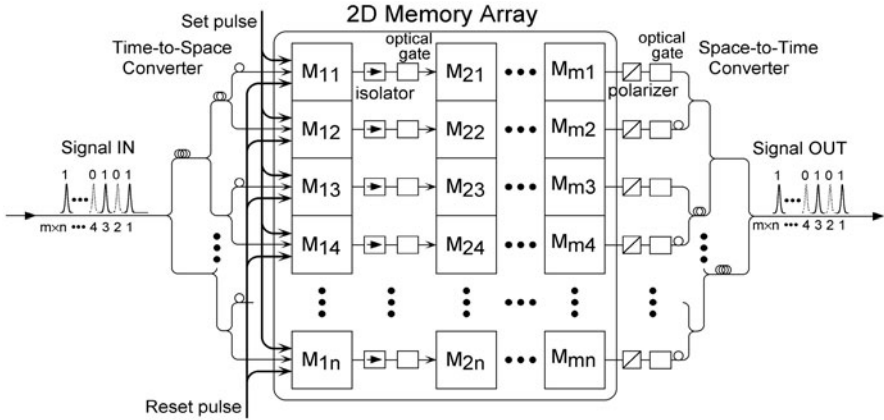
Fig. 1.8 Optical buffer memory with shift register function
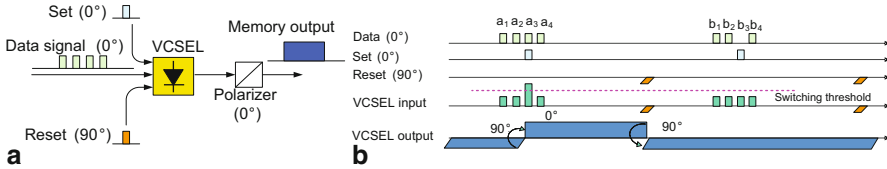
Fig. 1.9 1-bit buffering using polarization-bistable VCSEL. **a** Implementation and **b** timing chart

power of the optical signals representing "1" and that of the optical set pulse are weaker than the polarization switching threshold, but the sum of their powers exceeds the threshold. Thus, the VCSELs only change polarization (from $0°$ to $90°$) when the optical signals representing "1" and the optical set pulses are simultaneously injected into the VCSELs (i.e., AND gate operation). The output of each VCSEL of the first column is thus polarized depending on the bit state ("0" or "1") of the input signal that is simultaneously injected with the set pulse. The optical gates between the first column (M_{1x}) and second column (M_{2x}) are then opened, and the optical outputs of M_{1x} are injected into M_{2x} via optical isolators. The data stored in M_{1x} are transferred to M_{2x} and held there, since the polarizations of the M_{2x} array switch to match those of M_{1x}. Only the $90°$ outputs from the VCSELs of the last column (M_{mx}) transmitted through the polarizers. The output signal pulses are created from the CW outputs of the VCSELs by using optical gates, and are converted back into an ultrafast optical signal by using a space-to-time converter.

The AND gate and one-bit memory functions are achieved as follows (Fig. 1.9). The $90°$ ($0°$) polarization state of the polarization-bistable VCSEL is used to store "0" ("1") of the target bit in the data signal. Initially the polarization state is preset to $90°$ by injecting a reset pulse. Then a data signal with a $0°$ polarization direction is injected into the VCSEL. The injection power of the data signal is set to less than the polarization-switching threshold. A set pulse with a $0°$ polarization direction is

also injected. If the set pulse is injected at the same time as the "1" data signal and the combined injection power of the data and set pulses exceeds the polarization-switching threshold, the polarization state of the VCSEL switches from 90° to 0°. In this way, the polarization state of the VCSEL reflects the "0" or "1" of the target bit in the data signal. A polarizer placed after the VCSEL converts the polarization switching of the output light into on/off switching. The stored "0" or "1" of the target bit can be read out using an optical gate device at any timing.

1.4.2   Operating Conditions of Memory

If the carrier frequency of the data signal f_{data} is close to the oscillation frequency of the VCSEL f_0, the injected data signal remains in the VCSEL cavity for a long time [11]. Thus, the remaining pulses cause undesired switching when the bit length of the data signal is long. One solution for this problem is to increase the frequency detuning Δf (= $f_{data} - f_0$). A larger frequency detuning requires higher data signal power P_{data} for polarization switching to occur [12]. Therefore, it is important to understand the conditions for correct memory operation in terms of the $\Delta f - P_{data}$ relation.

A simulation and experiment were undertaken to investigate operating conditions for the memory to buffer 20-Gb/s, 2^6-1-bit pseudorandom bit sequence (PRBS) RZ data signals (Fig. 1.10). The solid lines show the minimum data power necessary to cause polarization switching by injection of a 25-ps one-bit "1" data signal and a 25-ps set pulse. This simulation assumed that the powers of the set pulse and the data signal were the same. The wavelength tolerance of the input optical pulse was wider on the longer wavelength side [12]. The dotted lines show the minimum switching power of a one-bit "1" data signal without a set pulse. The dashed lines show the switching thresholds of a long data signal (2^6-1-bit, PRBS) without a set pulse. When the data signal power is below the solid line, polarization switching does not occur even if the one-bit "1" data signal and set pulse are injected simultaneously. Thus, a "1" data signal cannot be stored. When the data signal power is above the dashed line, on the other hand, successive injection of the 2^6-1-bit PRBS data signal without the set pulse will cause undesired polarization switching. Furthermore, the one-bit "1" data signal will cause undesired polarization switching when the data signal power is above the dotted line. Therefore, the solid line indicates the lower limit of injection power and the dashed line indicates the upper limit of injection power for proper operation. The shaded regions enclosed by these two limit curves are thus the operating conditions, and the frequency detuning in this case should be set to $\Delta f < -24$ GHz.

1.4.3   Buffering 20-Gb/s PRBS RZ and 40-Gb/s NRZ Signals

The 980-nm VCSEL described in reference [10] was used to perform a one-bit memory operation for 20-Gb/s PRBS RZ data signals [13, 14]. It consisted of a three-quantum well $In_{0.18}Ga_{0.82}As/GaAs$ active layer and DBR mirrors. The cross
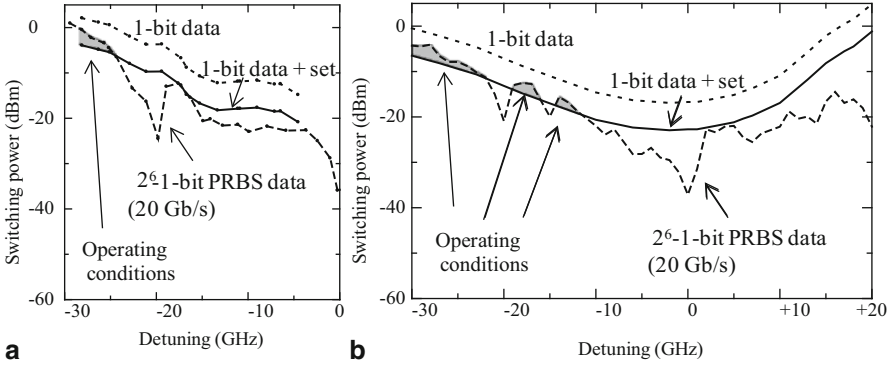
Fig. 1.10 Operating conditions for 20-Gb/s PRBS RZ data input. **a** Measured and **b** simulated. (From [13])

section of the square mesa was $6 \times 6 \ \mu m$. The bias current was set to about 9.28 mA in the bistable region. In the experiments, the maximum peak powers of the data signals and set pulses were 250 and 190 μW, respectively. The output power of the VCSEL was about 430 μW. The wavelength detuning of the data signal against the lasing wavelength of the $0°$ polarization mode was about $+ 74$ pm, which corresponds to $\Delta f = -22.9$ GHz. The wavelength detuning and power of the data and set pulses were about the same as the operating conditions shown in Fig. 1.10a. The wavelength detuning of the reset pulses against the lasing wavelength of the $90°$ polarization mode was about $+ 13$ pm ($\sim - 4.0$ GHz). The peak power of the reset pulses was set to 55 μW. This all-optical memory operation had an optical gain even for such a high data rate; *i.e.*, the VCSEL output power (430 μW) was higher than the data signal power (250 μW).

Figure 1.11 shows the results of storing 2^6-1-bit PRBS data signals. For the data signals in three successive groups (1)–(3), three set pulses were positioned to sample "0", "0", and "1" data at the beginning of each group (left part of Fig. 1.11b). The $0°$ polarization component of the VCSEL output is shown in the left part of Fig. 1.11c. When the "0" data signal and the set pulse were injected simultaneously (*i.e.*, only the set pulse was injected), switching did not occur. When the "1" data signal and the set pulse were injected simultaneously, polarization switching from the $90°$ state to $0°$ state was triggered. The polarization state returned to $90°$ when the reset pulse was injected. The middle and right parts of the figure show the results when the timing of the set pulses was changed. The three bits (middle and right parts of Fig. 1.11c) could be sampled by changing only the timing of the set pulses, without changing the power or the wavelength. These results show the ability of the current polarization-bistable VCSEL memory to handle 20 Gb/s RZ data signals.

A similar memory operation was also demonstrated for 6-bit 40-Gb/s NRZ signals. However, because of the limitations of the input optical power (250 μW for the data signals and 190 μW for the set pulses), the wavelength detuning of the data signals and set pulses against the VCSEL output light was limited to about $+ 63$ pm
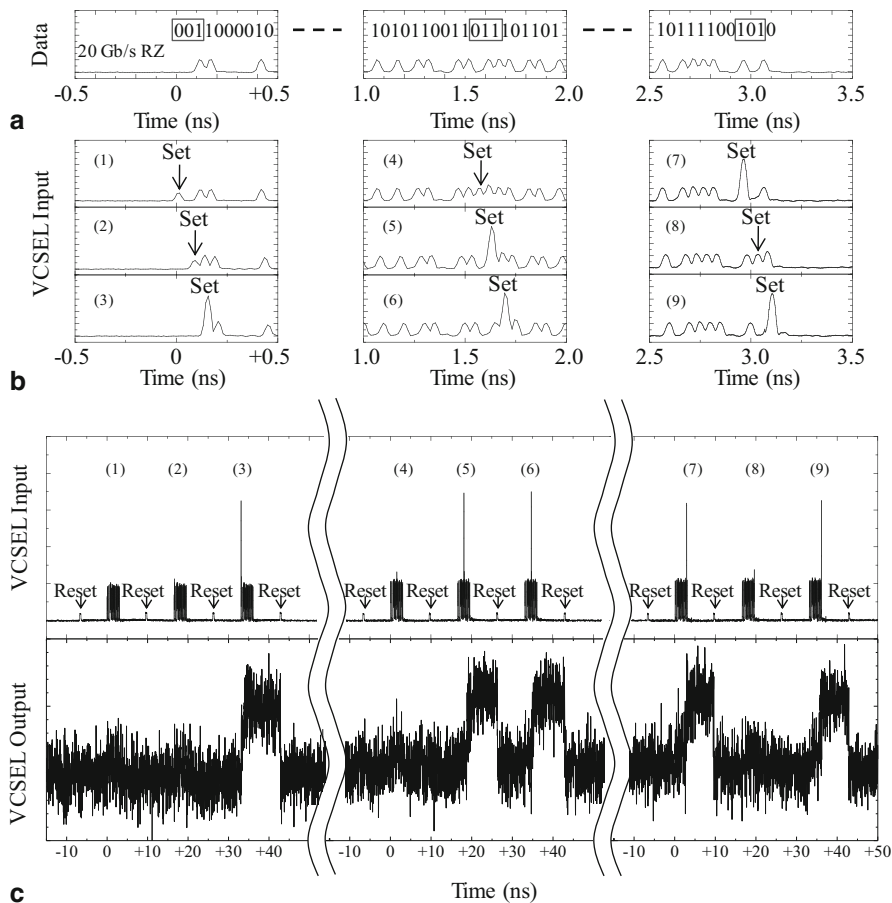
Fig. 1.11 Buffering 20-Gb/s, 2^6-1-bit PRBS RZ data signals. **a** Magnified data signal without set pulses (*top*) and VCSEL input (*bottom*), **b** VCSEL input, and **c** VCSEL output with 0° polarization. (From [13])

($\Delta f \sim -19.6$ GHz). The output power of the VCSEL in this case was about 320 μW, and the memory operation also had an optical gain.

1.4.4 Four-Bit Optical Buffer Memory

An experiment was conducted on four-bit optical buffer memory constructed from two optical buffer memories with shift register functions made from four 1.55-μm VCSELs [15]. In this memory, the shift registers are connected in parallel between a time-to-space converter and a space-to-time converter, as shown in Fig. 1.12. The four-bit data signal is divided into two (data signals A and B) and injected into
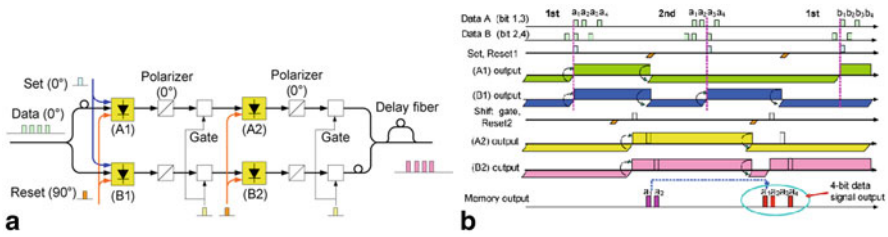
Fig. 1.12 4-bit optical buffer memory with a parallel shift register: **a** implementation and **b** timing chart

VCSEL(A1) and VCSEL(B1). Data signal A for A1 is delayed by a one-bit period. Thus, the first bit of the data pulse and the set pulse are simultaneously injected into A1. The second bit and the set pulse are simultaneously injected into B1. These bits are stored in each VCSEL. Then, the first and second bit signals are transferred to VCSEL(A2) and VCSEL(B2), respectively, by opening the shift register gates. After the transfer, A1 and B1 are reset and become available for storing the third and fourth bit data signals. The output pulses from A2 and B2 are created by opening the output gates. The output pulse from B2 is delayed for a one-bit period and combined with the output pulse from A2. Since two memories were connected in parallel in this experiment, the guard time between the first (bits 1 and 2) and second sets (bits 3 and 4) of the data signal is only a one-bit period. This guard time is too short to transfer the data from A1 to A2 and from B1 to B2 and reset A1 and B1. In the experiment, the four-bit data signal was input twice, and the first and second bits were stored using the first four-bit data signal, and the third and fourth bits were stored using the second four-bit data signal. To obtain exactly the same pattern as the input four-bit data signal, a delay line that corresponded to the interval in time between the two sets of four-bit data signals was added to the space-to-time converter. If the parallel scale of this setup is increased, it will be possible to store and read out the whole data signal using one data signal train .

Experimental results are shown in Fig. 1.13. The data signals consisted of four optical pulses that corresponded to 500-Mb/s RZ signals. The lasing wavelengths of the four polarization-bistable VCSELs were adjusted by controlling their device temperatures. However, the wavelength of the input pulse for the minimum switching power differed by several GHz for the set and reset operations, and this wavelength difference slightly depended on the device. Therefore, the input power of the reset pulses was increased from the minimum switching power for stable simultaneous operation of the VCSELs. As described before, the four-bit data signal was input twice. The four bits of the data signal were stored in the four VCSELs at the same time. The memory output power was much larger than the input data power. For example, the optical power of the data signal was 1.8 μW at the front of A1, whereas the output power of A2 was 680 μW. The input power of the four-bit data signal and the output power of the four-bit memory were estimated to be 12 and 24 μW, respectively, taking account of the losses of the 3-dB couplers and other optical
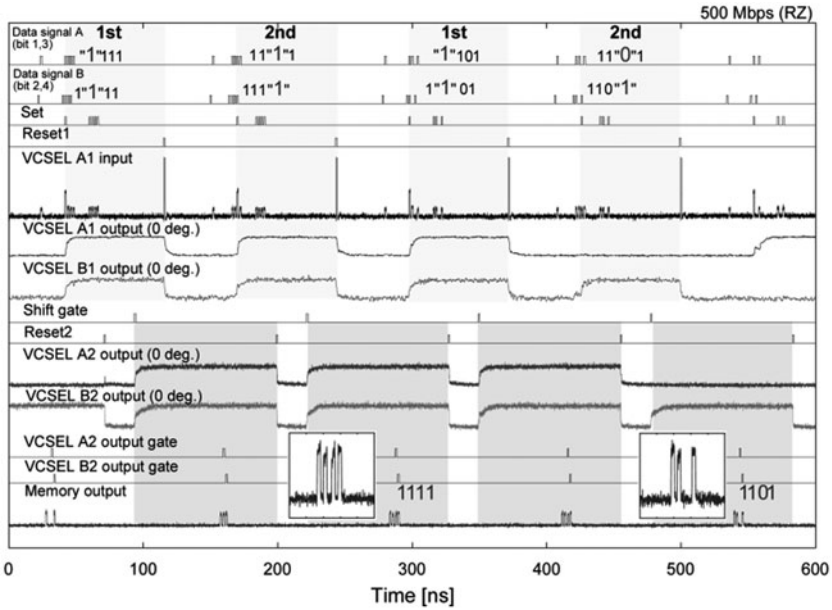
Fig. 1.13 Experimental results for 4-bit optical buffer memory with a parallel shift register. The 4-bit data signal was stored and the same signal pattern was read out. (From [15])

components. These results demonstrate the technical feasibility of multi-bit optical buffer memory without optical amplifiers.

1.5   All-Optical Header Recognition and Packet Switching

The concept of optical header recognition using a polarization-bistable VCSEL is shown in Fig. 1.14 [16]. The data signal and set pulse have 0° polarization, and the reset pulse has 90° polarization. All three of these signals are injected into the polarization-bistable VCSEL. The injection powers of the data signal and set pulse are set to less than the polarization switching threshold of the VCSEL, but when the data signal and set pulse are simultaneously injected, the injection power exceeds the polarization switching threshold and the lasing polarization switches from 90° to 0°. The lasing polarization is held at 0° until the reset pulse is injected. The light output from the VCSEL is put through a polarizer with its polarization axis oriented at 0° and then it is input to the control port of an all-optical switch such as a semiconductor optical amplifier Mach-Zehnder interferometer to switch the output port from the original one to another. Thus, the output of the payload is switched between output ports 1 and 0 depending on the state of one bit in the header (in this case, the second bit).
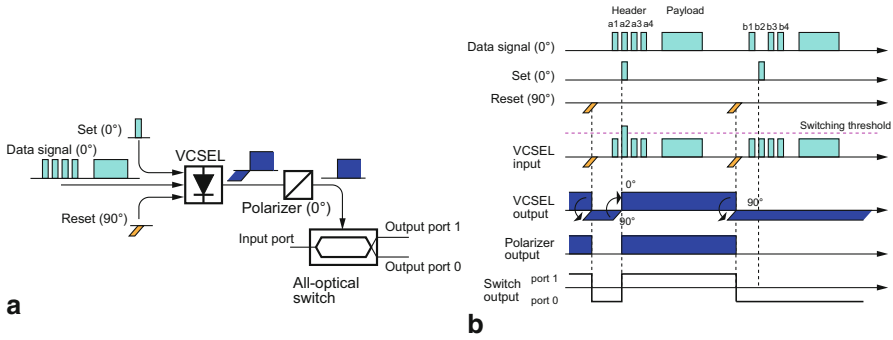
Fig. 1.14 Operation principle of optical header recognition. **a** implementation and **b** timing chart

The experimental setup is shown in Fig. 1.15. A 1.55-μm polarization-bistable VCSEL described in Reference 15 was used. The data signals consisted of the header and the payload. The format of the header was 500-Mb/s RZ with a four-bit length. The payloads were 500-Mb/s RZ PRBS data signals as that were 2^4-1-bits long. The 1-ns set pulses were generated by the same tunable laser as was used for the data signal. In order to recognize the second bit of the header, the timing of the set pulses was adjusted to the second bit of the headers and the set pulses were combined with the data signals. The data signals were divided and coupled to two fibers: one connected to the polarization-bistable VCSEL and the other to the optical switch. The light for the reset pulses was generated by another tunable laser. The wavelengths of these optical pulses were adjusted individually to operate with as low an injecting power as possible. The reset pulses with 90° polarization were combined with the data pulses with 0° polarization and the set pulses with 0° polarization with a polarization beam combiner (PBC). The polarization states of these pulses stayed the same as they were put through a circulator and into the VCSEL. The VCSEL output was passed through a polarizer with its polarization axis oriented at 0°; thus, it went through the polarizer when the second bit of the header was '1' and continued to go through until the reset pulse was sent. Due to limitations imposed by the instrumentation, this experiment used a 20-GHz photodiode and a 16-GHz LiNbO$_3$ switch (LNSW) instead of an all-optical switch. An EDFA and RF amplifier were used to obtain suitable signal levels for the LNSW.

The injection current of the VCSEL was set to 7.35 mA. The VCSEL exhibited polarization-bistable characteristics under this condition. The peak powers (pulse energies) of the data pulses, set pulses, and reset pulses at the VCSEL input were 0.5 μW (0.5 fJ), 0.6 μW (0.6 fJ), and 2.9 μW (2.9 fJ), respectively. The optimum frequency detuning of the data and set pulses was − 0.3 GHz from the lasing frequency of the VCSEL and that of the reset pulses was − 0.5 GHz.

The experimental results are shown in Fig. 1.16. When the second bit of the header was "1", VCSEL output light was observed through the 0° polarizer (VCSEL output (0°)). Therefore, when the headers were "1001" and "1011", the payloads were output from port 0 of the LNSW. In contrast, when the headers were "1101"
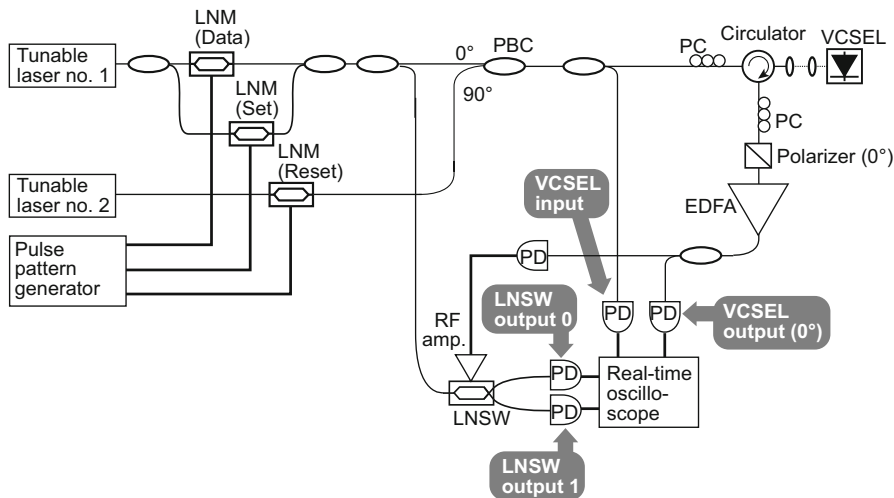
Fig. 1.15 Experimental setup. (From [16])

and "1111", the payloads were output from port 1. First, the operation principle of the system was demonstrated at a low bit rate of 500 Mb/s. In this experiment, the delay time between the VCSEL output and the LNSW output was set by adjusting the optical fiber length in order to separate the payloads from the headers.

The experiment then proceeded with optical header processing that switched 2^{11}-1 bits PRBS 40-Gb/s NRZ payloads to a designated port depending on the state of an arbitrarily chosen bit of the four-bit header in 500-Mb/s RZ format.

1.6 Summary

This chapter reviewed recent progress in polarization-bistable VCSELs and their applications. A 980-nm polarization-bistable VCSEL with an oxide current confinement structure was used to perform an all-optical flip-flop operation at an extremely low bias current of 0.85 mA. Furthermore, an ultrafast all-optical one-bit memory for 20-Gb/s RZ and 40-Gb/s NRZ signals was made and tested. A four-bit optical buffer memory with two shift-register memories connected in parallel was made from 1.55-μm polarization-bistable VCSELs. Finally, an optical header processing system was built to send a payload to the destination determined by the header. Together, these research achievements show the potential of using polarization-bistable VCSELs in future ultrafast all-optical networks.

In 2013, the author and his colleagues developed a high-index-contrast subwavelength grating (HCG)-VCSEL incorporating a polarization-independent HCG [17] coupled with two orthogonal in-plane output waveguides and numerically investigated the optical output characteristics from the waveguides [18]. The light coupled
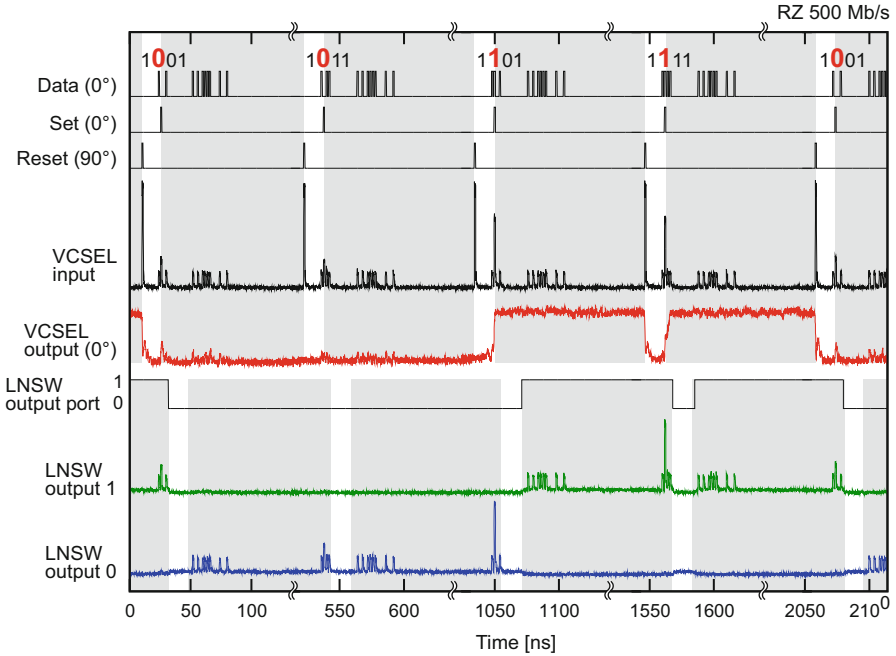
Fig. 1.16 Experimental results of header recognition and packet switching. (From [16])

more strongly to the waveguide in the direction perpendicular to the polarization of
the resonant mode than to that in the parallel direction. The propagating modes in the
strongly and weakly coupled waveguides were the TE and TM modes, respectively.
We also designed and fabricated a VCSEL incorporating a polarization-independent
HCG mirror on silicon-on-insulator (SOI) for a novel polarization-bistable de-
vice on a silicon substrate. The VCSEL consisted of the HCG mirror, an active
layer with InGaAsP quantum wells having optical gain around 1.55 μm, and an
$Al_{0.9}Ga_{0.1}As/Al_{0.16}Ga_{0.84}As$ DBR. We used direct wafer bonding for the bond-
ing between an active layer and an AlGaAs DBR, and benzocyclobutene (BCB)
bonding for the bonding between the active layer and a polarization-independent
HCG. The reflectivity of the HCG embedded with BCB was measured, resulting
in a 200-nm-high reflectivity band with reflectivity higher than 99 % and a small
polarization dependence of ± 1 %. The fabricated HCG-VCSEL lased under an op-
tical short pulse excitation [19]. This new type of VCSEL likely has polarization
bistable characteristics and may be suitable for use in optical memories and optical
interconnects.

References

1. Kawaguchi, H.: Bistabilities and Nonlinearities in Laser Diodes. Artech, Norwood (1994)
2. Kawaguchi, H., Mori, T., Sato, Y., Yamayoshi, Y.: Optical buffer memory using polarization bistable vertical-cavity surface-emitting lasers. Jpn. J. Appl. Phys. Express Lett. **45**(34), L894–L897 (2006)
3. Kawaguchi, H.: Polarization bistable vertical-cavity surface-emitting lasers-application for bit memory. Opto-electron. Rev. **17**(4), 265–274 (2009)
4. Calabretta, N., Jung, H.-D., Tangdiongga, E., Dorren, H.: All-optical packet switching and label rewriting for data beyond 160 Gb/s. IEEE Photon. J. **2**(2), 113–129 (2010)
5. Sawada, K., Uenohara, H.: High-speed optical label recognition technique using an optical digital-to-analog conversion and its application to optical label switch. IEEE J. Lightwave Technol. **28**(13), 1889–1896 (2010)
6. Takenaka, M., Takeda, K., Kanema, Y., Nakano, Y., Raburn, M., Miyahara, T.: All-optical switching of 40 Gb/s packets by MMI-BLD optical label memory. Opt. Express. **14**(22), 10785–10789 (2006)
7. Kawaguchi, H.: Bistable laser diodes and their applications: State of the art. IEEE J. Sel. Top. Quantum. **3**(5), 1254–1270 (1997)
8. Katayama, T., Yanai, A., Yukawa, K., Hattori, S., Ikeda, K., Koh, S., Kawaguchi, H.: All-optical flip-flop operation at 1-mA bias current in polarization bistable vertical-cavity surface emitting lasers with an oxide confinement structure. IEEE Photon. Technol. Lett. **23**(12), 1811–1813 (2011)
9. Mori, T., Sato, Y., Kawaguchi, H.: Timing jitter reduction by all-optical signal regeneration using a polarization bistable VCSEL. IEEE J. Lightwave Technol. **26**(6), 2946–2953 (2008)
10. Sato, Y., Mori, T., Yamayoshi, Y., Kawaguchi, H.: Polarization bistable characteristics of mesa structure 980 nm vertical-cavity surface-emitting lasers. Jpn. J Appl. Phys. **45**, L438–L440 (2006)
11. Mori, T., Kawaguchi, H.: 10-Gb/s optical buffer memory using a polarization bistable VCSEL. IEICE Trans. Electron. **E92C**, 957–963 (2009)
12. Mori, T., Yamayoshi, Y., Kawaguchi, H.: Low-switching-energy and high-repetition-frequency all optical flip-flop operations of a polarization bistable vertical-cavity surface-emitting laser. Appl. Phys. Lett. **88**, 101102 (2006)
13. Sakaguchi, J., Katayama, T., Kawaguchi, H.: All-optical memory operation of 980-nm polarization-bistable VCSEL for 20-Gb/s PRBS RZ and 40-Gb/s NRZ signals. Opt. Express **18**(12), 12362–12370 (2010)
14. Sakaguchi, J., Katayama, T., Kawaguchi, H.: High switching-speed operation of optical memory based on polarization bistable vertical-cavity surface-emitting laser. IEEE J. Quantum Electron. **46**(11), 1526–1534 (2010)
15. Katayama, T., Ooi, T., Kawaguchi, H.: Experimental demonstration of multi-bit optical buffer memory using 1.55-μm polarization bistable vertical-cavity surface-emitting lasers. IEEE J. Quantum Electron. **45**(11), 1495–1504 (2009)
16. Katayama, T., Okamoto, T., Kawaguchi, H.: All-optical header recognition and packet switching using polarization bistable VCSEL. IEEE Photon. Technol. Lett. **25**(9), 802–805 (2013)
17. Ikeda, K., Takeuchi, K., Takayose, K., Chung, I.-S., Mørk, J., Kawaguchi, H.: Polarization-independent high-index contrast grating and its fabrication tolerances. Appl. Opt. **52**(5), 1049–1053 (2013)
18. Tsunemi, Y., Ikeda, K., Kawaguchi, H.: Lasing-polarization-dependent output from othogonal waveguides in high-index-contrast subwavelength gating vertical-cavity surface-emitting laser. Appl. Phys. Express **6**(9), 092106-1∼4 (2013)
19. Tsunemi, Y., Yokota, N., Majima, S., Ikeda, K., Katayama, T., Kawaguchi, H.: 1.55-μm VCSEL with a polarization-independent HCG mirror on SOI. Opt. Express. **21**(23), 28685–28692 (2013)

Chapter 2
Tunable Lasers Based on Multimode Interference Effects

Daniel A. May-Arrioja, José E. Antonio-Lopez, José J. Sanchez-Mondragón and P. LiKamWa

Abstract We review the development of multimode interference (MMI) based wavelength tunable fiber lasers. The key advantages of MMI devices as tunable filters are its band-pass spectral response and the simplicity in their fabrication. Different approaches are reviewed in an effort to achieve wide tuning ranges. The maximum tuning range is close to 90 nm and a side-mode suppression ratio (SMSR) better than 50 dB is demonstrated with a single MMI filter. The wide tuning range demonstrates the potential of MMI devices for tunable laser applications.

2.1 Introduction

Fiber laser systems have received a great deal of interest due to their significant advantages as compared to their bulk counterparts. Due to their all-fiber configuration, inclusion into tunable fiber lasers is straight-forward and result in very stable, compact and robust laser systems. These lasers can also achieve very high output powers over a wide span of lasing wavelengths due to the availability of a variety of different gain media. Another feature that makes fiber lasers highly attractive for telecommunications and sensing applications is the ability to tune the lasing wavelength over a broad range. Over the years many different techniques have been proposed and demonstrated such as bulk gratings [1], fiber Bragg gratings [2–4], Mach-Zehnder interferometer [5], and Fabry Perot cavities [6–8]. The main issues with such techniques are that they are either expensive due to the fabrication process or require complex setups in which alignment issues could make the laser highly sensitive to environmental conditions.

D. A. M.-Arrioja (✉)
Fiber and Integrated Optics Laboratory, UAMRR Universidad Autónoma de Tamaulipas, 88779 Reynosa, TAMPS, México

J. E. A.-Lopez · P. LiKamWa
CREOL The College of Optics and Photonics, University of Central Florida, Orlando, FL 32816-2700, USA

J. J. S.-Mondragón
Instituto Nacional de Astrofísica, Óptica y Electrónica, A.P. 51 y 216, 72000 Tonantzintla, PUE, México

A device that is based on multimode interference (MMI) effects, has lately been successfully employed as a tunable filter for fiber laser applications. The main features of a MMI device are that it exhibits a band-pass spectral response with minimal transmission loss at the peak of the band and its fabrication is very simple. In fact since a MMI is fabricated by basically splicing a section of multimode fiber (MMF) between two single mode fibers (SMF), we do not require expensive or elaborate fabrication processes. This chapter provides an overview of the different techniques that have been used to achieve wavelength tunable lasers based on MMI effects.

2.2 Multimode Interference in Optical Fibers

The development of photonic devices based on multimode interference (MMI) effects was initially fueled by applications in the field of integrated optics [9–11]. This was mainly related to the great flexibility on the design of multimode waveguides (MMW) of almost any size and shape, input and output waveguides at any desired position, as well as active control via electro-optic and thermo-optic effects [12–14]. Since the only requirement to observe MMI effects is to have a MMW, a variety of applications have been recently developed using MMI effects in MMF such as sensors for different applications [15–19]. Here we provide an overview of the basic concepts behind the self-imaging process in MMI devices, as well as its potential application as a tunable filter for the development of tunable lasers.

2.2.1 Multimode Interference Effect

The key requirement in order to observe MMI effects in optical fibers is to use a MMF that is designed to support several modes (typically ≥ 3). This can be easily achieved in optical fibers using either commercial or specialty MMF. When light is coupled into the MMF, the modes that are supported by the MMF are excited and the interference between the propagating modes gives rise to an interference pattern along the MMF. At certain positions light is concentrated along the central axis of the MMF forming replicas of the input field known as self-images. The formation of such self-images can be better observed by using the commercial beam propagation software BeamPROP from the company RSoft. Here light propagates in a short segment of SMF that is spliced to another section of MMF. The parameters used in the simulations consists of a standard SMF (SMF-28) with a core diameter of 9 μm, and core and cladding refractive index (RI) of 1.4504 and 1.4447 at 1550 nm, respectively. The MMF is a special fiber known as No-Core fiber, which is a solid optical fiber with air effectively as its cladding. The No-Core MMF has a diameter of 125 μm and a RI of 1.4440 at 1550 nm. As shown in Fig. 2.1, after the light with a wavelength of 1550 nm is coupled into the No-Core MMF, we can observe the interference pattern as well as four positions (marked by arrows) where optical

Fig. 2.1 Light propagation in a MMI fiber device at 1550 nm. The arrows correspond to positions where images are formed
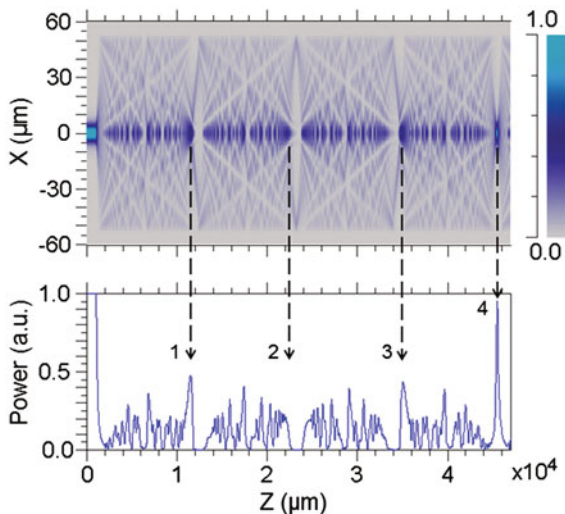
intensity is concentrated. By monitoring the transmitted intensity along the No-Core MMF axis with an area similar to that of the SMF, we can observe the quality of the images formed where the light is concentrated. The images labeled from one to three are known as pseudo-images. These images are formed due to the symmetric light coupling into the No-Core MMF and they exhibit more attenuation. The fourth image corresponds to the real self-image which exhibits significantly higher intensity as compared to the pseudo-images. Based on Fig. 2.1 it is clear that, if we manage to cleave the MMF exactly at the position where the self-image is formed and we splice a SMF, the light will be coupled to this output SMF with very low losses. Therefore, light at 1550 nm will be transmitted through this SMF-MMF-SMF device with negligible losses due to MMI effects.

2.2.2   Self-Imaging Properties

When light is coupled to a MMF that supports several modes, it is important to highlight that the number of excited modes is related to the transversal position where the light is coupled into the MMF. This has direct impact on the length at which the self-images are formed, as well as the number of self-images that are formed for a particular length. Typically, when a SMF fiber is spliced to a MMF using standard splicing procedures, the fundamental mode is coupled exactly at the center of the MMF. Under this condition light coupled in the MMF will be coupled preferentially to the modes that possess radial symmetry and only the LP_{0m} modes are excited in the MMF [20]. Due to the circular symmetry of the fundamental mode of the SMF, the input light can be assumed to have a field distribution of $\psi(r, \phi, 0)$, i.e. radial symmetry at $z = 0$. When the light is launched into the MMF, the input

field can be decomposed into the guided modes of the MMF as follows,

$$\psi(r,\varphi,0) = \sum_{\nu=1}^{m} c_\nu \phi_\nu(r,\varphi,0), \tag{2.1}$$

where m is the number of guided modes, $\phi_\nu(r,\varphi,0)$ is the electric field of the νth guided mode of the MMF, and c_ν is the mode expansion coefficient which can be determined using the overlap integral,

$$c_\nu = \frac{\iint \psi(r,\varphi)\phi_\nu(r,\varphi)ds}{\iint |\phi_\nu(r,\varphi)|^2 ds} \tag{2.2}$$

If we neglect mode conversion, we can assume that all the excited modes propagate independently inside the MMF. Therefore, we can obtain the field after propagating a distance z by

$$\psi(r,\varphi,z) = \sum_{\nu=1}^{m} c_\nu \phi_\nu(r,0)\, e^{-i\beta_\nu z}$$

$$= e^{-i\beta_1 z} \sum_{\nu=1}^{m} c_\nu \phi_\nu(r,0)\, e^{-i(\beta_\nu - \beta_1)z} \tag{2.3}$$

where β_1 and β_ν are the propagation constants of the fundamental and the νth guided mode in the MMF. We can observe from Eq. (2.3) that if the phase factor $(\beta_\nu - \beta_1)z$ is an exact multiple of 2π we obtain an exact replica of the input field. This distance corresponds, as we explained before, to the position where the self-image is formed.

An analytical solution can be obtained under the asymptotic formulation [21] by expressing the difference in the longitudinal propagation constants between two radial modes as a function of the MMF parameters (core RI and diameter) and the operating wavelength [22]. Therefore, by expressing the operating wavelength as a function of all other terms, the following expression is obtained,

$$\lambda_0 = p\frac{n_{MMF}D_{MMF}^2}{L_{MMF}} \quad with \quad p = 0, 1, 2, \ldots, \tag{2.4}$$

where λ_0 is the free space wavelength, L_{MMF} is the length of the MMF, n_{MMF} and D_{MMF} are respectively the effective RI and diameter of the fundamental mode. The factor p denotes the periodic nature of the imaging process along the MMF. Therefore, at every fourth image ($p = 4, 8, 12, \ldots$) we obtain the real self-image, and this is typically the position that we use for tuning applications. Other images obtained for any other value of p correspond to the pseudo-images. We can observe from Eq. (2.4) that the transmitted wavelength is inversely proportional to the MMF length. Therefore, we can control at will this wavelength by just changing the length of the MMF. We should also notice that the MMI response to variations in length is highly linear, which is good for tuning applications.
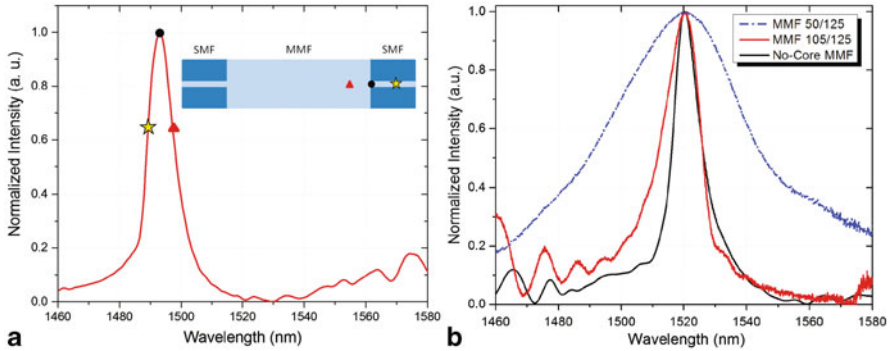
Fig. 2.2 a Spectral response of a MMI device (inset: self-image position along the MMF for different wavelengths) and **b** Spectral response of MMI devices with different MMF diameters

2.2.3   Spectral Response of MMI Devices

So far, we know that in a MMI device there is a particular wavelength that will be transmitted with very low attenuation, and that wavelength can be selected by setting the particular length of the MMF section. However, the most interesting property of MMI devices is in their spectral responses. In order to obtain the transmitted MMI intensity as a function of wavelength we use a tunable laser with a spectral range spanning from 1460 to 1580 nm. The laser beam is coupled to the MMI device and its wavelength is scanned while maintaining a constant intensity, and the transmitted power is measured using a photo-detector. As shown in Fig. 2.2a, the response exhibits a band-pass filter response whose peak wavelength is exactly the design wavelength as dictated by Eq. (2.4).

The band-pass behavior of the MMI device can be explained as follows. As shown in the inset of Fig. 2.2a, the peak wavelength exhibits maximum transmission because the MMI was designed to operate at such wavelength, and the self-image is formed right at the output MMF-SMF interface (circle). Any other wavelength will form a self-image before (longer wavelength, triangle) or after (shorter wavelength, star) the MMF-SMF interface, which will significantly reduce the light coupled to the output SMF. The diameter of the MMF also plays a significant role on the bandwidth of the band-pass filter. As shown in Fig. 2.2b the bandwidth is reduced when the diameter of the MMF is increased. The only drawback in this case is that a longer MMF is needed to obtain the same peak transmission wavelength. Therefore, there is a trade-off between diameter and length of the MMF in order to fabricate a MMI device with an optimum length. The band-pass filter response of the MMI presents itself as being ideal for wavelength tuning of lasers if the wavelength of the MMI peak transmission can be tuned in real time.
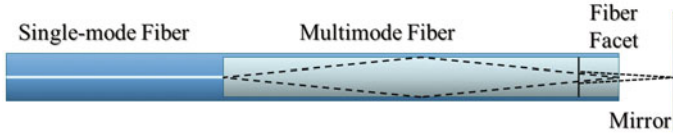
Fig. 2.3 Schematic of the free space wavelength tuning MMI device

2.3   Mechanically Tunable MMI Fiber Lasers

Based on Eq. (2.4), it is clear that in order to tune the MMI peak wavelength we have
limited options. A straightforward approach is to attempt to increase or decrease in
real time the length of the MMF. Since the peak wavelength is inversely proportional
to the MMF length we should also obtain a linear response which is beneficial for
developing tunable lasers.

2.3.1   Free Space Tunable Laser

In order to change the MMF length in real time the tuning mechanism of Fig. 2.3 was
proposed [23]. The basic idea is to calculate the MMF length where the self-image
will be formed for the operating wavelength using Eq. (2.4). Then, we cleave the
MMF at a length slightly shorter than the self-image distance. Therefore, the light
exiting the MMF will converge to a point beyond the fiber facet (in air) and forms a
beam waist with a plane wavefront. If a mirror is placed at this free-space location
where this self-image point occurs, the light will be reflected back into the MMF and
the operating wavelength will be coupled back to the input SMF fiber. Since the self-
image position is wavelength dependent, by changing the position of the mirror along
the MMF axis we can control the MMI peak transmission wavelength. Therefore,
this effect can be used to select a specific wavelength from a broad spectrum by
simple changing the position of the mirror. A broadband mirror is needed to operate
the device over a wide wavelength range.

   Using a beam propagation method the first pseudo-image is found to be formed at
a distance of 15.2 mm for a standard 105/125 MMF at a wavelength of 1080 nm. In
the experiments, the MMF was then cleaved at 15 mm. The tuning mechanism was
used to fabricate a wavelength tunable double-clad fiber laser. As shown in Fig. 2.4
it consists of a double-clad Ytterbium-doped fiber (DCYDF) with a core/cladding
diameter of 6/125 μm and a 0.14/0.45 numerical aperture [24]. The length of the
DCYDF was 16 m, which corresponds to 7.2 dB of pump absorption (only ∼80 %
of the pump light is absorbed by the active core). The DCYDF is end-pumped by a
fiber pig-tailed multi-mode laser diode with 3 W of fiber-coupled output power at a
wavelength of 915 nm. As can be seen in Fig. 2.4, the pump light was launched into
the DCYDF via a focusing lens that has a broadband anti-reflection coating covering
the pump wavelength. The end of the DCYDF used for pumping was cleaved to
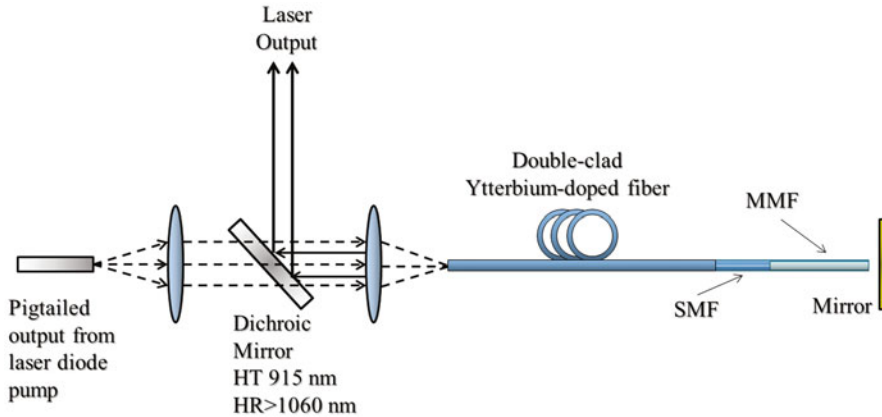
Fig. 2.4 Schematic of Ytterbium doped tunable fiber laser

provide feedback for laser oscillation, and also to operate as the output coupler for the laser. The other end of the fiber was spliced to the SMF of the tuning mechanism. A dichroic mirror placed between the fiber pigtailed laser and the DCYDF is used to separate the laser output from the path of the pump beam.

As shown in Fig. 2.5, as the mirror is moved away from the MMF the laser emission is tuned to shorter wavelengths. A total tuning range of 8 nm and average output power of 500 mW is achieved. The main limitation of the tuning mechanism to obtain a wider tuning range is related to the alignment of the MMF facet with the mirror. If the MMI facet and the mirror are not perfectly parallel to each other, the propagation losses increase very rapidly and maintaining optimal alignment becomes increasingly difficult as their separation is increased. Nevertheless, this is an excellent proof of principle to demonstrate the feasibility of using a MMI filter to achieve wavelength tunable fiber lasers.

2.3.2   Ferrule Based Tunable Laser

A simple way to significantly reduce the free space alignment issues highlighted in the previous section is by using the tunable MMI filter configuration as shown in Fig. 2.6 [25]. In this setup the ferrule is filled with an index matching liquid whose RI is higher than that of the ferrule material but lower than that of the No-Core MMF. In this way, a liquid MMF (LMMF) is created inside the ferrule while the liquid RI is low enough and does not alter the waveguide properties of the No-Core MMF. Therefore, any gap between the SMF and MMF is now a LMMF, and this effectively increases the length of the MMF. By changing the separation between the SMF and MMF, we control the effective MMF length and thus wavelength tuning should be achieved. Given the tight tolerances of the ferrule and No-Core fiber dimensions, the
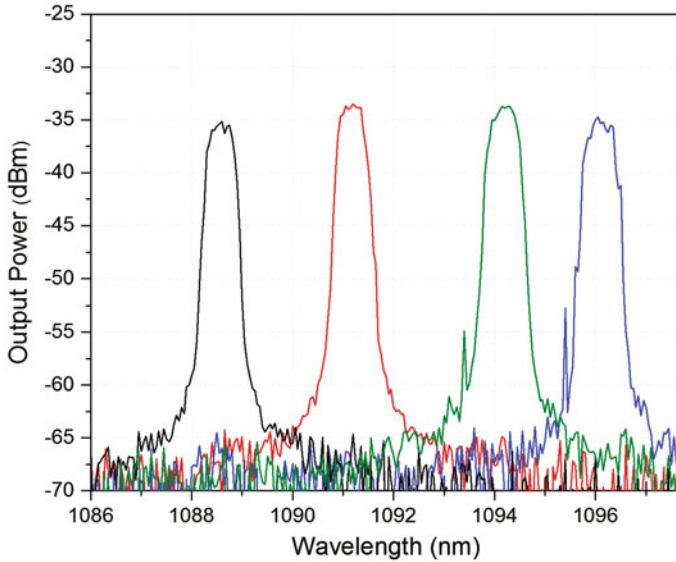
Fig. 2.5 Wavelength tuning characteristics of the double-clad Yb-doped fiber laser using the free space MMI tuning mechanism
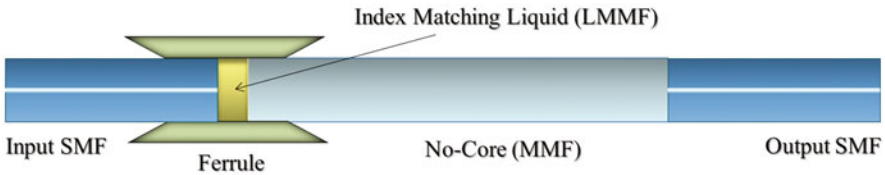
Fig. 2.6 Schematic of the ferrule based wavelength tuning MMI device

fibers are reasonably aligned in the transverse direction after their insertion into the ferrule. This also allowed us to move the fibers very smoothly along the propagation direction in order to tune the MMI filter.

The length of the fused silica ferrule (Polymicro Technologies) is 15 mm, with inner and outer diameters of 127 µm and 1700 µm respectively. The ends of the ferrule are flared to facilitate fiber insertion into the ferrule. The length of the No-Core fiber was 56 mm, which corresponds to a peak wavelength of 1611 nm, and the index controlled liquid RI was 1.442 (Cargille®). The tuning mechanism was characterized by first measuring the transmitted spectrum when the fibers inside the ferrule are in contact. The fibers are then separated in steps of 100 µm and the spectrum is acquired at each step. The MMI peak wavelength as a function of the separation of the fibers is shown in Fig. 2.7. A tuning range of 60 nm can be achieved with excellent linearity throughout the whole tuning range.
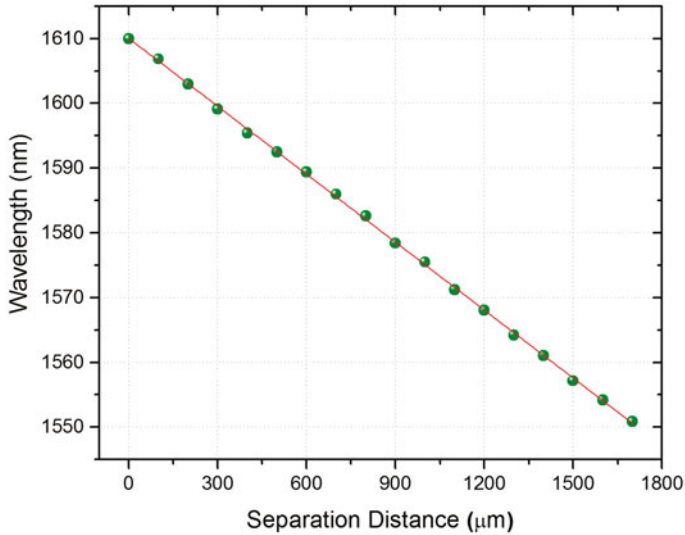
Fig. 2.7 Peak wavelength tuning range of the ferrule based tuning mechanism

The tuning mechanism was incorporated in an erbium-doped fiber laser (EDFL) with a standard ring cavity configuration, as shown in Fig. 2.8. The ring cavity is pumped by a 980 nm laser diode with 150 mW of maximum output power, which is coupled into the cavity using a 980/1550 wavelength division multiplexer (WDM). The WDM (port 3) was fusion-spliced with a 2.85 m long L-band Erbium-doped fiber (EDF) having a 0.25 NA and a concentration of 3000 ppm. The other cleaved end of the EDF was placed into the ferrule filled with liquid and works now as the input SMF into the MMI filter. The No-Core fiber spliced to the output SMF is inserted into the other end of the ferrule to complete the MMI filter. The output SMF in then spliced to a 10/90 coupler and the 90 % was spliced to an optical isolator to keep the ring cavity unidirectional. The ring cavity is closed by connecting the isolator output to the WDM (port 2). The 10 % output from the 10/90 coupler is used to monitor the laser output via an OSA. The laser was operated at the maximum pump power of 150 mW and the maximum laser output power was close to 1 mW. As shown in Fig. 2.8b the laser exhibits a total tuning range of 60 nm covering a wavelength range from 1549 nm to 1609 nm. The laser linewidth is close to 0.4 nm with a signal-to-noise (SNR) of 40 dB.

2.4 Optofluidically Tunable MMI Fiber Laser

An alternative way to tune the MMI peak transmission wavelength, as revealed in Eq. (2.4), is by modifying the effective RI and/or the diameter of the MMF. Heating the MMI device to achieve tuning via thermo-optics effects is not an option because
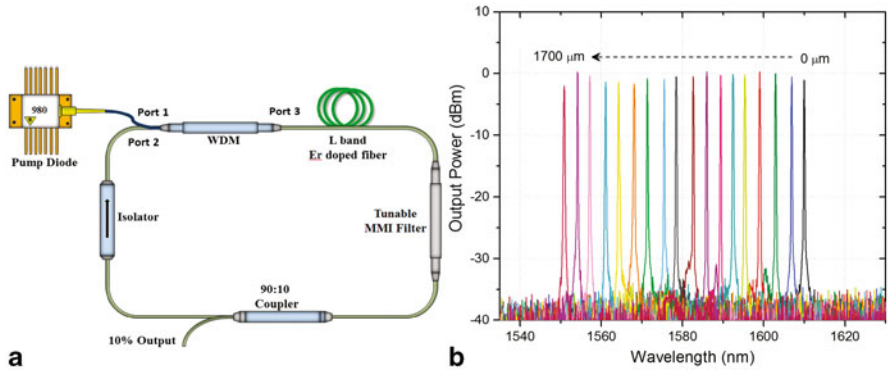
Fig. 2.8 a Schematic of the tunable ring cavity fiber laser based on MMI tunable filter and **b** Superimposed lasing spectra of the tunable laser with a total tuning range of 60 nm
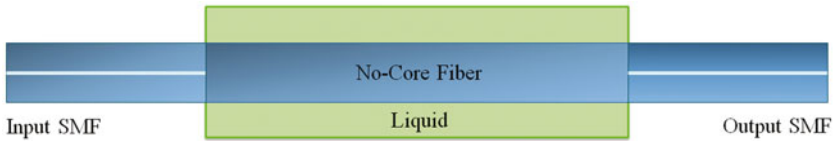
Fig. 2.9 Schematic of optofluidically tunable MMI filter

the thermo-optic effect in optical fibers is very small. In fact, MMI temperature sensors have been proposed and temperature sensitivities close to 15 pm/°C have been reported [26]. Such wavelength change as a function of temperature is too small to achieve a reasonable tuning range with small temperature increments. A simple way to change both effective RI and diameter is by using the No-Core fiber, and immersing it in liquids. Since the No-Core MMF has no cladding any changes to the liquid will alter the MMF parameters and thus the MMI peak wavelength.

2.4.1 Optofluidic Tuning of MMI Filter

The No-Core MMF becomes an ideal component if we want to modify the MMF parameters significantly. The fact that its core is completely exposed means that we can modify the MMF properties when the cladding region is modified. This is easily achieved by surrounding the No-Core fiber in liquids with different RI as shown in Fig. 2.9. When the index contrast between core and cladding is reduced, the effective RI and diameter of the No-Core fiber are increased and wavelength tuning of the MMI filter should be achieved [27].

Experimental demonstration of wavelength tuning is realized by splicing a 58.81 mm long No-Core MMF between two SMF, which corresponds to a MMI filter with a peak wavelength of 1534 nm. Liquids with different RI are obtained by
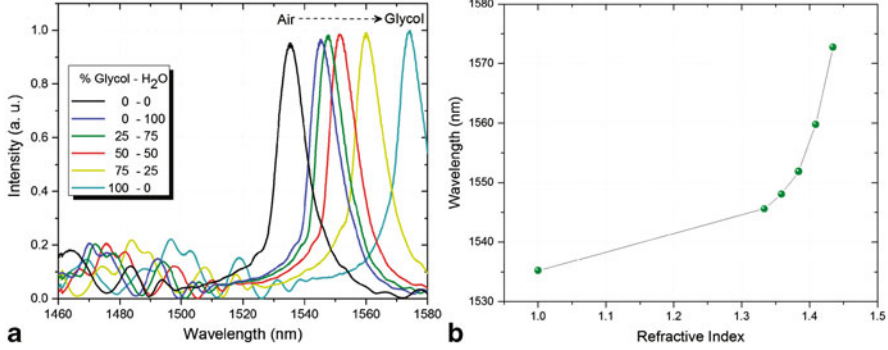
Fig. 2.10 a Spectral response of the MMI filter covered with different liquids and **b** Peak wavelength response as a function of liquid RI

mixing water ($n = 1.333$) with ethylene glycol ($n = 1.434$) at different ratios. The MMI spectral response was acquired by first introducing the liquid, and then measuring the transmitted power as the wavelength of a tunable input laser is scanned. As shown in Fig. 2.10a a tuning range of almost 40 nm from 1535 to 1575 nm was easily obtained when the medium surrounding the MMF is changed from air to pure ethylene glycol. We should highlight that there is a minimum change in contrast and bandwidth of the tunable filter response. We can also notice that the transmitted intensity of the filter is increased very slightly as the RI of the liquid is increased. We believe this is related to the reduction of scattering losses as the index contrast between the core and cladding is reduced. A quadratic dependence on the wavelength tuning response as a function of the value of the RI is observed, as shown in Fig. 2.10b. This means that the dominating term is the diameter of the MMF, which is expected from Eq. (2.4) since it has a square dependence.

2.4.2 Liquid Level Tunable Fiber Laser

Although tuning by replacing the liquid works quite well, it can be a little cumbersome in terms of a technological application. Replacing liquids requires not only an endless amount of liquid, but also a lot of different liquids in order to achieve fine wavelength tuning. An approach that is not immediately obvious is the one shown in Fig. 2.11. Rather than changing the RI around the entire No-Core fiber length, we gradually increase or decrease the length of No-Core MMF covered by the liquid. This is equivalent to having an MMI structure that is formed by two slightly different MMF.

In such a structure the peak wavelength is calculated by taking into account the proportional phase contribution of each MMF segment. Therefore, the peak wavelength of the self-image ($p = 4$) is now calculated by [17],

$$\lambda_0 = 4 \left[\frac{n_{LMMF} D_{LMMF}^2}{L_T} \left(\frac{L_{LMMF}}{L_T} \right) + \frac{n_{MMF} D_{MMF}^2}{L_T} \left(\frac{L_0}{L_T} \right) \right], \qquad (2.5)$$
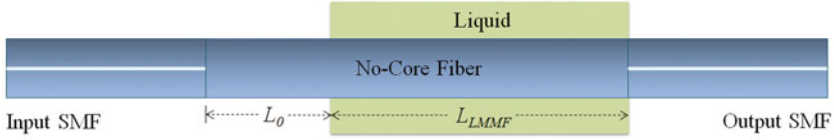
Fig. 2.11 Schematic of the liquid level wavelength tuning MMI device

where n_{LMMF} corresponds to the RI, D_{LMMF} is the diameter, and L_{LMMF} is the length of the No-Core MMF covered with liquid. Here L_0 is the No-Core fiber section without liquid and L_T is the total No-Core fiber length. The variables in the second term of Eq. (2.5) are the same as described in Eq. (2.2) for a No-Core MMF in air. The advantage of this tuning mechanism is that changes to the length of No-Core MMF, with and without liquid, exhibit a linear peak transmission wavelength response as a function of the liquid level. The slope of the response is controlled by the effective RI and diameter which is directly related to the RI of the liquid.

Since the RI of the liquid controls the slope of the response and thus the maximum tuning range, the tuning response of the MMI filter was evaluated by fabricating MMI filters with No-Core MMF lengths of 58.81, 59.91, and 61.28 mm, which correspond to peak wavelengths of 1534, 1506, and 1472 nm respectively. The liquids used for each MMI filter correspond to index matching liquids from Cargille® with RI values of 1.4050, 1.4340 and 1.4380 at 1550 nm, which are lower than the RI value of 1.444 of the No-Core fiber. The liquid level was increased in steps of 10 mm and the MMI spectral response was acquired with the OSA at each step. As shown in Fig. 2.12a, the peak wavelength shift as a function of the liquid level exhibits a linear response regardless of the RI of the liquid. Therefore we can select the maximum tuning range by just choosing the RI of the liquid. We should also mention that as the liquid RI approaches the RI of the No-Core MMF the losses are increased due the cut-off of higher order modes. On the other hand, when the liquid RI is much lower than the core RI of the No-Core MMF the signal increases due to elimination of scattering losses. Therefore, we can select a liquid RI that compensate both effects and have a MMI filter with negligible losses as shown in Fig. 2.12b.

A tunable ring laser was constructed as shown schematically in Fig. 2.13a. A semiconductor optical amplifier (BOA-1004 from COVEGA) was used as the gain medium because it provides a wider gain profile that extends beyond 90 nm. A polarization controller has to be included into the ring because the BOA is polarization dependent. Two optical isolators are included in the cavity to eliminate some resonances that are observed due to some reflections into the BOA. One end of the optofluidically tunable MMI filter was spliced to the isolator while the other end was spliced to the input of the 10/90 fiber output coupler. The 10 % output allow us to continuously monitor the lasing spectral response via an OSA with a resolution of 0.06 nm. The 90 % output arm is spliced to the input of the other isolator to close the ring cavity. In this case the MMI filter consisted of a No-Core MMF length of 60.98 mm which corresponds to a peak wavelength of 1480 nm, and we selected a liquid with a RI value of $n = 1.437$ to obtain a tuning range close to 90 nm. As
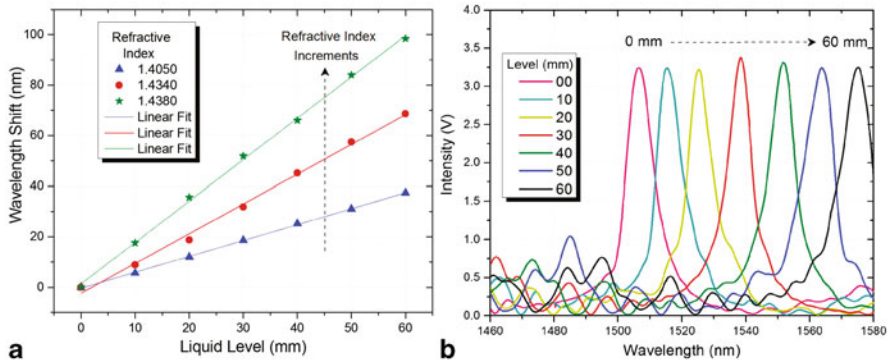
Fig. 2.12 a Peak wavelength response as a function of liquid level for liquids with different RI and **b** Spectral response of the MMI device for different liquid levels with liquid RI of $n = 1.434$
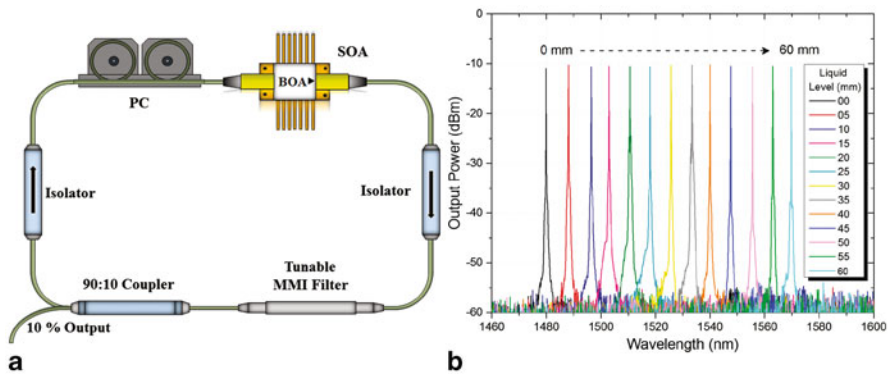
Fig. 2.13 a Schematic of the optofluidically tunable MMI BOA fiber laser and **b** Superimposed spectral response of the optofluidically tunable MMI BOA fiber laser

shown in Fig. 2.13b, we can tune the laser over a wavelength range of 90 nm while maintaining a low output power variation below 0.73 dB. The measured linewidth of the tunable laser output is less than 0.07 nm, and the side-mode suppression ratio (SMSR) is close to 50 dB.

2.5   Summary

Wavelength tunable lasers based on MMI devices represent a technology that can significantly enhance the development of a broad range of tunable fiber lasers. Regardless of their simplicity and cost-effectiveness they are capable of providing large wavelength tuning ranges on the order of 90 nm using a single MMI filter. Current tuning schemes rely on moving elements, either mechanically moving a fiber or

changing the liquid level, which for some applications can be a limiting factor. Therefore, future developments of tunable MMI filters should focus on the development of either electro-optical or thermo-optic tuning in order to avoid moving elements.

References

1. Chen, H., Babin, F., Leblanc, M., He, G., Schinn, G.W.: 70-nm tunable single-longitudinal mode erbium-doped fiber laser. Proc. SPIE. **4833**, 956 (2003)
2. Xia, L., Shum, P., Wang, Y.X., Cheng, T.H.: Stable triple-wavelength fiber ring laser with ultranarrow wavelength spacing using a triple-transmission-band fiber Bragg grating filter. IEEE Photon. Technol. Lett. **18**(20), 2162–2164 (2006)
3. Goh, C.S., Mokhtar, M.R., Butler, S.A., Set, S.Y., Kikuchi, K., Ibsen, M.: Wavelength tuning of fiber Bragg gratgin over 90 nm using a simple tuning package. IEEE Photon. Technol. Lett. **15**(4), 557–559 (2003)
4. Mokhtar, M.R., Goh, C.S., Butler, S.A., Set, S.Y., Kikuchi, K., Richardson, D.J., Ibser, M.: Fiber Bragg grating compression-tuned over 110 nm. Electron. Lett. **39**(6), 509–511 (2003)
5. Wang, X., Li, Y., Bao, X.: C- and L-band tunable fiber ring laser using a two-taper Mach–Zehnder interferometer filter. Opt. Letters. **35**(20), 3354–3356 (2010)
6. Chawki, M.J., Valiente, I., Auffret, R., Tholey, V.: "All fibre, 1.5 mu m widely tunable single frequency and narrow linewidth semiconductor ring laser with fibre Fabry Perot filter. Electron. Lett. **29**(23), 2034–2035 (1993)
7. Wei, Y., Hu, K., Sun, B., Wang, T.: All-fiber widely wavelength-tunable thulium-doped fiber ring laser incorporating a Fabry-Perot filter. Laser Phys. **22**(4), 770–773 (2012)
8. Yamashita, S.: Widely tunable erbium-doped fiber ring laser covering both C-band and L-band. IEEE J. Select. Topics Quantum Electron. **7**(1), 41–43 (2001)
9. Soldano, L.B. Pennings, E.C.M.: Optical multi-mode interference devices based on self-imaging: principles and applications. J. Lightwave. Technol. **13**(4), 615–627 (1995)
10. Wei, H., Yu, J., Liu, Z., Zhang, X., Shi, W., Fang, C.: Fabrication of 2×2 tapered multimode interference coupler. Electron. Lett. **36**(19), 1618–1619 (2000)
11. Chung, Lung-Wei Lee, San-Liang Lin, Yen-Juei: Principles and application of reduced beat length in MMI couplers. Opt. Express. **14**(19), 8753–8764 (2006)
12. Jiang, X., Li, X., Zhou, H., Yang, J., Wang, M., Wu, Y., Ishikawa, S.: Compact variable optical attenuator based on multimode interference coupler. IEEE Photon. Technol. Lett. **17**(11), 2361–2363 (2005)
13. Tomofuji, S., Matsuo, S., Kakitsuka, T., Kitayama, Ken-ichi: Dynamic switching characteristics of InGaAsP/InP multimode interference optical waveguide switch. Opt. Express **17**(26), 23380–23388 (2009)
14. Zhou, H., Song, J., Chee, E.K.S., Li, C., Zhang, H., Lo, G.: A compact thermo-optical multimode-interference silicon-based 1×4 nano-photonic switch. Opt. Express. **21**(18), 21403–21413 (2013)
15. Biazoli, C.R., Silva, S., Franco, M.A.R., Frazão, O., Cordeiro, C.M.B.: Multimode interference tapered fiber refractive index sensors. Appl. Opt. **51**(24), 5941–5945 (2012)
16. Antonio-Lopez, J.E., Lopez-Cortes, D., Basurto-Pensado, M.A., May-Arrioja, D.A., Sanchez-Mondragon, J.J.: All-fiber multimode interference refractometer sensor. Proc. SPIE. **7316**, 73161F (2009)

17. Antonio-Lopez J.E., Sanchez-Mondragon J.J., LiKamWa P., May-Arrioja D.A.: Fiber optics sensor for liquid level measurement. Opt. Lett. **36**(17), 3425–3427 (2011)
18. Gong, Y., Zhao, T., Rao, Y.J., Wu, Y.: All-fiber curvature sensor based on multimode interference. IEEE Photon. Technol. Lett. **23**(11), 679–681 (2011)
19. Guzman-Sepulveda, J.R., Aguilar-Soto, J.G., Torres-Cisneros, M., Ibarra-Manzano, O.G., May-Arrioja, D.A.: Measurement of curvature and temperature using multimode interference devices. Proc. SPIE. **8011**, 80115P (2011)
20. Shalaby, B.M., Kermene, V., Pagnoux, D., Barthelemy, A.: Transverse mode control by a self-imaging process in a multimode fibre laser using a single-mode feedback loop. J. Opt. A: Pure Appl. Opt. **10**(11), 115303 (2008)
21. Marcuse, D.: Mode conversion in optical fibers with monotonically increasing core radius. J. Lightwave Technol. **5**(1), 125–133 (1987)
22. Mohammed, W.S., Mehta, A., Johnson, E.G.: Wavelength tunable fiber lens based on multimode interference. J. Lightwave Technol. **22**(2), 469–477 (2004)
23. Selvas, R., Torres-Gomez, I., Martinez-Rios, A., Alvarez-Chavez, J.A., May-Arrioja, D.A., LiKamWa, P., Mehta, A., Johnson, E.G.: Wavelength tuning of fiber lasers using multimode interference effects. Opt. Express. **13**(23), 9439–9445 (2005)
24. Martinez-Rios, A., Starodumov, A.N., Po, H., Wang, Y., Demidov, A.A., Li, X.: Efficient operation of double-clad Yb^3 +-doped fiber lasers with a novel circular cladding geometry. Opt. Lett. **28**(18), 1642–16444, (2003)
25. Castillo-Guzman, A., Antonio-Lopez, J.E., Selvas-Aguilar, R., May-Arrioja, D.A., Estudillo-Ayala, J., LiKamWa, P.: Widely tunable erbium-doped fiber laser based on multimode interference effect. Opt. Express. **18**(2), 591–597 (2010)
26. Li, E., Wang, X., Zhang, C.: Fiber-optic temperature sensor based on interference of selective higher-order modes. Applied Physics Lett. **89**, 091119 (2006)
27. Antonio-Lopez, J.E., May-Arrioja, D.A., LiKamWa, Patrick: Optofluidic tuning of multimode interference fiber filters. Proc. SPIE. **7339**, 73390D (2009)

Chapter 3
Whispering Gallery Mode Microdisk Resonator with Dynamic Material Properties

Nataliya Sakhnenko

Abstract Accurate analysis of electromagnetic fields evolution in whispering gallery (WG) mode resonator with time dependent material parameters is presented. The excited fields are described by means of a rigorous mathematical approach that is based on the analytical solution in the Laplace transform domain and accurate evaluation of residues at singular points of the obtained functions. Transient response of WG mode on a sole time switching material parameters as well as on a pulse and packet of pulses are considered.

3.1 Introduction

Optical resonators have been attracting increasing attention recently due to their potential in a variety of scientific and engineering applications including low-threshold lasers [1], ultra-small filters [2] and miniature biosensors [3, 4]. In the simplest cases, such resonators have the shape of a thin disk, a ring or a sphere. In the vicinity of a curved surface whispering gallery (WG) modes can be excited due to almost total internal reflection of the light. Quality (Q) factor of these oscillations are extremely high because light becomes trapped within the resonator.

Dynamic resonators and photonic systems, in which material parameters can be varied by external forces, have pronounced benefit for their use in all-optical switchers and tunable filters [5] and represent a powerful approach for all-optical control of light. Permittivity modulation within microcavity systems can be exploited to stop, store and time-reverse of light pulse [6]. Modulation of permittivity in photonic crystals leads to changes of light colour [7] and reversed Doppler shifts [8]. Dynamic control of photonic bandgap can be used to coherently convert a propagating light pulse into stationary excitation which is effectively trapped in the medium [9]. Tuning in time of the refractive index can be used to realize fast frequency shift in linear material microcavity in photonic crystal [10] or dynamic WG mode

N. Sakhnenko (✉)
Kharkiv National University of Radio Electronics, Kharkiv, Ukraine
e-mail: n_sakhnenko@yahoo.com

Institute of Radio Physics and Electronics NASU, Kharkiv, Ukraine

spherical resonators [11]. In [12] has been shown that in periodic dynamic photonic structure the wavelength conversion process can be performed with efficiency close to one without affecting the shape and the coherence of the pulse. Delay lines play a significant role in optical signal processing [13]. In contrast to passive delay lines, dynamic structures can make this process controlled in time [14].

Electromagnetic wave propagation in time-varying media gives rise to new physical phenomena and possibility of novel applications. In practice, the temporal switching of the material refractive index can be realized by varying the input signal in a nonlinear structure [15]; by voltage control [16]; by a focused laser beam as a local heat source [17] or else by a free carrier plasma injection [5]. Typically the value of change in refractive index attainable with present day technology is of the order of 10^{-4}[18–20].

Theoretical studies of modern WG mode microresonator devices require highly accurate simulations that are complicated by both open nature and very high Q factors of these structures. The most widely used today numerical approach is FDTD method that is flexible but demands large computer memory. Moreover, conventional FDTD codes have problems with visualization of the high Q resonances [21].

In this chapter the rigorous mathematical method that allows analysing problems both in the frequency domain and in the time domain has been used. An analytical solution of the problem in the Laplace transform domain has been derived. The time domain electromagnetic field has been recovered by virtue of the computation of the inverse Laplace transform via the residue evaluation at singular points associated with eigenvalues of the structure. This approach guarantees accurate back transformation with controllable accuracy and allows extracting and interpreting physical phenomena easily. This method has been already successfully applied to a variety of time domain problems with different geometries [22–26].

For optimization of the existing devices and creation of new ones, it is crucial to gain a deep understanding of underlying physical mechanisms. In this chapter the transient response of WG mode to a sole abrupt time switching of refractive index is studied in details. Except for this abrupt change, the resonator materials are considered to be linear and nonmagnetic. The formulation of the problem in the above manner permits to build of an analytical solution. Features of the field evolution during transient period and steady-state regime are considered. Then the consideration has been extended to study of sole pulse and packet of pulses of medium properties switching.

3.2 Methodology

This section investigates initial boundary value problem of electromagnetic field transformation in thin circular disk microresonator, which occurs due to time variation of material parameters. This can be viewed as 2D model of 3D resonator within the effective refractive index approximation. To describe these fields, the polar system of coordinates (ρ, φ), centered in the microresonator, is introduced (Fig. 3.1), z-coordinate is assumed to be perpendicular to the (ρ, φ) plane.

Fig. 3.1 Schematic diagram of the resonator under consideration
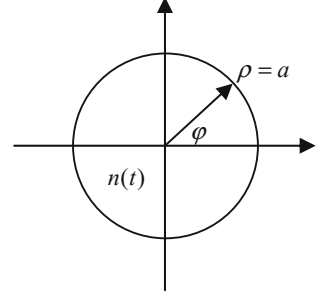
Maxwell's equations in nonmagnetic nondispersive media with time varying dielectric permittivity have the following form:

$$curl\ \vec{h}(\vec{r},t) = \partial_t \vec{d}(\vec{r},t), \tag{3.1}$$

$$curl\ \vec{e}(\vec{r},t) = -\partial_t \vec{b}(\vec{r},t). \tag{3.2}$$

Here $\vec{d}(\vec{r},t) = \varepsilon_0 \sqrt{n(t)} \cdot \vec{e}(\vec{r},t)$ is electric flux density, $\vec{b}(\vec{r},t) = \mu_0 \vec{h}(\vec{r},t)$ is magnetic flux density, $\vec{e}$ is electric field vector, $\vec{h}$ is magnetic field vector, $n(t)$ is time dependent refractive index, ε_0 and μ_0 are electric and magnetic constants, $\vec{r}$ denotes spatial coordinates, t is time. Hereafter, we restrict our consideration by perpendicularly polarized fields as this type of fields is dominant in thin disks. Maxwell's Eqs (3.1) and (3.2) give us the wave equations for z-component of magnetic field $h(\rho,\varphi,t)$ inside and outside the cavity

$$\Delta h(\rho,\varphi,t) - 1/c^2 \cdot \partial_t \left(n^2(t)\partial_t h(\rho,\varphi,t) \right) = 0, \rho < a, \tag{3.3}$$

$$\Delta h(\rho,\varphi,t) - 1/c^2\ \partial_{tt} h(\rho,\varphi,t) = 0, \rho > a, \tag{3.4}$$

where $\Delta = \partial_{\rho\rho} + 1/\rho\partial_\rho + 1/\rho^2\partial_{\varphi\varphi}$, $c = (\varepsilon_0\mu_0)^{-1/2}$ is speed of light in the vacuum.

We suppose that all changes of material parameters begin at some moment of time, which with no loss of generality can be considered as a zero moment. Besides, we assume that the field before zero moment of time is known and can be written as

$$h_0(\rho,\varphi,t) = \tilde{h}_0(\rho,\varphi)e^{i\omega_0 t} \tag{3.5}$$

Assume that refractive index changes abruptly from the value n_1 to the value n_2 at zero moment of time (see Fig. 3.2a).

In this case the problem allows analytical treatment. We apply the Laplace transform

$$H(p) = \int_0^\infty h(t)e^{-pt}dt \tag{3.6}$$

directly to the wave Eq. (3.3), that give us

$$\Delta H(\rho,\varphi,p) - n_2^2/c^2(p^2 H(\rho,\varphi,p) - ph(\rho,\varphi,+0) - \partial_t h(\rho,\varphi,+0)) = 0. \tag{3.7}$$

Fig. 3.2 Time dependence of the refractive index
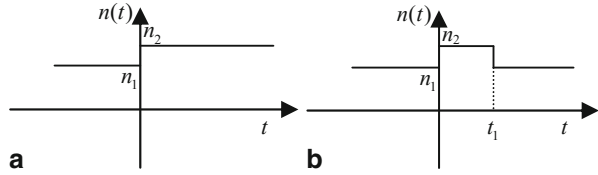
Corresponding initial conditions follow from the continuity of electric flux density $\vec{d}$ and the magnetic flux density $\vec{b}$ at zero moment of time [27]. In the transient area inside the disk they have the form as

$$h(\rho, \varphi, +0) = h_0(\rho, \varphi, -0), \tag{3.8}$$

$$\partial_t h(\rho, \varphi, +0) = n_1^2/n_2^2 \partial_t h_0(\rho, \varphi, -0). \tag{3.9}$$

Boundary conditions include continuity of the tangential field components at the circular boundary. Condition of continuity of z-coordinate of magnetic field vector is written as

$$H(\rho = -a, \varphi, p) = H(\rho = +a, \varphi, p) \tag{3.10}$$

Continuity of φ-coordinate of electric field vector after substitution into Maxwell's Eqs (3.1)–(3.2) and using the Laplace transform gives

$$\frac{1}{n_2^2} \frac{\partial}{\partial \rho} H(\rho = -a, \varphi, p) - \frac{i}{\omega_0} \frac{1}{n_2^2} \frac{\partial \tilde{h}_0(\rho = -a, \varphi)}{\partial \rho} =$$
$$= \frac{1}{n_1^2} \frac{\partial}{\partial \rho} H(\rho = +a, \varphi, p) - \frac{i}{\omega_0} \frac{1}{n_1^2} \frac{\partial \tilde{h}_0(\rho = +a, \varphi)}{\partial \rho}. \tag{3.11}$$

3.2.1 Initial Value Problem

From the methodological point of view we start with solution of initial value problem. We suppose that initial field (5) is a plane wave, which in polar coordinate has a following view

$$h_0(\rho, \varphi, t) = e^{i\omega_0 t} \sum_{s=-\infty}^{\infty} (-i)^s J_s(n_1 k_0 \rho) e^{is\varphi} \tag{3.12}$$

propagates in unbounded media. At zero moment of time refractive index of it changes from the value n_1 to the value n_2 (see Fig. 3.2a). Representing the image function of the seeking transformed field in the form

$$H(\rho, \varphi, p) = B(p) \sum_{s=-\infty}^{\infty} (-i)^s J_s(n_1 k_0 \rho) e^{is\varphi} \tag{3.13}$$

we can find unknown coefficient $B(p)$ substituting (3.13) into (3.7):

$$B(p) = \frac{n_2^2 p + in_1^2 \omega_0}{n_2^2 p^2 + n_1^2 \omega_0^2}. \tag{3.14}$$

Inverting obtained image function (3.13) into time domain we have the final expression for transformed field

$$h(\rho, \varphi, t) = \frac{1}{2n_2}((n_1 + n_2)e^{i\omega_1 t} + (n_2 - n_1)e^{-i\omega_1 t}) \sum_{s=-\infty}^{\infty} (-i)^s J_s(n_1 k_0 \rho)e^{is\varphi} \tag{3.15}$$

where $\omega_1 = \omega_0 n_1/n_2$. It is seen now that after abrupt time change of dielectric permittivity electromagnetic wave transforms in "time-transmitted" (TT) and "time-reflected" (TR) waves with new frequency ω_1 and amplitudes [27, 28]. Increasing of the refractive index leads to the decreasing of the TT wave amplitude and vise versa.

Now, let's consider the case of time variation of the dielectric medium where refractive index changes its value from n_1 to n_2 at zero moment of time and then changes back to the value n_1 at the moment of time t_1 (see Fig. 3.2b). At the disturbance time interval $0 \le t \le t_1$ expression for the field is given by (3.15). To obtain the field at the relaxation time interval ($t > t_1$) one should use treatment above considering (3.15) as initial field and taking into account time delay in (3.7). Finally in time domain magnetic field at this interval can be written as

$$h(\rho, \varphi, t) = (C_1 e^{i\omega_0(t-t_1)} + C_2 e^{-i\omega_0(t-t_1)})\Theta(t-t_1) \sum_{s=-\infty}^{\infty} (-i)^s J_s(n_1 k_0 \rho)e^{is\varphi} \tag{3.16}$$

$$C_1 = \frac{1}{4}((n_1 + n_2)^2 e^{i\omega_1 t_1} - (n_2 - n_1)^2 e^{-i\omega_1 t_1}), \tag{3.17}$$

$$C_2 = \frac{n_2^2 - n_1^2}{4}(e^{i\omega_1 t_1} - e^{-i\omega_1 t_1}). \tag{3.18}$$

Here $\Theta(..)$ is the Heaviside unit function. It is seen the restoration of the frequency to the initial value ω_0. Amplitudes of splitted TT and TR waves depend on n_1, n_2 and the duration of medium disturbance time interval t_1.

3.3 Sole Change of Refractive Index in WGM Resonator

Now we consider the initial-boundary value problem in a disk resonator of radius a with refractive index that undergoes the variation in time. Before switching refractive index, an initial field exists in the resonator which is a WG running wave described by

$$\tilde{h}_0 = e^{-i\omega_0 t^*}\Theta(t - t^*) \begin{cases} b_m J_m(n_1 k_0 \rho)e^{im\varphi}, \rho < a, \\ H_m^{(2)}(k_0\rho)e^{im\varphi}, \rho > a, \end{cases} \tag{3.19}$$

here $b_m = H_m^{(2)}(k_0 a)/J_m(n_1 k_0 a)$, $k_0 = \omega_0/c$, ω_0 is complex eigenfrequency that can be found from the following dispersion equation

$$n_1 J_m(n_1 k_0 a)H_m^{(2)'}(k_0 a) - J'_m(n_1 k_0 a)H_m^{(2)}(n_1 k_0 a) = 0. \tag{3.20}$$

The time dependence is assumed to be $e^{i\omega_0(t-t^*)}\Theta(t-t^*)$, where $t^* < 0$ is the moment of switching on the mode. The prime here represent differentiation with respect to the argument. At zero moment of time the refractive index of the resonator material changes in value from n_1 to n_2 in response to an external force. We now investigate the mechanisms that couple the initial mode to those of the cavity with a new permittivity. Assumption of the abrupt time change of the material permittivity allows obtaining the analytical solution in the Laplace transform domain. The solution of initial-boundary value problem consists of two parts: initial value solution and the term that is explicitly constructed as a superposition of the waves reflected from the structure boundaries [11]

$$H = \frac{1}{c}\frac{n_2^2 q + in_1^2 k_0}{q^2 n_2^2 + k_0^2 n_1^2} J_m(n_1 k_0 \rho)e^{-i\omega t^*}e^{im\varphi} + GI_m(n_2 q\rho)e^{im\varphi}(\rho < a), \tag{3.21}$$

$$H = \frac{1}{c}\frac{1}{q - ik_0} H_k^{(2)}(k_0\rho)e^{-i\omega t^*}e^{im\varphi} + FK_m(q\rho)e^{im\varphi}(\rho > a) \tag{3.22}$$

here $q = p/c$. The total field within the cavity consists of the unbounded term (first term in (3.21)) that is identical to (3.14) and additional contributions due to the boundary. Similarly, in the outer region the field comprises a superposition of the initial field (first term in (3.22)) and contributions due to the presence of the boundary (second term in (3.22)). Outside the cavity, the function $K_m(..)$ guarantees satisfaction of the Sommerfeld outgoing radiation condition at infinity, and G and F are unknown coefficients to be determined from the boundary conditions (3.10)—(3.11)

$$G = \frac{n_1 k_0 J_m(n_1 k_0 a)K'_m(qa) + q J'_m(n_1 k_0 a)K_m(qa)}{I'_m(n_2 qa)K_m(qa) - n_2 K'_m(qa)I_m(n_2 qa)} \cdot n_2 W \frac{b_m}{c}e^{-i\omega t^*} \tag{3.23}$$

$$F = \frac{n_2 q J'_m(n_1 k_0 a)I_m(n_2 qa) + n_1 k_0 I'_m(n_2 qa)J_m(n_1 k_0 a)}{I'_m(n_2 qa)K_m(qa) - n_2 K'_m(qa)I_m(n_2 qa)} \cdot \frac{1}{n_1} W \frac{b_m}{c}e^{-i\omega t^*} \tag{3.24}$$

$$W = \frac{iq(n_1^2 - n_2^2)}{(q - ik_0)(q^2 n_2^2 + k_0^2 n_1^2)}. \tag{3.25}$$

The expressions have both poles and branch-cut along the negative real axis of the complex q-plane. Those poles are associated with the frequency of the initial wave $q = ik_0$ and the transformed frequency $q = \pm ik_0 n_1/n_2$ due to the permittivity

changing (3.25). There is also an infinite number of poles associated with the zeros of the denominator Gand F in (3.23)–(3.24). They correspond to the eigenfrequencies of the resonator in its new state.

Using the asymptotic expansions of modified Bessel functions with large arguments, we have

$$qGI_m(n_2q\rho) \approx const \cdot e^{-n_2q(a-\rho)} \tag{3.26}$$

$$qFK_m(q\rho) \approx const \cdot e^{-q(\rho-a)}. \tag{3.27}$$

From (3.26) and (3.27) it is observed that, upon inversion to the time domain, the expressions corresponding to $GI_m(n_2q\rho)$ and $FK_m(q\rho)$ exhibit a time delay that can be expressed in terms of the unite Heaviside functions, $\Theta(tc/n_2 + \rho - a)$ and $\Theta(ct - \rho + a)$, inside and outside of the resonator, respectively.

In the "early time" regime ($tc/n_2 < a - \rho$) inside the resonator the field is described by the first term in (3.21) and exhibits the same wavenumber and shifted frequencies predicted from the abrupt change in the material parameters. It does not depend upon the boundary shape and depend only on relative change in refractive index. In the outer region, only the initial field is present. Near the boundary region, the transient waves appear that correspond to total field given in (3.21) and (3.22). In the time domain they are expressible in terms of a residue sum over all the singular points and an integral along the branch cut. Examination of (3.21) and (3.22) in more detail reveals that the singularities in the total field at $q = \pm ik_0n_1/n_2$ and $q = ik_0$ after moment of time $tc/n_2 = a - \rho$ do not contribute to the residue sum

Figure 3.3 represents the results of numerical simulation of WG $h_{8,1}$ (the notation $h_{m,l}$ stands for natural mode of TE polarization; the indices m and l determine the number of the angular field variation and number of field variations along the radius, respectively) transformation with $n_1 = 2.63$. Inset in Fig. 3.3 shows the near field distribution of the mode. For the modeling normalized time $T = tc/a$ and normalized distance $r = \rho/a$ are used.

The normalized eigenfrequency of the initial mode is $\omega_0a/c = 4.54342481 + 4.024 \cdot 10^{-4}i$. Assume that at zero moment of time effective refractive index changes to the value $n_2 = 2.631$. Figure 3.3 presents the time domain behaviour of the total field versus the normalized time near the centre of the resonator ($r = \rho/a = 0.2$, left panel) and near the rim ($r = 0.9$, right panel). Changing the refractive index leads to the excitation of all modes (leaky and WG ones) with the same angular dependence as initial one. Zeros of the denominator (3.23)–(3.24) $q = q' \pm iq''$ are associated with excited modes, '+' is for TT modes, '−' is for TR modes. The transition to a more usual frequency representation is made by substitution $q = i\omega/c$.

So, by finding residues at singular points, we can estimate the contribution of each excited mode into the total field. Thus, WG $h_{8,1}$ in resonator with new refractive index $n_2 = 2.631$ has frequency $\omega_t a/c = 4.5417998 + 3.999 \cdot 10^{-4}i$ (TT wave). Absolute value of the residue at this frequency (corresponding value is normalized by the amplitude of the initial mode) is 0.999985, normalized amplitude of the TR wave is $1.8 \cdot 10^{-4}$. Normalized frequency of the excited $h_{8,2}$ mode is $\omega a/c = 5.915798 + 1.53 \times 10^{-2}i$, amplitudes of the TT and TR waves are $1.3 \cdot 10^{-4}$ and
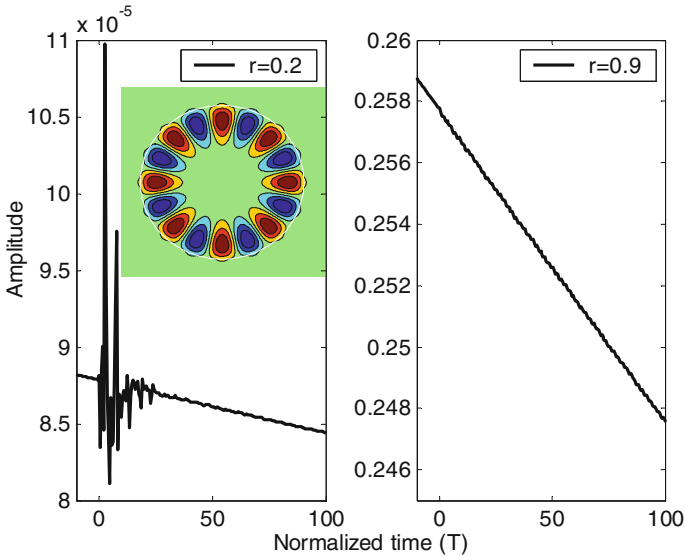
Fig. 3.3 Electromagnetic field evolution in WG mode resonator ($n_1 = 2.63$, $n_2 = 2.631$)

$1.7 \cdot 10^{-4}$, respectively. Other excited leaky modes give even smaller contribution into total field. Numerical simulation confirms that the integral along branch cut exhibits negligibly small contribution into total field as well.

Thus, we can conclude that after refractive index tuning the initial WG wave is converted to the TT WG wave of the resonator with new refractive index. Frequency shift from the value Re (ω_0) to the value Re (ω_t) is observable. This value of frequency shift is less than the one predicted from initial value problem. However, one can achieve a better result in the frequency shift considering the modes with greater angular numbers. This effect can be easily explained because with growing of the angular mode number the Q factor increases, which means that the mode field is stronger localized inside the cavity. Thus, the overlap of the initial mode field and the volume of the cavity involved into the change of refractive index is larger and this leads to a greater frequency shift [11].

Enhancement in frequency shift can also be achieved in coupled resonators for antisymmetrical modes [29, 30].

3.4 Time Change of the Refractive Index in the Form of a Single Rectangular Pulse

Assuming pulse change in dielectric constant we can also provide an analytical solution of the problem. Suppose that the refractive index of the disk resonator material at zero moment of time changes its value from n_1 to n_2 and then restores its

initial value at the moment of time t_1(see Fig. 3.1b). At the time interval $0 < t < t_1$ magnetic field is determined by (3.21)–(3.22). To find the magnetic field after moment t_1, one has to represent the field at previous time interval as a superposition of the excited modes neglecting the integral along branch and considering each particular mode as an initial field. The problem should be solved in the manner proposed above taking into account time delay due to nonzero value of t_1.

Thus, inner field that obtained as a result of the TT WG mode with initial wavenumber k_t has a form

$$L = \frac{qn_1^2 + ik_tn_2^2}{q^2n_2^2 + k_t^2n_1^2} Be^{i\omega_t t_1} J_m(n_2k_t\rho) + RBI_m(n_1q\rho)e^{i\omega_t t_1} \qquad (3.28)$$

$$R = \frac{n_2k_t J_m(n_2k_ta)K'_m(qa) + q J'_m(n_2k_ta)K_m(qa)}{I'_m(n_1qa)K_m(qa) - n_1 K'_m(qa)I_m(n_1qa)} \cdot \frac{iq(n_2^2 - n_1^2)n_1}{(q - ik_t)(q^2n_1^2 + k_t^2n_2^2)} \qquad (3.29)$$

here B is an amplitude of WG mode obtained from (3.23). The total field after moment t_1 can be viewed as a superposition of all excited transformed modes; however numerical simulation reveals that their amplitudes are negligibly small in comparison to TT WG mode.

On the time interval of material parameter relaxation (the refractive index is returned to its original value), frequency of the transformed WG mode restores to its initial value ω_0 while its amplitudes is a subject of altering.

Figure 3.4 represents amplitudes of the excited TT WG modes if refractive index changes from the value $n_1 = 2.63$ to the value $n_2 = n_1 + \Delta n$ versus the duration of material perturbation time interval. Amplitude of excited WG mode is normalized by the amplitude of initial mode, duration of the disturbance time interval is normalized by the period of initial mode (t_0), normalized time is considered as $T_0 = t_0c/a$, $T_1 = t_1c/a$.

Figure 3.5 represents evolution of the total field in time. If the observation point is placed near the center it is seen two wave fronts passing through the observation point associated with moments of refractive index changes.

3.5 Modulation of the Refractive Index in the Form of a Finite Packet of Rectangle Pulses

Similarly one can consider the packet on N pulses of the material parameters variation. Each modulation cycle has a form of rectangular pulse and consists of the disturbance interval of duration t_1 and relaxation interval of duration $t_2 - t_1$ where parameters of the medium return to the primary value (see Fig. 3.6).

Assuming $t_1 \geq t_0$ and $t_2 \geq t_0$ (t_0 is period of initial wave) we will restrict consideration by excited TT and TR high-Q WG modes. Figure 3.7 represents amplitudes of
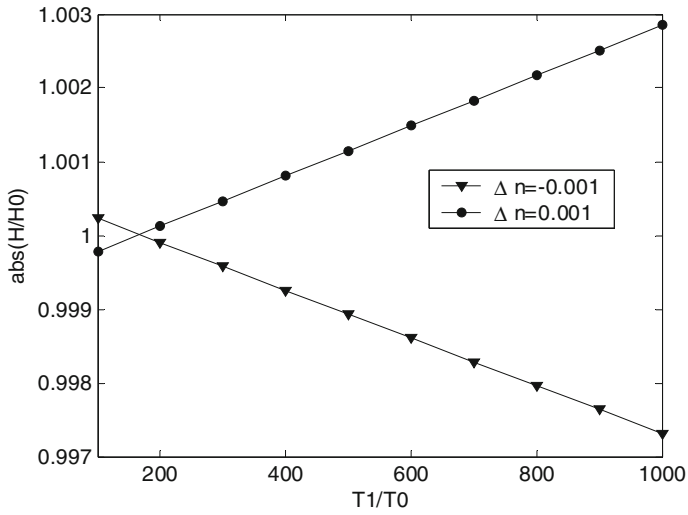
Fig. 3.4 Amplitudes of the excited TT WG modes versus duration of the disturbing pulse ($n_1 = 2.63$, $n_2 = n_1 + \Delta n$)
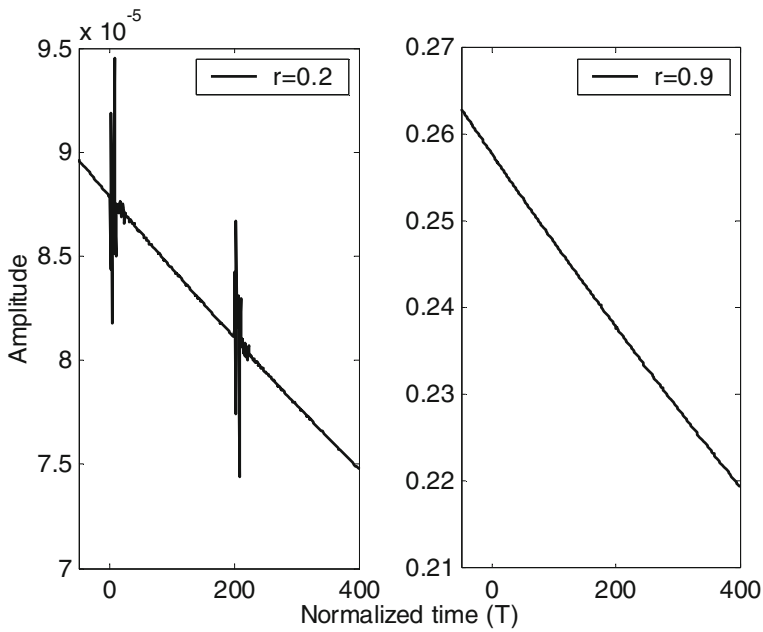
Fig. 3.5 Time dynamics of the transformed field due to pulse change of the refractive index ($n_1 = 2.63$, $n_2 = 2.631$, $T_1 = 200$)

Fig. 3.6 Time dependence of
the refractive index
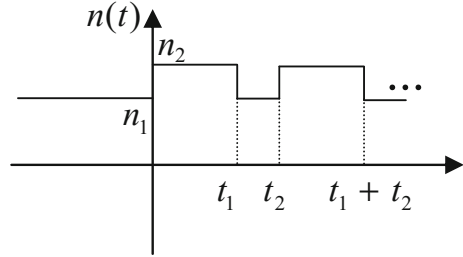
these modes on the interval of media parameters relaxation after packet of N disturbing pulses for different values of t_1. Period of modulation is $t_2 = 500t_0$, $n_1 = 2.63$, $n_2 = 2.631$.

For the same modulation frequency it is possible to observe amplitude growth or decay depending on the ratio t_1/t_2 and n_1/n_2. However TT waves demonstrate monotonic growth/decay while TR waves demonstrate irregular chaotic behavior (for more details see e.g. [31]). However we have to stress different vertical scales in Fig. 3.7 and pay attention that amplitudes of TR waves are negligibly small in comparison to TT waves.

Figure 3.8 represents time evolution of the field after packet of $N = 20$ disturbing pulses. Black line shows the field evolution in undisturbed resonator. Here $t_2 = 500t_0$,
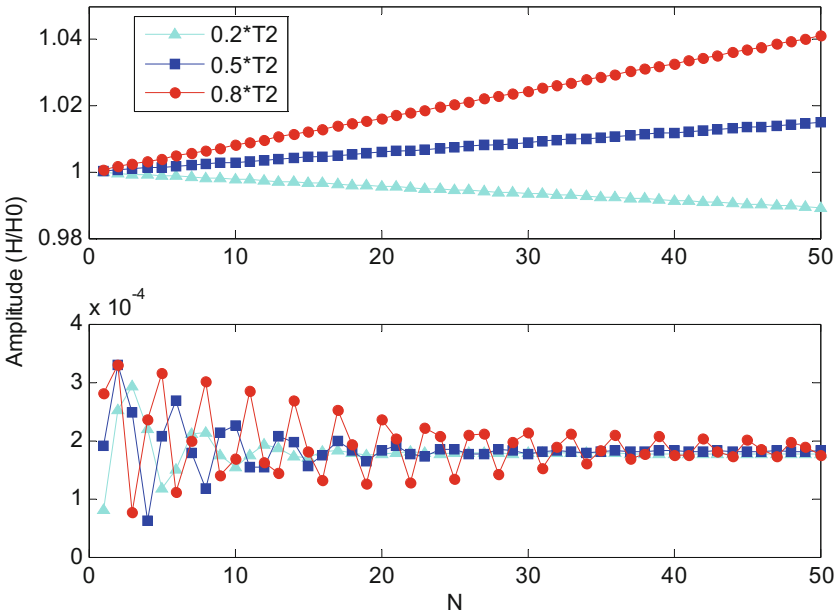
Fig. 3.7 Amplitudes of excited TT (upper panel) and TR (low panel) WG modes after packet on N disturbing pulses for different values of t_1, $t_2 = 500t_0$, $n_1 = 2.63$, $n_2 = 2.631$
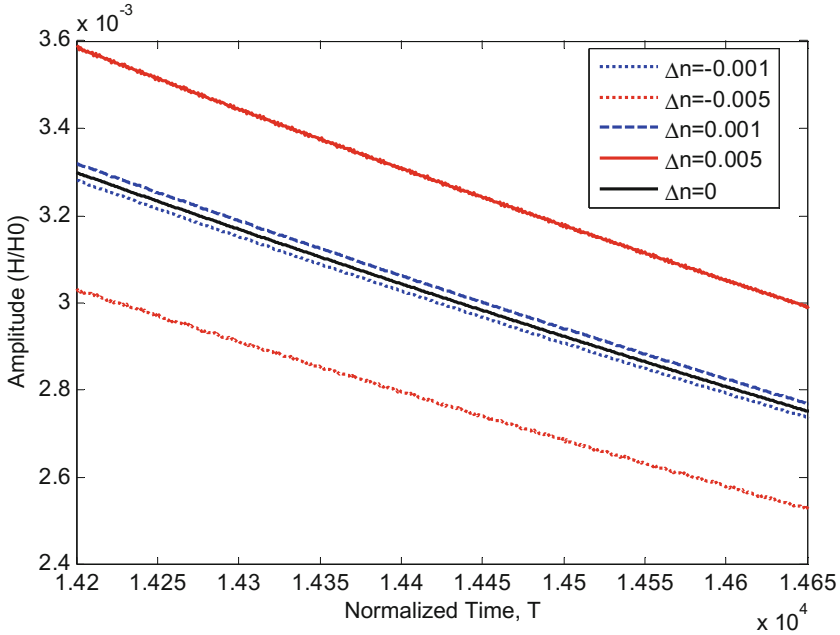
Fig. 3.8 Time domain behavior of the total transformed field after packet of $N = 20$ disturbing pulses ($t_2 = 500t_0$, $t_1 = t_2/2$, $n_1 = 2.63$, $n_2 = n_1 + \Delta n$)

$t_1 = t_2/2$, $n_1 = 2.63$, $n_2 = n_1 + \Delta n$, observation point is located near the rim. It is seen that such kind of modulation leads to variation of the field amplitude preserving spatial field distribution and frequency of the mode. Amplitude alternation can be enhanced by increasing the depth of modulation. Possible applications of this phenomenon include time control of persistence properties of photonic devises.

In conclusion, this chapter presents an analytical formulation of the WG mode transformation due to the temporal change of the refractive index in a thin circular microdisk resonator. The theory is based on the eigenfunction expansion in the Laplace transform domain and the solution inversion into the time domain through the residue evaluation. It has been shown possibility of using WG mode resonators for very fast and efficient frequency conversion due to sole variation in refractive index. Finite packet of medium disturbance allows amplitude control of WG mode and opens way for speeding up or slowing down the process of mode radiation.

References

1. Cai, M., Vahala, K.: Highly efficient hybrid fibre coupled microsphere laser. Opt. Lett. **26**, 884–886 (2001)
2. Little, B.E., Chu, S.T., Haus, H.A., Foresi, J., Laine, J-P.: Microring resonator channel dropping filters. J. Lightwave Tech. **15**, 998–1005 (1997)

3. Blair, S., Chen, Y.: Resonant-enhanced evanescent-wave fluorescence biosensing with cylindrical optical cavities. Appl. Opt. **40** (4), 570–582 (2001)
4. Boyd, R.W., Heebner, J.E.: Sensitive disk resonator photonic biosensor. Appl. Opt. **40**, 5742–5747 (2001)
5. Djordjev, K., Choi, S.-J., Choi, S.-J., Dapkus, R.: Microdisk tunable resonant filters and switches. IEEE Photon. Technol. Lett. **14** (6), 823–830 (2002)
6. Yanic, M., Fan, S.: Time reversal of light with linear optics and modulators. Phys. Rev. Lett. **93** (17), (2004) (173903-1-4)
7. Reed, E.J., Soljacic, M., Joannopoulos, J.D.: Color of shock waves in photonic crystals. Phys. Rev. Lett. **90** (20), (2003) (203904-1-4)
8. Reed, E.J., Soljacic, M., Joannopoulos, J.D.: Reversed Doppler effect in photonic crystals. Phys. Rev. Lett. **91** (13), (2003). (133901-1-4)
9. Andre, A., Lukin, M.D.: Manipulating light pulses via dynamically controlled photonic bandgap. Phys. Rev. Letters. **89** (14), (2002). (143602)
10. Notomi, M., Mitsugi, S.: Wavelength conversion via dynamic refractive index tuning of a cavity. Phys. Rev. A. **73**, (2006) (051803(R))
11. Sakhnenko, N.K., Nerukh, A.G.: Rigorous analysis of whispering gallery mode frequency conversion due to time variation of refractive index in a spherical resonator. J. Opt. Soc. Am. A. **29**(1), 99–104 (2012)
12. Gabuzzo, Z., Ghalinyan, M., Riboli, F., Pavesi, L., Recati, A., Carusotto, I.: Photon energy lifter. Opt. Expr. **14**(16), 7270–7278 (2006)
13. Almeida, V.R., Barriors, C.A., Panepucci, R. P., Lipson, M.: All-optical control of light on a silicon chip, Nature, **431**(7012), 1081–1084 (2004)
14. Yanik, M.F., Fan, S.: Dynamic photonic structures: stopping, storage, and time reversal of light. Stud. Appl. Math. **115**, 233–253 (2005)
15. Blom, F., Dijk, D., Hoekstra, H., Driessen, M., Popma, A.: Experimental study of integrated-optics microcavity resonators. Appl. Phys. Lett. **71** (6), 747–749 (1997)
16. Savchenkov, A.A., Ilchenko, V.S., Matsko, A.B., Maleki, L.: High-order tunable filters on a chain of coupled crystalline whispering-gallery-mode resonators. IEEE Photon. Technol. Lett. **17** (1), 136–138 (2005)
17. Benyoucef, M., Kiravittaya, S., Mei, Y., Rastelli, A., Schmidt, O.: Strongly coupled semiconductor microcavities: A route to couple artificial atoms over micrometric distances. Phys. Rev. B. **77**, (2008) (035108-1-8)
18. Bennett, B.R., Soref, R.A., Del Alamo, J.A.: Carrier-Induced change in refractive index of InP, GaAs, and InGaAsP. IEEE J. Quantum Electron. **26**, 113–122 (1990)
19. Liu, A., Jones, R., Liao, L., Samara-Rubio, D., Rubin, D., Cohen, O., Nicolaescu, R., Paniccia, M.: A high-speed silicon optical modulator based on a metal-oxide-semiconductor capacitor. Nature. **427**, 615–618 (2004)
20. Almeida, V.R., Barrios, C.A., Panepucci, R.R., Lipson, M., Foster, M.A., Ouzounov, D.G., Gaeta, A.L.: All-optical switching on a silicon chip. Opt. Lett. **29** (24), 2867–2869 (2004)
21. Boriskin, A.V., Boriskina, S. V., Rolland, A., Sauleau, R., Nosich, A.I.: Test of the FDTD accuracy in the analysis of the scattering resonances associated with high-Q whispering-gallery modes of a circular cylinder. J. Opt. Soc. Am. A. **25** (5), 1169–1173 (2008)
22. Bekker, E.V., Vukovic, A., Sewell, P., Benson, T.M., Sakhnenko, N.K., Nerukh, A.G.: An assessment of coherent coupling through radiation fields in time varying slab waveguides. Opt. Quant. Electron. **39** (7), 533–551 (2007)
23. Sakhnenko, N.K., Nerukh, A.G., Benson, T. M., Sewell, P.: Whispering gallery mode transformation in a switched micro-cavity with concentric ring geometry. Opt. Quant. Electron. **40** (11–12), 818–820 (2008)
24. Sakhnenko, N.K., Nerukh, A.G., Benson, T., Sewell, P.: Near field pattern images in 2D circular resonator with time varying plasma. IEEE Trans. Plasma Sci. **36** (4), 1222–1223 (2008)
25. Sakhnenko, N.K., Nerukh, A.G., Benson, T., Sewell, P.: Frequency conversion and field pattern rotation in WGM resonator with transient inclusion. Opt. Quant. Electron. **39**, 761–771 (2007)

26. Nerukh, A., Remaeva, T., Sakhnenko, N. K.: Frequency change of partial spherical waves indused by time change of medium permittivity. Opt. Quant. Electron. **41**, 327–335 (2009)
27. Nerukh, A.G., Sakhnenko, N.K., Benson, T., Sewell, P.: Nonstationary electromagnetics. Pan Stanford Publishing, Singapore (2012)
28. Morgenthaler, F.R. Velocity modulation of electromagnetic waves. IRE Trans. MTT. **6**, 167–172 (1958)
29. Sakhnenko, N.K.: Transient processes and steady state regimes in dynamic WGM microcavities with time dependent material parameters. In: Proc. of Int. Conf. on Advanced Optoelectronics and Lasers CAOL 9–13 Sept 2013, Sudak, Ukraine, 268–270, (2013)
30. Sakhnenko, N.K., Nerukh, A.G.: Frequency shift in a single dielectric resonator and in a chain of coupled resonators due to time change in permittivity. In: Proc. of Int. Conf. Asia-Pacific Microwave Conference APMC 7–10 Dec 2010, Yokohama, Japan, 853–856, (2010)
31. Ruzhitskaya, N., Nerukh, A.G., Nerukh, D.A.: Accurate modelling of pulse transformation by adjustable-in-time medium parameters. Opt. Quant. Electron. **35**, 347–364 (2003)

Chapter 4
Superradiant Lasing and Collective Dynamics of Active Centers with Polarization Lifetime Exceeding Photon Lifetime

Vl. V. Kocharovsky, A. A. Belyanin, E. R. Kocharovskaya and V. V. Kocharovsky

Abstract Analytic theory, numerical simulation, and qualitative analysis of the threshold conditions, nonlinear dynamics, and spectral features of the superradiant emission and cooperative radiative behavior of a dense many-particle system in a low-Q Fabry–Perot cavity with distributed feedback of counter-propagating electromagnetic waves are given. Various systems with extreme spatial-spectral density of radiating particles as active media of superradiant lasers are discussed, including those with almost homogeneous broadening as well as strongly inhomogeneous broadening of a spectral line. In the case of experimental verification, the phenomenon of CW superradiant lasing will be promising in the information optoelectronics and condensed matter physics, in particular, for managing novel oscillators with complicated dynamical spectra and for creating unprecedented diagnostics of quantum coherent many-particle effects.

4.1 Introduction. What is a class D laser?

Recent experiments on pulsed superfluorescence and prospects of CW superradiant lasing in various active media (see Sect. 4.2) require a systematic analysis of the threshold conditions and the non-stationary regimes of a cooperative emission based on mode superradiance (SR). This emission takes place in the case when a photon lifetime is much shorter than a polarization lifetime of an active center. The latter situation means a low-Q cavity and a dense active medium and corresponds to the so-called class D lasers [6, 28], which differ in many respects from the standard lasers of A, B, and C classes introduced by Arecchi and Harrison [3].

The key difference is related to the collective dynamics of the active centers which totally alters the dynamical spectra of their population inversion and cavity

Vl. V. Kocharovsky (✉) · V. V. Kocharovsky · E. R. Kocharovskaya
IAP RAS, 46, Ulyanov str., Nizhny Novgorod, Russia
e-mail: kochar@appl.sci-nnov.ru

A. A. Belyanin · V. V. Kocharovsky
Department of Physics and Astronomy, Texas A & M University, College Station TX, USA
e-mail: vkochar@physics.tamu.edu

field as compared to the standard lasers. As a result, one could easily manage the time profile, the correlation features, and the spectral properties of the generated radiation by tuning the parameters of class D lasers. At the same time, laser radiation carries fingerprints of the collective behavior of the active centers and, thus, may be used as a diagnostic tool for many-particle phenomena in the dense ensembles, for example, for the phase transitions involving a radiative interaction of particles (see, e.g ., [11, 25, 26, 33]).

In the present paper we outline a general theory of mode superradiant (SR) lasing for a low-Q Fabry-Perot cavity equipped with a distributed feedback (DFB) along the cavity which favors the intriguing cooperative dynamics of particles. First, we consider a simplified 1D laser model bearing in mind a general case of an active medium, when an inhomogeneous broadening is of the same order as a homogeneous one, and describe briefly the typical spectra of modes and necessary conditions for CW mode SR (Sect. 4.3). Then, we focus on the limiting cases of an almost homogeneous broadening (Sect. 4.4) and a strong inhomogeneous broadening (Sect. 4.5) when the lasing modes are the so-called polariton modes with negative energy and electromagnetic modes with positive energy, respectively. In both cases we analyze physical mechanisms responsible for various SR regimes and compare possible dynamical spectra of laser radiation. Special attention is paid to the number of lasing modes and their correlated behavior or independent generation, which may be used for managing the time profile of the outgoing radiation. In conclusion (Sect. 4.6) we summarize new nonlinear phenomena inherent to rich dynamics of the class D lasers and their relation to the specific problems of cooperative radiative behavior of many-particle systems in the condensed matter physics.

A short lifetime, T_2, of dipole optical oscillations (i.e., polarization) of individual active centers in available amplifying media (see, e.g., [1, 3, 28]) prohibits from lasing in the case of a low-Q cavity when the photon lifetime, T_E, is much less that the polarization lifetime:

$$T_E \ll T_2. \tag{4.1}$$

Nevertheless, these systems show great promise as class D lasers due to a fast accumulation-free field dynamics and a formation of cooperative many-particle states owing to the particle interaction via the self-consistent optical field.

High-quality polarization oscillations of active centers, which have different frequencies in the general case of inhomogeneous broadening of a spectral line, increase greatly the number of dynamical degrees of freedom under the condition (4.1) [6, 23, 28]. As a results, an outgoing radiation may be multi-periodic or quasi-chaotic and may contain well-correlated or weakly connected spectral components. As a whole, the radiation may have various spectral and correlation features, and its dynamical properties are defined mainly by the so-called collective spontaneous emission of active centers [12, 47]. Sometimes CW lasers of this type are called "superradiant" ones, though in general case their proper name is "the class D lasers" [6, 28]. Indeed, a short temporal scale ($< T_2$) in their dynamics and/or fluctuations [8, 17, 31], which is intrinsic to SR phenomenon, is absent in some cases.

Dynamical classes of all possible lasers in a 2-level model (Sect. 4.3), which is used throughout the paper, are defined by the relaxation parameters (see Table)

Table 4.1 Four classes of lasers

Dynamical class	A	B	C	D
Relaxation rates	$\gamma_E \ll \gamma_\perp, \gamma_\parallel$	$\gamma_\parallel \ll \gamma_E \ll \gamma_\perp$	$\gamma_\parallel \lesssim \gamma_\perp \sim \gamma_E$	$\gamma_\perp, \gamma_\parallel \ll \gamma_E$
Adiabatic Elimination	Polarization, Inversion	Polarization		Field, if $\omega_R \ll \gamma_E$

according to the works [3] (A, B, C classes) and [6, 28] (D class). In most lasers the slowest process is the relaxation of inversion (n) on the laser transition in an active medium, described by the relaxation rate $\gamma_\parallel = 1/T_1$. The relaxation rate of polarization, $\gamma_\perp = 1/T_2$, is usually the highest, and these are the class B lasers. They cannot generate without high-Q cavities which guarantee a slow field relaxation, $\gamma_E = 1/T_E$, so that it is the field (and, maybe, the inversion, but not the adiabatically eliminated polarization) which governs the dynamics of the class A and B lasers (Table 4.1).

The polarization dynamics becomes important already in the intermediate case of the class C lasers where $\gamma_E \sim \gamma_\perp$ (see, e.g., [1, 3, 28]). However, its full effect shows only in the class D lasers, where the field dynamics may be important as well. The latter is not reduced to the situation when the field adiabatically follows the polarization because, due to SR, the field amplitude, E, can be high enough during some time periods, so that the cavity relaxation rate, γ_E, appears to be smaller than the Rabi frequency, $\omega_R = dE/\hbar$, and, hence, than the rate of stimulated transitions between the energy levels of active centers (d is a dipole moment of the 2-level transition, $\hbar$ the Planck constant) [28]. Then the adiabatic elimination of the field is impossible and the lasing is expected to be non-stationary, especially because the radiation pulses generated by a class D laser will leave a low-Q cavity to a considerable extent during one pass along the cavity length, B, with the speed of light, $c/\sqrt{\varepsilon_0}$.

4.2 Two Types of Media with Extreme Spatial-Spectral Density of Active Centers

It is well-known [6, 35, 47] that an inverted 2-level medium gives rise to SR or superfluorescence under the condition

$$v_c^2 T_2 > 1/T_2 + 1/T_2^*, \tag{4.2}$$

and mode SR in the class D lasers will appear under stronger condition

$$v_c^2 T_E > 1/T_2 + 1/T_2^* \tag{4.3}$$

(see Eqs. (4.1) and (4.9)) when a continuous-wave collective spontaneous emission does not contribute much. We use here a so-called cooperative frequency $v_c = (2\pi d^2 \omega_0 N_0/\hbar \varepsilon_0)^{1/2}$, ε_0 is an average (with respect to a cavity length and a frequency

range of generation) dielectric constant of a host medium, N_0 a density of active centers inverted by pumping, $1/T_2^*$ an inhomogeneous broadening of their spectral line centered at a frequency ω_{21}.

According to Eqs. (4.2) and (4.3), SR requires a medium with extremely high spatial and spectral density of active centers. An increase of a cooperative frequency by means of the dense packing of active centers is complicated by their coupling which shortens a lifetime of polarization, T_2, and widens an inhomogeneous broadening, $1/T_2^*$, due to uncontrolled shifts of the transition frequencies of active centers. In addition, a pumping creating an inversion of a laser transition may shorten the polarization lifetime as well.

The class D lasers are not yet studied experimentally because they require very low-Q cavities and, hence, exotic active media with extremely high spatial density and spectral density of active centers: $\nu_c^2 > 1/T_2^2$ or [47] $\nu_c^2 > 1/T_2 T_2^*$ if $1/T_2 < 1/T_2^*$. However, modern technologies seem to become capable of fabricating the media of both types. Sub-monolayer quantum-dot heterostructures [31, 44] are most promising for the realization of a class D laser with strong inhomogeneous broadening. Other possibilities are solid-state matrices with active centers [14, 35] and molecular j- and h-aggregates [4, 32, 36]. Examples of suitable media with almost homogeneous broadening are excitonic Bose-condensates in semiconductor heterostructure [19, 27, 31, 33, 43] and cold atomic gases, especially, alkaline-earth-metal ones [8, 17, 37, 38, 42].

There are unambiguous observations of superfluorescence (not SR lasing) under ultrashort pulsed incoherent pumping of this kind of media. (Here the term "superfluorescence" is used instead of the more common term "SR" because in many experimental and theoretical works the latter implies that there is some preliminary coherent resonant pulse initiating a collective spontaneous emission.) Similar observations are made for the superfluorescent recombination in semiconductor samples with modest inhomogeneous broadening of active particles, which include free electrons and holes in magnetized GaAs quantum wells [21, 22], degenerate electron-hole gas in semiconductors [29], excitons in ZnTe crystals [10, 34], and In-centers in $Cd_{0.8}Zn_{0.2}Te$ crystals [13]. Based on CW pumping, the class D lasers are expected [31] to have variety of operation regimes, rich multi-mode spectra, and flexible pulse profiles, which are promising for the pulse shaping technologies and the pulse processing in "information optics" [18, 39, 45].

For brevity, we won't discuss any details of media suggested for SR lasing. In what follows we focus on typical features of that lasing in two limiting cases of active media, namely, with almost homogeneous ($T_2 \ll T_2^*$) and strongly inhomogeneous ($T_2 \gg T_2^*$) broadening of a spectral line. To our knowledge, a uniform comprehensive analysis of the SR dynamics of the two types of the class D lasers has been done for the first time.

4.3   Basic Equations and Main Conditions of Superradiant Lasing

Let us consider the simplest 2-level laser model [1, 3, 28] with an active medium which is subject to a space-frequency independent CW pumping and fills up homogeneously a Fabry–Perot cavity supplemented with DFB of counter-propagating waves. DFB is taken as a mechanism (not unique) of mode selection in favor of SR and may originate from Bragg reflections on a periodic modulation of the dielectric constant, $\varepsilon_m(z)$, of a host medium or on corrugated side walls along a cavity. Limited volume of the paper leaves no place for discussion of other SR laser schemes, e.g., based on an nonlinear (say, Raman) scattering of the pumping and generated waves [5, 20, 26] or on a feedback resulted from the wave scattering by chaotic inhomogeneities of the active or/and host media [40, 46]. 1D geometry of the problem is assumed for simplicity and may be related to a cylindrical shape of an active sample with a Fresnel number on order of unity or to a single-mode waveguide which forms a laser.

The present theory of SR lasing is based on an nonlinear 1D system of Maxwell-Bloch equations [6, 31, 47] for complex amplitudes of counter-propagating waves of the optical field and polarization density

$$E = \mathrm{Re}\,[A_+(z,t)e^{i\kappa_0 z} + A_-(z,t)e^{-i\kappa_0 z}]e^{-i\omega_0 t},$$

$$P = \mathrm{Re}\,[P_+(z,t)e^{i\kappa_0 z} + P_-(z,t)e^{-i\kappa_0 z}]e^{-i\omega_0 t}$$

(truncated at the Bragg resonance with a frequency ω_0 and a wave number $\kappa_0 = \omega_0 c^{-1}\sqrt{\epsilon_0}$) and for two respective components of the inversion density

$$N = \left[n(\Delta) + \mathrm{Im}\,[n_z(\Delta)e^{2i\kappa_0 z}]\right]/(N_0 f(\Delta)) \tag{4.4}$$

(determined, like the polarization, per unit frequency interval of the spectral line), namely, the slowly varying component n and the modulated in space component n_z, with a period equal to a half wavelength, $\lambda/2$, of the laser radiation:

$$\left[\frac{\partial}{\partial\tau} + \Sigma \pm \frac{\partial}{\partial\zeta}\right]a_\pm = i\beta a_\mp + \int_{-2\Delta_0}^{2\Delta_0} p_\pm(\Delta)f(\Delta)d\Delta,$$

$$\left[\frac{\partial}{\partial\tau} + \Gamma_2 + i(\Delta - \Phi)\right]p_\pm = -\sqrt{I}\left(in(\Delta)a_\pm \pm n_z^{1,*}(\Delta)a_\mp/2\right),$$

$$\left[\frac{\partial}{\partial\tau} + \Gamma_1\right](n(\Delta) - n_p) = -\sqrt{I}\,\mathrm{Im}\left(a_+ p_+^*(\Delta) + a_- p_-^*(\Delta)\right), \tag{4.5}$$

$$\left[\frac{\partial}{\partial\tau} + \Gamma_1\right]n_z(\Delta) = \sqrt{I}\left(a_-^* p_+(\Delta) - a_+ p_-^*(\Delta)\right).$$

Here polarization **P** means the amplitude of the spatial-spectral density of the optical dipole moments of active centers, and for simplicity all these moments are assumed to be directed along the optical electric field **E** which is linearly polarized.

A star stands for a complex conjugate. The quasi-periodic modulation of inversion, $n_z(\zeta)$, originates from the beating of counter-propagating waves and interferes with the Bragg selection of "hot" modes, which is owing to the corrugation of a laser waveguide or (that is much the same) to the spatial modulation of the host dielectric constant with an amplitude $\overline{\beta}$:

$$\varepsilon_m = \varepsilon_0 \, \mathrm{Re}[1 + 4\overline{\beta} \exp{(2i\kappa_0\zeta)}]. \tag{4.6}$$

The following dimensionless parameters and variables are used here: $I = v_c^2/\omega_{21}^2$, $\beta = \overline{\beta}/\sqrt{I}$ is a real amplitude of the Bragg modulation (4.6) (a ratio of a half-width of the photonic band gap to the cooperative frequency), $\tau = t v_c$ and $\zeta = z v_c/B_c$ are the normalized time and coordinate (where $B_c = c\sqrt{\varepsilon_0}/v_c \equiv \lambda/(2\pi\sqrt{I})$ is the so-called cooperative length and λ a wavelength in a medium), $\Gamma_{1,2} = 1/(v_c)T_{1,2}$ the relaxation rates of inversion and polarization, $p_\pm = P_\pm/(dN_0 f(\Delta))$ and $a_\pm = A_\pm \varepsilon_0/(2\pi dN_0)$ the amplitudes of polarization and field of counter-propagating waves, n_p is an inversion of a 2-level active center produced by CW pumping, $\kappa_0 = k_0 B_c \equiv \omega_0 v_c^{-1} \approx 1/\sqrt{I}$ the Bragg wave number, $\Phi = (\omega_0 - \omega_{21})/v_c$ a shift between the center of the spectral line of an active medium, ω_{21}, and the Bragg resonance frequency, ω_0. The cavity lifetime T_E (calculated without an inverted medium, $n = 0$, i.e. for a so-called "cold" resonator) influences a lot the laser dynamics, though it does not enter directly the Maxwell-Bloch equations. This time T_E is defined by the boundary conditions at laser facets $\zeta = \pm L/2$, where for the Fabry-Perot cavity the ratio of the amplitudes of the counter-propagating waves is equal to a reflection factor R, and in the limiting case of a pure DFB cavity ($R = 0$) the reflection-free boundary conditions are imposed: $a_+(-L/2) = 0$ and $a_-(L/2) = 0$.

For definiteness, an inhomogeneous broadening is described by the Lorentz function $f(\Delta) = \Delta_0/[\pi(\Delta^2 + \Delta_0^2)]$, where $\Delta = (\omega - \omega_{21})/v_c$ is a normalized frequency shift, $\Delta_0 = 1/(T_2^* v_c)$ a broadening parameter. For $\Delta_0 \gg 1$ a typical SR pulse is formed by a group of phased-in active centers with close frequencies from an interval $\Delta\nu = 2\overline{v}_c \cong 2v_c/\Delta_0$. The latter equals to two times a so-called *active cooperative frequency*, $\overline{v}_c$, which is calculated as the cooperative frequency for active centers from the same spectral interval. It is responsible for the formation of an individual SR pulse and sets a minimal limit of its duration: $\Delta t \sim 1/\overline{v}_c$, i.e., $\Delta\tau \sim \Delta_0$. That duration is almost independent on the Bragg parameter β and the relaxation times, if $\Delta t \lesssim T_2$, i.e., $\Delta_0 \lesssim \Gamma_2^{-1}$ (see Sect. 4.5). For definiteness, in the subsequent numerical plots Eqs. (4.5) are solved for the following initial condition: $n = 1, n_z = 0$, $p_\pm = 0.001, a_\pm = 0$.

Also, for dynamical examples in Sects. 4.4 and 4.5 the normalized laser length, $L \equiv B/B_c$, is taken close to an optimal value, $L \sim 2$ and $L \sim 2\Delta_0$, respectively, which is defined by the cooperative length, B_c, and the effective cooperative length, $\overline{B_c} = B_c \Delta_0 \equiv c/(\overline{v}_c\sqrt{\varepsilon_0})$. For simplicity, we always assume exact tuning of the Bragg resonance at the center of spectral line, $\Phi = 0$, and neglect Ohmic losses.

In low-Q cavities of Fabry-Perot type with DFB, the modes consist of superposition of two counter-propagating waves, each wave being split by Bragg scattering into two spatial harmonics which have close wave numbers slightly shifted from

Fig. 4.1 Typical nondimensional growth rates, Im [Ω] , (*dashed line*) and frequency shifts, Re [Ω], (*solid line*) of modes in a 1D DFB laser vs a wave-number shift, κ, for **a** unstable polariton modes in the case of an active medium with homogeneous broadening and **b** unstable electromagnetic modes in the case of an active medium with strong inhomogeneous broadening. The values $\Omega = 0, \kappa = 0$ correspond to the Bragg resonance of the DFB tuned to the center of laser transition
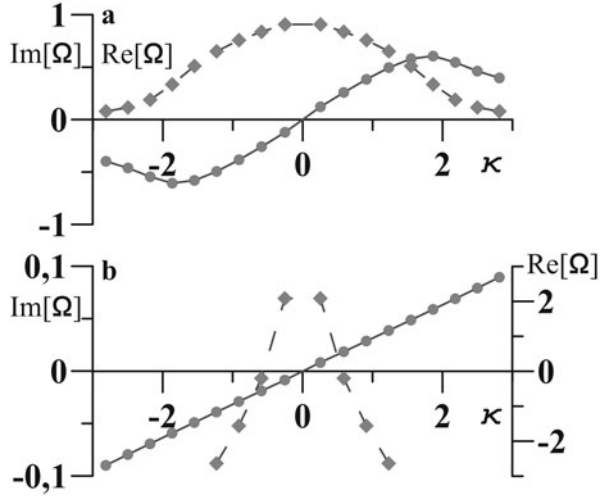
the resonant Bragg value. Spectral inhomogeneity of mode gains gives rise to an efficient selection of modes and results in one-, two- or multi-mode SR lasing under the condition (4.3). More details on the mode SR threshold as well as typical spectra and growth rates of modes (shown in Fig. 4.1 for a pure DFB cavity in the case of homogeneous and inhomogeneous broadening) follow from the linearized equations of laser dynamics under a given inversion ($n = $ const, $n_z = 0$). For an homogeneous active sample one has the well-known dispersive and characteristic equations:

$$\kappa^2 + \beta^2 = \left(\Omega + \frac{n}{\Omega + i(\Delta_0 + \Gamma_2)} \right)^2 ,$$

$$\Omega + \frac{n}{\Omega + i(\Delta_0 + \Gamma_2)} = \frac{2R\beta}{1 + R^2} + \frac{\kappa(1 - R^2)}{1 + R^2}(1 + e^{2i\kappa L})/(1 - e^{2i\kappa L}). \quad (4.7)$$

The first equation is owing to local properties of a medium with due account of the Bragg scattering of waves. It gives a relation between the frequency, $\Omega = (\omega - \omega_0)/\nu_c$, and the wave-number shift, $\kappa = (k - k_0)B_c$, of a mode. The second equation results from the boundary conditions and picks out the discrete wave numbers, κ, of counter-propagating waves satisfying the boundary conditions.

There is an inevitable phasing-in of active centers responsible for an instability of a mode with a growth rate which exceeds the polarization relaxation rate, Im[ω] > $1/T_2$. These centers will emit collectively, i.e., *superradiate*, so that during some time the intensity of their radiation becomes much greater than the sum of radiation intensities of the individual centers if they were not phased-in.

4.4 Homogeneous Broadening. Superradiant Lasers on Polariton Modes with Negative Energy

CW lasing is possible if the pumping and/or active sample length are above the respective instability threshold values for at least one mode. It happens approximately at $n_p v_c^2 T_2 T_E > 1$, and the lasing can be multi-mode at larger values of the pumping and laser length. In the case of a spectral line with homogeneous broadening, all laser modes are known as polariton (not electromagnetic) ones and have negative energy [47]. The latter means that the switching on of the pumping starts a radiative dissipative instability of polariton modes, i.e., their amplitudes will grow due to transition of their energy into the energy of a field radiated outside a cavity.

A dispersion of waves caused by a dense active medium with homogeneous broadening guarantees essential differences of mode growth rates (mode qualities) in a Fabry–Perot cavity without any DFB or other mode selection means. So, this case is quite representative for analysis, say, of the single or double mode SR lasing. Thus, in the present section we will analyze mainly the case of Fabry–Perot cavity ($\beta = 0$), bearing in mind that the dynamics of a class D laser with a combined DFB Fabry-Perot cavity is qualitatively the same under the condition $\beta L < 1$.

In the general case, a complex spectrum of the polariton modes is slightly asymmetric with respect to the central frequency $\omega_{21} = \omega_0$ in the presence of a discrepancy, $|\delta| < 1/2$, between a "half-wavelength" laser length, $k_0 B / \pi = m_0 - \delta$, and an integer of this value, m_0:

$$(\omega_m - \omega_{21})T_2 = n v_c^2 T_2 T_E x_m \big/ (1 + x_m^2) + i[n v_c^2 T_2 T_E \big/ (1 + x_m^2) - 1]. \qquad (4.8)$$

Here we introduced a ratio of the real and imaginary parts of a partial frequency of an mth electromagnetic mode of a Fabry–Perot cavity: $x_m = (m - m_0 + \delta)\pi / \ln |R|^{-1}$. According to Eq. (4.8) a width of the polariton mode spectrum is less than $2 n v_c^2 T_E$ and may exceed the width of a spectral line, $2/T_2$, only by a factor equal to the ratio of the quantity $n v_c^2 T_2 T_E$ to its value (~ 1) at the laser threshold.

In a laser with the combined DFB Fabry-Perot cavity, a spectrum of the polariton modes is similar to that given by Eq. (4.8) (see Fig. 4.1), if $\beta L < 1$. Note that a center of the cavity is fixed at a point where the DFB structure (4.6) has a central maximum since we assume that $\beta = \text{Re}[\beta]$. Equations (4.5) take into account a subwavelength mismatch of the cavity length from its integer-wavelength value by means of a phase of a complex reflection factor R related to the value δ.

In the case $\beta \ll 1/L$, according to a geometrical optics with neglect of the coupling of the counter-propagating waves, Eqs. (4.7) and the spectrum (4.8) are valid also when the inversion, $n(\zeta)$, is slow varying and the wave-number shift, $\kappa(\zeta)$, is inhomogeneous, if both functions are substituted with their spatially averaged values, $\bar{n}$ and $\bar{\kappa}$. To simplify mode analysis, we assume that the opposite laser facets have equal complex reflection factors: $R_1 = R_2 = R$. However, even in this case the actual profiles of the counter-propagating fields may be asymmetric with respect to the cavity center, $\zeta = 0$, due to an nonlinear inversion grating, $n_z(\zeta)$, and polarization jumps at the facets of an active sample. The grating modifies DFB, i.e., changes an

effective value of β, and the jumps make complex (and different) corrections to the reflection factors $R_{1,2}$.

Usually, an equation for mode lasing thresholds, $\text{Im}[\omega_m] = 0$, yields the most resonant polariton mode, $m = m_0$: $\overline{n}L/(\Gamma_2 \ln |R|^{-1}) = 1 + (\pi\delta/\ln |R|^{-1})^2$. Above this so-called *first lasing threshold*, $n_p > \overline{n} = n_{m_0}$, a single mode steady-state lasing will appear. A spectral width of that almost harmonic field may be extremely narrow due to an negligible income from a cavity noise as compared to a quantum polarization noise. The latter may be very small in cold active media [8, 17, 37] and makes it possible to fabricate frequency (and time) oscillators with the spectral line widths much less than that in the standard oscillators based on the class A or B lasers.

The stronger the pumping, n_p, the greater is the amplitude of the lasing mode. At the same time, an average level of inversion is regulated by an induced emission and does not depend on the pumping, $\overline{n} = n_{m_0} = \text{const}$, as it is fixed by the boundary conditions so that an amplification factor of the field along the cavity length is equal to a given value $1/R$. However, increasing of the pumping changes the profile of inversion, $n(\zeta)$, which will grow in the cavity center, where the mode field is weaker, and decrease at the cavity sides, where the mode field is stronger and eats away the inversion more effectively. (This effect as well as the formation of an inversion grating, n_z, are much less pronounced in the class A and B lasers.) As a result, at high enough pumping (or long enough active sample) the class D lasing may turn into non-stationary double or multi-mode regime of generation.

In the case of quite independent and stable lasing of each polariton mode, the overall spectrum will consist of two or several harmonics with almost constant amplitudes and weak spectral broadening. Even in the case of symmetric cavity ($R_1 = R_2$) and symmetric "linear" modes (4.8), the field of quasi-stationary lasing modes may be asymmetric due to the inversion grating and the facet jumps of the polarization of an active medium. That spontaneous symmetry breaking involves also the inversion profile, which is self-consistent with the field of modes and automodulated due to their beating. An overall spectral width of the polariton modes (and, hence, an intermode spacing) does not exceed the value $2\overline{n}\nu_c L/\ln |R|^{-1} \sim 2/T_2$, which is considerably less than an intermode spacing, $\pi\nu_c/L = \pi c/B\sqrt{\varepsilon_0}$, of the corresponding electromagnetic modes of a "cold" cavity if the laser length is not too long, $L \lesssim \sqrt{\pi(\ln |R|^{-1})/2\overline{n}}$.

In a 1D class D laser with Fabry-Perot cavity, a quasi-stationary lasing of more than one mode is possible only in an almost degenerate case $\delta \approx \pm 1/2$ when the thresholds of two central modes (4.8) are nearly equal. Then, in a wide range of parameters, there is the quasi-stationary lasing of two polariton modes with almost equal intensities proportional to pumping, and the mode spacing, $\pi/T_2 \ln |R|^{-1}$, does not depend practically on the laser length, the cooperative frequency, and the pumping. That lasing is accompanied by an automodulation, with a beating period $T_2 \ln |R|^{-1}$, of the output intensity, the inversion of an active medium, and the mode amplitudes.

Similar double mode lasing is possible in the presence of DFB when the thresholds of two polariton modes are leveled by choosing proper values of $\beta \lesssim 1/L$ and/or $\Phi = (\omega_0 - \omega_{21})/\nu_c$ or by including (within the model (4.5)) a weak inhomogeneous

broadening $1/T_2^* \lesssim 1/T_2$ and/or weak inhomogeneities of the density, $N_0(\zeta)$, and pumping, $n_p(\zeta)$. All these factors weaken the competition of modes and favor their simultaneous lasing. There are, of course, other factors of this type which are not included in the model (4.5), say, the polarization degeneracy of modes or the non-resonance, e.g. thermal nonlinear, action of modes on an active medium.

In any case, in the space of operating laser parameters there is a boundary, called *a second laser threshold*, that separates a domain of the steady-state lasing and a domain of the non-stationary lasing of a single mode. That threshold may exceed the first one by many times and is very sensitive even to a weak inhomogeneous broadening, so that the difference of the two thresholds becomes small at $1/T_2^* \gtrsim 1/T_2$. The papers [23, 24] contain analytical studies of the influence of homogeneous broadening on the first threshold of a laser with Bose–Einstein distribution of active centers and on the second threshold of a single mode class D laser within a model of splitting of a spectral line with homogeneous broadening into two similar lines shifted symmetrically with respect to the frequency of a partial mode of a laser cavity. That papers contain also a numerical analysis of the single, double and multi-mode non-stationary generation of the class D laser with homogeneous and weak inhomogeneous broadening.

What is specific to the class D lasers is that they demonstrate another mechanism of the transition to non-stationary lasing regimes which is more efficient and very different from the above-mentioned two- and multi-mode mechanisms know for the class A and B lasers. Namely, it is related to a global instability of a steady-state lasing mode due to its non-adiabatic destruction via a SR drop of inversion in a considerable part of an active sample with a time scale less or on the order of the polarization relaxation time, T_2. The same SR mechanism may destroy the two- or multi-mode quasi-stationary generation far above the first lasing threshold. Of course, the SR mechanism may be accompanied and complicated by other instabilities of mode lasing (say, modulation or parametric ones) favored by the Rabi-oscillations and inhomogeneous profile of inversion, which are unavoidable in a strong and highly inhomogeneous field of a class D laser. Such instabilities are present also in the class A and B lasers (see, e.g., Chap. 3 in [28]) and owing to a so-called Rabi-splitting of a lasing mode, which leads to its parametric decay into the neighbouring modes, and an inversion grating, which originates from beating of the counter-propagating waves within each mode and favors the intermode scattering, the automodulation of radiation, and the growth of inhomogeneities of the field and inversion.

Due to low-Q cavities in the class D lasers, the unique SR instability of modes is started by an initiated collective spontaneous emission in a central region of an active sample where there is perceptible (maybe, multiple) excess of inversion over an average level, $\overline{n_m}$, of a quasi-stationary generation. The catastrophic SR drop of inversion makes a major part of an active sample incapable of the field amplification during a time period on order of T_1. Hence, a pulsed generation (under CW pumping!) becomes inevitable, and the field, polarization, and inversion become highly inhomogeneous and variable. The latter does not allow one to describe the details of SR lasing on the basis of one or several polariton modes calculated according to a quasi-stationary or average distribution of the inversion in an active sample.

A qualitative analysis and numerical simulations show that the SR mechanism of instability of a single steady-state lasing mode (responsible for the second laser threshold) or double (maybe, multi-) mode lasing takes place if the polarization relaxation time, T_2, exceeds considerably, say, by two or more times, the time scale of unidirectional SR [47], $\sim (n_{max} v_c^2 T_E)^{-1}$, in a central region of length $\sim B/\ln|R|^{-1}$, where an inversion profile is close to a maximum value, $n \approx n_{max}$. This maximum should also exceed considerably the corresponding laser threshold, $\overline{n_m}$, which, by the way, may be essentially smaller than a "linear" estimate based on Eq. (4.8), n_m, due to the modifications of effective DFB (β) and reflection factors ($R_{1,2}$) by the dynamical grating, $n_z(\tau, \zeta)$, and the jumps of the polarization at the laser facets.

It is worth noting that all our mode analysis of the class D lasing is valid only for short lasers when

$$L \lesssim \ln|R|^{-1}/\sqrt{n_p}, \text{ i. e., } T_E \lesssim 1/v_c\sqrt{n_p}. \qquad (4.9)$$

In the opposite case of long samples, $L \gg \ln|R|^{-1}/\sqrt{n_p}$, even for considerable reflections, $\ln|R|^{-1} \sim 1$, and not far from the first laser threshold, $n_p \sim n_{m_0}$, the leading part in emission is taken by a coherent unidirectional superfluorescence, i. e., a collective spontaneous emission of continuous waves (not discrete modes). The latter will be formed independently in sections of size $\sim \ln|R|^{-1}/\sqrt{n_{m_0}}$ and reabsorbed in neighbouring sections of the same size, so that the coherent mode emission will be suppressed, and there will be created a noise-like low coherent emission with a smooth spectrum which can be even wider than the spectral line $(2/T_2)$.

On the contrary, the single, double and multi-mode SR regimes under the condition (4.9) show well-defined coherent pulses and regular dynamical spectra of the field and inversion. These spectra may exhibit some mode structure and can be much wider than the gain spectrum, approaching a value $\sim v_c \sqrt{n_{m_0}} \gg 1/T_2$ related to a minimal SR pulse duration. In these SR lasing regimes, an increase in the pumping, n_p, results in a rise of a pulse production rate and an increase of an average (over the laser length and time) inversion which may exceed the laser threshold. Further increase of the pumping leads to an overlapping of the SR mode pulses and a formation of a chaotic structure of the output oscillograms and dynamical spectra of the field and inversion, where well-defined modes are absent.

In the particular case of a symmetrical cavity, $R_1 = R_2$, the SR mode lasing will cause a dynamical spontaneous symmetry breaking of the mode field profiles and the self-consistent inversion profile which are averaged over a long enough time scale, $\Delta T \gg T_1$, to cover several (not too many) typical sets of pulses of all modes. The origin of the dynamic asymmetry is similar to that of the asymmetry in the case of the quasi-stationary mode lasing. However, the former may be metastable, i.e., on a time scale much longer than ΔT the regions of maximum inversion and minimal intensity of the mode field may be shifted irregularly to the left side or to the right side from the cavity center.

Dynamics of the mode SR lasing is sensitive not only to the level of pumping, n_p, but also to the pumping power related to the inversion relaxation rate, $1/T_1$.
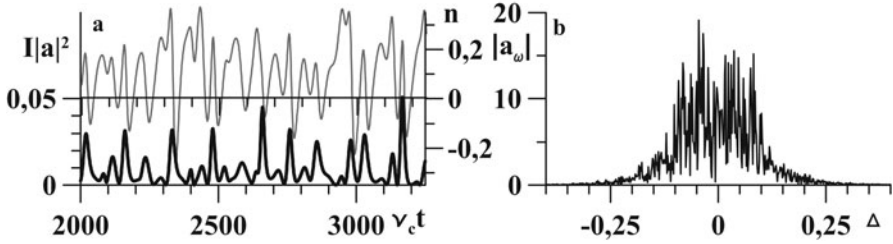
Fig. 4.2 Typical SR generation of a class D laser with DFB and an active medium with homogeneous broadening: $n_p = 1$; $L = 1$; $\beta L = 1$; $\Gamma_1 = 0.01$; $\Gamma_1 = 0.02$. **a** Time dependence of the field intensity, $I|a|^2$, (*black line down*) and the inversion, n, (*gray line up*). **b** Spectrum of the field amplitude, $|a_\omega|$

Indeed, after formation of each SR pulse the inversion falls down sharply and may achieve even negative values in some domains of an active sample. It means that a laser will be switched off for a short time ($\sim T_1$), until the pumping restores a high enough level of the inversion. That dynamics is especially transparent in the case of a single mode SR lasing, when the pulses are very regular and powerful (they may be described analytically, see [30]), and is observed also in the case of the double or even multi-mode SR lasing, when there is a nonlinear competition between pulses of different modes which sometimes weaken and lengthen each other since they all are generated by the same ensemble of active centers.

SR pulses of a class D laser may differ considerably (see Fig. 4.2), even by many times, in their duration, amplitude and delay time since an underlying process of the initiated collective spontaneous emission depends strongly on the instantaneous inversion profile and begins each time from new configurations of weak field and polarization left in the cavity after a previous pulse. Analysis of the pulse parameters and efficiency of the SR generation (by definition the latter is equal to a percentage of energy emitted in the form of SR pulses) makes it possible to find optimal parameters of a class D laser as a SR oscillator [31]. For example, in the case of pure DFB cavity with a given factor β an optimal laser length is $L \sim 1/\beta$.

4.5 Inhomogeneous Broadening. Mode Selection as a Way to the Superradiant Generation

Let us consider the class D lasers with strong inhomogeneous broadening of a spectral line of an active medium: $1/T_2^* \gg \nu_c \gg 1/T_2$. They have close values of the first and second laser thresholds (what is similar to the class B lasers [28]), even in the case $1/T_2^* \sim 1/T_2$). So, we may skip a discussion of the quasi-stationary generation of one or several modes which takes place in a narrow range of laser parameters, corresponds to a low intensity of emission and leads to a narrow hole burning in an inversion profile at the frequencies defined by the lasing modes. Below we'll focus on

the main problem: whether one can achieve the generation of well-resolved powerful SR pulses in this kind of CW class D lasers?

Now, contrary to the case of homogeneous broadening, the laser modes in an inverted medium have a positive energy, and their spectrum in the case of not too short lasers with $T_E \gtrsim T_2^*$ (according to Eq. (4.7) with $\Delta_0 \gg \Gamma_2$) is very similar to the spectrum of electromagnetic modes calculated in the case of a "cold" cavity with zero inversion [6, 30, 47]: $\omega_m \approx m\pi c/B\sqrt{\varepsilon_0}$. It is not valid only in a close vicinity of the photonic band gap $|\Omega| \lesssim \beta$, which is owing to the Bragg resonance, in the case $L \gtrsim 1/\beta$ (for the mode numbers m near $m_0 = k_0 B/\pi + \delta$, see Eq. (4.8)). Here, with that exception, for the low-Q cavities of the standard Fabry-Perot type the growth rates (and other parameters) of neighbouring longitudinal modes are very close each other if the necessary conditions of SR are fulfilled (see Eqs. (4.2) and (4.3)):

$$1/T_2 \ll \bar{\nu}_c\sqrt{n_p} = \bar{\nu}_c\sqrt{n_p}/\Delta_0 \lesssim 1/T_E. \qquad (4.10)$$

The last inequality means $L \lesssim \Delta_0 \ln|R|^{-1}/\sqrt{n_p}$, that is similar to Eq. (4.9) with the substitution $\nu_c \to \overline{\nu_c}$. In the opposite case of long samples, $L \gg \Delta_0 \ln|R|^{-1}/\sqrt{n_p}$, even in the close vicinity of the first laser threshold and even for strong reflections, $\ln|R|^{-1} \sim 1$, the leading emission process is an unidirectional superluminescence, i.e., an incoherent amplified spontaneous emission of continuous waves, not discrete modes. This process will consume all inversion along the laser, suppress the coherent mode emission, and create a noise-like incoherent emission throughout the whole inhomogeneous spectral line, $2/T_2^*$ (similar to a coherent superfluorescence in a homogeneous spectral line, as discussed after Eq. (4.9)).

So, a non-stationary, in particular, SR mode generation will involve a large number of modes since intermode spacing, $\pi c/B\sqrt{\varepsilon_0} \sim 1/T_E$, is much less than the width of an inhomogeneous broadening, $2/T_2^*$, in the case under consideration when $\Delta_0 L \gtrsim 1$. It means that the laser emission will be quasi-chaotic, noise-like, without clear individual pulses of mode SR. Moreover, spreading of the frequencies of active centers within a bandwidth of each mode used to destroy the phasing-in of their emission and to suppress the SR mechanism of cooperative pulsed emission even far above the second laser threshold.

Therefore, to support a coherent pulsed SR emission in the class D lasers with inhomogeneous broadening one should introduce an additional mode selection, i.e., increase a growth rate (or an amplification factor) of one or several modes as compared to all others. It is DFB of counter-propagating waves that makes this selection possible in our 2-level laser model (4.5). DFB in a low-Q Fabry-Perot cavity intensifies also the dispersion and non-equidistance of a small number of longitudinal modes situated close to the photonic band gap (which has a bandwidth $2\bar{\beta}$ and is centered at the frequency ω_0). These modes could support the SR pulsed generation in the vicinity of the photonic band gap and do not affect quasi-stationary generation of a number of longitudinal modes of a Fabry–Perot cavity far enough from the photonic band gap. Note that the efficient Bragg selection of modes makes the 2-level model (4.5) insensitive to a profile of inhomogeneous broadening since the mode SR

effect requires the conditions $\beta L \gtrsim 2\pi R$ and

$$\Delta_0 \equiv \frac{1}{T_2^* \nu_c} \gg 1 \gtrsim \beta \equiv \frac{\overline{\beta}\omega_0}{\nu_c} \gtrsim \frac{1}{\Delta_0} \equiv \frac{\overline{\nu_c}}{\nu_c} \gtrsim \Gamma_2 \equiv \frac{1}{T_2 \nu_c}, \qquad (4.11)$$

which leave for lasing only active centers from a narrow central part of a spectral line, where $f(\Delta) \approx 1/\pi = \text{const}$.

From Eqs. (4.5) it is easy to find the maximum growth rate of each mode and to estimate a number of lasing modes for a given level of inversion: $M \lesssim \beta L$ (π exp $(-nL/\Delta_0)$) in the case $R = 0$ taken for simplicity's sake. A threshold length of a cavity, calculated at $n = n_p$, reads approximately $L_{th} \approx (\Delta_0/n_p) \ln(2\pi/\beta L) \sim \Delta_0/n_p$, where the former equality is valid in the case $R \ll \beta L$ only, and the latter estimate is general and valid for $\ln|R|^{-1} \sim \ln(2\pi/\beta L) \sim 2$. That may be not only the first, but also the second laser threshold, and even the SR threshold exceeding the second one.

First of all, let us analyze a pure DFB cavity, bearing in mind more or less freely escaping radiation that is necessary for the SR lasing. The latter means not too large both the length, L, and the Bragg parameter, β, so that the value βL and, hence, the resonance reflection factor, $R_0 = \tanh(\beta L)$, are smaller than or of the order of unity and the photonic band gap of width 2β contains no longitudinal modes. Then, according to the Bragg selection mechanism, a quasi-periodic sequence of bunches of SR pulses can be generated. They are formed by one or several pairs of modes which are the nearest to the photonic band gap. In this CW lasing, a sharp SR growth of the field with a mode profile inside a cavity happens every time after a delay period on order of T_1 it takes for pumping to restore an inversion of the laser transition of those active centers which are responsible for the collective excitation of a given SR mode.

An analysis of the dynamical spectra of the field and the inversion shows that the most powerful pulses are produced by the correlated pairs of modes which are situated symmetrically with respect to the photonic band gap. In a spectral band of a given mode, several subgroups of phased-in active centers with close frequencies may be formed. Each subgroup emits an individual SR pulse, and the pulses from different subgroup have some delay with respect to each other. A spectral width of a subgroup is defined by the actual cooperative frequency: $\Delta \simeq 2\overline{\nu_c} \approx 2\nu_c/\Delta_0$ (see Sect. 4.3). If $\Delta_0 < \Gamma_2^{-1}$, an increase of the polarization relaxation time T_2 up to the maximum value $T_1/2$ does not practically change a pulse profile of the well developed SR lasing. On the contrary, when the polarization relaxation time T_2 decreases below the critical value $1/(\nu_c^2 T_2^*)$ (so that $\Delta_0 > \Gamma_2^{-1}$ and the principal SR condition (4.2) becomes invalid), the SR pulses disappear and the CW lasing cannot support the collective spontaneous emission.

In general, for the class D laser, we observe five qualitatively different regimes, namely, quasi-stationary (Fig. 4.3a, b), self-modulated (Fig. 4.3c, d), regular pulsed (Fig. 4.3e, f), irregular bunched (Fig. 4.3g, h), and quasi-chaotic (Fig. 4.3i, j) ones. Three last regimes of SR type may be achieved by changing the laser length, L, the width of the photonic band gap, β, the pumping level, n_p, and other laser parameters.
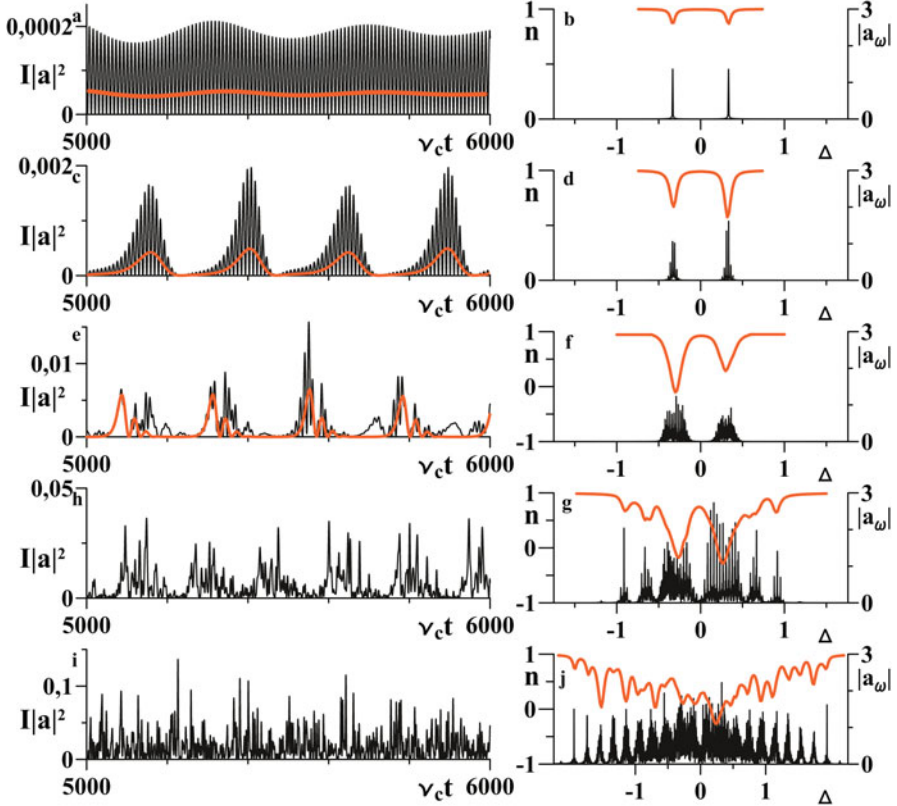
Fig. 4.3 Transition from an ordinary two-mode quasi-stationary generation to a multi-mode quasi-chaotic SR lasing in the CW class D lasers as a result of changing of an active sample length: a,b) $L = 6.7$; c,d) $L = 7$; e,f) $L = 8$; g,h) $L = 10$; i,j) $L = 14$. Other laser parameters are: $n_p = 1$; $R = 0.1$; $\Delta_0 = 4$; $\Gamma_1 = 0.01$; $\Gamma_2 = 0.03$. *Left column* shows the oscillograms of intensity of the field, $I|a|^2$, at the laser edge; the intensity of one mode (from two similar modes on the plots a,c,e) is shown by *orange*. *Right column* shows the spectra of the output field, $|a_\omega|$, (*black lines*) and the inversion, n, (*orange lines*)

If the pumping is strong enough, the spectral widths of the SR modes, defined mainly by their Rabi frequencies, may be as large as the actual cooperative frequency; thus, overlapping of mode spectra is possible (Fig. 4.3j).

For the class B lasers, two modes (two upper dots on the right plot in Fig. 4.1) with utmost quality factors dominate over other modes because of higher quasi-monochromatic fields. The latter burn deep and wide holes in the inversion spectral profile. As a result, the multi-mode non-stationary (automodulated) lasing is possible only under very strong pumping or in the case of very long cavity, and the inversion never becomes negative. On the contrary, for the class D lasers, the steady-state lasing is almost impossible due to the SR phenomenon, and two or several modes may demonstrate simultaneous pulsed generation even in the case of short enough

laser cavity and at the pumping level on the order of the laser threshold value (Fig. 4.2). In this case the hole burning proceeds in a remarkable pulsed regime, the widths of these holes may be rather narrow as compared to an intermode spectral spacing, and the inversion inside the holes can reach negative values during some periods of time (Fig. 4.3f, h, j).

Too strong coupling of counter-propagating waves in the case $\beta \gg 1/L$ favor the irregular generation of a large number of SR pulses at different frequencies in different laser section of a length $\sim 1/\beta$. These pulses lengthen and delay a bit, due to reabsorption in the neighbouring sections of an active medium, and form a quasi-chaotic sequence at the laser output (Fig. 4.3i). Similar reabsorption and chaotic behavior of pulses take place even in the case of an optimal DFB, $\beta \sim 1/L$, if one increases the pumping power and/or rate (n_p, T_2^{-1}). Then an additional pumping energy does not transform into the SR mode pulses, but contributes mainly to a slowly modulated and less coherent emission of waves with continuous spectrum typical for the unidirectional collective spontaneous emission.

Let us turn to mode SR in a *combined DFB Fabry-Perot cavity*. In the most interesting case of a rather short laser (see Eq. (4.10)), the intermode spacing is greater than the mode growth rates even under the maximum inversion, $n = n_p$. Then each mode with the growth rate greater than $2/T_2$ (they all have frequencies close to the Bragg band gap) will emit independent SR pulses. Each pulse is formed by the active centers from a narrow spectral interval, $\delta\omega$, which is on the order of either the mode growth rate ($\delta\omega \lesssim \overline{n}\,\overline{\nu_c}$) at small field amplitudes or the Rabi frequency ($\delta\omega \sim \omega_R$) at high field amplitudes. For a multi-mode SR laser, a typical feature of the output dynamical spectra is a specific order of the mode switching on and switching off which makes the regular frequency shifts in the consecutive mode SR pulses.

As a rule, when the reflections from laser facets increase and are not very high, the number of lasing modes increases also and their spectrum shows asymmetry, being dependent on a phase of the reflection factor, arg R. If only a few modes are SR lasing, their pulses appear usually as a sequence of bunches with a period on the order of T_1 (like in Fig. 4.3g, h). The pulses in each bunch are well correlated, and the respective pulses in neighbouring bunches may be shifted in phases. When some laser parameters are changed, say, by two times or even less, there are essential changes in the number of lasing modes, their average spectral positions and overall dynamical spectrum of emission; the profiles and correlation features of both SR pulses and their bunches are also changed. At the same time, there is a broad range of the laser parameters, where a class D laser is a single-mode and emits a quasi-periodic sequence of almost similar SR pulses, as shown in Fig. 4.4.

A remarkable regime appears in the case when only one or a few modes are SR lasing and most of other modes are almost in the steady-state regime. Namely, in addition to the bunches of the SR pulses, there exists a periodic series of the coherent pulses with the period equal to one or one half of the cavity round-trip time (see Fig. 4.5). That self-mode-locking effect does not require any mode-locking technique [28] (passive or active) and provides a duration of the pulses less or on the order of the relaxation times of both the inversion and polarization of an active
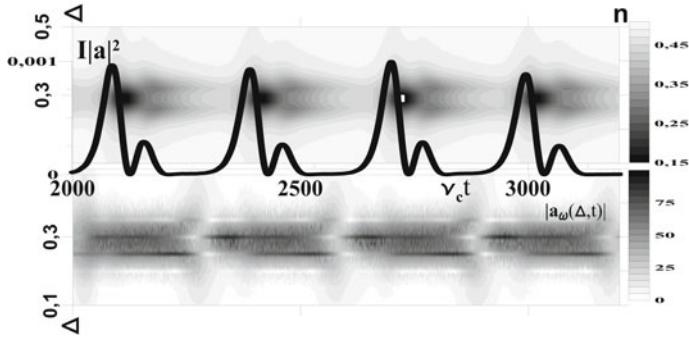
Fig. 4.4 Single-mode SR lasing in a combined DFB Fabry–Perot cavity in the case of an active medium with strong inhomogeneous broadening. Holes burned in the dynamical spectrum of the inversion, $n(\Delta, t)$, (*black regions on the upper plot*) correspond to peaks in the dynamical spectrum of the field amplitude, $|a_\omega(\Delta, t)|$, (*dark regions on the lower plot*) and peaks in the oscillogram of intensity of the output field, $I|a|^2$, (*black thick line*). Laser parameters are: $n_p = 0.5$; $R = 0.1$; $L = 10$; $\beta L = 1$; $\Delta_0 = 4$; $\Gamma_1 = 0.01$; $\Gamma_2 = 0.03$

center. The effect is owing to the SR mode pulses which form a quasi-periodic series (with a period $\gtrsim T_1$) and burn the deep holes of inversion (even eliminate it, i.e., change its sign: $n < 0$) in some spectral intervals during some periods of time. Under these conditions, if the reflection factor R is not much less than the DFB parameter βL, there exists partial self-locking of the quasi-stationary lasing modes which have smaller growth rate, greater shifts from the photonic band gap, and more or less equal frequency spacing, but do interact with the SR modes in a coherent way. The SR modes can also contribute directly to the pulse traveling periodically around the cavity.

The formation of this pulse yields an example of the dynamical spontaneous symmetry breaking in the class D lasers with inhomogeneous broadening which is not possible in the case of homogeneous broadening of a spectral line (cf. Sect. 4.4). The energy contents of the self-mode-locked pulse, the SR mode pulses, and the accompanying non-stationary quasi-continuous radiation may be of the same order. The relative weights of these three field components depend on the laser parameters.

For a low-Q cavity with relatively high DFB quality, $\beta L \gtrsim 1 \gg R$, the train of the "self-mode-locked" pulses and the bunches of SR pulses are less pronounced and less regular due to stronger reabsorption and nonlinear mixing of the individual mode pulses. Nevertheless, there is a wide range of parameters where the class D lasers are capable of generation of a quasi-periodic train of powerful ultrashort coherent pulses in the absence of any additional elements for self-mode locking. According to estimates [31], that lasing regime may be achieved in CW-pumped heterostructures with sub-monolayer quantum dots InAs /GaAs and a lateral Bragg grating ensuring a proper selection of longitudinal modes.
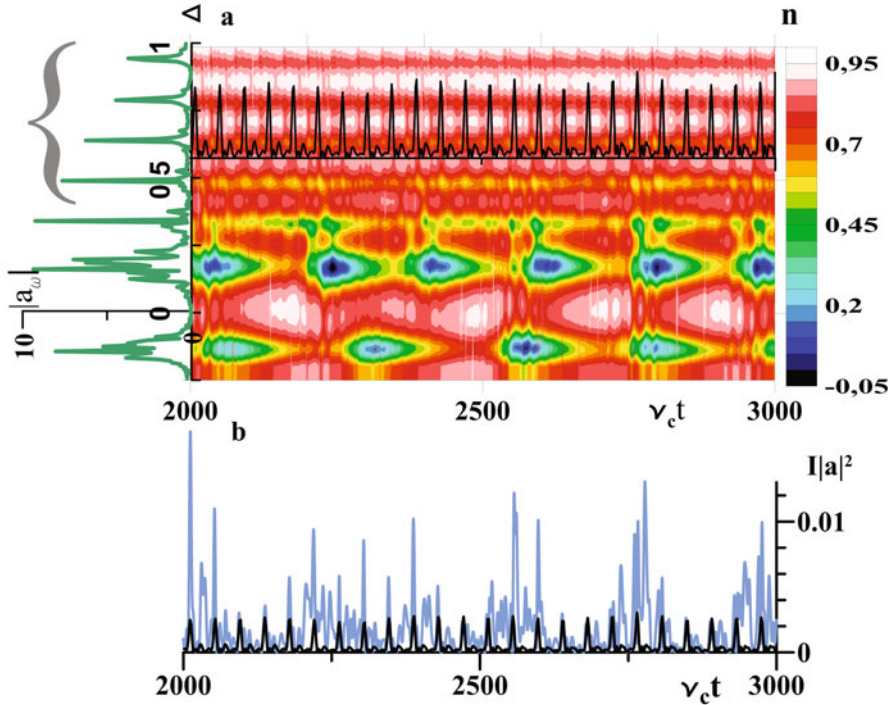
Fig. 4.5 Spontaneous self-mode-locking in a SR laser with strong inhomogeneous broadening of an active medium in a combined DFB Fabry–Perot cavity. The deep holes of the inversion (*blue drops* in the bottom part of an inversion dynamical spectrum **a**), caused by the SR pulses of the main two modes, play part of a saturable absorber and ensure synchronization of the other four steady-state modes (marked by a brace at the upper left corner). The latter form an output field (*thick black lines* on the plots **a** and **b**) which is periodic and responsible for about 30% of the laser output power, according to an oscillogram **b**. The laser parameters are: $n_p = 1$; $R = 0.1$; $L = 20$; $\beta L = \sqrt{3}$; $\Delta_0 = 13$; $\Gamma_1 = 0.01$; $\Gamma_2 = 0.03$

4.6   Conclusions

Dense ensembles of active centers capable of lasing under the condition (4.1) are promising for both fundamental and applied research, e.g., for an ultrafast information processing in an optical system of strongly interacting particles. These ensembles have a large number of dynamical degrees of freedom, much greater than the number of modes of a low-Q cavity which is necessary for the mode SR lasing and let the radiation come out freely, without suppression of the coherent polarization dynamics. That is why the dynamics of such class D lasers, especially with inhomogeneous broadening of an active medium, becomes extremely rich and results in complicated, though quite regular dynamical spectra of emission.

As a whole, the class D lasers are very intriguing systems which can provide smooth transitions between various non-stationary multi-mode regimes of generation by means of tuning of a low-Q cavity, an active medium, and a pumping. The presence of inhomogeneities of a medium or a pumping in a laser cavity and, moreover, the presence of different active or passive media taking part in the resonance interaction via the self-consistent electromagnetic field may lead to new unexpected dynamical consequences and practical applications (cf., e.g., [2, 9, 26, 41]).

Nonlinear phenomena in the class D lasers originate from the collective radiative behavior of active centers and become more and more important in condensed matter physics for various many-particle systems (e.g., [11, 19, 25, 26, 33]). These phenomena could give rise to unique sources of the coherent pulsed emission with guided spectral-correlation features. They can serve as unique diagnostic tools of the cooperative states of strongly-interacting particle ensembles. One can change the dynamical spectra of emission by adapting a proper coherent composition of the "hot" lasing modes via managing the parameters of pumping, an active sample, and a low-Q cavity. On the other hand, one can get information on the transitions between cooperative states in a many-particle system (including phase transitions) by tracing the changes in its "hot" mode composition and dynamical spectra of emission. Thus, it seems that the SR lasing and other nonlinear phenomena in the class D lasers will enter soon the modern technologies of information optics and diagnostics of many-particle states.

References

1. Abraham, N.B., Mandel, P., Narducci, L.M. Progress in Optics, vol. 25, pp. 1–190. Noth-Holland, Amsterdam (1988) (ed. by E. Wolf)
2. Ammerlahn, D., Kuhl, J., Grote, B. et al.: Collective radiative decay of light- and heavy-hole exciton polaritons in multiple-quantum-well structures. Phys. Rev. B **62**(11), 7350 (2000)
3. Arecchi, F.T., Harrison, R.G.: Instabilities and Chaos in Quantum Optics. Springer, London (2011), Chapters 1–3
4. Arias, D.H., Stone, K.W., Vlaming, S.M., et al.: Thermally-Limited Exciton Delocalization in Superradiant Molecular Aggregates. J. Phys. Chem. B **117**, 4553–4559 (2013)
5. Avetisyan, Yu.A., Trifonov, E.D.: Maxwell-Schrödinger equations for a dilute gas Bose-Einstein condensate coupled to an electromagnetic field. J. Exp. Theor. Phys. **106**, 426 (2008)
6. Belyanin, A.A., Kocharovsky, V.V., Kocharovsky, Vl.V.: Collective QED processes of electron-hole recombination and electron-positron annihilation in a strong magnetic field. Quant. Semicl. Opt. JEOS, Part B **9**, 1–44 (1997)
7. Blokhin, S.A., Maleev, N.A., Kuzmenkov, A.G., et al.: Vertical-cavity surface-emitting lasers based on submonolayer InGaAs quantum dots. IEEE J. Quant. Electron. **42**, 851–858 (2006)

8. Bohnet, J.G., Chen, Z., Weiner, J.M., et al.: A steady-state superradiant laser with less than one intracavity photon. Nature **484**, 78–81 (2012)

9. Boiko, D.L., Vasil'ev, P.P.: Superradiance dynamics in semiconductor laser diode structures. Opt. Express **20**(9), 9501 (2012)

10. Dai, D.C., Monkman, A.P.: Observation of superfluorescence from a quantum ensemble of coherent excitons in a ZnTe crystal: Evidence for spontaneous Bose-Einstein condensation of excitons. Phys. Rev. B **84**, 115206 (2011)

11. Deng, H., Haug, H., Yamamoto, Y.: Exciton-polariton Bose-Einstein condensation. Rev. Mod. Phys. **82**, 1489 (2010)

12. Dicke, R.H.: Coherence in Spontaneous Radiation Processes. Phys. Rev. **93**, 99 (1954)

13. Ding, C.R., et al.: Observation of In-related collective spontaneous emission (superfluorescence) in Cd0.8Zn0.2Te:In crystal. Appl. Phys. Lett. **101**, 091115 (2012)

14. Florian, R., Schwan, L.O., Schmid, D.: Time-resolving experiments on Dicke superfluorescence of O2-centers in KCl. Two-color superfluorescence. PRA **29**, 2709 (1984)

15. Germann, T.D., Strittmatter, A.: High-power semiconductor disk laser based on InAs/GaAs submonolayer quantum dots. Appl. Phys. Lett. **92**, 101123 (2008)

16. Gibbs, H.M., Khitrova, G., Koch, S.W.: Exciton-polariton light-semiconductor coupling effects. Nat. Photon. **5**, 273 (2011)

17. Greenberg, J.A., Gauthier, D.J.: Steady-state, cavity-less, multimode superradiance. Phys. Rev. A **86** 013823 (2012)

18. Heritage, J.P., Weiner, A.M.: Advances in spectral optical code-division multiple-access communications. IEEE J. Sel. Top. Quant. Electron. **13**, 1351 (2007)

19. High, A.A., Leonard, J.R., Remeika, M., et al.: Condensation of excitons in a trap. Nano Lett. **12**, 2605 (2012)

20. Inouye, S., Chikkatur, A.P., Stamper-Kurn, D.M., et al.: Superradiant Rayleigh scattering from a Bose-Einstein condensate. Science **285**, 571 (1999)

21. Jho, Y.D., Wang, X., Kono, J., et al.: Cooperative Recombination of a Quantized High-Density Electron-Hole Plasma in Semiconductor Quantum Wells. Phys. Rev. Lett. **96**, 237401 (2006)

22. Jho, Y.D., Wang, X., Reitze, D.H., et al.: Cooperative recombination of electron-hole pairs in semiconductor quantum wells under quantizing magnetic fields. Phys. Rev. B **81**, 155314 (2010)

23. Kalinin, P.A., Kocharovsky, V.V., Kocharovsky, Vl.V.: Conditions and features of the lasing in traps for the bose condensation of dipolar excitons. Radiophys. Quantum Electron. **54**, 316–333 (2011)

24. Kalinin, P.A., Kocharovsky, V.V., Kocharovsky, Vl.V.: On the problem of lasing in traps for the bose condensation of dipolar excitons. Semiconductors **46**, 1351–1357 (2012)

25. Kalinin, P.A., Kocharovsky, V.V., Kocharovsky, Vl.V.: Lasing threshold in traps for bose-condensation of dipolar excitons. Solid St. Comm. **152**, 1008–1011 (2012)

26. Keeling, J., Bhaseen, M.J., Simons, B.D.: Phys. Rev. Lett. **105**, 043001 (2010)

27. Keeling, J., Marchetti, F.M., Szymanska, M.H., et al.: Collective coherence in planar semiconductor microcavities. Semicond. Sci. Technol. **22**, R1 (2007)

28. Khanin, Ya.I. Fundamentals of Laser Dynamics, 1st edn. Cambridge International Science Publishing, Cambridge, (2006), Chapters 1, 3, 4, 7

29. Kim, J.-H., NoeII, G.T., McGill, S.A., et al.: Fermi-edge superfluorescence from a quantum-degenerate electron-hole gas. Sci. Rep. **3**, 3283 (2013)

30. Kocharovsky, V.V., Kocharovsky, Vl.V., Golubyatnikova, E.R.: Mode Instability and Nonlinear Superradiance Phenomena in Open Fabry-Perot Cavity. Comput. Math. Appl. **34**, 773 (1997)

31. Kocharovsky, Vl.V., Kalinin, P.A., Kocharovskaya, E.R., et al.: Nonlinear Waves 2012. IAP RAS, Nizhny Novgorod, pp. 398–428. (2013) (in Russian) (ed. by A. Litvak)

32. Lanzani, G.: The Photophysics Behind Photovoltaics and Photonics, 1st edn. Wiley, New York (2012), Chapter 3

33. Lozovik, Yu.E.: Strong correlations and new phases in a system of excitons and polaritons. A polariton laser. Phys. Usp. **52**, 286 (2009)

34. Majumder, F.A., Kalt, H., Klingshirn, C., et al.: Carrier dynamics and lasing in epitaxial ZnTe layers on GaAs. Phys. Stat. Sol. B. **188**, 191–198 (1995)
35. Malcuit, M.S., Maki, J.J., Simkin, D.J., Boyd, R.W.: Transition from Superfluorescence to Amplified Spontaneous Emission. Phys. Rev. Lett. **59**, 1189 (1987)
36. Meinardi, F., Cerminara, M., Sassella, A., et al.: Superradiance in molecular H aggregates. Phys. Rev. Lett. **91**, 247401 (2003)
37. Meiser, D., Ye, J., Carlson, D.R., et al.: Prospects for a Millihertz-Linewidth Laser. Phys. Rev. Lett. **102**, 163601 (2009)
38. Meiser, D., Holland, M.J.: Intensity fluctuations in steady-state superradiance. Phys. Rev. A **81**, 063827 (2010)
39. Monmayrant, A., Weber, S., Chatel, B., et al.: A newcomer's guide to ultrashort pulse shaping and characterization. J. Phys. B At. Mol. Opt. Phys. **43**, 103001 (2010)
40. Noginov, M.A., Zhu, G., Fowlkes, I., Bahoura, M.: GaAs random laser. Laser Phys. Lett. **1**, 291 (2004)
41. Olle, V.F., Vasil'ev, P.P., Wonfor, A., et al.: Ultrashort superradiant pulse generation from a GaN/InGaN heterostructure. Opt. Express **20**(7), 7035 (2012)
42. Slama, S., Krenz, G., Bux, S., et al.: Controlling mode locking in optical ring cavities. Phys. Rev. A **75**, 063620 (2007)
43. Timofeev, V.A., Gorbunov, A.V., Larionov, A.V.: Long-range coherence of interacting Bose gas of dipolar excitons. J. Phys. Cond. Mat. **19**, 295209 (2007)
44. Ting, D.Z.-Y., Bandara, S.V., Gunapala, S.D.: Submonolayer quantum dot infrared photodetector. Appl. Phys. Lett. **94**, 111107 (2009)
45. Weiner, A.M.: Fourier information optics for the ultrafast time domain. Appl. Opt. **47**, A88 (2008)
46. Wiersma, D.S., Noginov, M.A.: Nano and random lasers. J. Opt. **12**, 020201 (2010)
47. Zheleznyakov, V.V., Kocharovskii, V.V., Kocharovskii, V.V.: Polarization waves and superradiance in active media. Sov. Phys. Usp. **32**, 835–870 (1989)

Chapter 5
The Control of Energy, Temporal and Spatial Characteristics a Microchip Laser with Active Output Mirror

V. V. Kiyko, V. A. Kondratyev, S. V. Gagarsky, E. N. Ofitserov, A. G. Suzdaltsev A. N. Sergeev and V. I. Kislov

Abstract Presented are results of the theoretical and experimental investigation of the Nd^{+3}:YAG microchip laser with passive Q-switch modulation based on Cr^{+4}. The laser operation is analyzed within the operator model of a microchip laser with an active output mirror based on Fabry-Perot interferometer. The feasibility of control over temporal and spatial characteristics of micro-chip laser radiation is demonstrated. The experimental and theoretical results are in a good agreement.

5.1 Introduction

An important point in creating lasers is producing radiation with given temporal and spatial parameters and energy. An ideal laser source should allow real-time control of the output radiation characteristics. The progressing use of laser diode pumping in recent studies provided possibilities for active control of these characteristics via changing pump radiation configuration. This approach is especially effective in case of solid-state lasers with traditional transversal pumping [1]. A combination of controllable pumping and a variable resonator with a flexible multi-element rear mirror allows changing the output radiation characteristics over a wide range [2]. However, such possibilities are essentially limited in case of longitudinal pumping. Controlling the pump profile and setting up the controllable element as the cavity end mirror is technically very difficult, or even absolutely impossible for completely integrated lasers.

On the other hand, exactly this type of lasers is widely used in mobile devices as compact sources of coherent radiation with high peak power. As a rule, a microchip laser contains two or more chips connected to each other and playing the

V. V. Kiyko (✉) · V. A. Kondratyev · E. N. Ofitserov · A. G. Suzdaltsev · V. I. Kislov
Prokhorov General Physics Institute, Russian Academy of Science, Moscow, Russia
e-mail: vkiyko62@gmail.com

S. V. Gagarsky · A. N. Sergeev
Mechanics and Optics, Saint Petersburg National Research University of Information Technologies, Saint-Petersburg, Russia

roles of laser active element, passive switch, nonlinear frequency converters, spectrum selectors or additional transparent heat sinks [3]. Dielectric coatings deposited directly on the side faces of the single-body assemblies act as resonator mirrors. If the optical setup of such a compact laser contains certain elements (such as resonator mirrors, quality modulator elements, etc.), and also if the free dispersion region of the resonator is comparable with the amplification bandwidth of the active medium, and generated pulse length lies in the subnanosecond range, such generators can be called minilasers.

Application of solid-state diode-pumped minilasers in various fields, such as medicine, micromachining of metallic, dielectric, and semiconducting materials, as well as local optical treatment of biological objects, requires a certain temporal shape of the laser pulse. Solving various problems within one application field may require different radiation characteristics. However, controlling these in the microchip lasers with their small resonator length and subnanosecond pulse length is impossible. Almost all such lasers are systems with rigidly set output radiation parameters. Up to now controlling the pulse shape was realized only for the supershort pulses (with pulse length below several picoseconds) and relatively long ones (hundreds of microseconds and more) [4]. Controlling the pulse shape in the range most interesting for practical applications (hundreds of picoseconds up to several nanoseconds) was considered impossible. This limitation was due to the fact that changing the shape of supershort pulses was done only with external devices based on spatial effects: liquid crystal-based spatial modulators (SLM — Spatial Light Modulator) [5–8], acoustooptics programmable dispersion filters (DAZZLER) [8, 9], nonlinear crystals [10], optical fiber amplifiers with saturation [11, 12]. The longer pulses were controlled with devices having response time of the order of pulse length (controllable active switches and controllable pump sources).

Below we present the research results on controlling the temporal shape of the pulses generated by a minilaser based on a microchip laser with passive Q-switch modulation via using an active resonator mirror with controllable phase-amplitude spatial-temporal reflection coefficient. We have shown the feasibility of controlling the single pulse shape and duration in such systems, as well as producing a train of a limited pulse number with required pulse repetition rate within the train.

5.2 Operator Model of a Laser with an Active Output Mirror

5.2.1 Model of the System

The scheme of the system used in this study (laser resonator and an additional active mirror) is shown in Fig. 5.1.

Here AE is the active element, TL is the thermal lens, M_0 and M_1 are the cavity end mirror and the output mirror; M_2 is the output mirror of the interferometer. This system was modeled using a development of the operator model [13], which was suggested for a Fabry-Perot interferometer with non-plane mirrors and an adjustable

Fig. 5.1 Optical scheme
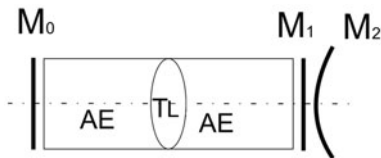
base. The eigenvalues γ (EV) and eigenfunctions U of the system in this model can be found from the equation

$$R_{\text{int}} H_{rez} U = \gamma U \tag{5.1}$$

where U describes the field distribution at the output mirror of the resonator; H_{rez} is the round –trip propagation operator for the resonator [14]; R_{int} is the reflection coefficient operator for the interferometer [13, 14]. Further we use the relations for the operators obtained for a system with infinitesimally thin non-absorbing reflectors. The field reflection coefficients for M_0, M_1, and M_2 are R_0, R_1, and R_2, respectively, and they are assumed to be independent of the position of the points on the reflectors' apertures. The coefficient R_0 is defined for the field within the laser resonator, and R_1 and R_{2-} for that within the interferometer. The transmission coefficients T_j ($j = 0, 1, 2$) are related to R_j based on the energy conservation relations as follows: $|R_j|^2 + |T_j|^2 = 1$. The reflection and transmission coefficients for the field incident on M_1 from the resonator side are $-R_1^* \exp(i\Psi)$ and $T_1^* \exp(i\Psi)$, respectively [15] (symbol * stands for the complex conjugation); Ψ is an additional phase shift (constant). The shape and aperture of the reflectors is accounted for by the operators $M_j = A_j \exp(i\alpha_j)$, ($j = 0, 1, 2$). Here A_j is determined by the aperture shape of the reflector M_j; $\alpha_j = 2k\delta$; k is the wave number ($k = 2\pi/\lambda$, λ is the radiation wavelength); δ describes the deviation of the reflector's shape from a plane. Taking into account the above assumptions and definitions, we obtain the following:

$$R_{\text{int}} = (-R_1^* + (R_2|T_1|^2 H_{\text{int}})/(E - R_1 R_2 H_{\text{int}}))\exp(i\Psi) \tag{5.2}$$

$H_{\text{int}} = \sqrt{M_1} K_{21} M_2 K_{12} \sqrt{M_1}$ is the round trip operator of the interferometer with reflection from the mirrors M_1 and M_2; K_{12} and K_{21} are the operators of propagation between the apertures of the interferometer's reflectors M_1, M_2 and M_2, M_1, respectively; E is the unity operator. In Eq. (5.1) $H_{rez} = \sqrt{M_1^*} K_{01} M_0 K_{10} \sqrt{M_1^*}$ is the round trip operator of the laser resonator with reflections from mirrors M_0 and M_1; K_{10} and K_{01} are the operators of propagation between the apertures of the reflectors M_1, M_0 and M_0, M_1, respectively.

The field at the system's output may be calculated using the following formula:

$$U_T = (T_1^* T_2 \exp(i\alpha_1) K_{12}/(E - R_1 R_2 H_{\text{int}}))U \exp(i\Psi) \tag{5.3}$$

The Eqs. (5.1)–(5.3) were derived from the following set of equations:

$$
\begin{cases}
U_{01} = \exp{(k_a)}K_{01}R_0 M_0 K_{10} U_{10} \\
U_{21} = K_{12} M_2 R_2 K_{21} U_{12} \\
U_{10} = T_1 U_{21} - \exp{(i\Psi)}M_1^* R_1^* U_{01} \\
U_{12} = \exp{(i\Psi)}T_1^* U_{01} + R_1 M_1 U_{21}
\end{cases}
\tag{5.4}
$$

The set of Eq. (5.4) contains 4 variables U_{nm}. U_{nm} describes the distribution of the field propagating from M_n towards M_m; all the fields are defined at the aperture of mirror M_1. The first equation in the set contains the factor $\exp{(k_a)}$ describing the amplification and the additional (with respect to the geometrical one) phase shift for a round trip of the laser resonator.

Below we explain the physical meaning of the equations in the set (4). The first one describes the round trip of the radiation within the laser resonator, including the amplification effect. The second one is the equation of the round trip of the interferometer mirror; the third one describes the laser field formation taking into account the radiation incoming into the resonator from the interferometer; the fourth one describes the field formation in the interferometer taking into account the radiation coming from the laser resonator. This system may be easily solved via algebraic transformation and substituting $\exp{(k_a)}$ with $1/\gamma$. The field in Eq. (5.1) is then given by the expression $U = U_{01}\sqrt{M_1^*}$, and the field (5.3) at the output of the system is $U_T = T_2 K_{12} U_{12}$.

Equation (5.1) is valid both in the geometrical optics and the diffraction approximations. In the latter case the operator in the denominator in formula (2) can be substituted with the following series: $(E - R_1 R_2 H_{int})^{-1} = \sum_0^\infty (R_1 R_2 H_{int})^n$. This representation as series corresponds to the summation of the fields reflected between the interferometer mirrors. When the integral approach is used, each following beam is derived from the previous one as follows: $(R_1 R_2 H_{int})^{n+1} = (R_1 R_2 H_{int})(R_1 R_2 H_{int})^n$. In the present study we used matrix representation of the operators; this is due to fact substituting the integration (in the diffraction approximation) with summation of discrete values [13]. The operator $(E - R_1 R_2 H_{int})^{-1}$ is determined in this case as the inverse matrix of $(E - R_1 R_2 H_{int})$.

This model allows optimizing the characteristics of the system including resonator and mirror interferometer taking into account the thermal lens and the requirements for the parameters of the output radiation. Further we discuss the results of numerical simulation of the system consisting of a microchip laser and an active mirror.
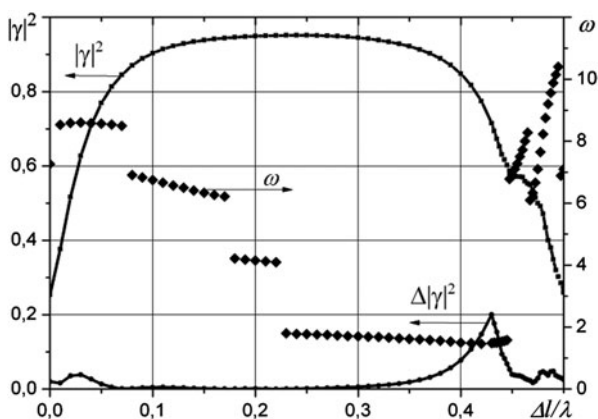
5.2.2   Results of the Numerical Simulations

Some of the simulation results for the basic characteristics of the laser system are shown in Figs. 5.2–5.4. The data in Figs. 5.2 and 5.3 are for the two dimension

Fig. 5.2 $|\gamma|^2$ vs. mode number n
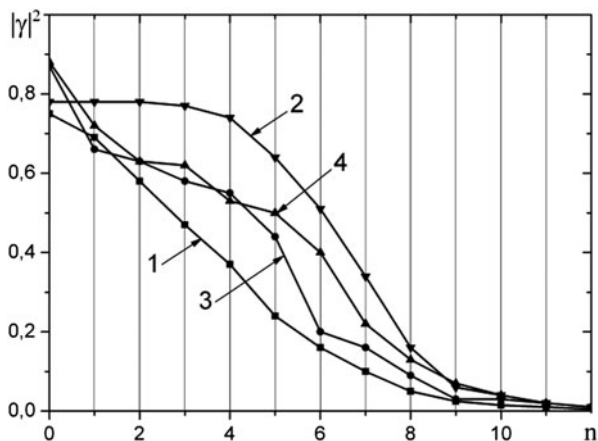
Fig. 5.3 Dependences of $|\gamma|^2$, $\Delta|\gamma|^2$, and ω on the detuning $\Delta l/\lambda$


cavity case, and those in Fig. 5.4 are for the system with cylindrical symmetry (round mirrors).

The initial resonator is composed of the flat mirrors M_0 and M_1, and the interferometer is formed by the output mirror of the resonator M_1 and the spherical semitransparent mirror M_2. Below the interferometer is termed stable or unstable according to the classification used for describing optical resonators.

Figure 5.2 shows the dependences of $|\gamma|^2$ on the mode number for the microchip laser. Curve 1 in Fig. 5.2 is for the flat resonator without a TL, curve 2 is for that with a TL, curve 3 is for the resonator with a stable interferometer and a TL, and curve 4 is for the resonator with an unstable interferometer and a TL. The parameters of the system are as follows: curvature radius of the output mirror is $\pm 0,06$ m; $\lambda = 1.064\mu$m is the radiation wavelength; $l = l_0 + \Delta l$ is the interferometer length; $l_0 = 100\lambda$; Δl is the interferometer detuning, which lies in the range from 0 to $\lambda/2$; $d = 200$ μm is the diameter of the interferometer output mirror; $R_1 = R_2 = 0.8$; focal length of the TL is 6 mm; the resonator length is 5.5 mm, the refraction index

Fig. 5.4 $|\gamma|^2$ vs. mode number n
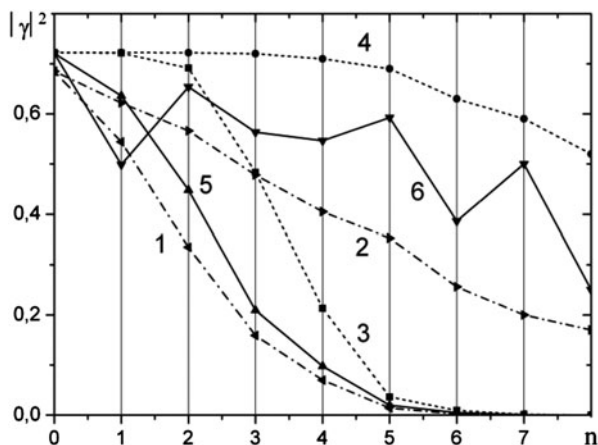
of the active element is 1.82. Herein, the analysis of the simulation results given in Fig. 5.2 shows that the presence of a TL (curve 2) makes the resonator a multimode one. The angle of divergence of the output radiation for the resonator with a TL is greater by a factor of 2–2.5 than for that without a TL. Using an interferometer as an output mirror (curves 3, 4) allows to realize the generation regime in the system close to the single mode one.

The characteristics of the system including the resonator and the mirror interferometer depend essentially on the controlled interferometer detuning Δl (Fig. 5.3). The parameter ω in Fig. 5.3 is proportional to the energy divergence Θ of the output radiation in the far field at the level of half that of the dominant mode, $\Theta = 2\lambda\omega/\pi d$; $|\gamma|^2$ is the EV modulus squared for the dominant mode; $\Delta|\gamma|^2$ is the difference between EV modulus squared for the dominant mode and its nearest neighbor. The data in Fig. 5.3 are for an unstable interferometer. When the detuning is within (0.22–0.45)λ, TEM$_0$ is the dominant mode, whereas in the detuning range of (0.18–0.22)λ TEM$_1$ is dominant. The jumps in the ω dependence in Fig. 5.3 are caused by the change in the dominant mode number for a changed interferometer detuning. The value of $|\gamma|^2$ (and therefore the output radiation power of the laser) depends essentially on the interferometer detuning. Thus $|\gamma|^2$ for the TEM$_0$ mode varies within the range of 0.58–0.9. The divergence of the output radiation in this case varies for not more than 25 %.

Numerical simulations for the case of cylindrical symmetry (round mirrors) were also performed. Some of the results of these calculations are shown in Fig. 5.4. Herein, the modes in the system may be identified in the same way (TEM$_{nm}$) as those in spherical laser resonators [15]. The indices in the mode identifiers n, m $= 0$, 1, 2... are the azimuthal and radial indices, respectively.

Curves 1 and 2 in Fig. 5.2 are for the basic resonator without a TL, curves 3 and 4 are for the basic resonator with a TL, 5 and 6 are for the system of resonator with a TL + unstable interferometer. Curves 1, 3, 5 correspond to the TEM$_{no}$ modes; and curves 2, 4, 6 correspond to the TEM$_{0n}$ modes. Detuning Δl in this system is 0.32 λ;

curvature radius of the interferometer output mirror is 0.02 m; the other parameters are the same as in the two dimension cavity case considered above.

Taking into account the thermal lens (TL) in the numerical simulation causes an increase in radiation divergence by a factor of 4–6 in the case of flat resonator mirrors. The divergence was evaluated taking into account the number of modes within the range of $\left|\gamma^2\right| > \overline{\left|\gamma^2\right|}$, where $\overline{\left|\gamma^2\right|} = 0.2 \div 0.4$ is the threshold value corresponding to the radiation amplification in a microchip laser with Nd:YAG active medium. Introducing the interferometer mirror into the system causes a decrease in divergence by a factor of 1.5–2.5. The quasioptimal detuning Δl in this case was (0.28–0.38) λ when the TEM_{00} mode was the dominant one. The influence of the active mirror on the system's selectivity was more expressed for the radial index (Fig. 5.4). Lower selectivity with respect to the azimuthal index was due to the cylindrical selectivity of the interferometer mirror.

5.3   Experimental Setup

YAG:Nd3+ - based microchip laser 2 was the core of the experimental setup (Fig. 5.5). This laser was diffusely bonded with a YAG:Cr4+ passive switch. The cavity end mirror and the output mirror of the resonator were deposited on the front faces of the active element and the switch, respectively. The pump radiation was introduced through the cavity end mirror. The basic parameters of the microchip laser are shown below.

Active element............ 1 at. %	Cr^{4+}:YAG [110] Nd^{3+}:YAG [111]
Passive switch	1 at. %
Total length, mm	6
Diameter, mm	3
Initial transmission of the switch, %, at $\lambda p = 1064$ nm	60
Reflection coefficient R_2 of the output mirror, %, at $\lambda p = 1064$ nm	70
Cavity end mirror transmittance, %, at $\lambda p = 808$ nm	94

The active element was pumped with a pulsed laser diode 8 (JOLD 70 QPXF-1L with up to 70 W peak power), fed and controlled by LDMPS100 driver [16] connected to a personal computer 9. The pump radiation is fed into an optical fiber with 400 μm diameter and numerical aperture Na = 0.22. Focusing of pump radiation into the active element is performed via a two-lens objective 1, providing tunable beam waist with diameter in the range of 340–400 μm. Changes in the longitudinal position of the beam waist with respect to the input face of the laser rod ensures additional possibilities to control the generation regime via changing the ratio of the diameter of the effectively pumped zone and the basic eigenmode of the resonator.
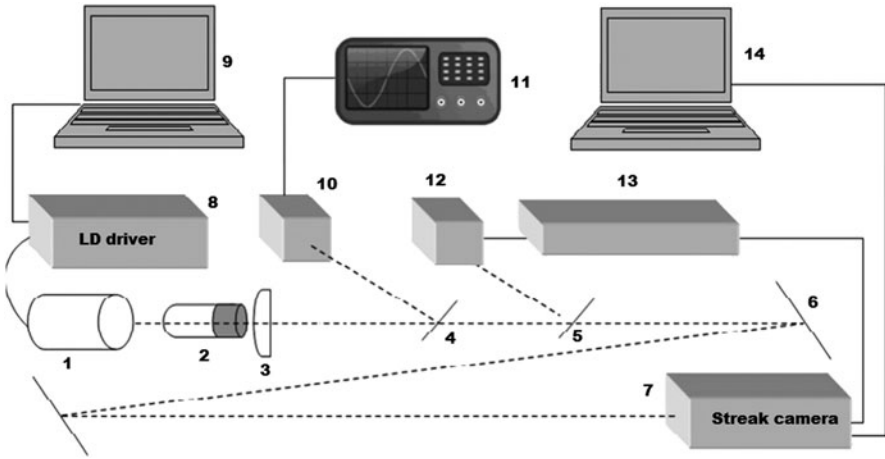
Fig. 5.5 Experimental setup

Partial polarization of pump radiation and the minilaser mounting setup ensured polarization of the output radiation with contrast at least 1:100. Pumping was pulsed with duration of 120–250 μs. The pump pulse energy (controlled mainly via the pulse duration) was chosen so that either a single laser pulse or a pulse train was generated during the pump pulse. The repetition period of the pulses in the train, controlled by the peak power of the pump pulse, was 40–100 μs. In order to reduce the impact of the thermal lens induced in the active element the repetition frequency of the pump pulses was set not higher than 1 kHz. Temporal structure of radiation was observed through beam splitters *4*, *5*, and *6*, also the splitter beam was used to trigger electronics devices. The overall temporal structure was measured with Thorlabs DET10 A/m radiation detector *10* with time constant of 600 ps, connected to LeCroy WaveJet 352A oscilloscope *11*. The oscilloscope bandwidth is 500 MHz and in conjunction with the radiation detector this provided the time constant of ca. 2 ns. Such a time resolution allows only a qualitative estimate of the form and structure of the generated pulses. In order to study finer details of the spatial-temporal structure of the generated pulses a VICA-03 streak camera *7* with picosecond time resolution was used. The streak camera was triggered by a signal of the avalanche photodetector *12*.The precise temporal coordination of the streak camera triggering signal and the arrival of the generated pulse was achieved with the electronic delay unit *13* and the optical delay line with the total length of 30 m formed by mirrors 6. Visualization and processing of the image obtained from the streak camera screen was done with a computer *14*.

The temporal characteristics of the microchip laser were controlled by an additional output mirror with the reflection coefficient R_3. It was set up so that, together with the output mirror R_2 of the microchip laser deposited on the face of the active element, it forms a Fabry-Perot interferometer (Fig. 5.6a). This setup with the double output reflector does not cause an essential increase of the resonator base and the
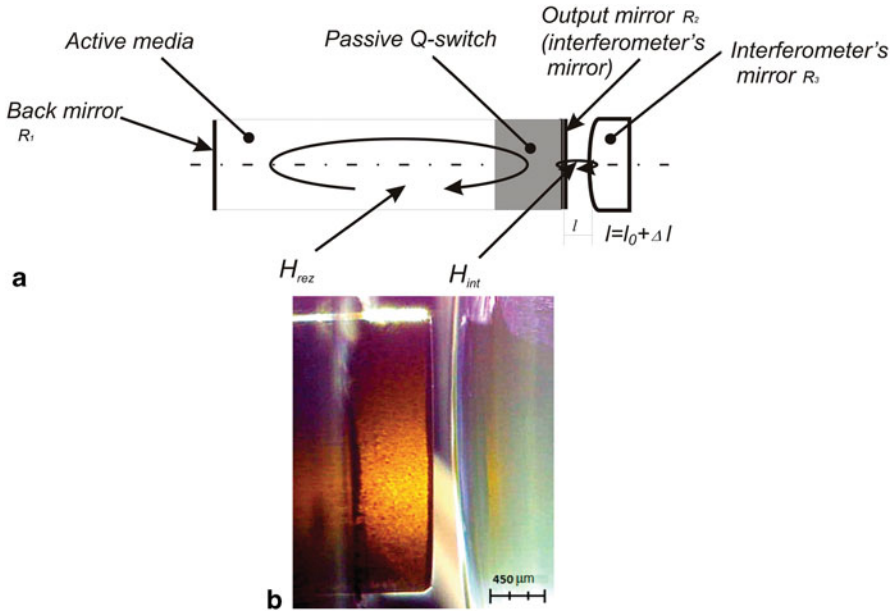
Fig. 5.6 a optical scheme of the microchip laser with active output mirror; **b** interferometer gap between output and additional mirror

corresponding round trip time, so that the minimal generated pulse duration is not increased

A convex mirror with the curvature radius of 50.8 mm and reflection coefficient of 55 % was mounted on a ring piezoelectric element ensuring displacement of the mirror within 2.5 μm along the optical axis. In order to cover the total generation bandwidth, the interferometer base l is chosen so that the spectral range of the interferometer is much greater than the laser generation line width Δv [17]:

$$l < {}^c/_{2\Delta v} \tag{5.5}$$

where c is the speed of light

The value of l in the experiments performed was ca. 200 μm. An enlarged image of the interferometer formed by the output mirror R_2 of the microchip laser and the additional spherical mirror R_3 is shown in Fig. 5.6b.

Since one of the interferometer mirrors is not flat, variation in the base l changes the phase-amplitude spatial coefficient of the equivalent output mirror. This enable an active control of the spatial, temporal, and energy characteristics of the generated radiation [13, 17, 18, 19].

Fig. 5.7 Output beam in far
field for two configuration of
the interferometer


5.4 Experimental Results and Discussion

The basic features of radiation generation in lasers with an active output mirror
based on a Fabry-Perot interferometer with non-flat mirrors were described in papers
[13, 17, 18], and the influence of the interferometer on the spatial characteristics
of radiation was studied in detail. However, for the minilaser setup considered in
the present work the spatial characteristics should evidently influence the temporal
processes of generation.

As is well known, the concept of the mode structure has just limited applicability
[20, 21] for pulsed radiation in case of spatially inhomogeneous saturation of gain
in the active medium and saturation of absorption in the passive switch. Therefore
this concept is used in the discussion below only for the sake of brevity. Since the
current amplification and nonlinear absorption coefficient, as well as the effective
reflection coefficient of the combined output mirror depend on the radial coordinate,
the generation threshold can be exceeded non-simultaneously in different parts of
the active medium.

The following two cases may be distinguished for such systems. When the
generation conditions are satisfied for a single transverse mode, non-simultaneous
generation is possible in different areas of this mode's cross-section. This can help
to control the temporal shape of the generated pulse over a wide range. When the
effectively pumped region of the active medium is much larger, then higher-order
transversal modes can be generated (Fig. 5.7b). In this case not only the shape of the
total pulse can be controlled, but temporal separation of the moments of generation
in different parts of the transversal cross-section of the active medium can be tuned
via controlling the transversal arbitrary distribution of the reflection coefficient of
the output mirror over a very wide range. In practice we can obtain a train of 2, 3
or 4 output pulses separated by time intervals comparable with the individual pulse
length

At the first stage of the experiments the waist of the pump beam with the minimum
possible width was positioned near the back mirror of the active element. This ensured
generation of the basic transversal mode by the microchip laser. Herein, the output
beam diameter in the plane of the output beam was changed in the range of 200–300
μm depending on the pulse repetition rate (see Fig. 5.7a). Radiation caustic in the
output mirror plane lies completely within the zero-order ring of the interferometer,
and the reflection coefficient of the output mirror within the beam aperture changes
in the range of 20–100 % [13]:

$$|R_{\text{int}}|^2 = \frac{(R_2 - R_3)^2 + 4R_2R_3\sin^2(\varphi/2)}{(1 - R_2R_3)^2 + 4R_2R_3\sin^2(\varphi/2)} \qquad (5.6)$$
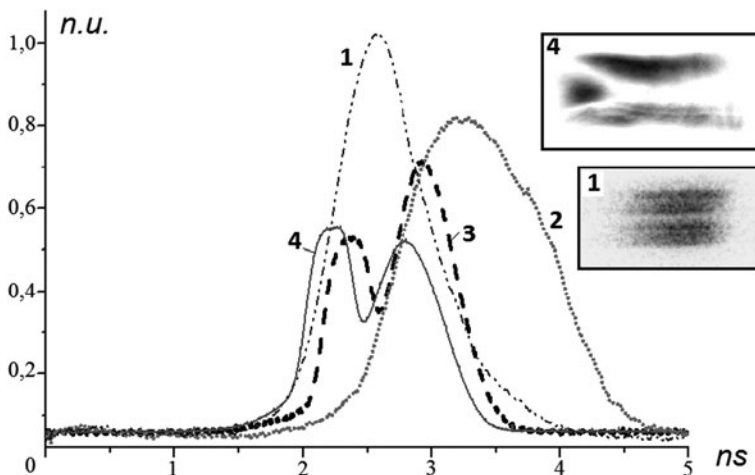
Fig. 5.8 Temporal shapes of the pulses for different values of the interferometer base

here $|R_{int}|$ is the power reflection coefficient of the interferometer; $\phi = 2kl - \Delta\phi$, where $\Delta\phi$ is an additive to the geometrical phase shift for the round trip of the resonator, $k = 2\pi/\lambda$ is the wave number.

A change in the interferometer base causes a change in the spatial distribution of its reflection coefficient over the beam's cross-section over a wide range. The maximum in the reflection coefficient R_{int} is reached near the resonator's axis, which ensures the generation conditions in the axial part of the beam and the maximum relative energy yield of the pumped zone of the active element at the front edge of the pulse. A decrease of the reflection coefficient in the center to the minimum value ensures the energy conversion in the central region with the maximum inversion up to the total pulse length. The shape of the pulse can be varied over a very wide range in this case.

Figure 5.8 shows the experimentally obtained temporal dependences of the power of the generated pulses $P(t)$ for various interferometer base varied in 0, 75 λ. These profiles were calculated via integration over the transversal coordinate of the photochronographic images from the streak camera screen. Curves *1–4* correspond to different voltages applied to the piezoelectric element: *1*–0, *2*–50, *3*–100, *4*–150 V; photochronographic images of the pulse for regimes *1* and *4* are given in the frames. One may see that base variation may cause pulse duration change by a factor of 2.5, change in the pulse shape, as well as energy redistribution between the front edge and the trailing edge of the pulse. In order to study the possibility of temporal separation of separate modes' generation, the optical pumping scheme was changed. The volume of the pumped region was increased so that higher-order modes could be generated. The transversal beam size in this case fitted within the first two rings of the interferometer (see Fig. 5.7b).
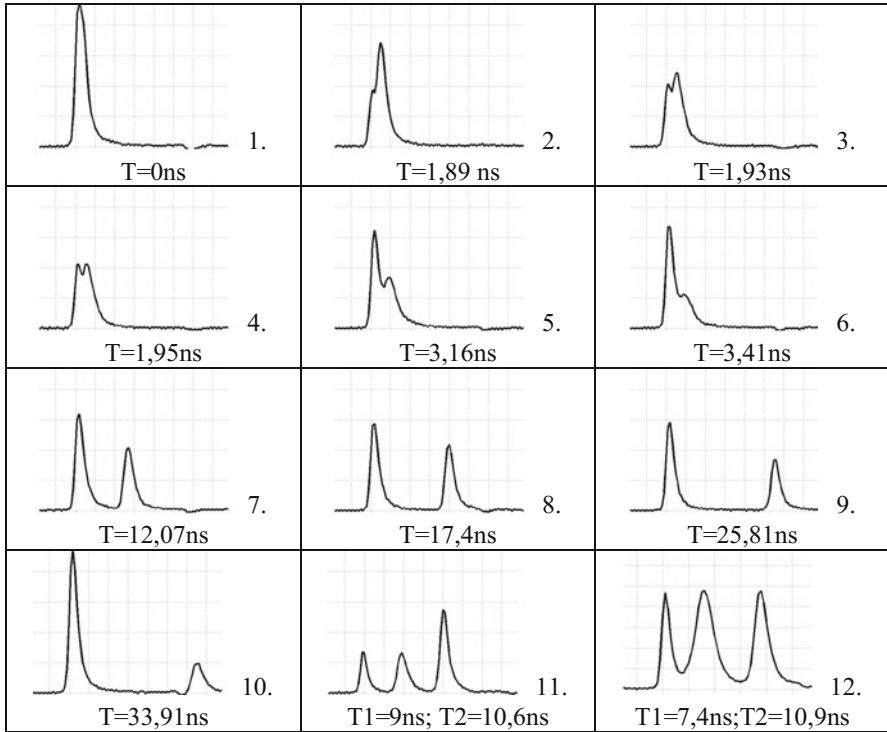
Fig. 5.9 Forming of the pulses train

This enabled to control the gain/loss ratio for the generated modes over a wide range and to provide conditions for generating pulse trains with limited pulse number and the distance between the pulses in the train comparable to the pulse length. Figure 5.9 shows the sequence of generation development in case of step-wise changes of the interferometer base. Time interval T shown for each image corresponds to the distance between the pulse peaks in the train. The images were obtained using oscilloscope. All the temporal characteristics were determined via processing the streak camera data. The image clearly shows gradual transition to generation of higher-order modes (images 1–10), which is also indirectely confirmed by the increase of T due to the increase of generation development time for higher-order modes. Further increase in the cross-section of the pump region caused a third pulse to appear in the train (images 11, 12). Notably, fine tuning of the interferometer base allowed producing almost any ratio between the pulse energies in the train.

5.5 Conclusion

The theoretical and experimental studies of a minilaser with a passive switch and an intracavity active mirror have shown that an active output mirror based on Fabry-Perot interferometer with non-flat mirrors enables to control effectively both the spatial structure and output power of the generated radiation, as well as its temporal structure. We have also shown that the length and shape of a single pulse can be tuned, and a train of a controllable number of pulses can be produced with desired pulse repetition rate within the train. Such spatial-temporal structure can be applied effectively for developing laser equipment, especially such that include nonlinear optical frequency converters.

Control of the temporal structure of the irradiation with the output active mirror is possible over a very wide range, especially for pulse duration of nanosecond and subnanosecond range, which cannot be achieved with any other known technique. The approach studied enables real-time control of the temporal characteristics of laser radiation and is prospective for use in modern miniature lasers.

References

1. Grechin, S.G., Nikolaev, P.P.: Diode-side-pumped laser heads for solid-state lasers. Quantum Electron. **39**(1), 1–17 (2009)
2. Kiyko, V.V., Kislov, V.I., Ofitserov, E.N.: Resonator with a back deformable mirror for the formation of a beam with a given intensity distribution. Quantum Electron. **41**(10), 939–944 (2011)
3. Zayhowski, J.J.: Microchip lasers. Linc. Lab. J. **3**(3), 427–446 (1990)
4. Ren, B., Frihauf, P., Rafac, R.J., Krstic, M.: Laser pulse shaping via extremum seeking. Control. Eng. Pract. **20**, 674–683 (2012)
5. Oron, D., Silberberg, Y.: Spatiotemporal coherent control using shaped, temporally focused pulses. Opt. Express. **13**(24), 9903–9908 (2005)
6. Meshulach, D., Yelin, D., Silberberg, Y.: Adaptive real-time femtosecond pulse shaping. J. Optic. Soc. Amer. B. **15**(5), 1615–1619 (1998)
7. Weiner, A.M.: Femtosecond pulse shaping using spatial light modulators. Rev. of Sci Instrum. **71**(5), 1929–1960 (2000)
8. Ghigo, A., Vicario, C., Petrarca M., Cialdi S.: Laser temporal pulse shaping based on the dazzler. Coordinated accelerator research in Europe (CARE) Reports. 019, 1–11 (2007)
9. Verluise, F., Laude, V., Huignard, J.P., Tournois, P., Migus, A.: Arbitrary dispersion control of ultrashort optical pulses with acoustic waves. J. Optic. Soc. Amer. B. **17**(1), 138–145 (2000)
10. Cialdi, S., Castelli, F., Boscolo, I.: Rectangular pulse formation in a laser harmonic generation. Appl. Phys. B. **82**, 383–389 (2006)
11. Schimpf, D.N., Ruchert, C., Nodop, D., Limpert, J., Tunnermann, A., Salin, F.: Compensation of pulse-shaping due to saturation in fiber-amplifiers. Proc. of SPIE. **7195**, 71951E (2009)
12. Vu K.T., Malinowski, A., Richardson, D.J., Ghiringhelli, F.H., Zervas, L.M.B.: Adaptive pulse shape control in a diode-seeded nanosecond fiber MOPA system. Opt. Express. **14**, 10996–11001 (2006)
13. Kiiko, V.V., Kislov, V.I., Ofitserov, E.N.: Mirror with reflectance variable in amplitude and phase. 1. Modelling of a mirror with reflectance variablein amplitude and phase. Quantum Electron. **40**(6), 556–560 (2010)
14. Anan'ev, Yu.A.: Optical Resonator and Problem of Laser Radiation. Nauka, Moscow (1990)

15. Troickiy, Yu.V.: Multiray Interferometers of the Reflective Light. Nauka, Novosibirsk (1985)
16. Togatov, V.V., Gagarsky, S.V., Gnatyuk, P.A., Cherevko, Yu.I.: Pulsed power supply of laser diode modules for pumping of the solid state lasers. Instrum. Exp. Tech. **50**(2), 158–159 (2007) (in russian)
17. De Silvestri, S., Laporta, P., Mangi, V., Svelto, O.: Radially variable reflectivity output coupler of novel design for unstable resonators. Optics Lett. **12**(2), 84–86 (1987)
18. Kiiko, V.V., Kislov, V.I., Ofitserov, E.N.: Mirror with a variable amplitude-phase reflectance. 2. Modelling of a laser resonator with an active output mirror. Quantum Electronics. **41**(3), 239–242 (2011)
19. Kijko, V.V., Ofitserov, E.N.: Study of thermooptic distortions of a Nd: YVO_4 active element at different methods of its mounting. Quantum Electronics. **36**(5), 483–486 (2006)
20. Yao, G., Shouhuan, Z., Wang, P., Lee, K.K., Chen, Y.C.: Dynamic of transverse mode in self-Q-switched solid-state lasers. Opt. Commun. **114**, 101–105 (1995)
21. Okhrimchuk, A.G., Shestakov, A.V.: The time and spatial dynamics of the YAG:Nd3+/YAG:Cr4+microchip laser emission. Proc. of SPIE. **6610**, 661002-1–661002-10 (2007)

Chapter 6
Recent Advances in Secure Transmission with Chaotic Carriers

Silvano Donati and Valerio Annovazzi-Lodi

Abstract After an outline of optical chaos generation and synchronization in semiconductor lasers, we discuss the fundamentals of optical secure transmission of data using chaotic carriers, based on different schemes, such as CM (Chaos masking) and CSK (Chaos Shift Keying). We present different versions of such schemes, which have been numerically evaluated and/or experimentally tested with discrete components or with a PIC (Photonic Integrated Circuit) realization of the crypto-systems. Finally, we outline some recent developments of the chaos secure transmission technique.

6.1 Introduction

Chaos is a quite interdisciplinary subject of research, with founding contributions coming from mathematics and physics [1], and with applications being developed almost everywhere in applied science. Indeed, chaos is the novel phenomenon we first encounter when the level of system complexity [2, 3]—the number of individual entities or number of differential equations and of nonlinearities in the system—departs markedly from the ground level of the Lagrangian system of the nineteenth century. Because of the added complexity, classical reductionism fails, and the pseudo-random—or chaos—evolution of the system unveils new conceptual phenomena unpredictable with the lower level description, as well as it opens a new ground of applications for development.

In optics, Haken [4, 5] has been the first to point out that the Maxwell-Block equations describing the laser [5, 6] can be brought to coincide with the Lorenz equations describing convective flow in the atmosphere, a well known paradigm for chaos. Since then, the rate equations in three variables for the laser are known as

S. Donati (✉) · V. Annovazzi-Lodi
Department of Electrical, Computer and Biomedical Engineering,
University of Pavia, Pavia, Italy
e-mail: silvano.donati@unipv.it

V. Annovazzi-Lodi
e-mail: valerio.annovazzi@unipv.it

Fig. 6.1 Coupled-lasers: *top*,
mutual (can be symmetrical
or asymmetrical) *bottom*,
self-coupling
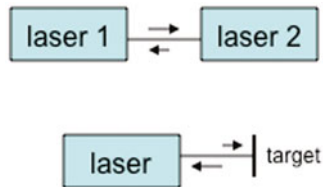
Lorenz-Haken (L-H) equations, and they were soon shown by Arecchi [6] to be the
base to identify classes of stable and unstable lasers.

Actually, semiconductor lasers belong to class B [6], and are stable unless a new
term is added into the L-H equations, such as external injection from another laser
or the feedback from a remote mirror. With this term, the L-H set become the well
known Lang and Kobayashi equations [7] (or, Lamb's equations when excitation is
decoupled from electric field) and system may experience chaos when driven heavily
enough into feedback—a favourable condition because it allows easy control of the
desired working regime.

6.2 Chaos in Lasers

The basic scheme to study the high-complexity dynamical regimes is that of Fig. 6.1,
where we can have either a double-source arrangement (either in the mutual, symmet-
rical or asymmetrical, or in the unidirectional case) or a single-source subject to back-
reflection from an external target (the so called delayed feedback or self-mixing case).

Self-mixing has two distinct applications at two different levels of injection:

1. at weak injection (when the return is barely 10^{-8} to 10^{-3} of emitted power) pertur-
   bations of the laser field are frequency and amplitude (AM and FM) modulations
   of the cavity field, depending on external amplitude and phase of the return, and
   the system can be used in instrumentation for measurements of the external path-
   length (the self-mixing interferometer [8]) or as an optical radar detecting weak
   echoes [9, 10], also known as a coherent injection detector [9];
2. at moderate/large coupling (10^{-3} to a few 10^{-2}) the system enters a more complex
   dynamical regime and starts generating periodic and multiperiodic oscillations
   and chaos, opening new avenues in communications and information technology.

An exhaustive literature is available on optical chaos and its applications, and recently
ample reviews have appeared on the physics principles [11] and on the application
repertoire [12] of chaos and related phenomena, to which we direct the interested
reader.

About the analytical approach to study the new chaos phenomena, the Lang-
Kobayashi equations [7], provide a powerful tool [12, 13, 14, 15, 16, 17], well
confirmed by experimental evidence, also considering the effect of noise [18]. Using
these equations to study the double-source unidirectional coupling case (Fig. 6.1,
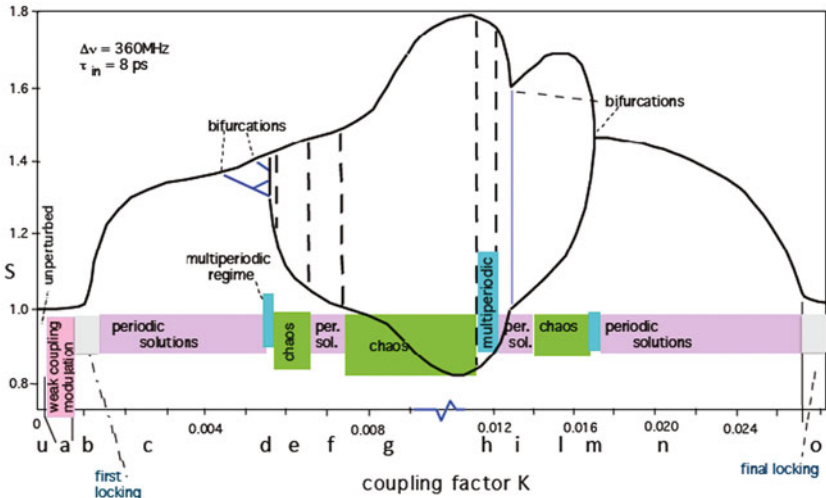
Fig. 6.2 Beating amplitude of master and slave oscillations of the coupled system, vs. the strength of coupling K, starting from the unperturbed regime (region *u*) and unveiling regimes of periodic solutions (regions *c,f,i,n*), multiperiodicity (*d,h,m*) and chaos (*e,g,l*), passing through first locking (*b*) to final locking (region *o*). (From Ref.[12])

top), the route to high dynamics behaviour and chaos is readily unveiled, as depicted in Fig. 6.2.

The parameter used to depict the system evolution is the beating amplitude $S = E_1 E_2^*$ of oscillations in laser 1 and 2 (master and slave arrangement), vs. the coupling strength K (fraction of field injected from laser 1 into laser 2) [18]. The regimes are identified based on three indicators: (i) the time series [or amplitude S(t)], (ii) the frequency spectrum S(f), and the state diagram, S vs dS/dt [5, 11].

In unperturbed conditions, the time series is a sinusoid, the spectrum is a single peak and the state diagram is a circle. Then, we encounter a locking state, and signal S disappears. But, at increased K, S reappears and now the time series has a distortion every other period, the spectrum carries sub-harmonics and the state diagram is a double loop figure, all indicative of the so-called period-1 oscillation regime. At even larger K, the sub-harmonics increase in number and amplitude, and the state diagram has multiple loops: it is the multiperiodic regime. Last, when harmonics accompany the sub-harmonics and broaden the spectrum widely, the time series is random-like looking, and the state diagram spread all over the available space of coordinates, we have chaos [12, 19]. As K is further increased, the system enters less complex regimes, including again periodic and multiperiodic solutions, and, after passing new chaotic regions, eventually reaches a new stable (locked) regime (Fig. 6.2, right end).

An example of the three diagrams for multiperiodic solutions and chaos is reported in Fig. 6.3.
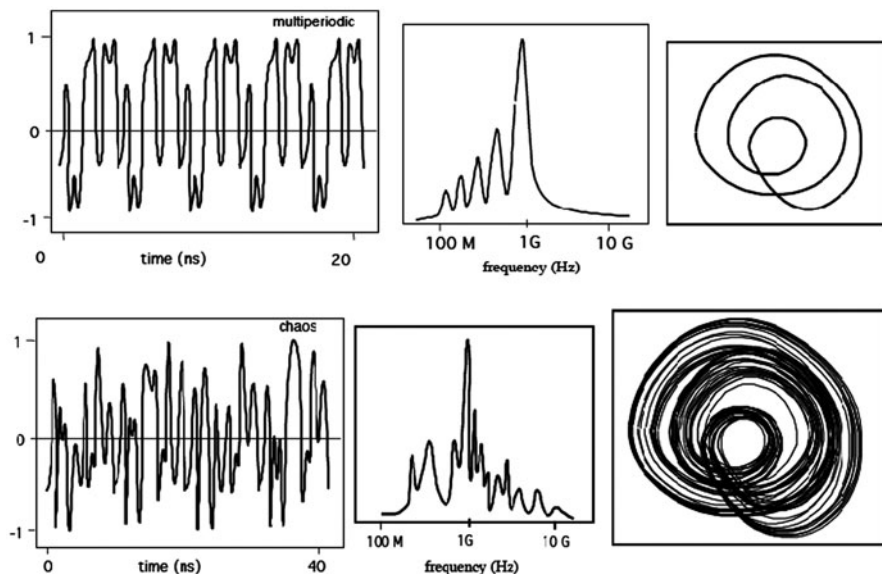
Fig. 6.3 Time series (*left*), frequency spectrum (*center*) and state diagram (*right*) of the beating signal S for the multiperiodic regime (regions *d,h,m* in Fig. 6.2) and *chaos* (*e,g,l*). (From Ref.[12])

6.3 Synchronizing Chaos

The waveforms generated by a chaotic laser can be thought as a sort of free-response or eigenfunctions of the complex system, similar to sinusoidal oscillations being the free response of a second-order system or oscillator. On this analogy, we may think of injecting from outside a chaos waveform into the system, in the conjecture that the system synchronizes, i.e, that it will adjust itself to follow the dynamical evolution of the injected signal. And, since to lock a linear second-order oscillator we need a frequency close to the free oscillation frequency, thus we expect that we need to stay close to the system free response to be able to synchronize the chaos generator.

The synchronization scheme of Fig. 6.4, with two identical coupled-lasers systems, system 1 with LD1 and LD2, and system 2 with LD3 and LD4 is considered in [20]. The output of system 1 (out 1) is connected to the sum node in system 2, at the input of LD4; in addition, the LD4 output is sent to the subtraction node in system 2. By this arrangement, when the LD2 and LD4 outputs differ, system 1 applies a correction to system 2 and brings it closer, until system 2 tracks the other, i.e., it is synchronized.

By using a modified L-K equation set [15] to model the synchronization scheme (Fig. 6.4), we find that output of system 2 reaches the steady-state solution irrespective of the arbitrary starting point, with an amplitude error (E2-E1)/E0 damping quickly to zero, after a few cycles of oscillation, with a small residual error, for all the different generated chaos waveforms.
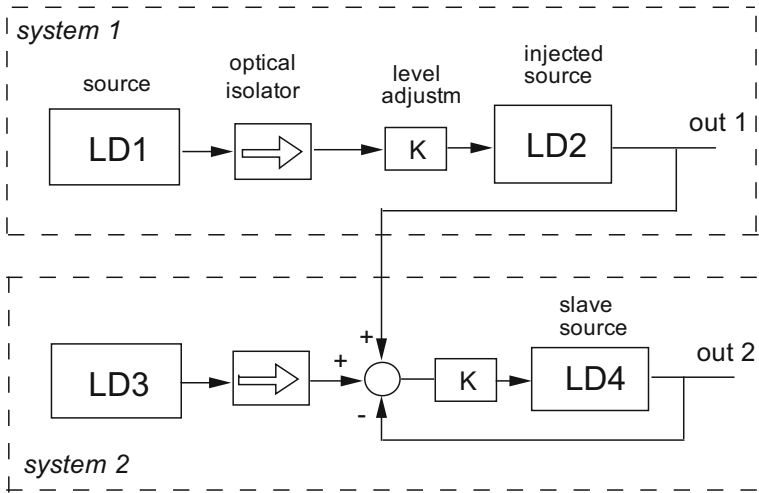
**Fig. 6.4** Scheme of synchronization: two identical coupled-laser systems (*LD1/LD2* and *LD3/LD4*) are used. Out 1 is sent to the sum node at the input of slave laser *LD4* of *system 2*, and the output of *LD4* is sent back in subtraction, so that when *out 2* is equal to *out 1* (it is synchronized) no further correction is applied. (From Ref.[20])

One critical issue is sensitivity to system parameters: we find that small deviations from nominal values of the parameters are tolerated, whereas beyond a certain threshold (for example, 0.5 %) synchronization isn't achieved any longer. Dotted lines indicate this ideal condition (Fig. 6.5). For a real system, the error (E2-E1)/E0 is a function of the rms mismatch allowed for the parameters (Fig. 6.5, left); removing the effect of gain mismatch (of E2 and E1) we obtain the diagram of Fig. 6.5, right. Interesting to note, upon changing the laser parameters over a wide range of reasonable values doesn't affect the general trend of synchronization. And, for the error to be small, we need a parameter mismatch less than ~ 0.2 %, while error becomes large and synchronization is lost for a mismatch larger than ~ 0.8 %, typically. The sensitivity of chaos synchronization to system parameters is the key of secure transmission, usually referred to as Chaos Cryptography, as it will be shown in the next paragraph.

6.4   Using Chaos to Protect Data

A first scheme of cryptography, CM (Chaos Masking) readily follows from synchronization: summing (incoherently) to the generated chaos a small signal carrying the desired message will not impair synchronization of the slave because the (small) deterministic signal will be ignored (it is not a system eigenfunction), and upon subtracting the synchronized output (chaos) from the received signal (chaos + message) we will free out the message [20].
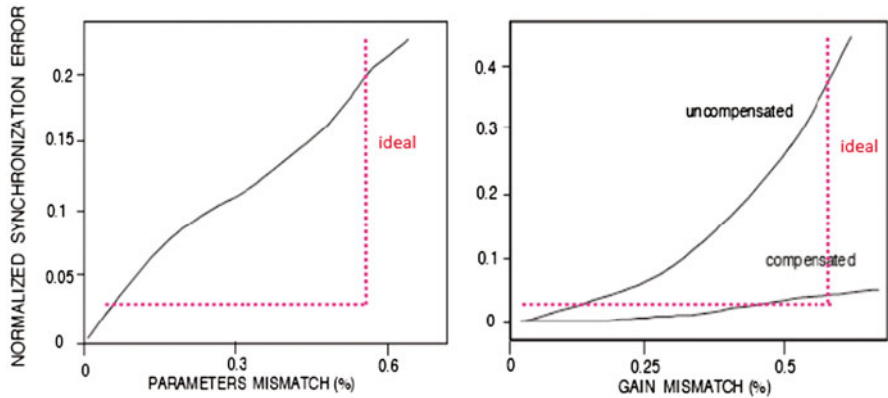
Fig. 6.5 Synchronization error vs. relative mismatch of system parameters (*left*) and vs. gain mismatch, in uncompensated and amplitude-normalized conditions (*right*). (From Ref.[20])

However, the CM scheme has some drawbacks. First, if the sum of signal to chaos is made at a slightly different λ, clever filtering could reveal the message. Second, the small amplitude of the message (e.g., 5 % of the transmitted power) makes the transmitted power mostly used by chaos rather than message, and thus SNR cannot be very high. So, the quest is on a method allowing for a message as large as the chaos.

The answer is chaos shift keying (CSK) [19]. In CSK, we encode the "0"s and "1"s bits of the digital message on different chaos waveforms (or, more correctly, on different orbits in the phase space), by acting on one of the several parameters governing the dynamical evolution of the system, e.g., the drive current of the laser [20].

Thus, each bit uses the entire chaos waveform and associated power, and we fully exploit the available photons (and increase SNR).

As shown in Fig. 6.6, at the transmitter the drive current of laser LD1 is switched from J_0 to J_1, to code the bit "0" and bit "1" of the message, and we get a sequence of piece-wise chaos waveforms for the coded message. At the receiver end, two twin systems are set at bias J_0 (LD3/LD4) and J_1 (LD5/LD6). Injection of the received waveform synchronizes the designated bit, "0" for system LD3/LD4 and "1" for system LD5/LD6.

The CSK and CM cryptography schemes, however, are difficult to implement with the two-laser structure of the basic coupled-system cell, which is not minimum part-count. To go to a practical system, we need a simpler scheme, and this is indeed possible with the self-mixing (also called DOF—Delayed Optical Feedback) chaos cell (Fig. 6.7).

In a typical all-fiber DOF setup (Fig. 6.8 top), the laser diode is conjugated through a lens to a single-mode fiber, whose end-face is angled (8–12 deg. typ.) to avoid back-reflection. The fiber ends on a mirror, partially reflecting back the outgoing signal. By varying the distance of fiber tip to the mirror we can adjust the level K of feedback. In this case a so-called long-cavity system is realized. The message can be added to chaos by an external amplitude modulator.
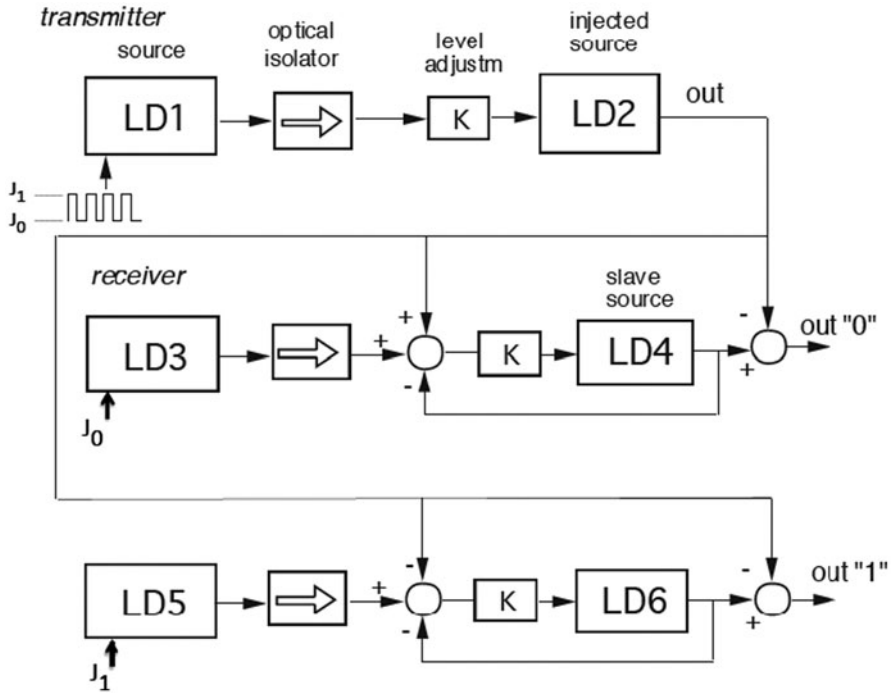
Fig. 6.6 CSK cryptography: the binary message modulates levels J_0 and J_1 of the bias current, and lasers *LD1/LD2* generate a sequence of chaos waveforms, for the "0" and "1" of the message. At the receiver end two twin systems are biased at J_0 (*LD3*) and J_1 (*LD5*) and injection of transmitted waveform makes them synchronize on its designated bit, "0" for system *LD3/LD4* and "1" for *LD5/LD6*. (From Ref.[20])

Fig. 6.7 DOF (delayed optical feedback) chaos generator: the laser is subject to a self-injection-coupling regime from the mirror. The beamsplitter injects an external signal for synchronization
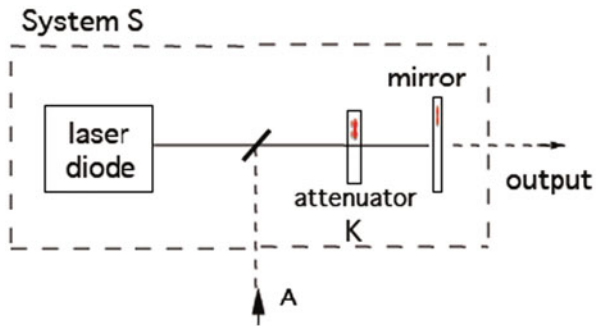
We can also implement the DOF cell by an integrated optics technology (Fig. 6.8 bottom and Fig. 6.9), incorporating in a single photonic integrated circuit (PIC) the active source (a DFB laser), an active waveguide for amplitude and/or phase modulation, and the retro-reflector (the mirror-like cleaved facet of the chip). This solution offers a more stable short-cavity system [21]; also, the integrated optics
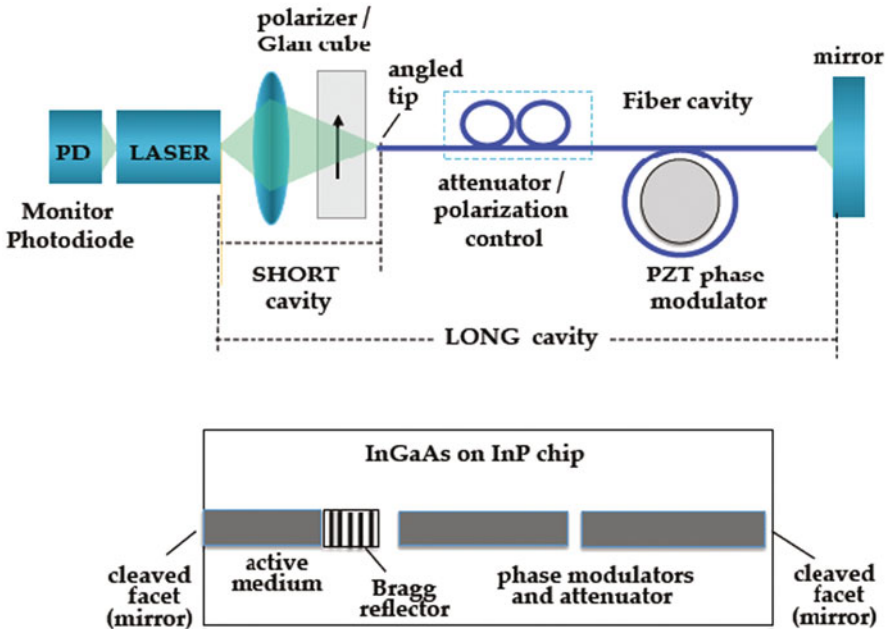
Fig. 6.8 Technologies for implementing the DOF scheme: all-fiber (*top*) and integrated optics (*bottom*)
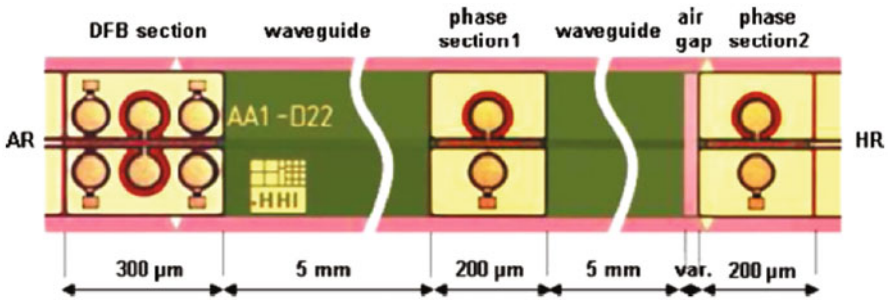

Fig. 6.9 A DOF short-cavity PIC-chip, fabricated by InGaAs waveguides on a InP substrate, and incorporating a DFB laser, two 5-mm waveguides and two phase modulators, to realize an integrated crypto-system. (From Ref.[22])

approach offers the possibility of developing more advanced chaos generators, which would be difficult to implement in bulk or micro-optics [22].

Practical solutions of CM and CSK schemes are available in the literature. An example of a CSK-PM system is reported in Fig. 6.10 [23], using a short-cavity DOF generator and a LiTaO$_3$ phase modulator to impress the message as a phase $\Delta\psi_{in}$ added to the optical pathlength 2 ks. As the short-cavity DOF is sensitive to the external cavity phase, the chaos waveform is somehow coded by phase $\Delta\psi_{in}$.
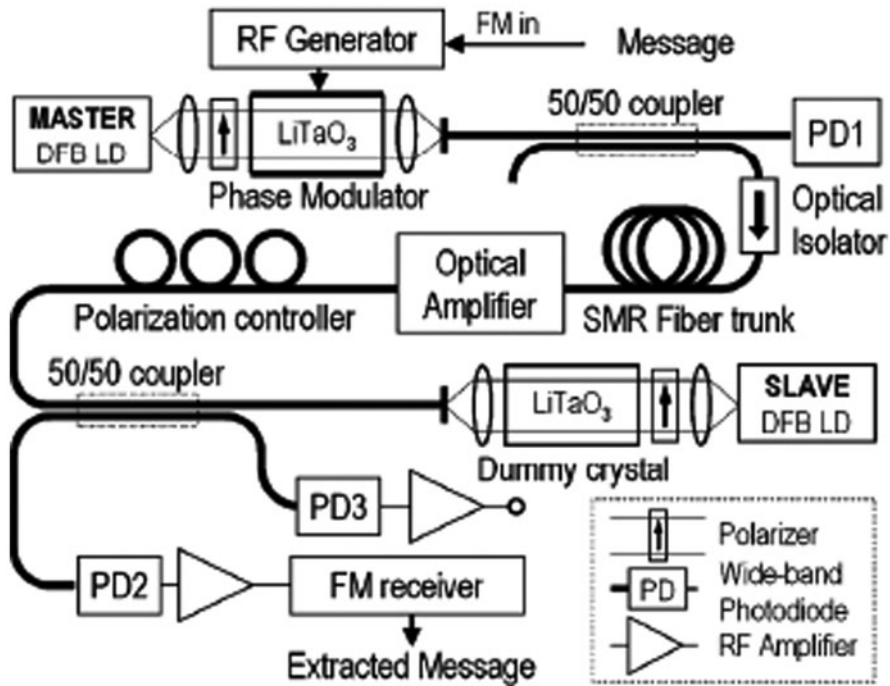
Fig. 6.10 A short-cavity DOF-CSK system, uses a LiTaO$_3$ phase modulator to impress the message as a phase variation in the cavity and hence in the chaos waveform generated by the DOF. At the receiver, a dummy modulator synchronizes only when phase is zero. Photodetector and an FM receiver act as phase-to-amplitude converter, thus extracting the message. (From Ref.[23])

At the receiver end, an identical DOF generator has the phase modulator set at zero voltage. Thus, the receiver is synchronized only for zero input message or phase $\Delta\psi_{in}$ Correlation of receiver and transmitter chaos waveforms progressively decreases at the increase of the phase difference, and this process is a sort of phase-to-amplitude conversion. With photodetection followed by a PM conversion we get a signal proportional to $\Delta\psi_{in}$ and hence to input signal.

In all the proposed solutions for secure transmission using chaos, security is based on synchronization sensitivity to laser parameters. The two users must share a 'twin' laser pair, i.e., two lasers of very similar parameters (selected from the same wafer). Thus, for an eavesdropper, it is very difficult to find a laser compatible with the twin pair, to synchronize chaos and decode the message.

With the standard two-laser system, chaotic transmission of digital signals in the GHz range has been demonstrated on the metropolitan network of Athens [24]. Also, transmission of RF analog signals has been experimentally proven (Fig. 6.11.) [25]. Several basic building blocks for future long-distance transmission have been already proposed, such as a chaotic wavelength converter for WDM transmission [26], and a chaotic repeater [27]. Moreover, dual-channel operation [28], chaotic multiplexing

Fig. 6.11 Experiment of transmission of a video signal: **a** plaintext message, **b** message hidden in chaos, **c** recovered message. (From Ref. [25])
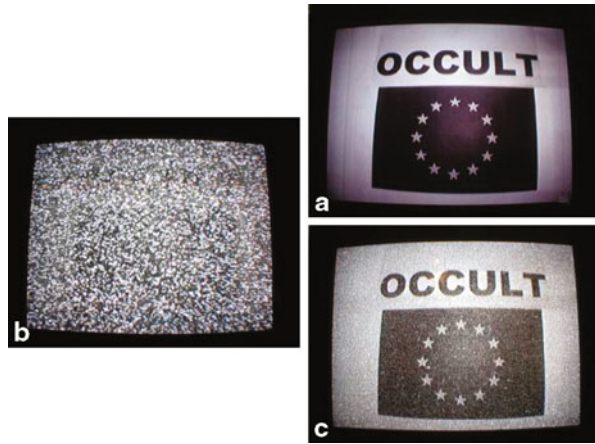
[29] and coding solutions for a more efficient signal protection have been studied [30, 31].

Alternative solutions based on the electro-optical feedback have been also proposed [32]. In the basic scheme, chaos is generated by using a nonlinear modulator fed by an auxiliary laser, the output of which is applied to the electrical input of the transmitter laser, after photodetection. The feedback loop is closed, by applying the photodetected laser output signal to the modulator electrical input. The message is added to chaos at the transmitter laser input node.

At the receiver, the optical signal (chaos + message), is photodetected and applied to the same modulator/laser combination, but working at open loop, to extract chaos by nonlinear filtering. The message is finally recovered by subtraction, from the received signal, of photodetected chaos.

This approach avoids optical injection and laser alignment procedures, and does not require the integrated optics technology for a practical in field implementation, since a compact and stable micro-optics realization is possible. On the other hand, its security relies on matched nonlinear modulators, instead on the more challenging (for an eavesdropper) matched lasers.

6.5 Recent Achievements

In addition to the basic two-laser scheme, open or close loop [33], more advanced setups have been developed, which offers a better synchronization quality to the authorized subscribers, who share the matched laser pair, as well as a better security against an eavesdropper attack. Both results are based on such schemes being symmetrical (differently from the basic two-laser solution), since both Tx and Rx lasers are injected by a third (possibly unmatched) chaotic laser (called the driver Drv).
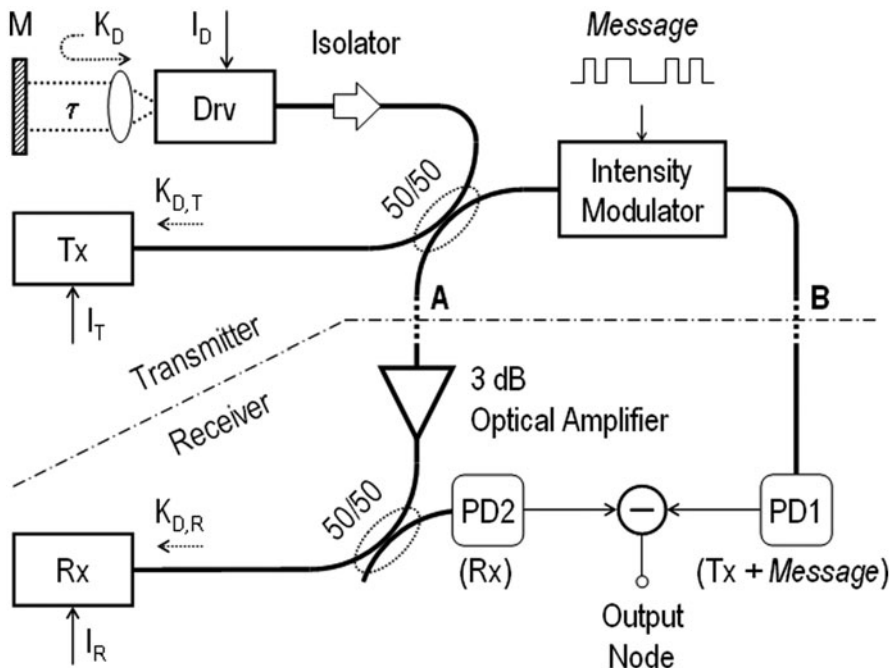
Fig. 6.12 A three-laser CM crypto-system uses a common source driver (*Drv*) to route into chaos and synchronise a pair of twin lasers (*Tx* and *Rx*). The message is recovered as in the basic scheme by chaos cancellation at the receiver. (From Ref. [34])

A CM implementation setup of such three-laser scheme [34] is shown in Fig. 6.12. In this case, the Drv laser is routed to chaos by delayed optical feedback, while Rx and Tx may have no feedback, or may experience a weak local optical feedback by a mirror. Numerical results for RF power spectra of Drv, Tx and Rx, and their difference are in Fig. 6.13. In Fig. 6.14, transmission of a 5 Gb/s message is simulated, with the RF spectra of the plaintext message, of the same message hidden in chaos, and of the recovered message after chaos subtraction. The eye-diagram of the recovered message is also shown.

In experiments, the high cancellation levels of Fig. 6.13 cannot be achieved. However, the advantage of the three-laser over the two-laser scheme has been confirmed. The requirement of using a supplementary laser is not really a drawback, since in a network the same Drv can be used to assist several interconnections between couples of users.

The three-laser scheme can be easily modified for use in free space propagation. The recent interest in FSOLs (Free Space Optical Links), especially for countries rapidly expanding their communication infrastructure, also requires a careful design for security, since the open optical beams can be easily intercepted by an eavesdropper.
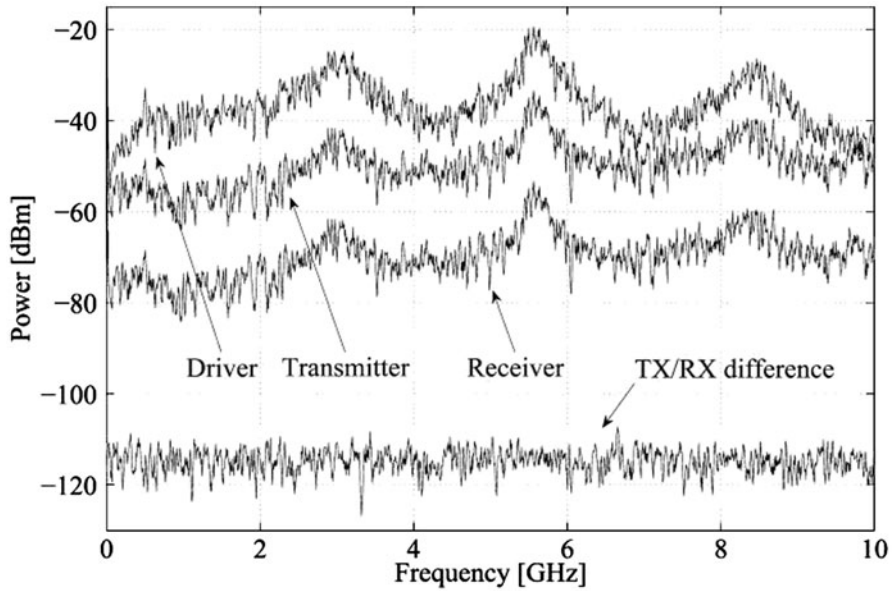
Fig. 6.13 Numerical RF power spectra for *Drv*, *Tx* and *Rx* in the scheme of Fig. 6.10. For better visualization, the traces of *Drv* and *Rx* have been shifted upwards by 20 dB and downwards by 20 dB, respectively. The difference signal is also shown. (From Ref.[34])
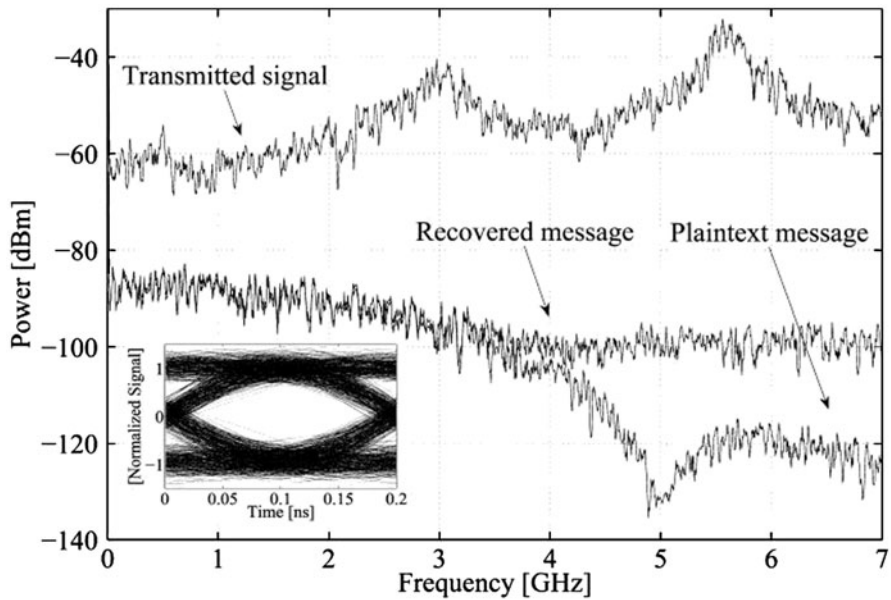
Fig. 6.14 Numerical RF spectra for CM transmission of a 5 Gb/s digital message with the scheme of Fig. 6.10. The eye diagram of the recovered message is shown in the inset. (From Ref.[34])
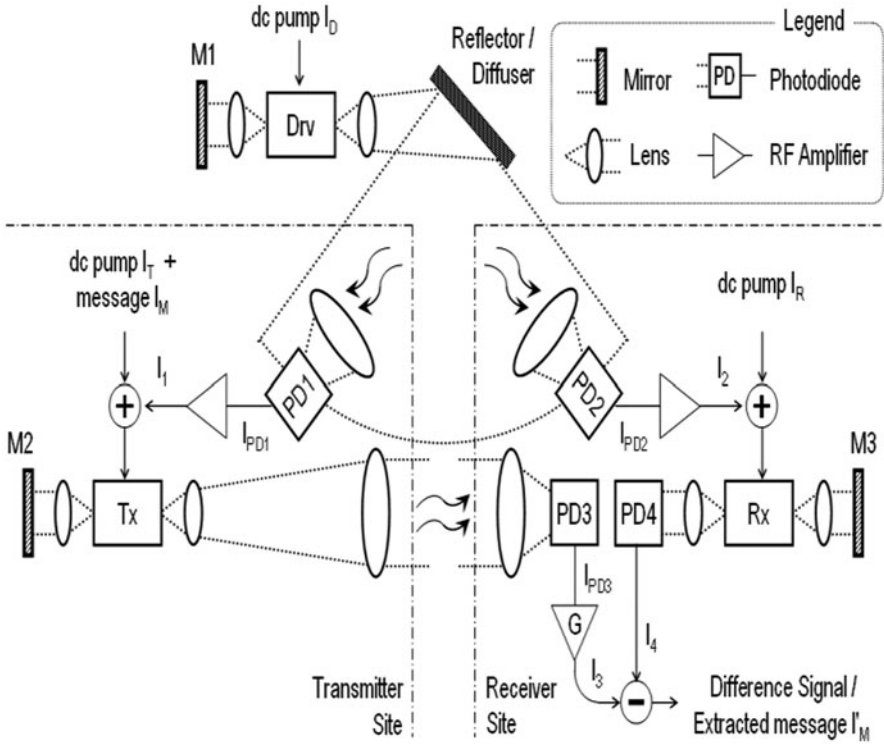
Fig. 6.15 Configuration for secure data transmission in free-space. Due to high channel attenuation, the optical emission of the Drv is photodetected and amplified before injection into *Rx* and *Tx*. The same is done for *Tx* to *Rx* injection. (From Ref.[35])

A suitable three-laser scheme [35] for such application, where attenuation is usually high, is proposed in Fig. 6.15.

The optical emission of Drv is photodetected and amplified before injection into Rx and Tx. The same is done for Tx to Rx injection. Electrical amplification is a convenient solution, with respect to optical amplification, and results in a lower cost, easier to align system. This scheme offers a viable solution also for indoor secure transmission, in a room or on a train or airplane, where many users share the same diffused channel, as well as the Drv, which can be installed, e.g., on the ceiling.

Another evolution of the standard setup has been in the direction of providing a real multi-user network protected by chaos.

All the schemes considered so far are practically restricted to transmission between two specific users, sharing a twin laser pair. However, in most cases, it is required to organize a network of several users that can freely transmit data to one-another in a secure way. In practice, it is difficult to find more than a few matched devices on a wafer, which can all synchronize efficiently to one another, and thus multi-user transmission would require that each user holds a laser (of a twin pair) for each
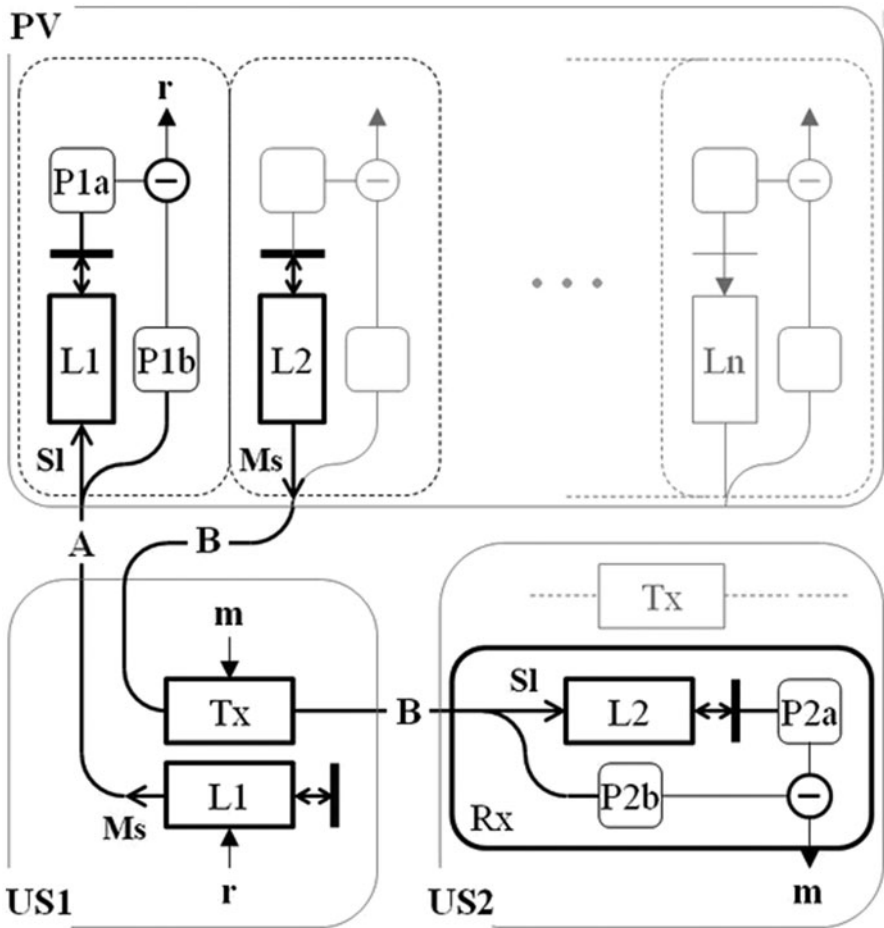
Fig. 6.16 Multi-user network configuration for secure data transmission. Path A is the connection between the provider (*PV*) and the first user (*US1*), while *B* is the connection between the two users (*US1* and *US2*). *Tx* is a modulator to introduce message m and Pij are photodiodes. (From Ref.[36])

potential partner. This is clearly unpractical. Alternatively, one could increase the message amplitude, so that a lower synchronization level can be tolerated, but in this case the security level would be poor.

A possible solution has been recently proposed [36], derived from the well-known public-key cryptography.

With this new approach, it is possible to exchange data between any couple of subscribers in a network. This can be done by introducing a provider, who is responsible of the network security, as shown in Fig. 6.16. For each subscriber, a couple of twin chaotic lasers is required, one being held by the provider and the other by the subscriber himself. The basic two-laser (or the three-laser) scheme of chaotic

transmission is then used for secure data exchange, both between a subscriber (US) and the provider (PV), and between two subscribers (US1, US2).

With reference to Fig. 6.16, when subscriber US1 wants to send a message m to US2, it first sends a request to PV (message r). This is done in a protected way, by using lasers L1, i.e., the twin pair common to the provider PV and to US1. As a response to the request of US1, the provider routes the chaotic carrier generated by laser L2 to US1. User US1 can now transmit message m to US2 by modulating this carrier, implementing, for example, CSK (Chaos Shift Keying) or CM (Chaos modulation). Only user US2 can retrieve the message, since he is the only one to hold the corresponding twin laser. Other users, or an eavesdropper, cannot extract the message.

Several arrangements can be considered, based on this architecture. Extra security can be offered by protecting path B, since, in principle, an eavesdropper could intercept this carrier between PV and US1 and use it to send a message to US2, pretending it comes from an authorized subscriber. To tackle this problem, a possible solution is to hide the transmission carrier in chaos on its turn. The same laser pair L1, already used to send the request r from US1 to PV, can be used to this end, by implementing for example a two-laser scheme, where the roles of Ms and Sl subsystems (Fig. 6.16) are now interchanged, and the 'message' in this case is the chaotic carrier of L2.

References

1. see for example International Journal of Bifurcation and Chaos, 23, 2013. WSP (Singapore) ISSN: 0218–1274
2. see for example: Journal of Complexity, 29, 2013. Elsevier B.V.(Amsterdam) ISSN: 0885–064X
3. Tsoukas, H.: Chaos, complexity and organization theory. Organ. **5**, 291–313 (1998)
4. Haken, H.: Analogy between higher instabilities in fluids and lasers. Phys. Lett. A. **53**, 77–78 (1975)
5. Ohtsubo, K.: Semiconductor Lasers: Stability, Instability and Chaos, 2nd edn. (Springer Series Optical Sciences 111). Springer, New York (2009)
6. Arecchi, F.T., Puccioni, G.L., Tredicce J.R.: Deterministic chaos in laser with injected signal. Optics Commun. **51**, 308–314 (1984)
7. Lang, R., Kobayashi, K.: External optical feedback effects on semiconductor injection laser properties. IEEE J. Quant. Electron. QE-**16**, 347–355 (1980)
8. Donati, S.: Developing self-mixing interferometry for instrumentation and measurements. Laser Photon. Rev. **6**, 393–417 (2012)
9. Donati, S.: Responsivity and noise of self-mixing photodetection schemes", IEEE J. Quantum Electron. **47**, 1428–1433 (2011)
10. Donati, S.: "Photodetectors", Prentice Hall, Upper Saddle River (2000), see Sect. 8.4.
11. Soriano, M.C., Garcia-Ojalvo, J., Mirasso, C., Fischer, I.: complex photonics: dynamics and applications of delay-coupled semiconductors Lasers. Rev. Mod. Phys. **85**, 421–470 (2013)
12. S. Donati, S.-K. Hwang: Chaos and high-level dynamics in coupled lasers and their applications. Prog. Quantum Electron. **36**(2–3), 293–341 (2012)
13. Donati, S., Mirasso, C. (eds.): Optical chaotic cryptography. Feature Issue of: IEEE. J. Quantum Electron. QE-**38,** 1138–1184 (2002)

14. Larger, L., Goedgebuer, J.-P. (eds): Special Number on Criptography using Optical Chaos, Comptes Rendus de l'Academie des Sciences-Dossier de Physique, vol. 6, n. 5 (2004)
15. Ohtsubo, J.: Chaos synchronization and chaotic signal masking in semiconductor lasers with optical feedback. IEEE J. Quantum Electron. **38**(9), 1141–1154 (2002)
16. Annovazzi-Lodi, V., Donati, S., Manna, M.: Chaos and locking in a semiconductor laser due to external injection. IEEE J Quantum Electron. QE-**30**, 1537–1541 (1994)
17. Mirasso, C.R., et al: Synchronization properties of chaotic semiconductor lasers and applications to encryption. C. R. Phys. **5**, 613–622 (2004)
18. Ju, R., Spencer, P.S., Shore, K.A.: The relative intensity noise of a semiconductor laser subject to strong coherent optical feedback. J. Opt. B-Quantum Semiclass Opt. **6**(8), S775–S779 (2004)
19. Annovazzi-Lodi, V., Donati, S., Scirè, A.: Synchronization of chaotic injected-laser systems and its application to optical cryptography. IEEE J. Quantum Electron. QE-**32**, 953–959 (1996)
20. Annovazzi-Lodi, V., Donati, S., Scirè, A.: Synchronization of chaotic lasers by optical feedback for cryptographic applications. IEEE J. Quantum Electron. QE-**33**, 1449–1454 (1997)
21. Syvridis, D., Argiris, A., Bogris, A., Hamacher, M., Giles, I.: Integrated devices for optical chaos generation and communications applications. IEEE J. Quantum Electron. **45**(11), 1421–1428 (2009)
22. Tronciu, V.Z., Mirasso, C., Colet, P., Hamacher, M., Benedetti, M., Vercesi, V., Annovazzi-Lodi, V.: Chaos generation and synchronization using an integrated source with an air gap. IEEE J. Quantum Electron. **46**(12), 1840–1846 (2010)
23. Annovazzi-Lodi, V., Benedetti, M., Merlo, S., Perez, T., Colet, P., Mirasso, C.: Message encryption by phase modulation of a chaotic optical carrier. IEEE Photon. Technol. Lett. **19**, 76–78 (2007)
24. Argyris, A., Syvridis, D., Larger, L., Annovazzi-Lodi, V., Colet, P., Fischer, I., Garcia-Ojalvo, J., Mirasso, C., Pasquera, L., Shore, K.A.: Chaos-based communication link at high bit rate using commercial fiberoptic link. Nat. Lett. **438**, 343–346 (2005)
25. Annovazzi-Lodi, V., Benedetti, M., Merlo, S., Norgia, M., Provinzano, B.: Optical chaos masking of video signals. IEEE Photon. Technol. Lett. **17**, 1995–1997 (2005)
26. Annovazzi-Lodi, V., Aromataris, G., Benedetti, M., Cristiani, I., Merlo, S., Minzioni, P.: All-optical wavelength conversion of a chaos masked signal, IEEE Photon. Technol. Lett. **19**, 1783–1785 (2007)
27. Matsuura, T., Uchida, A., Yoshimori, S.: Chaotic wavelength division multiplexing for optical communication. Opt. Lett. **29**, 2731–2733 (2004)
28. Paul, J., Sivaprakasam, S., Shore, K.A.: Dual-channel chaotic optical communications using external–cavity semiconductor lasers. J. Opt. Soc. Am. B. **21**, 514–521 (2004)
29. Lee, M.W., Shore, K.A.: Demonstration of a chaotic optical message relay using DFB laser diode. IEEE Photon. Technol. Lett. **18**, 169–171 (2006)
30. Ursini, L., Santagiustina, M., Annovazzi-Lodi, V.: Enhancing chaotic communication performances by manchester coding. IEEE Photon. Technol. Lett. **20**, 401–403 (2008)
31. Bogris, A., Chlouverakis, K.E., Argyris, A., Syvridis, D.: Enhancement of the encryption efficiency of chaotic communications based on all-optical feedback chaos generation by means of subcarriers modulation. In: Proceedings CLEO-Europe/IQEC, 2007, paper CH4-MON
32. Goedgebuer, J.P., Larger, l., Porte, H.: Optical cryptosystem based on synchronization of hyperchaos generated by a delayed feedback tunable laserdiode. Phys. Rev. Lett. **80**, 2249–2252 (2008)
33. Vicente, R., Perez, T., Mirasso, C.: Open-versus closed-loop performance of synchronized chaotic external-cavity semiconductor lasers. IEEE J. Quantum Electron. **38**(9), 1197–1204 (2002)
34. Annovazzi-Lodi, V., Aromataris, G., Benedetti, M., Merlo, S.: Private message transmission by common driving of two chaotic lasers, IEEE J. Quantum Electron. **46**, 258–264 (2010)
35. Annovazzi-Lodi, V., Aromataris, G., Benedetti, M., Merlo, S.: Secure optical transmission on a free space optics data link IEEE J. Quantum Electron. **44**, 1089–1095 (2008)
36. Annovazzi-Lodi, V., Aromataris, G., Benedetti, M.: Multi-user private transmission with chaotic lasers. IEEE J. Quantum Electron. **48**, 1095–1101 (2012)

Chapter 7
Superwicking Surfaces Produced by Femtosecond Laser

A. Y. Vorobyev and Chunlei Guo

Abstract Modifying material wetting properties using femtosecond laser surface nano/microstructuring has recently become an actively studied area due to many promising applications. In this chapter, we overview briefly the newly emerged femtosecond laser-based approaches for modifying the wetting properties of materials and describe recent developments in producing a novel type of surface structures that transform a regular surface of solids to superwicking. This novel type of the surface structure is an array of parallel nanostructured microgrooves. In a gravity defying way, water runs vertically uphill on the created superwicking surfaces. The fast self-propelling motion of the liquid is due to strong capillary force generated in the surface structure. The unique wetting and wicking properties of these novel materials may find a wide range of applications in nano/microfluidics, optofluidics, lab-on-chip technology, fluidic microreactors, chemical sensors, biomedicine, and heat transfer devices (e.g., heat pipes for cooling of electronic devices).

7.1 Introduction

In nature, there are numerous examples of biological materials with remarkable wetting properties due to surface nano/microstructures. Examples are the leaves of water-repellent plants such as Lotus (*Nelumbo nucifera*) and Lady's mantle (*Alchemilla mollis*), which are superhydrophobic due to a combination of micro- and nano-structures on the surface of their leaves [1, 2]. Due to their superhydrophobicity, these plants have self-cleaning properties, known as "Lotus effect". When water drops roll over the leaves, they pick up dust particles and remove them when rolling off the leaves. Another example is the surface nano/microstructures on the wings of the Morpho butterfly that have two wonderful functions, the generation of the structural blue color and making the wing surface superhydrophobic/self-cleaning similar to Lotus plant [3].

A. Y. Vorobyev (✉) · C. Guo
The Institute of Optics, University of Rochester, Rochester, NY 14627, USA
e-mail: vorobyev@optics.rochester.edu

Surface morphology of a solid is a factor that influences the wetting properties of materials. Modification of wetting properties of materials using surface nano/micro structuring has been extensively studied in the past [4–8]. Traditionally, surface textures for altering the wetting properties are prepared using photolithography [8], electron beam lithography [9], wet chemical etching [10], and plasma techniques [11]. Recently, a new approach based on femtosecond laser surface nano/microstructuring has been developed for modifying the wetting properties of various materials [12–17]. This novel approach has become an active research area due to a number of advantages and many promising applications. The advantages of the femtosecond laser approach include: (i) ability to process a large variety of materials (metals, semiconductors, glasses, and polymers), (ii) simplicity, and (iii) capability to process complicated shapes with the size of the textured surface area as small as a tightly focused laser spot, i.e., down to about $10\,\mu$m, or as large as needed when a raster scanning of the laser beam is used.

Modification of wetting properties using femtosecond laser has been first demonstrated in Refs. [12, 13], where silicon wafers were treated with high-intensity ultrashort laser pulses in SF_6 environment to produce quasi-ordered arrays of conical microspikes. Folowing the laser surface treatment, Zorba *et al.* [13] produced superhydrophobic silicon. A water contact angle as high as $160°$ was reported. The authors of Ref. [12] produced superhydrophobic silicon by coating the conical microspikes with a layer of fluoroalkylsilane molecules. The authors of Refs. [18, 19] have found that depositing various functional coatings on the laser-nano/microstructured silicon allows producing engineered surfaces with wetting properties that can be changed by external stimuli (light, electric field, and pH). Effects of various surface textures induced by femtosecond laser pulses on wetting properties of platinum has been studied in [14]. The studied surface textures included irregular nanostructures, periodic surface structures, and hierarchical structures (combinations of nano- and micro-structures). It has been found that laser-structured surfaces become hydrophobic or even superhydrophobic for some textures. For example, a water contact angle as high as $158°$ was observed on the hierarchical surface structures. A detailed study of the wetting properties of stainless steel and titanium alloy following femtosecond laser surface structuring has been performed in [15]. It was observed that the treated surfaces are hydrophilic immediately after femtosecond laser processing but subsequently become superhydrophobic with time. The dramatic change in wetting behavior was attributed to accumulation of carbon on the laser-treated surface. The authors of Ref. [20] have studied the wetting properties of polymethyl methacrylate (PMMA) following femtosecond laser ablation. In this study, both hydrophilic and hydrophobic surfaces were produced depending on laser fluence. The hydrophobic surfaces were generated at a low laser fluence between 0.4 and 2.1 J/cm^2, while hydrophilic surfaces were produced at a laser fluence in the range of 2.1–52.7 J/cm^2. Different wetting behavior of the laser-treated PMMA was explained by laser-induced chemical bond changes, not to the produced surface texture. A superhydrophobic surface texture on poly(dimethylsiloxane) (PDMS) following femtosecond laser processing has been reported in Ref. [21]. The fabricated superhydrophobic surface had a contact angle higher than $170°$ and sliding angle less than $3°$.

The authors of Ref. [22] altered initially hydrophilic surface of polyethersulfone to superhydrophobic through femtosecond laser-induced both structural and chemical modifications.

Recently, novel superwicking surfaces have been created using direct femtosecond laser writing. These novel materials can make liquids run vertically uphill against the gravity over an extended surface area. Furthermore, they exhibit superhydrophilic and superwetting properties. The unique wetting and wicking properties of these novel materials may find a wide range of applications in thermal management, nano/microfluidics, optofluidics, lab-on-chip technology, fluidic microreactors, chemical sensors, and biomedicine. In this chapter, we overview the recent developments in producing superwicking surfaces and describe their potential applications.

7.2   Basic Idea of Wicking Structures and Their Fabrication Using Femtosecond Laser

The creation of superwicking structures using a femtosecond laser has been previously reported in [16, 23, 24]. The basic idea of wicking structures produced in [16, 23, 24] is as follows. The capillary effect in a pipe is a well known phenomenon demonstrated in Fig. 7.1a. A much less known fact is that the capillary force is also generated in a half-pipe as illustrated in Fig. 7.1b. Therefore, through engraving an array of paralel microgrooves on a surface of a solid, one can fabricate a wicking (capillary) surface of a large area as schematically shown in Fig. 7.1c. However, the capillary force in the half-pipe is much smaller than in the pipe [25]. Therefore, for enhancing the capillary action in the microgrooves, the authors of Refs. [16, 23, 24] used femtosecond laser nanostructuring of the surface of the microgrooves. The machanism of enhancing the capillary action in the microgrooves through nanostructuring of their surface is explained as follows. It is known that the capillary action of various capillary systems depends on the hydrophilicity of the surface that is in contact with the liquid. For example, the maximum capillary rise of a liquid in the tube is given by [26]

$$h = \frac{2\gamma \cos \theta}{\rho g R} \qquad (7.1)$$

where γ is the liquid-air surface tension, θ is the contact angle, ρ is the density of liquid, g is the gravitational acceleration, and R is the tube radius. The formula (7.1) shows that the smaller the contact angle θ (the higher hydrophilicity), the stronger the capillary action.

Following the Wenzel model, the wetting of a rough surface is described by relation [4]

$$\cos \theta^* = r \cos \theta \qquad (7.2)$$
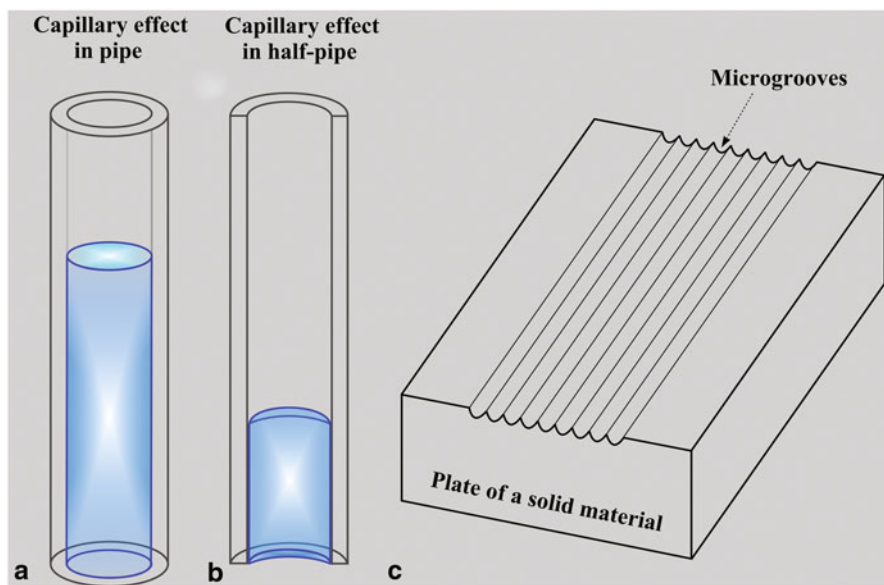
Fig. 7.1 Basic idea of producing the wicking (capillary) surfaces

where $\theta*$ is the apparent contact angle on a rough surface, r is the roughness factor (the ratio of the actual surface area to the geometrically projected area on the horizontal plane), and θ is the contact angle on a smooth horizontal surface of the same material (Young contact angle). Since r is always greater than 1, the surface texture enhances the hydrophilicity of an originally hydrophilic surface ($\theta < 90°$) and enhances the hydrophobicity of an originally hydrophobic surface ($\theta > 90°$). Since the materials used in capillary systems are intrinsically hydrophilic, the texturing of the surfaces that are in contact with the liquid will enhance the hydrophilicity (reduce the contact angle θ) and thereby will enhance the capillary action. Over the last few years, the direct femtosecond laser surface nano/microstructuring has been established as a versatile approach for controllable producing a large variety of surface structures at nano- and micro-scales on metals, semiconductors, glasses, polymers, and other materials [27–43]. Therefore, the femtosecond laser is a very efficient tool for producing the microgrooves with nanostructured surface. A typical setup used for producing the capillary microgrooves with nanostructured surface is shown in Fig. 7.2. Pulses from a femtosecond laser are focused by a lens onto a sample mounted on a computer-controlled XY-translation stage. A beamsplitter and joulemeter are used for monitoring the femtosecond laser pulse energy. An electromechanical shutter is used to block the laser beam in raster scanning. A neutral density filters are used to vary laser fluence incident on the sample. The femtosecond laser setup shown in Fig. 7.2 is suitable for producing a single microgroove when sample is translated along the X- or Y-axis, or an array of parallel microgrooves over
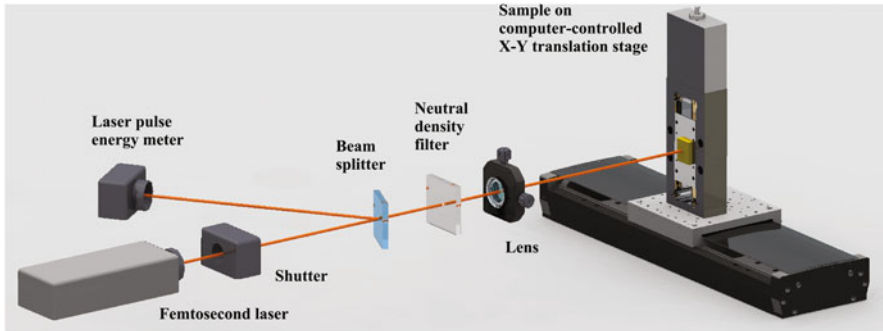
Fig. 7.2 Typical experimental setup for producing microgrooves on the surface of solids

a large surface area when the sample is raster scanned. By varying the parameters of the laser pulses incident upon the treated metal, the microgroove geometry can be controlled. Commonly, the capillary microgrooves are produced in two steps. In the first step, the microgrooves are produced using high laser fluence. In the second step, the microgrooves surface is then nanostructured using low or moderate laser fluence for achieving a maximum enhancement of the hydrophilicity. For some materials, even one-step processing can be sufficient for producing efficient capillary microchannels due to nanostructures commonly left on the microgroove surface after processing at high laser fluence. In the following section, we discuss the capillary action of femtosecond laser fabricated superwicking structures.

## 7.3 Spreading of Liquids on Superwicking Surfaces

Glass is a widely used material in microfluidics, optofluidics, lab-on-chip technology, and biomedical devices [44–46]. Although the glass is a transparent material, it can be easily processed using tightly focused femtosecond laser pulses due to nonlinear absorption of high-intensity light [47]. Figure 7.3a shows a photograph of the femtosecond laser treated glass sample, where the superwicking structure is an array of parallel microgrooves with a nanostructured surface. Figure 7.3b shows a 3D optical image of the treated surface, where we can see that the microgroove period, depth, and width are about 100, 32, and 28 μm, respectively. Figure 7.3c and 7.3d show the details of the surface structural features. One can see that the surface of both ridges and valleys of the microgrooves has engraved nano- and fine micro-structures. Figure 7.3d shows that the laser-induced nanostructures include both nanoprotrusions and nanocavities, while fine microstructures include microcavities and microscale aggregates composed of nanoparticles that fuse onto each other and on the glass surface. The average size of superimposed fine microstructures is about 2.7 μm.
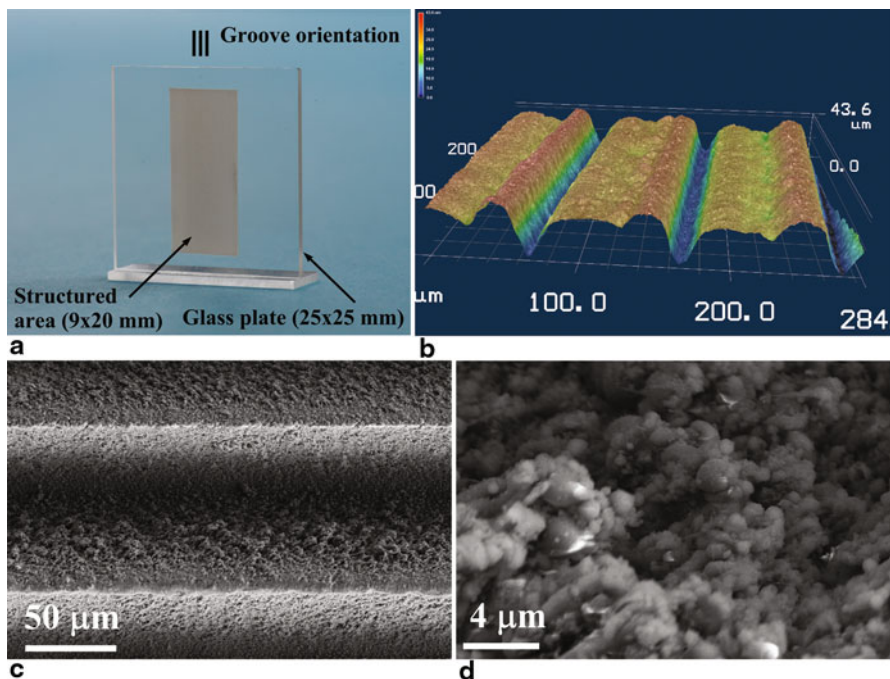
Fig. 7.3 a Photograph of the femtosecond laser treated glass sample. **b** A 3D optical image of the surface capillary microgrooves. **c** and **d** fine micro- and nano-structural features on the microgrooves [24]

The capillary action of the sample shown in Fig. 7.3 is demonstrated in Figs. 7.4 and 7.5. Figure 7.4 shows the spreading dynamics of a 3-μl water droplet deposited on the horizontally-positioned structured glass surface. For a comparison, the behavior of a 3-μl water droplet deposited on an untreated glass surface is also shown in Figs. 7.4a, 7.4b, 7.4c, 7.4d, 7.4e, 7.4f. Figure 7.4 shows that the water spreading is highly anisotropic on the treated area and it occurs preferentially along the microgrooves. One can deduce from Fig. 7.4b that average initial velocity of water front spreading is about 5.8 cm/s within the first 0.2 s. However, the spreading velocity decreases with time, as seen from Figs. 7.4c, 7.4d, 7.4e, 7.4f. The experiments with different volumes of water in the range of 1–6 μl show the similar highly anisotropic spreading behavior. Figure 7.5 shows the spreading dynamics of a 3-μl water droplet pipetted on the vertically-positioned glass sample with the microgrooves oriented vertically. The snapshots of water spreading shown in Figs. 7.5a, 7.5b, 7.5c, 7.5d, 7.5e, 7.5f demonstrate that the water deposited on the bottom of the groove area immediately sprints vertically uphill against the gravity. It is seen that this gravity-defying uphill motion easily extends over several centimeters. This experiment clearly demonstrates that the femtosecond laser processing makes a regular glass surface to be superwicking, with a driving force much stronger than the
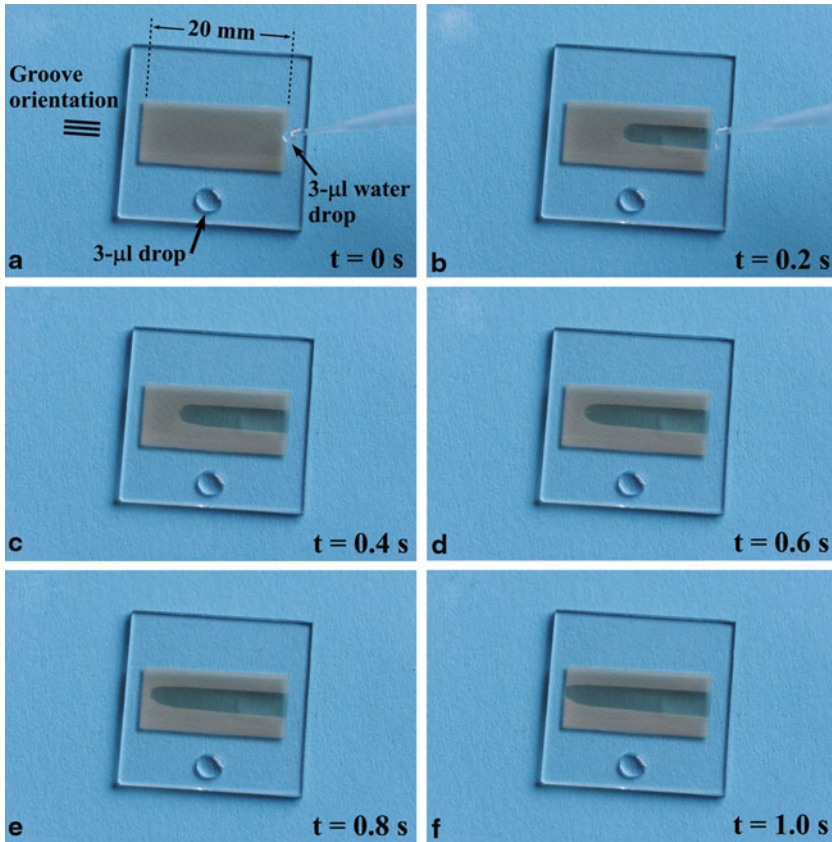
Fig. 7.4 Spreading dynamics of water on a horizontally-positioned glass sample. The average water spreading velocity is about 3.8 cm/s within the first 0.2 s and it reduces to about 2 cm/s for the time interval of 1 s [24]

gravity. One can deduce from Fig. 7.5b, that the average water front spreading velocity is about 3.8 cm/s within the first 0.2 s, and this velocity is lower than the water spreading along the horizontal grooves in Fig. 7.4b. As seen in Figs 7.5a, 7.5b, 7.5c, 7.5d, 7.5e, 7.5f, the spreading velocity decreases with time similar to the case of horizontal orientation of the microgrooves (Figs. [4], 7.4b, 7.4c, 7.4d, 7.4e, 7.4f).

In the past, fluid flow has been studied in various capillary systems such as tubes, open surface grooves, and two-dimensional arrays of pillars. It has been shown by Washburn [48] that flowing of a wetting liquid in a capillary tube follows a diffusion law as $z(t) \propto (Dt)^{1/2}$, where z is the distance traveled by the liquid, t is the time, and D is the diffusion constant. Spreading of wetting fluids has been also studied in open capillary systems, such as surface grooves [49–52] and two-dimensional arrays of pillars [6, 8]. It has been shown that the spreading dynamics in open V-shaped
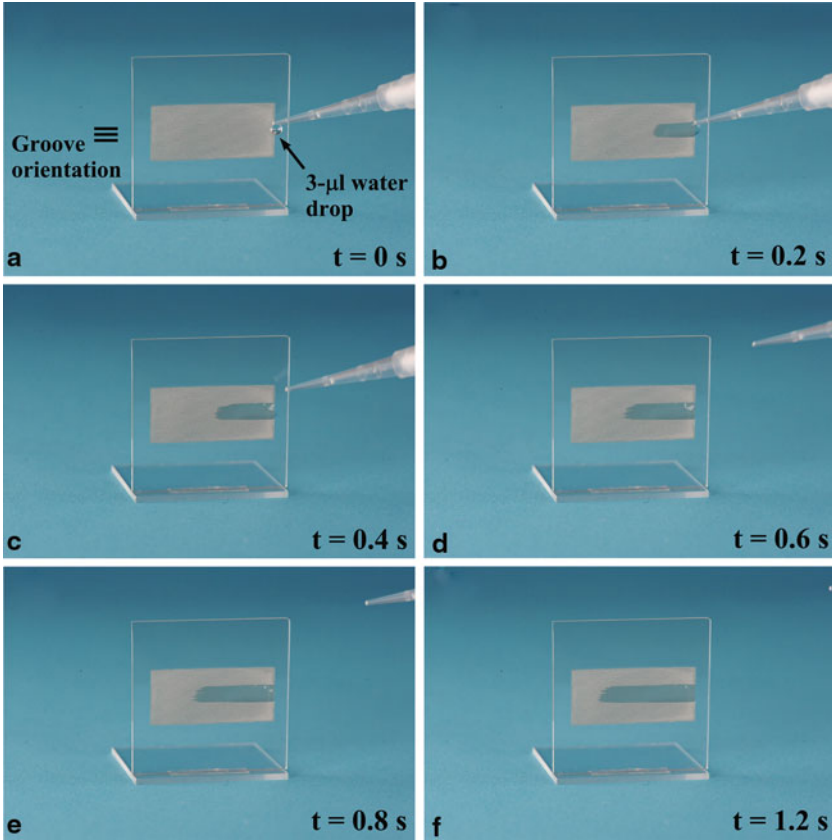
Fig. 7.5 Dynamics of water running uphill against the gravity on a vertically-standing glass sample with grooves oriented vertically. **a–f** Snapshots of water spreading vertically uphill with time [24]

grooves also follows the $t^{1/2}$ dependence [50]

$$z^2 = K(\alpha, \theta)[\gamma h_0/\mu]t \tag{7.3}$$

where $K(\alpha, \theta)$ is the geometry term with α and θ being the groove angle and the contact angle, γ and μ are the surface tension and viscosity of the liquid, and h_0 the groove depth. The authors of Refs. [6, 8] have demonstrated that the Washburn-type dynamics also holds on surfaces textured with regular arrays of pillars. There is a general consensus that a structured surface can be viewed as a network of open capillaries, where the liquid spreading from a reservoir usually follows the Washburn-type scaling law $z \propto (Dt)^{1/2}$ [6, 8, 49, 50, 53, 54]. In contrast to previously studied open grooves, the surface of the open grooves produced by ultrafast laser has a highly hierarchical structure. Figure 7.6 shows a plot of the uphill travel distance z as a function of $t^{1/2}$ for the vertically standing glass sample shown in Fig. 7.5. It is
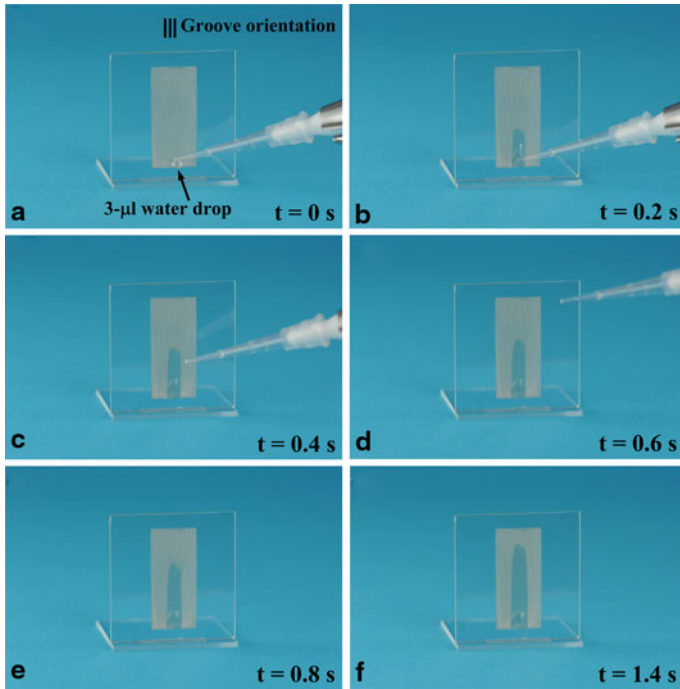
Fig. 7.6 Uphill distance traveled by water front as a function of $t^{1/2}$ [24]

seen that the water spreading distance linearly depends on $t^{1/2}$ despite of extremely sophisticated surface topology. This observation indicates that the Washburn-type $t^{1/2}$ dynamics is indeed universal for the various capillary systems. The structure of the open capillary systems produced by femtosecond laser [16, 23, 24] can be considered as composed of two substructures: (1) an array of microgrooves and (2) irregular structures on nano- and fine micro-scales superimposed on the surface of the microgrooves. Therefore, the capillary action of the laser-produced open capillary systems is a combined capillary effect from both substructures. Thus, the texture on the microgroove surface plays two roles. First, it enhances the hydrophilicity of the microgroove surface. Second, it generates its own capillary flow. Previously, Bico et al. [55] have modeled capillary rise in a tube with a surface textured by a designed regular roughness. Their model predicts two different capillary rises in a tube decorated with regular spikes: one inside the entire volume of the tube and the other only inside the spikes. The liquid spreading in the spikes forms a film that spreads faster than the main meniscus, causing a broadening of the liquid front. Is this also holds for femtosecond laser produced open microgrooves is not yet studied.

At present, the superwicking effect has been demonstrated for a number of solid materials, including glass, silicon, metals, and biological hard tissues [16, 23, 24, 56, 57]. Recently, wicking surfaces have been produced using nanosecond laser pulses [58].

7.4   Potential Applications of Capillary Superwicking Structures

Areas of potential applications of the capillary superwicking materials produced by femtosecond laser processing include cooling devices, nano/microfluidics, optofluidics, lab-on-chip technology, fluid microreactors, biomedicine, and biochemical sensors. Below, we give a short overview of some applications.

As devices and components in electronics, telecommunication, and computers become smaller and smaller, the demand for miniaturized high-performance cooling systems becomes important. Currently, the heat flux at both the chip and module levels of packaging can be so high (> 1000 W/cm^2) that it exceeds the practical limit of the traditional air-cooling. To combat this problem, microfluidic cooling of the chips is actively pursued. Tuckerman and Pease [59] have demonstrated that a microchannel heat sink integrated into a silicon chip is capable of dissipating a circuit power density of 790 W/cm^2. Presently, the microchannels in IC microfluidic heat sinks are commonly fabricated using deep reactive ion etching. One can expect that the laser fabricated capillary channels with textured surfaces will enhance the cooling performance of microchannel heat sinks by optimizing both nanostructure-induced turbulences in the microchannels and surface wettability. Cooling through liquid-vapor phase transition is potentially the most efficient way to dissipate high heat flux due to a high latent heat of the liquid-vapor phase transition. In the case of two-phase (flow boiling) microfluidic cooling, the superwicking microchannels can improve the cooling performance through larger surface area, enhancing fresh liquid refilling of the vapor bubble voids, and enhancing prevention of dry-out spots. Furthermore, the superwicking microchannels can find applications in miniature heat pipes for returning the working liquid from the condenser back to the evaporator.

In microfluidic systems, a pump is the most expensive and complicated component with a high failure rate. Therefore, passive microfluidic systems, where fluids are driven by capillary wicking action, are beneficial. The strong capillary action of the microchannels fabricated by the femtosecond laser [16, 23, 24] is a promising way to produce efficient capillary-driven microfluidic-based devices. Furthermore, this technique is promising for the fabrication of various other microfluidic components. For example it can be used for fabricating T- and Y-micromixers, where the microchannels with bas-relief structures, such as ribs [60] and staggered-herringbone grooves [61] on the floor and walls, are used for enhanced mixing of solutions in the microchannels through enhancing chaotic advection. Another potential application of this novel laser technique is the fabrication of capillary-driven microvalves that are used in microfluidic biochemical devices for stopping and delaying fluids in the microchannels. Operation of these passive capillary microvalves is based on an abrupt change in the geometry and wetting properties of the capillary microchannels [62, 63]. The femtosecond laser technology can be also used for fabricating separators [64] and capillary pumps [65]. Moreover, this laser technology has a great potential for the fabrication of superior autonomous microfluidic capillary sensing systems, where all required operations (pumping, valving, separating, and synchronization) are capillary-driven, without any external actuators [66]. Since the femtosecond laser technology of producing microfluidic systems and their components can be easily

integrated into a Computer Numerical Control (CNC) laser machine, this technology is attractive from a commercialization point of view.

Good wettability of enamel and dentin surfaces is desirable in enhancing adhesion of restorative materials in dentistry. At the present time, surface texturing of the enamel and dentin surfaces through etching with an acidic or basic solution for improving the wettability is a widely used approach in adhesive dentistry. In contrast to the traditional chemical etching that produces random surface roughness, the authors of Ref. [57] developed a new approach, which is based on producing engineered surface structures using the femtosecond laser surface nano/microstructuring technique. The engineered surface structure consists of an array of parallel microgrooves that generate a strong capillary force. Figure 7.7a shows the photograph of the femtosecond laser treated dentin specimen. The 3D optical image of the array of microgrooves produced on the dentin specimen is shown in Fig. 7.7b. Fine structural details of the microgroove surface are shown in Fig. 7.7c and 7.7d. The water contact angle before the laser treatment was measured to be 42° and 48° on the enamel and dentin specimens, respectively. After laser treatment, the contact angle on the laser-treated surface was measured to be $\sim 0°$ for both the enamel and dentin specimens. This means that the treated surfaces are superwetting [67]. The superwetting behavior can be seen from Figs. 7.7e and 7.7f, where a 1 µl water droplet sprints vertically uphill on a vertically standing laser-treated dentin surface. From these snapshots, the average water spreading velocity on the vertical dentin surface can be deduced to be about 21.7 mm/s within the first 0.2 s. From practical point of view, this means that wetting occurs instantaneously. The method reported in Ref. [57] for controllable enhancement of the wettability can be extended to human bones (because both the human teeth and bones are mainly composed of hydroxyapatite) and can be also used for the hydroxyapatite coatings of implants. This method for modifying the wettability is also suitable for a variety of biocompatible materials used in dentistry, medicine, biomedicine, and biosensing.

7.5 Conclusions

Over the past 7 years, significant progress has been made in applying femtosecond laser nano/microstructuring technology to alter the wetting properties of materials. It has been found that this approach is also capable of producing superwicking materials. The surface structure of these materials is an array of parallel microgrooves extensively covered by nano- and micro-scale structures. The capillary action of the created superwicking surfaces is so strong that the treated surfaces can make liquids run vertically uphill over an extended surface area. The wicking dynamics follows the classical square root of time dependence despite of a very complex geometry of the created wicking surface structure. The superwicking effect has been demonstrated on a number of solid materials, including glass, silicon, metals, and biological hard tissues. The femtosecond laser technology is suitable for processing complicated surface shapes at various dimensions. In contrast to commonly used surface
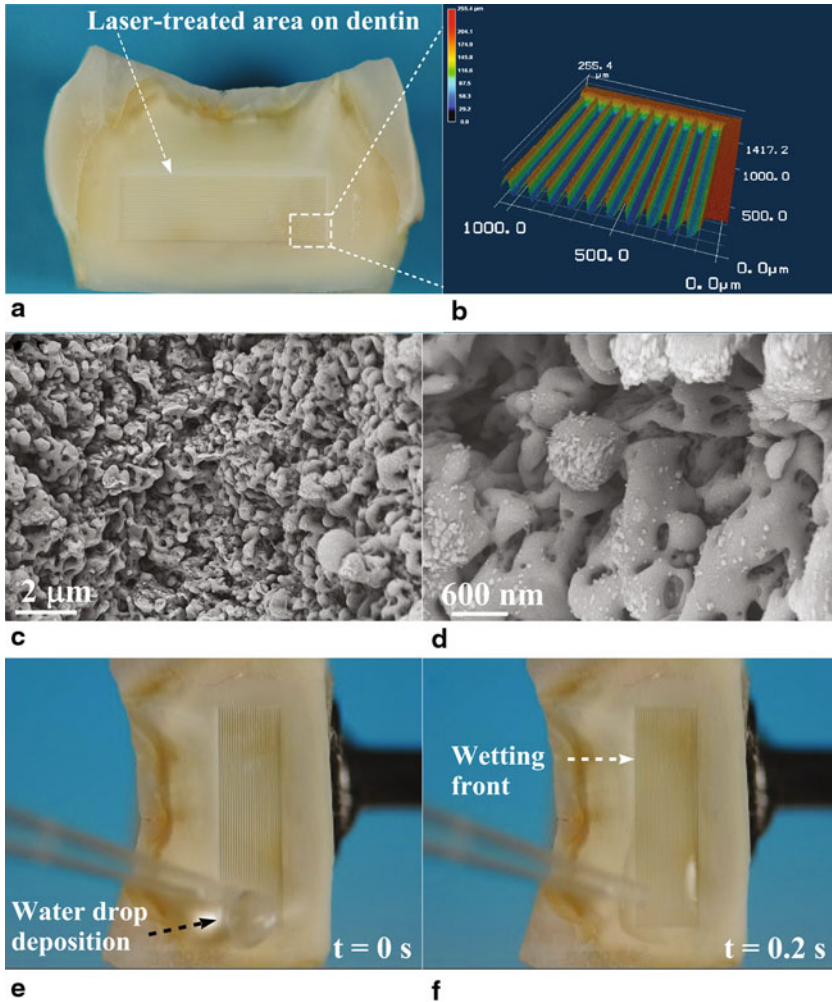
Fig. 7.7 a Photograph of a tooth with a laser-treated area on the dentin surface (a surface area textured with the microgroove pattern is 2.2 (6 mm^2). **b** 3D optical image of the laser-produced microgrooves. **c** and **d** SEM images showing fine micro- and nano-roughness on the surface of the microgrooves. **e** and **f** Water spreading on the laser-treated dentin surface positioned vertically [57]

lithography techniques, the laser processing does not utilize chemical etchants and is therefore free of chemical contamination. The superwicking materials produced by femtosecond laser processing may find a wide range of applications in chromatography, nano/microfluidics, optofluidics, cooling devices, lab-on-chips, biomedicine, biochemical sensors, and fluid microreactors.

References

1. Barthlott, W., Neinhuis, C.: Purity of the sacred lotus, or escape from contamination in biological surfaces. Planta **202**(1), 1–8 (1997)
2. Otten, A., Herminghaus, S.: How plants keep dry: a physicist's point of view. Langmuir **20**(6), 2405–2408 (2004)
3. Gu, Z.Z., Uetsuka, H., Takahashi, K., Nakajima, R., Onishi, H., Fujishima, A., Sato, O.: Structural color and the lotus effect. Angew. Chem. Int. Ed. **42**(8), 894–897 (2003)
4. Wenzel, R.N.: Resistance of solid surfaces to wetting by water. Ind. Eng. Chem. **28**(8), 988–994 (1936)
5. Cassie A.B.D., Baxter S.: Wettability of porous surfaces. Trans. Faraday Soc. **40**, 546–551 (1944)
6. Bico, J., Tordeux, C., Quere, D.: Rough wetting. Europhys. Lett. **55**(2), 214–220 (2001)
7. McHale, G., Shirtcliffe, N.J., Aqil, S., Perry, C.C., Newton, M.I.: Topography driven spreading. Phys. Rev. Lett. **93**(3), 036102 (2004)
8. Courbin, L., Deniel, E., Dressaire, E., Roper, M., Ajdari, A., Stone, H.A.: Imbibition by polygonal spreading on microdecorated surfaces. Nat. Mater. **6**, 661–664 (2007)
9. Martines, E., Seunarine, K., Morgan, H., Gadegaard, N., Wilkinson, C.D.W., Riehle, M.O.: Superhydrophobicity and superhydrophilicity of regular nanopatterns. Nano Lett. **5**(10), 2097–2103 (2005)
10. Wang, Q., Zhang, B.W., Qu, M.N., Zhang, J.Y., He, D.Y.: Fabrication of superhydrophobic surfaces on engineering material surfaces with stearic acid. Appl. Surf. Sci. **254**(7), 2009–2012 (2008)
11. Woodward, I., Schofield, W.C.E., Roucoules, V., Badyal, J.P.S.: Super-hydrophobic surfaces produced by plasma fluorination of polybutadiene films. Langmuir. **19**(8), 3432–3438 (2003)
12. Baldacchini, T., Carey, J.E., Zhou, M., Mazur, E.: Superhydrophobic surfaces prepared by microstructuring of silicon using a femtosecond laser. Langmuir. **22**(11), 4917–4919 (2006)
13. Zorba, V., Persano, L., Pisignano, D., Athanassiou, A., Stratakis, E., Cingolani, R., Tzanetakis, P., Fotakis, C.: Making silicon hydrophobic: wettability control by two-lengthscale simultaneous patterning with femtosecond laser irradiation. Nanotechnology. **17**(13), 3234–3238 (2006)
14. Fadeeva, E., Schlie, S., Koch, J., Chichkov, B.N., Vorobyev, A.Y., Guo, C.: Femtosecond laser-induced surface structures on platinum and their effects on hydrophobicity and fibroblast cell proliferation. In: Mittal, K.L. (ed.) Contact Angle, Wettability And Adhesion, vol. 6, pp. 163–171. VSP/Brill, Leiden (2009)
15. Kietzig, A.M., Hatzikiriakos, S.G., Englezos, P.: Patterned superhydrophobic metallic surfaces. Langmuir. **25**(8) 4821–4827 (2009)
16. Vorobyev, A.Y., Guo, C.: Metal pumps liquid uphill. Appl. Phys. Lett. **94**(22), 224102 (2009).
17. Kruse, C., Anderson, T., Wilson, C., Zuhlke, C., Alexander, D., Gogos, G., Ndao, S.: Extraordinary shifts of the Leidenfrost temperature from multiscale micro/nanostructured surfaces. Langmuir. **29**(31), 9798–9806 (2013)
18. Papadopoulou, E.L., Barberoglou, M., Zorba, V., Manousaki, A., Pagkozidis, A., Stratakis, E., Fotakis, C.: Reversible photoinduced transition of hierarchical ZnO structures. J. Phys. Chem. C **113**(7), 2891–2895 (2009)
19. Stratakis, E., Ranella, A., Fotakis, C.: Biomimetic micro/nanostructured functional surfaces for microfluidic and tissue engineering applications. Biomicrofluidics. **5**(1), 013411 (2011)
20. Wang, Z.K., Zheng, H.Y., Lim, C. P., Lam, Y.C.: Polymer hydrophilicity and hydrophobicity induced by femtosecond laser direct irradiation. Appl. Phys. Lett. **95**(11), 111110 (2009)

21. Yoon, T.O., Shin, H.J., Jeoung, S.C., Park, Y. I.: Formation of superhydrophobic poly(dimethysiloxane) by ultrafast laser-induced surface modification. Opt. Express. **16**(17), 12715–12725 (2008)
22. Pazokian, H., Selimis, A., Barzin, J., Jelvani, S., Mollabashi, M., Fotakis, C., Stratakis, E.: Tailoring the wetting properties of polymers from highly hydrophilic to superhydrophobic using UV laser pulses. J. Micrimech. Microeng. **22**(3), 035001 (2012)
23. Vorobyev, A.Y., Guo, C.: Laser turns silicon superwicking. Opt. Express. **18**(7), 6455–6460 (2010)
24. Vorobyev, A.Y., Guo, C.: Superwicking glass produced by femtosecond laser. J. Appl. Phys. **108**, 123512 (2010)
25. Raphael, E.: Capillary rise of a wetting fluid in a semi-circular groove. J. Phys. France. **50**(4), 485–491 (1989)
26. Batchelor, G.K.: An introduction to fluid dynamics. Cambridge University Press (1967)
27. Vorobyev, A.Y., Guo, C.: Enhanced absorptance of gold following multi-pulse femtosecond laser ablation. Phys. Rev. B **72**(19), 195422 (2005)
28. Vorobyev, A.Y., Guo, C.: Femtosecond laser nanostructuring of metals. Opt. Express. **14**(6) 2164–2169 (2006)
29. Vorobyev, A.Y., Guo, C.: Femtosecond laser structuring of titanium implants. Appl. Surf. Sci. **253**(17), 7272–7280 (2007)
30. Zhakhovskii, V.V., Inogamov, N. A., Nishihara, K.: New mechanism of the formation of the nanorelief on a surface irradiated by a femtosecond laser pulse. JETP Lett. **87**(8), 423–427 (2008)
31. Zavestovskaya, I.N., Kanavin, A.P., Men'kova, N.A.: Crystallization of metals under conditions of superfast cooling when materials are processed with ultrashort laser pulses. J. Opt. Technol. **75**(6), 353–358 (2008)
32. Stratakis, E., Zorba, V., Barberoglou, M., Fotakis, C., Shafeev, G.: Laser writing of nanostructures on bulk Al via its ablation in liquids. Nanotechnology. **20**(10), 105303 (2009)
33. Barmina, E.V., Barberoglu, M., Zorba, V., Simakin, A.V., Stratakis, E., Fotakis, C., Shafeev, G.A.: Surface nanotexturing of tantalum by laser ablation in water. Quantum Electron. **39**(1), 89–93 (2009)
34. Barmina, E.V., Stratakis, E., Fotakis, C., Shafeev, G.A.: Generation of nanostructures on metals by laser ablation in liquids: new results. Quantum Electron. **40**(11), 1012–1020 (2010)
35. Oliveira, V., Ausset, S., Vilar, R.: Surface micro/nanostructuring of titanium under stationary and non-stationary femtosecond laser irradiation. Appl. Surf. Sci. **255**(17), 7556–7560 (2009)
36. Demaske, B.J., Zhakhovsky, V.V., Inogamov, N.A., Oleynik, I.I.: Ablation and spallation of gold films irradiated by ultrashort laser pulses. Phys. Rev. B. **82**(6), 064113 (2010)
37. Li, X., Yuan, C., Yang, H., Li, J., Huang, W., Tang, D., Xu, Q.: Morphology and composition on Al surface irradiated by femtosecond laser pulses. Appl. Surf. Sci. **256**(13), 4344–4349 (2010)
38. Dai, Y., He, M., Bian, H., Lu, B., Yan, X., Ma, G.: Femtosecond laser nanostructuring of silver film. Appl. Phys. A. **106**(3), 567–574 (2012)
39. Zuhlke, C.A., Alexander, D.R., Bruce III, J.C., Ianno, N.J., Kamler, C.A., Yang, W.: Self-assembled nanoparticle aggregates from line focused femtosecond laser ablation. Opt. Express. **18**(5), 4329–4339 (2010)
40. Nayak, B.K., Gupta, M.C.: Self-organized micro/nano structures in metal surfaces by ultrafast laser irradiation. Opt. Lasers Eng. **48**(10), 940–949 (2010)
41. Hwang, T. Y., Vorobyev, A. Y., Guo, C.: Ultrafast dynamics of femtosecond laser-induced nanostructure formation on metals. Appl. Phys. Lett. **95**(12), 123111 (2009)
42. Sivakumar, M., Venkatakrishnan, K., Tan, B.: Characterization of MHz pulse repetition rate femtosecond laser-irradiated gold-coated silicon surfaces. Nanoscale Res. Lett. **6**(1), 78 (2011)
43. Vorobyev, A.Y., Guo, C.: Direct femtosecond laser surface nano/microstructuring and its applications. Laser Photonics Rev. **7**(3) 385–407 (2013)
44. Psaltis, D., Quake, S.R., Yang, C.: Developing optofluidic technology through the fusion of microfluidics and optics. Nature. **442**, 381–386 (2006)

45. Monat, C., Domachuk, P., Eggleton, B. J.: Integrated optofluidics: a new river of light. Nat. Photonics. **1**, 106–114 (2007)
46. Tokeshi, M., Minagawa, T., Uchiyama, K., Hibara, A., Sato, K., Hisamoto, H., Kitamori, T.: Continuous-flow chemical processing on a microchip by combining microunit operations and a multiphase flow network. Anal. Chem. **74**(7), 1565–1571 (2002)
47. Gattass, R.R., Mazur, E.: Femtosecond laser micromachining in transparent materials. Nature Photonics. **2**, 219–225 (2008)
48. Washburn, E.W.: The dynamics of capillary flow. Phys Rev. **17**(3), 273–283 (1921)
49. Romero, L.A., Yost, F.G.: Flow in an open channel capillary. J. Fluid Mech. **322**, 109–129 (1996)
50. Rye, R.R., Mann, J.A., Yost, F.G.: The flow of liquids in surface grooves. Langmuir. **12**(2), 555–565 (1996)
51. Khare, K., Herminghaus, S., Baret, J.-C., Law, B. M., Brinkmann, M., Seemann, R.: Switching liquid morphologies on linear grooves. Langmuir. **23**(26), 12997–13006 (2007)
52. Baret, J.-C., Decre, M.M.J., Herminghaus, S., Seemann, R.: Transport dynamics in open microfluidic grooves. Langmuir. **23**(9), 5200–5204 (2007)
53. Hay, K.M., Dragila, M.I., Liburdy, J.: Theoretical model for the wetting of a rough surface. J. Colloid Inteface Sci. **325**(2), 472–477 (2008)
54. Mai, T.T., Lai, C.Q., Zheng, H., Balasubramanian, K., Leong, K.C., Lee, P.S., Lee, C., Choi, W.K.: Dynamics of wicking in silicon nanopillars fabricated with interference lithography and metal-assisted chemical etching. Langmuir. **28**(31), 11465–11471 (2012)
55. Bico, J., Thiele, U., Quere, D.: Wetting of textured surfaces. Coll. Surf. A: Physicochem. Eng. Aspects. **206**(1–3), 41–46 (2002)
56. Vorobyev, A.Y., Guo, C. Laser makes silicon superwicking. Optics & Photonics News. December, p. 38. (2010). Video at http://www.opnmagazine-digital.com/opn/201012/?pg=40#pg40
57. Vorobyev, A.Y., Guo, C.: Making human enamel and dentin surfaces superwetting for enhanced adhesion. Appl. Phys. Lett. **99**(20), 031146 (2011)
58. Zhou, M., Yu, J., Li, J., Wu, B., Zhang, W.: Wetting induced fluid spread on structured surfaces at micro scale. Appl. Surf. Sci. **258**(19) 7596–7600 (2012)
59. Tuckerman, D.B., Pease, R.F.W.: High performance heat sinking for VLSI. IEEE Electron Device Lett. **2**(5), 126–129 (1981)
60. Stroock, A.D., Dertinger, S.K.W., Ajdari, A., Mezic, I., Stone, H.A., Whitesides, G.M.: Chaotic mixer for microchannels. Science. **295**(5555), 647–651 (2002)
61. Johnson, T.J., Ross, D., Locascio, L.E.: Rapid microfluidic mixing. Anal. Chem. **74**(1), 45–51 (2002)
62. Melin, J., Roxhed, N., Gimenez, G., Griss, P., van der Wijngaart, W., Stemme, G.: A liquid-triggered liquid microvalve for on-chip flow control. Sens. Actuators. B. **100**(3), 463–468 (2004)
63. Zimmermann, M., Hunziker, P., Delamarche, E.: Valves for autonomous capillary systems. Microfluid. Nanofluid. **5**(3). 395–402 (2008)
64. Brody, J.P., Yager, P.: Diffusion-based extraction in a microfabricated device. Sens. Actuators A. **58**(1). 13–18 (1997)
65. Zimmermann, M., Schmid, H., Hunziker, P., Delamarche, E.: Capillary pumps for autonomous capillary systems. Lab Chip. **7**, 119–125 (2007)
66. Juncker, D., Schmid, H., Drechsler, U., Wolf, H., Wolf, M., Michel, B., de Rooij, N., Delamarche, E.: Autonomous microfluidic capillary system. Anal. Chem. **74**(24), 6139–6144 (2002)
67. Drelich, J., Chibowski, E.: Superhydrophilic and superwetting surfaces: definition and mechanisms of control. Langmuir. **26**(24), 18621–18623 (2010)

Chapter 8
Optical Processors as Conceptual Tools for Designing Nonconventional Devices

Jorge Ojeda-Castañeda, Sergio Ledesma, Emmanuel Yépez-Vidal, Cristina M. Gómez-Sarabia and Miguel Torres-Cisneros

Abstract We discuss the use of nonconventional optical processors for generating irradiance distributions, which are useful for visualizing the characteristics of imaging devices that extend the depth of field. Our discussion starts with the use of binary masks for generating nonconventional irradiance distributions, which display the variations of the impulse response with focus errors. By using an anamorphic optical processor these irradiance distributions can easily be transformed into variations of the optical transfer function vs focus errors. Next, another anamorphic optical processor is used for generating the ambiguity function of a pupil aperture, which helps to visualize the variations of the optical transfer function with variable focus error. Finally, we translate the integral transform associated with the evaluation of the ambiguity function into tunable devices for controlling the depth of field, without modifying the size of the pupil aperture.

8.1 Introduction

In image science, the word apodization is used for describing a large set of techniques for shaping the Point Spread Function (PSF) of an optical system. However, the word apodization [1–6] was coined in optical spectroscopy for describing the use of tapered 1-D pupil masks that reduce diffraction bands, or optical side lobes, on the PSF. It was recognized that this type of tapering masks also expand the width of the PSF, while reducing the presence of the side lobes. These two previous features are useful for extending the axial PSF of a 2-D, radially symmetric optical systems [7–9]. For this type of applications, it is convenient to recognize that the normalized version of the axial PSF expresses the Strehl ratio vs focus error [10].

J. Ojeda-Castañeda (✉) · S. Ledesma · E. Y.-Vidal · M. T.-Cisneros
Electronics Department, Engineering Division, Campus Salamanca, University of Guanajuato, Guanajuato, Mexico
e-mail: jojedacas@ugto.mx

C. M. Gomez-Sarabia
Digital Arts Department, Engineering Division, Campus Salamanca,
University of Guanajuato, Guanajuato, Mexico

Of course, one can extend the depth of field of an imaging device, simply by closing down the pupil aperture or by using annular pupil apertures. However, these solutions reduce the resolution as well as the light gathering power of the optical system. Hence, there is an optical engineering endeavor that aims to reduce the influence of focus errors on the optical transfer function (OTF), without substantially reducing either the resolution or the light gathering power of an optical system [11–14].

In Sect. 8.2, we discuss the use of binary masks that have unit transmittance only along a very narrow slit, which follows suitable paths for generating optical path differences [15–18].

In Sect. 8.3, we show that a display of the ambiguity function [19–23] is rather useful diagram for visualizing the impact of focus error on the OTF. The ambiguity function of the pupil aperture exhibits (in a single picture) the influence of focus error on the OTF. Furthermore, the ambiguity function helps to expand the defocused OTF as a Taylor series expansion in terms of the focus error coefficient. Half of the terms of the Taylor series can be reduced to zero if the complex amplitude transmittance of the pupil aperture is a hermitian function. Hence, one needs to explore the use of masks whose amplitude variations are described by even functions, while the phase variations are described by odd functions [24].

By using a suitable mask one can obtain an OTF that does not have zero values inside the passband, and the OTF varies slowly with focus errors. Thus, one can preserve the spatial frequency content of several planar images, which are located at different depths. These images are recorded with virtually the same amount of contrast reduction. Consequently, one can use the same digital filter for restoring the contrast of all recorded images [25].

The present technology allows producing nonconventional masks, with complex amplitude transmittance. Furthermore, there several fast digital algorithms for improving the quality of an image. Hence, nowadays one can use both nonconventional devices with complex amplitude transmittance, as well as fast digital algorithms for extending the depth of field [26–31].

In Sect. 8.4, we show that the schematics of an optical processor are useful for gaining physical insights, on the design of tunable devices for controlling the depth of field. To this end, we translate the integral transform associated with the evaluation of the ambiguity function into tunable devices for controlling the depth of field, without modifying the pupil aperture. These types of devices are here denoted as Alvarez-Lohmann lenses. In Sect. 8.5, we summarize our contribution.

8.2 Visualizing a PSF with High Depth of Focus

We start by writing Helmholtz differential equation that describes the propagation of a 2-D scalar wave $\varphi(x, z)$. That is,

$$[\partial_x^2 + \partial_z^2 + k^2]\varphi(x, z) = 0. \tag{8.1}$$

In Eq. (8.1) the wave number is denoted as $k = 2\pi/\lambda$. It is easy to verify that its formal solution is

$$\varphi(x, z) = \exp\left[ikz\sqrt{k^{-2}\partial_x^2 + 1}\right]\varphi(x, 0). \tag{8.2}$$

The exponential operator in Eq. (8.2) is to be used as a power series expansion of the differential operator ∂_x^2. See for example references from 32 to 34. One can relate the formal solution in Eq. (8.2) to the angular spectrum of planes waves, by assuming that the initial condition $\varphi(x, z = 0)$ can be expressed as the inverse Fourier transform of the plane wave spectrum $\Phi(\mu)$. That is,

$$\varphi(x, 0) = \int_{-\infty}^{\infty} \Phi(\mu)\exp(i2\pi x\mu)d\mu \tag{8.3}$$

In Eq. (8.3) we use the Greek letter μ for denoting the spatial frequency along the horizontal axis, which is of course related to direction cosine along the horizontal axis α as follows, $\mu = \alpha/\lambda$. If one applies the exponential operator in Eq. (8.2) to the inverse Fourier transform in Eq. (8.3) one obtains

$$\exp\left[ikz\sqrt{k^{-2}\partial_x^2 + 1}\right]\varphi(x, 0)$$

$$= \int_{-\infty}^{\infty} \Phi(\mu)\exp[ikz\sqrt{1 - \lambda^2\mu^2}]\exp(i2\pi x\mu)\, d\mu. \tag{8.4}$$

As one should expect. The result in Eq. (8.4) can be usefully rewritten in the following manner. As is depicted in Fig. 8.1, let us assume that that in a classical optical processor the input is a pinhole size source, which is represented by the mathematical expression

$$u_0(x, z) = \delta(x)\delta(z). \tag{8.5}$$

As is depicted in Fig. 8.1, at the Fraunhofer plane with spatial frequency variables (μ, ζ), we place a mask with complex amplitude transmittance
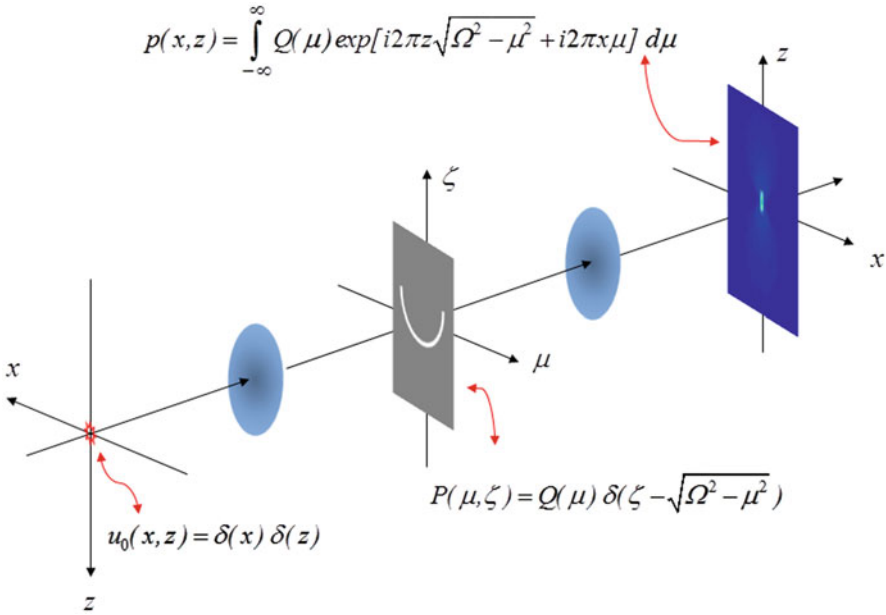
$$P(\mu, \zeta) = Q(\mu)\delta(\zeta - \sqrt{\Omega^2 - \mu^2}). \tag{8.6}$$

At this stage, we set $Q(\mu) = \text{rect}(\mu/2\Omega)$ where the Greek letter Ω denotes the cut-off value of the spatial frequency μ. The second term in Eq. (8.6) describes a very narrow slit that follows the curve $\zeta = \sqrt{(\Omega^2 - \mu^2)}$. The amplitude impulse response of the coherent optical processor is

$$p(x, z) = \int_{-\infty}^{\infty}\int_{-\infty}^{\infty} P(\mu, \zeta)\exp[i2\pi(x\mu + z\zeta)]d\mu d\zeta \tag{8.7a}$$

Or equivalently, by using Eq. (8.6), one can write Eq. (8.7a) as

$$p(x, z) = \int_{-\infty}^{\infty} Q(\mu)\exp[i2\pi(x\mu + z\sqrt{\Omega^2 - \mu^2})]d\mu \tag{8.7b}$$

$$p(x,z) = \int_{-\infty}^{\infty} Q(\mu)\exp[i2\pi z\sqrt{\Omega^2-\mu^2}+i2\pi x\mu]\,d\mu$$

$$P(\mu,\zeta) = Q(\mu)\,\delta(\zeta-\sqrt{\Omega^2-\mu^2})$$

$$u_0(x,z) = \delta(x)\,\delta(z)$$

Fig. 8.1 Schematic diagram of an optical processor using a pupil mask in the form of narrow slit

By a simple comparison, between Eqs. (8.4) and (8.7b), it is apparent that the optical processor is able to display, in a single 2-D picture, the propagation the scalar wave $\varphi(x, z)$; where $\Omega = \lambda^{-1}$.

One can generalize this remarkably simple result by selecting the complex amplitude distribution, at the Fraunhofer plane, as

$$Q(\mu) = \Phi(\mu)rect\left(\frac{\mu}{2\lambda^{-1}}\right). \tag{8.8}$$

We discuss next other useful examples. In the paraxial regime, the propagation of a 2-D wave scalar wave $\varphi(x, z)$ can be is described using the differential equation

$$\left[\partial_x^2 + i2k\partial_z\right]\phi(x,z) = 0 \tag{8.9}$$

It is straightforward to show that for this case, as depicted in Fig. 8.2, on needs a mask with complex amplitude transmittance

$$P(\mu,\zeta) = Q(\mu)\delta\left(\zeta+\frac{\mu^2}{2\Omega}\right); \tag{8.10}$$

where again $\Omega = \lambda^{-1}$. In Fig. 8.3 we show the irradiance distributions associated to the pictures describing the propagation of an initial point source, as predicted by Helmholtz equation; as well as the picture that portraits wave propagation within the paraxial approximation. It is interesting to note that the picture describing propagation in the paraxial regime (left hand side of Fig. 8.3) has a wider diverging angle
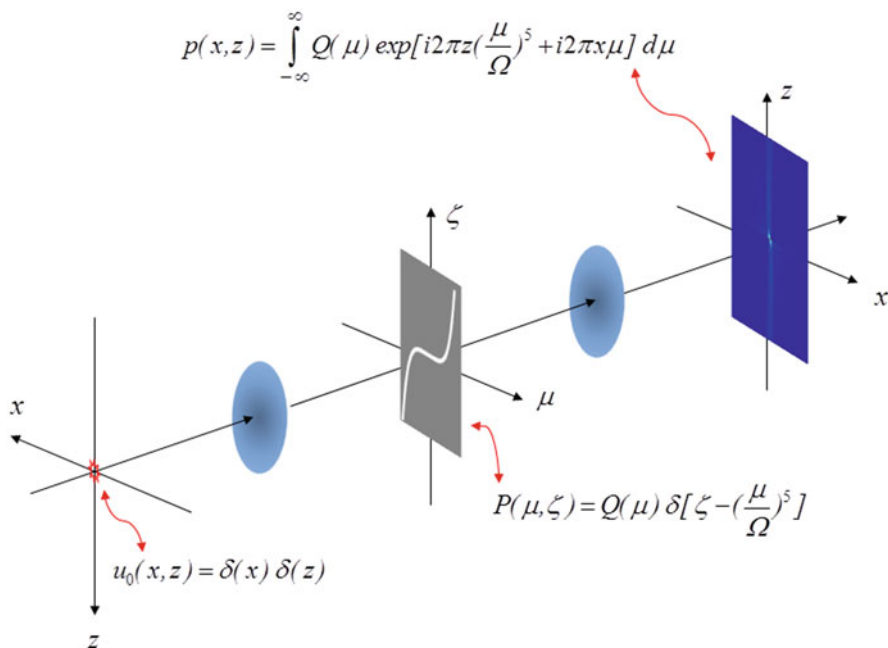
$$p(x,z) = \int_{-\infty}^{\infty} Q(\mu)\, exp(-i\pi\lambda z\mu^2 + i2\pi x\mu)\, d\mu$$

$$P(\mu,\zeta) = Q(\mu)\, \delta(\zeta + \frac{\lambda\mu^2}{2})$$

$$u_0(x,z) = \delta(x)\,\delta(z)$$
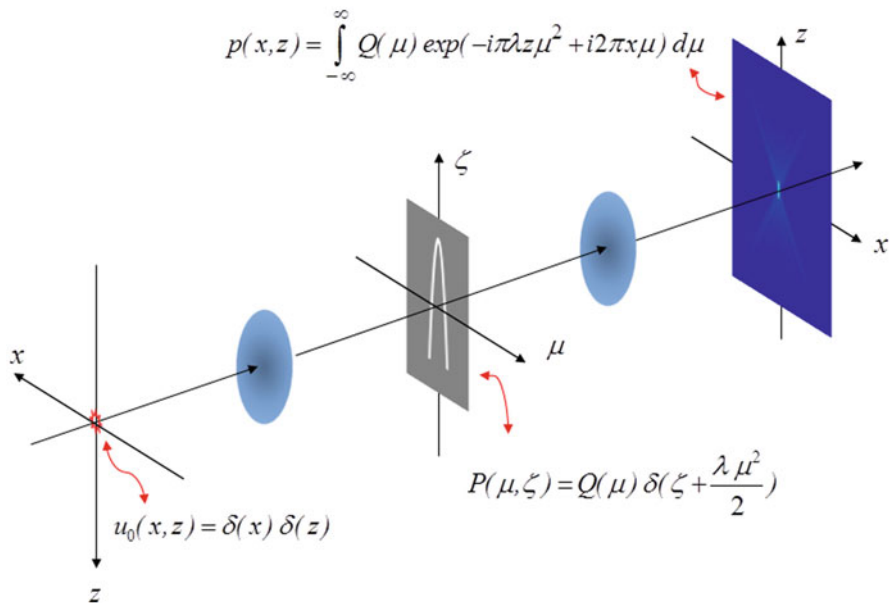
Fig. 8.2 Optical processor used for visualizing the propagation of a 2-D scalar wave, in the paraxial regime

$$\delta(\zeta - \sqrt{\Omega^2 - \mu^2})$$

$$\delta(\zeta + \frac{\lambda\,\mu^2}{2})$$
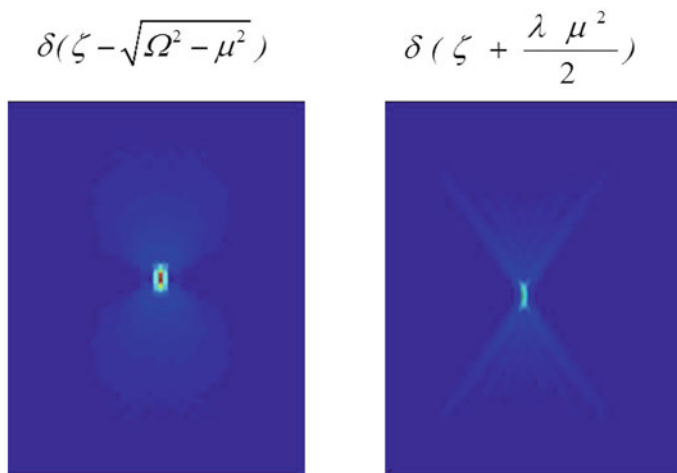
Fig. 8.3 Irradiance distributions displaying the impulse response at the (x, z) plane

than the picture describing propagation according to Helmholtz equation (right hand side of Fig. 8.3).

Next, we discuss an interesting variant of our previous results. As depicted in Fig. 8.4, let us assume that the mask has the following complex amplitude transmittance

$$p(x,z) = \int_{-\infty}^{\infty} Q(\mu)\, exp[i2\pi z(\frac{\mu}{\Omega})^5 + i2\pi x\mu]\, d\mu$$

$$u_0(x,z) = \delta(x)\,\delta(z)$$

$$P(\mu,\zeta) = Q(\mu)\,\delta[\zeta - (\frac{\mu}{\Omega})^5]$$

Fig. 8.4 Optical processor using a pupil mask in the form of narrow slit, which follows a fifth power curve

$$P(\mu, \zeta) = Q(\mu)\delta\left[\zeta - \sigma\left(\frac{\mu}{\Omega}\right)^5\right]. \tag{8.11}$$

At the output plane of the coherent optical processor, the complex amplitude distribution is

$$p(x,\, z) = \int_{-\infty}^{\infty} Q(\mu) exp\left\{i2\pi\left[x\mu + z\sigma\left(\frac{\mu}{\Omega}\right)^5\right]\right\}\, d\mu . \tag{8.12}$$

The complex amplitude distribution in Eqs. (8.11) and (8.12) have now the following interpretation.

At the Fraunhofer plane the curve $\zeta = (\mu/\Omega)^5$ represents a phase profile to the fifth power. Hence, now at the output plane, the z-axis denotes the maximum value of the optical path difference, which is reached at the edge ($\mu = \pm\Omega$) of the 1-D pupil aperture. Again the pupil aperture is described by the function $rect(\mu/2\Omega)$. Consequently, in this later example, the variable ζ is a dimensionless variable. Its Fourier transform pair is the dimensionless variable

$$z = (N - 1)\frac{t}{\lambda} \tag{8.13}$$

Table 8.1 Possible curve for the narrow slit in the Fraunhofer plane. The displays that are described along the third column are obtained using the optical processor in Fig. 8.1. And the displays along the third column are obtained using the optical processor in Fig. 8.6.

Describing	Binary Mask	Display 1	Display 2
Nonparaxial propagation	$P(\mu,\zeta) = Q(\mu)\delta(\zeta - \sqrt{\Omega^2 - \mu^2})$	PSF along the Z-axis	MTF along the Z-axis
Paraxial propagation	$P(\mu,\zeta) = Q(\mu)\delta\left(\zeta + \frac{\mu^2}{2\Omega}\right)$	PSF along the Z-axis	MTF along the Z-axis
Asymmetric quadratic phase mask	$P(\mu,\zeta) = Q(\mu)\delta\left[\zeta - \text{sgn}(\mu)\left(\frac{\mu}{\Omega}\right)^2\right]$	PSF vs OPD	MTF vs OPD
Cubic phase mask	$P(\mu,\zeta) = Q(\mu)\delta\left[\zeta - \left(\frac{\mu}{\Omega}\right)^3\right]$	PSF vs OPD	MTF vs OPD
Fractional wavefront	$P(\mu,\zeta) = Q(\mu)\delta\left[\zeta - \text{sgn}(\mu)\left|\frac{\mu}{\Omega}\right|^{3.75}\right]$	PSF vs OPD	MTF vs OPD
High order phase mask	$P(\mu,\zeta) = Q(\mu)\delta\left[\zeta - \left(\frac{\mu}{\Omega}\right)^5\right]$	PSF vs OPD	MTF vs OPD

Hence, as is indicated in Eq. (8.13), the Latin letter z describes the variation of optical path difference of an optical element. We denote with the letter N the refractive index, and we assume that the optical element is surrounded by air, an d that it has a physical thickness t.

A similar interpretation can be applied to other narrow slits that follow other curves in the Fraunhofer domain, namely

$$P(\mu,\zeta) = Q(\mu)\delta\left[\zeta - \sigma\left|\frac{\mu}{\Omega}\right|^m\right]. \tag{8.14}$$

In Eq. (8.14) the Latin letter m is a real number that the indicates power of the monomial μ/Ω. At the output plane of the coherent optical processor, in Fig. 8.3, the complex amplitude distribution displays the changes of the coherent impulse response in terms of the position variable x, as well as in terms of the dimensionless variable z, which represents the variations of optical path difference caused by a refractive optical element; as is indicated in Eq. (8.13).
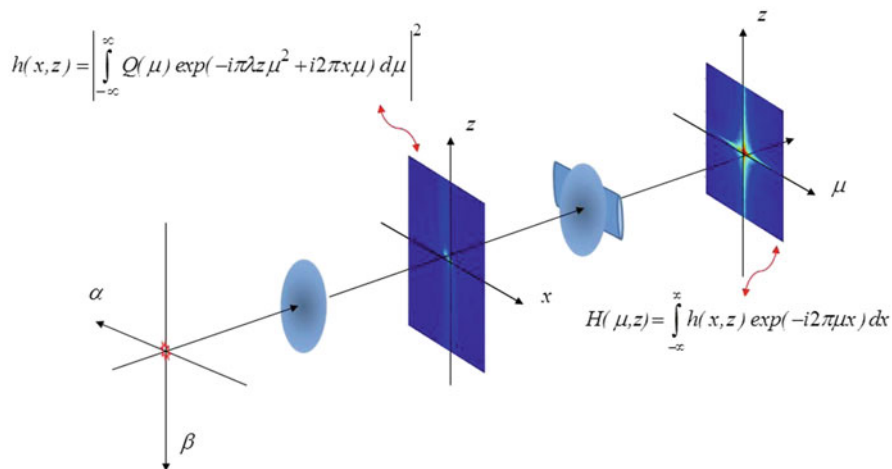
In Table 8.1 we summarize other possible options when selecting the curve that the narrow slit must follow in the Fraunhofer domain. It is to be noted by using this procedure one can visualize the impact of optical path difference on the behavior of the impulse response for rather unconventional phase delays; as indicated in Fig. 8.5. From this latter figure, it is apparent the unique behavior of the phase mask with fractional power phase profile. Otherwise, we note that the selected phase masks generate asymmetric irradiance distributions, which spread out as the optical path difference increases.

In Fig. 8.6, we show the schematics of an anamorphic optical processor. Now, for the new optical processor, the input is the irradiance distribution that is obtained at the output plane of the previous optical processor. As is apparent from the schematic

$$\delta[\,\zeta - sgn(\mu)(\frac{\mu}{\Omega})^2\,] \quad \delta[\,\zeta - (\frac{\mu}{\Omega})^3\,] \quad \delta[\,\zeta - sgn(\mu)\left|\frac{\mu}{\Omega}\right|^{3.75}\,] \quad \delta[\,\zeta - (\frac{\mu}{\Omega})^5\,]$$
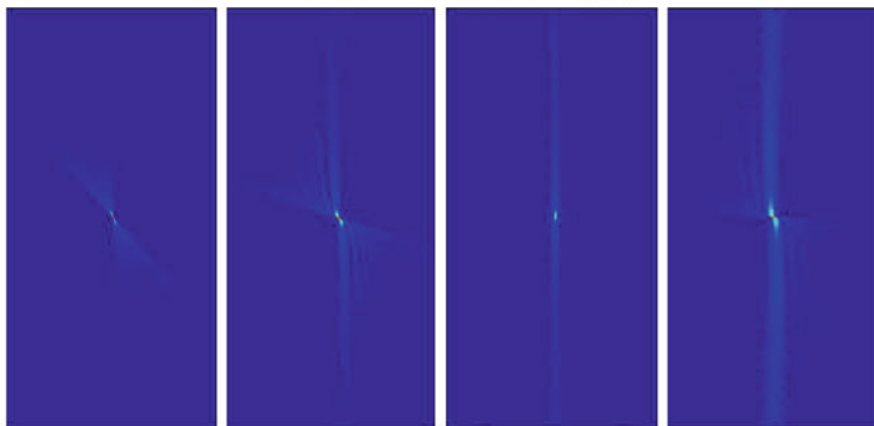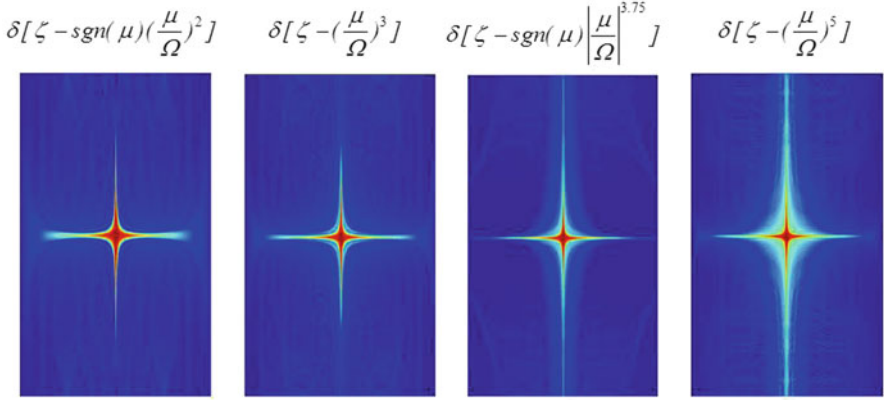

Fig. 8.5 Impulse response as a function of the position and of the optical path difference of several nonconventional optical elements

$$h(x,z) = \left| \int_{-\infty}^{\infty} Q(\mu)\, exp(-i\pi\lambda z\mu^2 + i2\pi x\mu)\, d\mu \right|^2$$

$$H(\mu,z) = \int_{-\infty}^{\infty} h(x,z)\, exp(-i2\pi\mu x)\, dx$$

Fig. 8.6 Anamorphic optical processor for displaying (as irradiance variations) the OTF's of several optical elements

diagram in Fig. 8.6, the new anamorphic optical processor implements an imaging operation, with magnification equals to unity, along the vertical axis while it implements a Fourier transformation along the horizontal axis. That is, at the output plane of the new optical processor, the complex amplitude distribution is

$$\delta[\zeta - sgn(\mu)(\tfrac{\mu}{\Omega})^2] \qquad \delta[\zeta - (\tfrac{\mu}{\Omega})^3] \qquad \delta[\zeta - sgn(\mu)\left|\tfrac{\mu}{\Omega}\right|^{3.75}] \qquad \delta[\zeta - (\tfrac{\mu}{\Omega})^5]$$

Fig. 8.7 Variations of the MTF as a function of the spatial frequency μ (*horizontal* axis) as well as a function of the optical path difference (*vertical* axis) for four different phase profiles

$$H(\mu, z) = \int_{-\infty}^{\infty} \int_{-\infty}^{\infty} |p(x, z')|^2 exp(-i2\pi\mu x)\delta(z - z')dx dz'$$

$$= \int_{-\infty}^{\infty} |p(x, z)|^2 exp(-i2\pi\mu x)dx. \qquad (8.15)$$

The result in Eq. (8.15) indicates the following. At the output plane of the anamorphic optical processor in Fig. 8.6, one can obtain optically a complex amplitude distribution that is proportional to the Optical Transfer Function (OTF) as a function of both the spatial frequency μ and the axial distance z.

Of course, when visualizing the OTF one uses a square law detector for obtaining the square modulus of the OTF. Hence, the irradiance distribution at the output is the square value of the Modulation Transfer Function (MTF).

In Fig. 8.7 we show the display of the MTF's that are obtained when using, respectively, the curve $\zeta = sgn(\mu)(\mu/\Omega)^2$, as well as the curves that are described along the lines 3, 4 and 5 in Table 8.1. It is apparent from Fig. 8.7 that as the optical path difference increases, the MTF's tend to spread out. However, the MTF's exhibit spurious oscillations. It is clear from Fig. 8.7 that again the phase mask with phase profile with fractional power (m = 3.75) has reduced spurious oscillations. In the following section, while we describe another method for visualizing the impact of focus error on the MTF, we discuss an optical technique that strongly reduces the spurious oscillations on the MTF.

Several years ago, some of us established a link between the OTF suffering from focus errors and the ambiguity function of the pupil aperture [23]. Later on, the ambiguity function was applied as a mathematical tool for proposing optical masks that reduce the impact of focus error on the OTF [35].

$$P(\mu,\nu) = Q(\mu)\,exp[i\,2\pi W(\tfrac{\mu}{\Omega})^2\,]\,rect(\tfrac{\mu}{2\Omega})$$

$$Q(\nu)\,exp[i\,2\pi W(\tfrac{\nu}{\Omega})^2\,]\,rect(\tfrac{\nu}{2\Omega})$$

$$p(x,y;W) = \int\limits_{-\infty}^{\infty}\int\limits_{-\infty}^{\infty} P(\mu,\nu)\,exp[i2\pi(x\mu+y\nu)\,d\mu\,d\nu$$
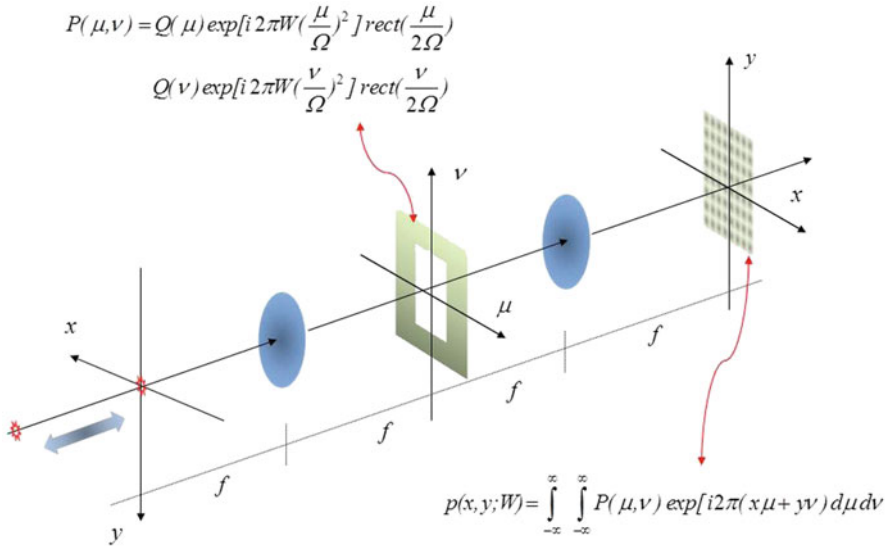
Fig. 8.8 Schematics of an optical processor that is used for analyzing out-of-focus imagery

8.3   Visualizing the MTF with Extended Depth of Field

Here, for the sake of completeness of our presentation, we discuss briefly the out-of-focus image formation process when using a classical optical processor; as is depicted in Fig. 8.8. For further details please see reference [36]. In what follows we consider that the square law is located at fixed position, at the output plane, while the pinhole size source moves along the optical axis of the optical processor. Consequently, the geometrical image of point source is located before or after the detector plane. From the viewpoint of wave aberration, within the paraxial regime, one can represent the location of the point source along the optical axis, by using the following generalized pupil function

$$P(\mu; W_{2,0}) = Q(\mu)exp\left\{i2\pi\left(\frac{W_{2,0}}{\lambda}\right)\left(\frac{\mu}{\Omega}\right)^2\right\}. \qquad (8.16)$$

In Eq. (8.16) we denote as $Q(\mu)$ the complex amplitude transmittance of the pupil mask; and the letter $W_{2,0}$ denotes the wavefront focus error coefficient. The Greek letter Ω denotes the cut-off spatial frequency of the rectangular pupil aperture.

For simplifying the notation it is convenient to employ the dimensionless parameter

$$W = \frac{W_{2,0}}{\lambda} \qquad (8.17)$$
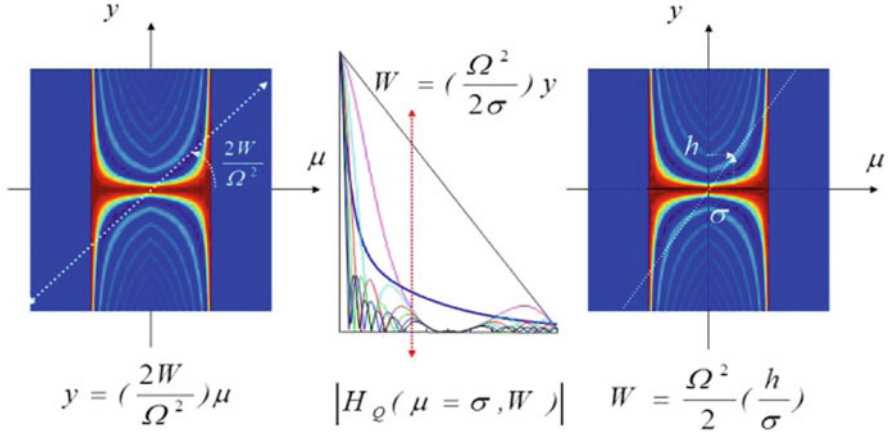
Fig. 8.9 Scanning lines along the ambiguity function for obtaining the values of the out-of-focus MTF

As is well known, the OTF of Eq. (8.16) is

$$H_Q(\mu; W) = N_{orma} \int_{-\infty}^{\infty} P\left(v + \frac{\mu}{2}\right) P^*\left(v - \frac{\mu}{2}\right) dv$$

$$H_Q(\mu; W) = N_{orma} \int_{-\infty}^{\infty} Q\left(v + \frac{\mu}{2}\right) Q^*\left(v - \frac{\mu}{2}\right) exp\left[i2\pi\left(\frac{2W\mu}{\Omega^2}\right)v\right] dv.$$

(8.18)

In Eq. (8.18) the upper case letter N_{orma} denotes a suitable normalization factor. On the other hand, the ambiguity function of the pupil mask, $Q(\mu)$, is

$$A_Q(\mu, y) = N_{orma} \int_{-\infty}^{\infty} Q\left(v + \frac{\mu}{2}\right) Q^*\left(v - \frac{\mu}{2}\right) exp\left[i2\pi yv\right] dv.$$

(8.19)

From a simple comparison between Eqs. (8.18) and (8.19), we note that

$$y = \left(\frac{2W}{\Omega^2}\right)\mu.$$

(8.20)

If in the display of the ambiguity function (as that at the left hand-side of Fig. 8.9) one traces a straight-line, crossing the origin; the slope is proportional to the amount of focus error; as indicated in Eq. (8.20). If one selects a value of the spatial frequency, say $\mu = \sigma$, then the variations of the OTF for variable focus errors can be visualized by moving up or down along a vertical line; as depicted at the centre of Fig. 8.9. Furthermore, for a given position along the vertical line, say $y = h$, the focus error coefficient is $W = (\Omega^2/2) (h/\sigma)$.

Next, we recognize that for displaying the ambiguity function, one can use the anamorphic processor in Fig. 8.10. See for example reference [36]. In Fig. 8.10, we
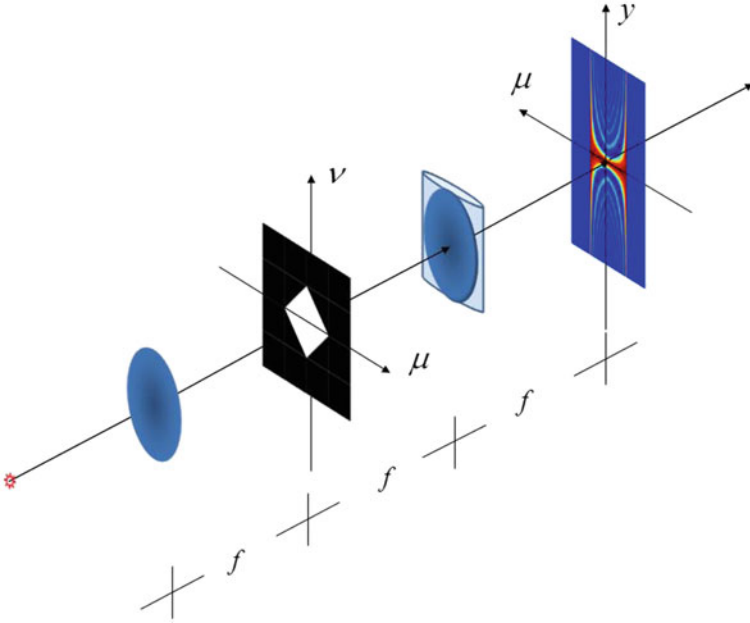
Fig. 8.10 Anamorphic optical processor that is used for visualizing the Ambiguity function

indicate that the input for the anamorphic processor is the *Product Spectrum*, which is

$$P_Q(\mu, v) = Q\left(v + \frac{\mu}{2}\right) Q^*\left(v - \frac{\mu}{2}\right). \tag{8.21}$$

For a clear pupil aperture, $Q(\mu) = \text{rect}(\mu/2\Omega)$ then the Product Spectrum is

$$P(\mu, v) = \text{rect}\left(\frac{\mu}{4\Omega}\right) \text{rect}\left(\frac{v}{2\Omega - |\mu|}\right). \tag{8.22}$$

We note that the anamorphic processor, in Fig. 8.10, performs an imaging operation, with unit magnification, along the horizontal axis. From Fig. 8.10 and Eq. (8.22) the following considerations are apparent. Inside the passband, $|\mu| \leq 2\Omega$, a vertical line along the product spectrum is bounded by the function *rect* $[v/(2\Omega - |\mu|)]$.

Hence, at the output plane of the optical processor, along the vertical axis one has the Fraunhofer diffraction pattern of a rectangular window. Thus, at the output plane of the optical processor, the complex amplitude distribution is

$$A_Q(\mu, y) = \left(1 - \frac{|\mu|}{2\Omega}\right) \text{sin} c\left[\left(1 - \frac{|\mu|}{2\Omega}\right) y\right] \tag{8.23}$$

In other words, the ambiguity function is composed by a series of sinc functions with variable half-width. Consequently, the out-of-focus OTF exhibits a large number of
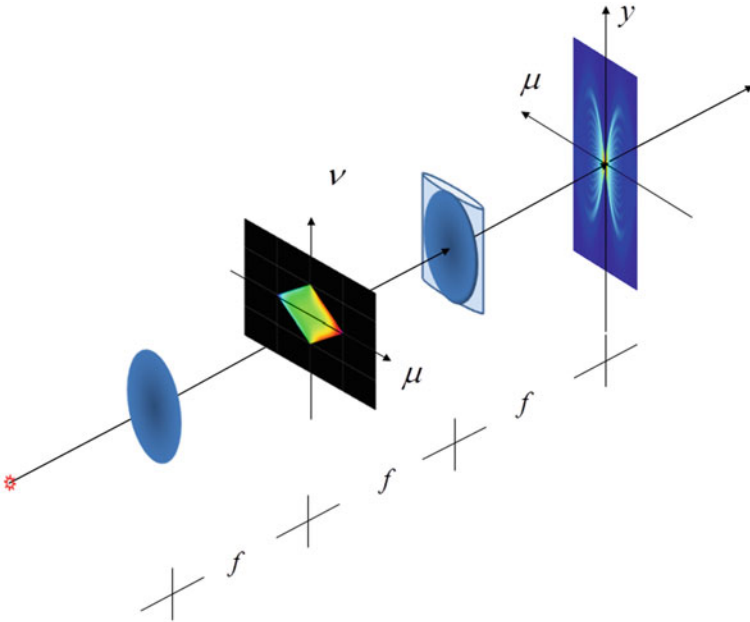
Fig. 8.11 Use of phase-only masks for obtaining ambiguity functions with "Bow-Tie" effect

zero crossings. If one wants to modify this result, then one needs to consider another possible ambiguity functions. For example, if at the **Product spectrum** we have a vertical line that has a quadratic phase factor,

$$P(\mu, v) = exp \left[i2\pi a(\frac{v}{\Omega})^2 \right] rect \left[\frac{v}{2\Omega - |\mu|} \right] rect \left[\frac{\mu}{4\Omega} \right]. \qquad (8.24)$$

For obtaining this type of **Product Spectrum**, one needs a cubic phase mask, as proposed by Dowski and Cathey. If, as depicted in Fig. 8.11, now we take the complex amplitude transmittance along a vertical line vertical axis, and we evaluate the Fourier transform of Eq. (8.24), we obtain

$$A_Q(\mu, y) = rect \left(\frac{\mu}{4\Omega} \right)$$

$$\int_{-\frac{(2\Omega - |\mu|)}{2}}^{\frac{(2\Omega - |\mu|)}{2}} exp \left\{ i2\pi \left[a\left(\frac{\mu}{\Omega}\right)^2 + yv \right] \right\} dv. \qquad (8.25)$$

It is apparent from Eq. (8.25) that along the y-axis, the ambiguity function results from the lateral superposition of Fresnel diffraction patterns of rectangular windows, which have variable width. See Fig. 8.11.

Since any vertical line is a Fresnel diffraction pattern, then the ambiguity function spreads all over the (μ, y) plane. This behaviour is known as the "bow-tie effect".

See reference [37]. As a consequence, the OTF's have low sensitivity to focus errors. Of course, one can extrapolate this previous result, by exploring the use of high order aberration polynomials. That is,

$$Q(\mu) = exp\left\{i2\pi a\left(\frac{\mu}{\Omega}\right)^{2m+1}\right\} rect\left(\frac{\mu}{2\Omega}\right). \qquad (8.26)$$

One can guess that the phase mask described in Eq. (8.26) will be able to spread the ambiguity function along the vertical axis; as is depicted in Fig. 8.11. Consequently, one expects that this type of masks will be able to extend the depth of field. However, it is relevant to note that these types of high order phase masks (including the cubic phase mask) introduce spurious oscillations. For reducing this undesirable feature, one can use a Gaussian apodizer on the pupil aperture; as part of the spatial filter. In other words, now the complex amplitude transmittance of the pupil aperture is

$$Q(\mu) = exp\left\{i2\pi a\left(\frac{\mu}{\Omega}\right)^{2m+1} - c\left(\frac{\mu}{\Omega}\right)^2\right\} rect\left(\frac{\mu}{2\Omega}\right). \qquad (8.27)$$

In Eq. (8.27) the lower case letter "c" denotes a damping factor, in the amplitude variations, which are described by a Gaussian profile. See reference [38].

At the top of Fig. 8.12, we show the MTF of a cubic phase mask for W = 0 and for W = 3. One can note that there are spurious oscillations. At the bottom of Fig. 8.12, we show the MTF that is obtained if one use the complex amplitude transmittance in Eq. (8.27) for m = 1. From the results at the bottom of Fig. 8.12, it is apparent that a Gaussian apodizer is able to reduce unwanted oscillations in the MTF; without spoiling the low sensitivity of the MTF to focus errors.

The tapering mask with Gaussian profile has the following additional advantages, which are illustrated in Fig. 8.13. First, by using a Gaussian apodizer the 2-D rectangular pupil aperture is transformed into a nearly circularly symmetric aperture; as is indicated along the first column of Fig. 8.13.

Furthermore, the Gaussian apodizer reduces the diffraction lobes in the asymmetric PSF; as depicted along the second column of Fig. 8.13. We note also that the Gaussian apodizer broadens the MTF, as shown along the third column of Fig. 8.13. The above results can also be visualized in terms of the product spectrum and the ambiguity function; as we depict next.

Along the first column in Fig. 8.14, we show the influence that a Gaussian mask has on the product spectrum. Along the second column, first line, in Fig. 8.14 we display zero-phase variations inside the support of the product spectrum. Along the second column, line two, of Fig. 8.14 we show as colour variations the profile of a 2-D cubic phase mask. And along the second column, line three, in Fig. 8.14 we show the phase delays of a 2-D cubic phase mask.

From the third column in Fig. 8.14 the following characteristics are apparent. Along the first line and third column of Fig. 8.14, we have that the modulus of the ambiguity function has several regions with zero values. Then as depicted in the second line and third column of Fig. 8.14, if one uses a cubic phase masks the modulus of the ambiguity function has extended regions with nonzero values. However, the
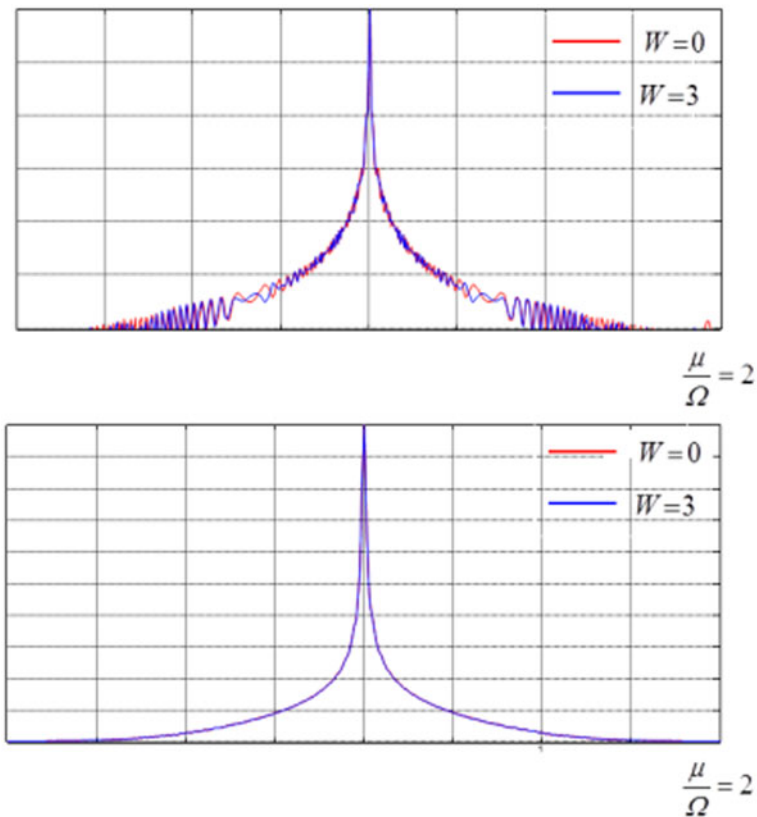
Fig. 8.12 Use of a Gaussian mask for reducing the spurious oscillations on the in-focus MTF and out-of-focus MTF

nonzero values have spurious oscillations. Finally, as shown in the second line and third column of Fig. 8.14, if one uses a Gaussian mask together with a cubic phase masks one can reduce the spurious oscillations on the regions with nonzero values.

For obtaining the numerical simulations in Fig. 8.14, which are described by Eq. (8.27), we select the values $a = 33$, $n = 1$ and $c = 0.44$. These results are generalized in reference [39], where we use the following definition for hyper Gaussian masks. In what follows we consider that the complex amplitude transmittance of the pupil aperture is

$$Q(\mu) = exp\left\{i2\pi\, sgn\,(\mu)\left|\frac{\mu}{\Omega}\right|^{m}\right\}$$

$$exp\left\{-c\left|\frac{\mu}{\Omega}\right|^{n}\right\} rect\left(\frac{\mu}{2\Omega}\right) \tag{8.28}$$

In Eq. (8.28) the letters m and n denote real positive numbers. Since the values of m are no longer integer numbers, then the first term in Eq. (8.28) represents a fractional
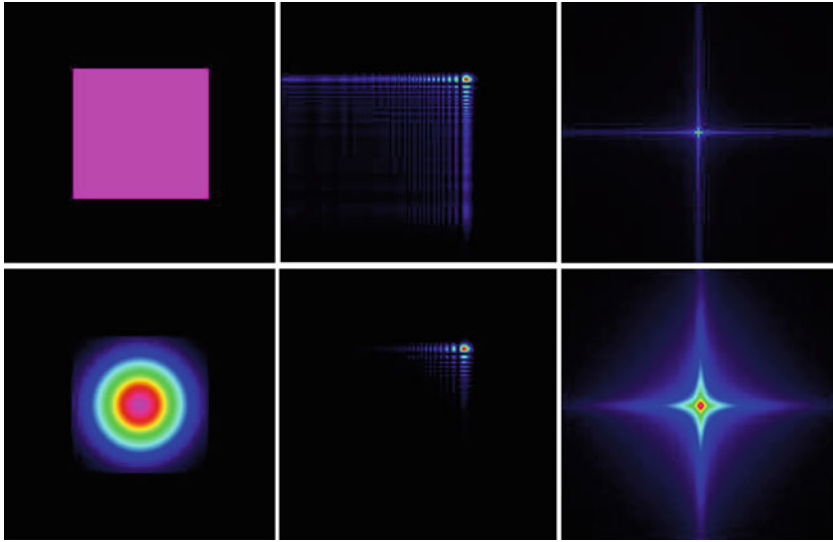
Fig. 8.13 Influence of Gaussian tapering on the pupil aperture, the PSF and the MTF
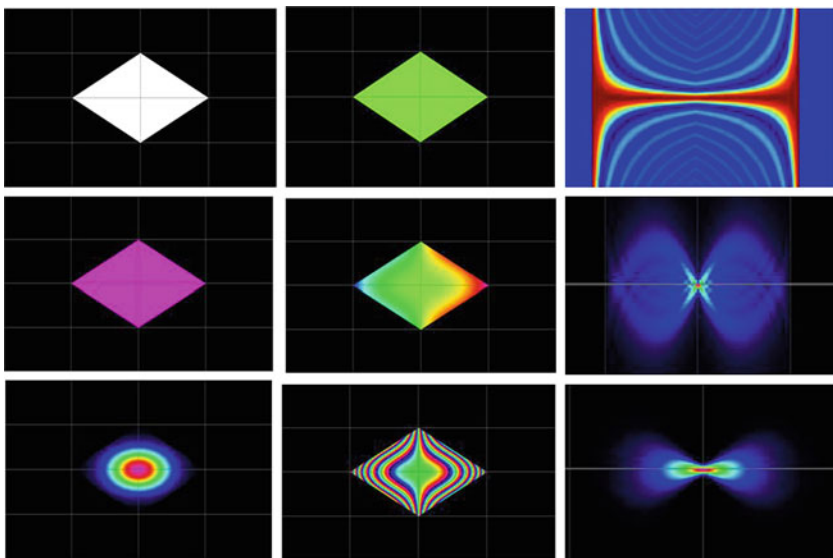
Fig. 8.14 The impact of a Gaussian apodizer on product spectrum, and the resultant ambiguity function

order wavefront. Due to the factor sgn(μ), denoting the signum function, the wavefront has phase delays that are odd functions. Furthermore, regarding the second term in Eq. (8.28), for values of n such that $n < 2$ the amplitude transmittance is denoted as sub Gaussian function; for $n = 2$, the amplitude transmittance is represented by a

Gaussian function; while for $n > 2$, the amplitude transmittance is denoted as super Gaussian function. We employ the generic word hyper Gaussian for encompassing the cases under exploration with $0 < n < 10$.

For our numerical simulations we use the following definitions that apply for the 1-D case. For variable values of focus error, the normalized irradiance distribution of the impulse response is

$$|q(x; W)|^2 = \left| \int_{-\infty}^{\infty} Q(\mu) exp \left[i2\pi \left(W \left(\frac{\mu}{\Omega} \right)^2 + x\mu \right) \right] rect \left(\frac{\mu}{2\Omega} \right) d\mu \right|^2. \quad (8.29)$$

And of course, the MTF is

$$|H(\mu; W)| = \int_{-\infty}^{\infty} |q(x; W)|^2 exp(-i2\pi \mu x) dx. \quad (8.30)$$

We evaluate numerically Eqs. (8.29) and (8.30) using the fast Fourier transform (FFT) algorithm described in reference [40]. We use 1024 points and a set of Graphic User Interface (GUI) elements. The numerical process is written in C++ language. Our numerical search starts by considering the values that were identified in the previous section. Then, we modify the parameters "a" and "c" in Eq. (8.28) until the variations of the MTF have a mean square error that is less than 10^{-4}.

Once that the 1-D sub Gaussian masks were identified, $Q(\mu)$ in Eq. (8.28), the complex amplitude transmittance of the 2-D masks are obtained as the product $Q(\mu)$ $Q(\nu)$. After extensive numerical evaluations, we identify the following interesting result.

Inside the range $0 \le W \le 3$, one can obtain a MTF that varies slowly with focus error, by using a fractional wavefront $m = 2.75$ that has a maximum optical path difference value $a = 27$, together with a sub Gaussian mask $n = 1.75$ and attenuation factor $c = 1.61$.

In Fig. 8.15, along the second column, we plot the 1-D profiles. And along the third column, we show the following 2-D displays. In the first line, we place a pseudo color picture of the 2-D amplitude transmittance variations. In the second line, we place an interferogram of the 2-D phase variations. In the third line and the fourth line, we use pseudo color pictures for displaying the 2-D variations of the PSF and the MTF, respectively.

Finally, we note that these optical characteristics preserve the resolution associated with a full aperture. However, these results come at the expense of reducing the light gathering power by a factor slightly greater than two.

8.4   Tunable Devices for Extending the Depth of Field

According to Plummer, Baker and van Tassel [41], Kitajima was the first person that proposed to implement suggested variable optical power lenses, by using a pair of cubic phase masks [42]. Years later, Lohmann [43–45] and Alvarez [46, 47] re-discovered independently and simultaneously Kitajima's technique .
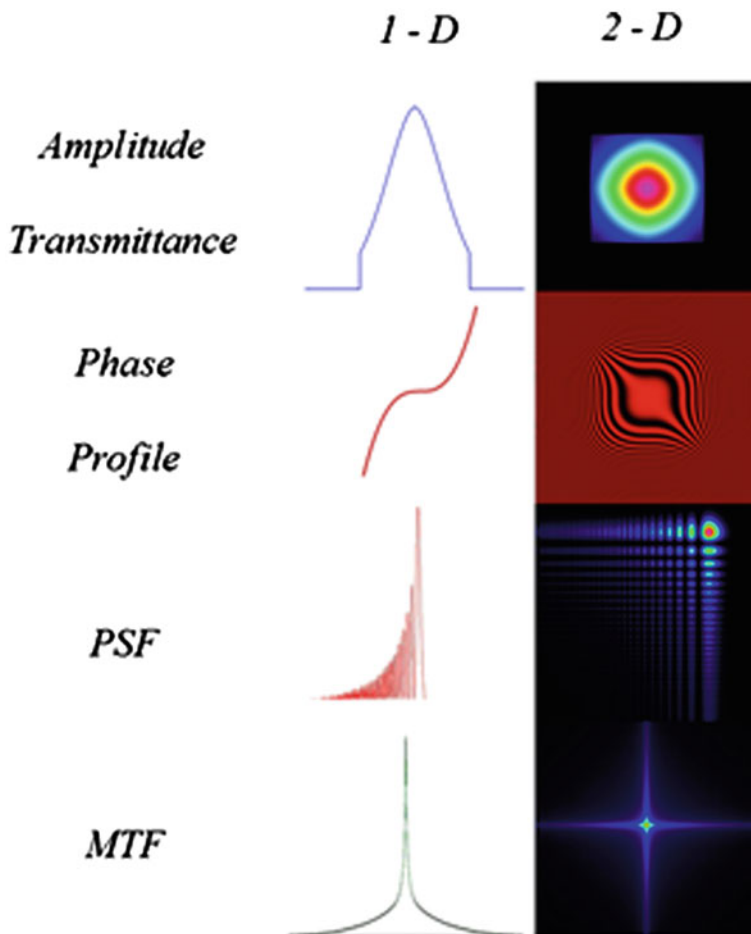
Fig. 8.15 Resultant PSF and resultant MTF associated to the hyper Gaussian apodizer in Eq. (8.28)

In what follows, our aim is threefold. First, we indicate that Kitajima's technique, commonly known as Alvarez-Lohmann lenses, is also useful for implementing tunable absorption masks, which are useful for setting hyper Gaussian apodizers with tunable half-width. Second, we show that by using two suitable helical refractive elements, one can control the optical path difference of radial focalizers. And third, we discuss the use of a pair of helical distributed amplitude masks for tuning the damping coefficient of Gaussian-like windows.

For achieving our first goal, we note that Alvarez and Lohmann lenses employ two phase masks that form a pair. The amplitude transmittance of a single mask is the complex conjugate of the other mask. Then, by introducing a lateral displacement between the two masks, say by the spatial frequency σ, one sets a varifocal lens. In mathematical terms, for the 1-D case, a single element of the pair has the following complex amplitude transmittance

$$Q(v) = exp\left\{i2\pi a\left(\frac{v}{\Omega}\right)^3\right\}. \tag{8.31}$$

In Eq. (8.31) the lower case letter "a" denotes the optical path difference in units of the wavelength λ. Next, it is convenient to use two elements. Each element has the complex amplitude transmittance in Eq. (8.31). However when setting the pair, one element is the complex conjugate of the other. Then, one introduces a lateral displacement between the elements of the pair. In this manner, the overall complex amplitude transmittance is

$$P_Q(v;\sigma) = Q\left(v + \frac{\sigma}{2}\right) Q^*\left(v - \frac{\sigma}{2}\right)$$
$$= exp\left\{i\left(\frac{a\pi}{2}\right)\left(\frac{\sigma}{\Omega}\right)^3 + i2\pi\left(\frac{a\sigma}{\Omega}\right)\left(\frac{v}{\Omega}\right)^2\right\}. \tag{8.32}$$

In Eq. (8.32) the quadratic variation, in the variable v, is similar to the amplitude transmittance of a lens. However, it is important to recognize that by changing σ, one can tune the power of a lens.

Moreover, we recognize that the physical procedure for obtaining the result in Eq. (8.32) is similar to the mathematical operation that is involved when evaluating the OTF in Eq. (8.18). Hence, we claim the following.

By visualizing the amplitude PSF of the pair in Eq. (8.32), one visualizes the ambiguity function of a single element of the pair, as in Eq. (8.18). That is,

$$p_Q(x;\sigma) = N_{orma}\int_{-\infty}^{\infty} P_Q(v,\sigma)exp\left[i2\pi xv\right]dv = A_Q(\sigma,x). \tag{8.33}$$

Now, we have a physical method (the use of a pair of phase masks) for understanding the influence that a single element has on the behavior of the ambiguity function.

Furthermore, one can propose the use of a mask that has phase variations to the four-power for implementing a cubic phase mask, with controllable optical path difference.

For this application, we consider that the complex amplitude transmittance of a single element is

$$Q(v) = exp\left\{i2\pi a\left[\left(\frac{v}{\Omega}\right)^4 - \frac{1}{2}\left(\frac{v}{\Omega}\right)^2\right]\right\}. \tag{8.34}$$

As before, we employ a phase conjugated pair and we introduce a lateral displacement between the members of the pair. Then, we generate the following generalized pupil function

$$P_Q(v;\sigma) = Q\left(v + \frac{\sigma}{2}\right) Q^*\left(v - \frac{\sigma}{2}\right)$$
$$= exp\left\{i2\pi\left(\frac{4a\sigma}{\Omega}\right)\left(\frac{v}{\Omega}\right)^3\right\}$$
$$exp\left\{i2\pi\left(\frac{a\sigma}{\Omega}\right)\left[\left(\frac{\sigma}{\Omega}\right)^2 - 1\right]\left(\frac{v}{\Omega}\right)\right\}. \tag{8.35}$$

From Eq. (8.35) one notes that by changing the value of σ, one can change the optical path difference of a cubic phase mask. In other words, we can implement a varicubic phase masks. However, the proposed phase mask generates also a linear phase variation. The influence of this unwanted term can be reduced by properly selecting the values of the initial optical path difference and the maximum value of the lateral displacement. See for example [48–50].

For achieving our second goal, in this section, we describe the use of a pair of amplitude masks that help for setting a Gaussian spatial filter, with adjustable half-width [50]. We start our discussion, by considering the amplitude transmittance of the first amplitude element of the proposed pair

$$T_1(\mu) = exp\left\{-c\left[1 + \left(\frac{\mu}{\Omega}\right)^3\right]\right\} rect\left(\frac{\mu}{4\Omega}\right). \tag{8.36}$$

As before, in Eq. (8.36) we use a lower case letter "c" for denoting a dimensionless damping factor of the Gaussian function. From Eq. (8.36), we note that the length of the mask is 4Ω. At its edges the amplitude transmittance has real positive values. Now, the amplitude transmittance of the of the second mask is

$$T_2(\mu) = exp\left\{-c\left[1 - \left(\frac{\mu}{\Omega}\right)^3\right]\right\} rect\left(\frac{\mu}{4\Omega}\right). \tag{8.37}$$

Again the length of the mask is 4Ω, and at its edges the amplitude transmittance has real positive values. By introducing a lateral displacement, σ; between the masks, the overall amplitude transmittance inside the pupil aperture is

$$T(\mu; \sigma) = T_1\left(\mu + \frac{\sigma}{2}\right) T_2\left(\mu - \frac{\sigma}{2}\right). \tag{8.38}$$

If one substitutes Eqs. (8.36) and (8.37) in Eq. (8.38) one obtains

$$T(\mu; \sigma) = exp\left\{-2c\left[1 + \left(\frac{\sigma}{2\Omega}\right)^3\right]\right\}$$

$$exp\left\{-\left(\frac{3c\sigma}{4\Omega}\right)\left(\frac{\mu}{\Omega}\right)^2\right\} rect\left(\frac{\mu}{2\Omega}\right). \tag{8.39}$$

It is apparent from Eq. (8.39) that inside the pupil aperture, the overall amplitude transmittance varies as a Gaussian function. Its half-width can be modified by changing the lateral amount of displacement in the Fourier domain. In reference [51] we have extended the above result to 2-D.

Here it is relevant to note that if one uses simultaneously the tunable cubic phase mask and the tunable Gaussian amplitude mask, then one has two extra degrees of freedom for setting the pre-processing filter; as was discussed in the previous section. However, we also note that so far our tunable devices are only useful when the complex amplitude profiles can be expressed as monomials to an integer power. We discuss next an optical technique for overcoming this limitation.

After proposing his varifocal technique, Lohmann applied his result for generating tunable zone plates. Lohmann and Paris have proposed the use of helical modulations [52] for generating other types of varifocal zone plates. In their proposal, Lohmann and Paris suggested the use of an average angular operation for achieving tunable devices that have only radial variations.

Later on, Burch and Williams [53] used Lohmann's technique for implementing an alignment device, which has the interesting twist of incorporating and additional phase factor as proposed for Alvarez in his varifocal technique.

Bernet and coworkers have revisited the use of ***diffractive elements*** for implementing varifocal lenses using helical variations [54–56]. And rather recently, some of us, have suggested the use of two helical ***refractive elements*** for setting several varifocal devices [57, 58]. In what follows we revisited these latter proposals.

For achieving our final goal, in this section, we note that Bryngdahl analysed interferograms in terms of polar coordinates [59]. In Fig. 8.16 we show some schematic diagrams for describing the generation of interference patterns. The interferograms are generated by superimposing a plane reference wavefront with one of the following object beams. At the top of Fig. 8.16 the object beam has quadratic radial variations; while at the middle of Fig. 8.16 the object beam has linear helical variations (angular variations). At the bottom of Fig. 8.16 the object beam has both radial as well as helical variations.

For describing the optical devices of our interest, we consider the following complex amplitude transmittance

$$Q(\rho, \varphi) = exp\{iaR(\rho)\varphi\}. \tag{8.40}$$

In Eq. (8.40) we use the Greek letters ρ and φ for denoting the radial spatial frequency and the polar angle at the pupil aperture, respectively. The Latin letter a represents the optical path difference of the optical device. For making comparisons it is useful to remember that a lens, with fixed optical power, has the following complex amplitude transmittance

$$Q(\rho, \varphi) = exp\left\{ia\left(\frac{\rho}{\Omega}\right)^2\right\}. \tag{8.41}$$

In Eq. (8.41) the Greek letter Ω denotes the maximum value of the radial spatial frequency. This value is typically called the cut-off spatial frequency of the pupil aperture. The interferogram of the quadratic phase variation in Eq. (8.41) is a Fresnel zone plate; as is shown in the left-hand side of Fig. 8.17.

If the lens has also helical variations then the complex amplitude transmittance is

$$Q(\rho, \varphi) = exp\left\{ia\left(\frac{\rho}{\Omega}\right)^2\varphi\right\}. \tag{8.42}$$

At the right hand side of Fig. 8.17, we show the interference pattern that is generated between a plane wavefront and the complex amplitude transmittance in Eq. (8.42). At the left-hand side of Fig. 8.18, we show the phase variations in Eq. (8.42).
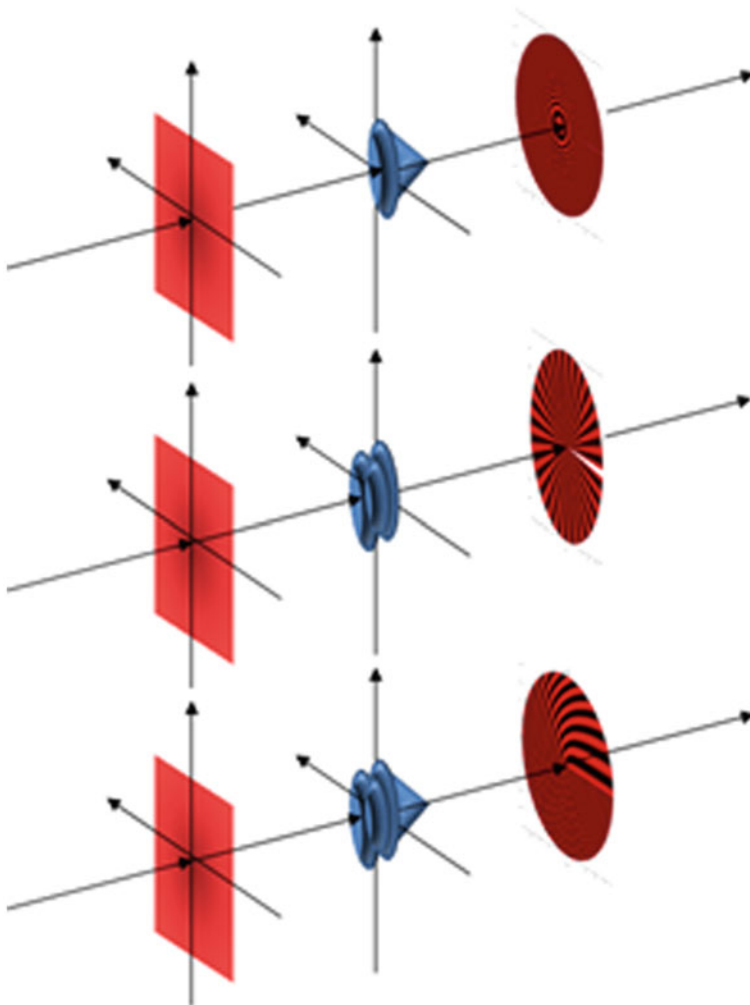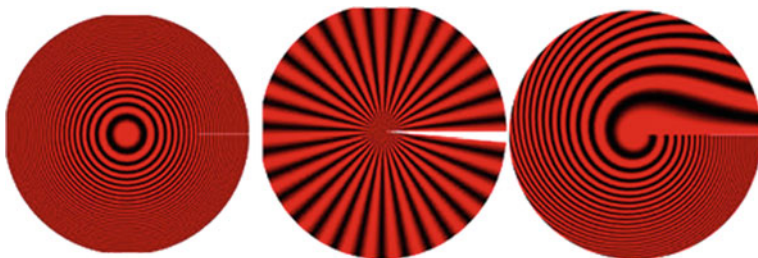
Fig. 8.16 Interferograms obtained as the interference between a reference plane wavefront and three different object beams: **a** radial beam, **b** helical beam, and **c** a beam having both radial and helical variations. The object beam is obtained after passing through the optical device

The interferogram, at the right-hand side of the same figure, was first discussed by Lohmann and Paris.

Next, we note that rather than introducing a lateral displacement between the elements of the pair (as depicted in at the left-hand side of Fig. 8.19) we can introduce an in-plane rotation between the elements of the pair (as depicted at the right-hand side of Fig. 8.19).

Fig. 8.17 Interference patterns that are obtained using a reference plane wavefront and three different object beams: radial beam, helical beam, and a beam having both radial and helical variations, respectively
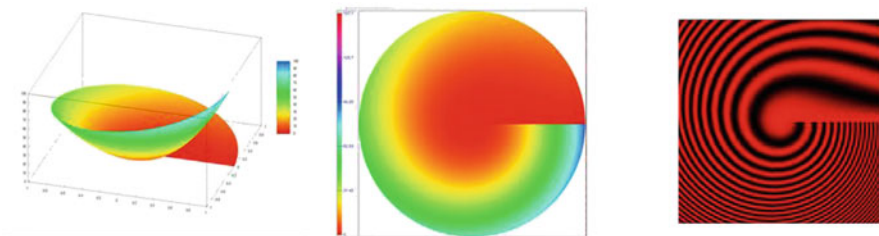
Fig. 8.18 Three different views of the helical phase in Eq. (8.41): 3-D curve, 2-D pseudo color variations and the interference pattern that is generated when using as reference beam a uniform plane wave
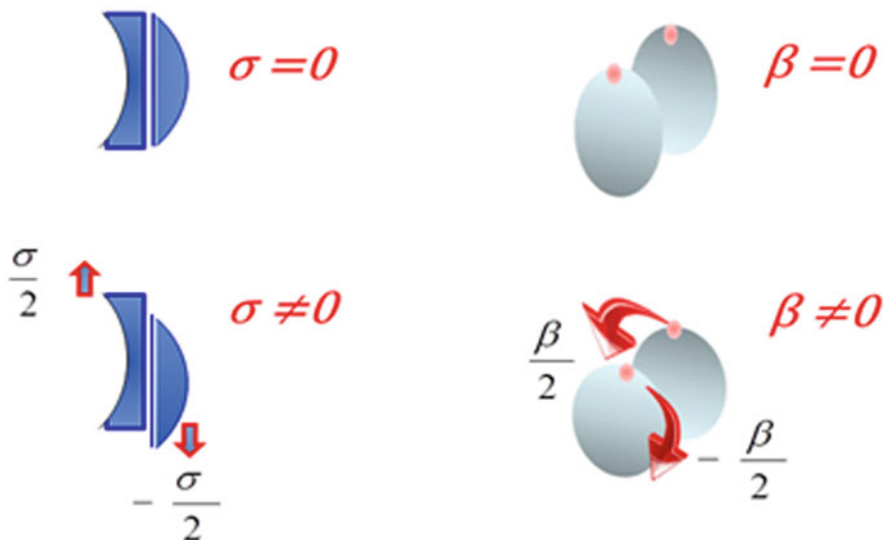
Fig. 8.19 Tunable devices using a controllable lateral shear, with spatial frequency σ, or a controllable in-plane rotation angle β

For this later application, we consider that the complex amplitude transmittance of the first refractive element is

$$T_1(\rho, \varphi) = exp\left\{i2\pi a\varphi\left(\frac{\rho}{\Omega}\right)^m\right\}.$$ (8.43)

In Eq. (8.42) the Latin letter m denotes the power of the radial variable. The complex amplitude transmittance of the second refractive element is the complex conjugate of the first element. That is,

$$T_2(\rho, \varphi) = exp\left\{-i2\pi a\varphi\left(\frac{\rho}{\Omega}\right)^m\right\}.$$ (8.44)

Now, if both refractive elements are used as a pair, and we introduce an in-plane rotation between the elements of the pair (say by an angle β) the overall complex amplitude transmittance is

$$T(\rho; \beta) = T_1\left(\rho, \varphi + \frac{\beta}{2}\right) T_2\left(\rho, \varphi - \frac{\beta}{2}\right)$$
$$= exp\left\{i2\pi a\beta\left(\frac{\rho}{\Omega}\right)^m\right\}.$$ (8.45)

It is apparent from Eq. (8.44) that the complex amplitude transmittance of the pair is independent of the helical variable φ. Furthermore, we recognize that the angle β modifies linearly the value of the optical path difference. And in this manner, one can exploit the angular variation for controlling the optical path difference of the radial focalizer.

In Fig. 8.20, we show the use of the tunable focalizer as spatial filters in an afocal, optical processor. It is convenient to note that the proposed optical technique, as expressed in Eq. (8.44), can be extended to wide range of radial variations. In mathematical terms,

$$T(\rho; \beta) = exp\left\{i2\pi a\left(\varphi + \frac{\beta}{2}\right) R(\rho)\right\}$$
$$exp\left\{-i2\pi a\left(\varphi - \frac{\beta}{2}\right) R(\rho)\right\}$$
$$= exp\{i2\pi a\beta R(\rho)\}.$$ (8.46)

Next we describe a method for optically tuning the half-width of hyper Gaussian apodizers; as is discussed in references [60, 61]. As depicted in Fig. 8.20, we consider that at the Fraunhofer plane we place two amplitude masks forming a pair. The amplitude transmittance of the first mask is

$$T_1(\rho, \varphi; n) = exp\left\{-\frac{1}{2}\left(\frac{\rho}{\Omega}\right)^n\left(1 + \frac{\varphi}{2\pi}\right)\right\} circ\left(\frac{\rho}{\Omega}\right).$$ (8.47)
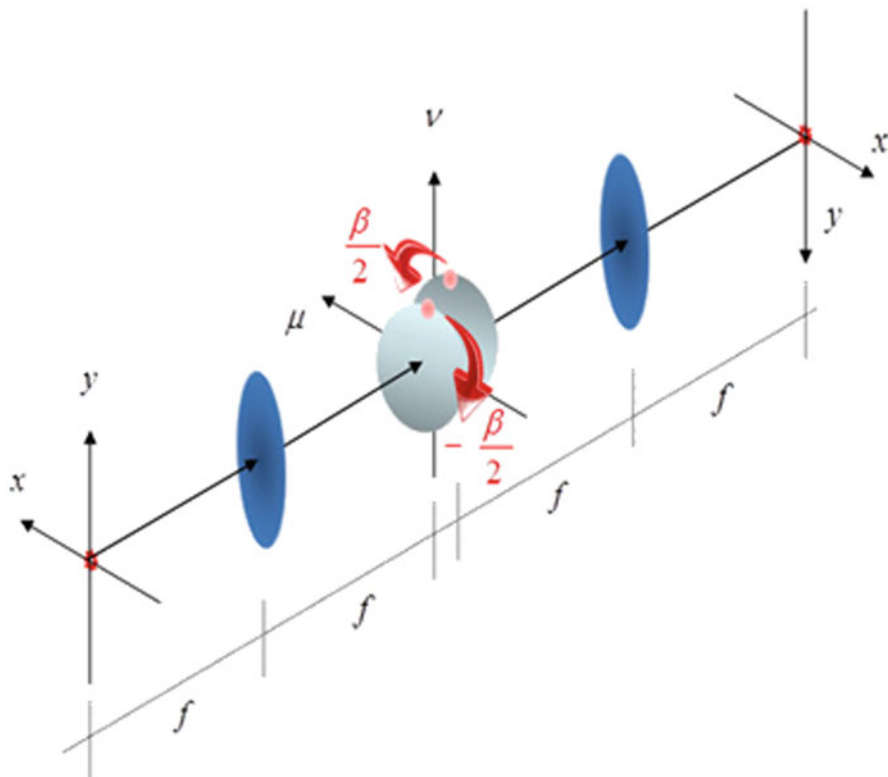
Fig. 8.20 Optical processor that employs a pair of helical masks at the Fraunhofer plane

In Eq. (8.47) the Greek letters ρ and φ denote again the polar coordinates in the pupil aperture. The maximum value of the polar coordinate, ρ, is the cut-off spatial frequency Ω. The circ function represents the pupil aperture, $0 \leq \rho \leq \Omega$. The Latin letter "n" denotes the power of the radial variable. The polar angle varies inside the interval $0 \leq \varphi < 2\pi$. We note that if $n = 2$, one has an amplitude transmittance that is proportional to a Gaussian function. A sub Gaussian mask is defined by a value of $n < 2$. And again if $n > 2$, one has super Gaussian masks. We denote as hyper Gaussian any amplitude transmittance within the range $0 < n < 10$. We recognize that the amplitude transmittance in Eq. (8.47) is bounded.

The amplitude transmittance of the second mask is

$$T_2(\rho, \varphi; n) = exp\left\{-\frac{1}{2}\left(\frac{\rho}{\Omega}\right)^n\left(1 - \frac{\varphi}{2\pi}\right)\right\} circ\left(\frac{\rho}{\Omega}\right). \tag{8.48}$$

Again we note that the amplitude transmittance in Eq. (8.48) is bounded. Next, we place in contact these two previously described masks for setting a pair. The overall complex amplitude transmittance becomes
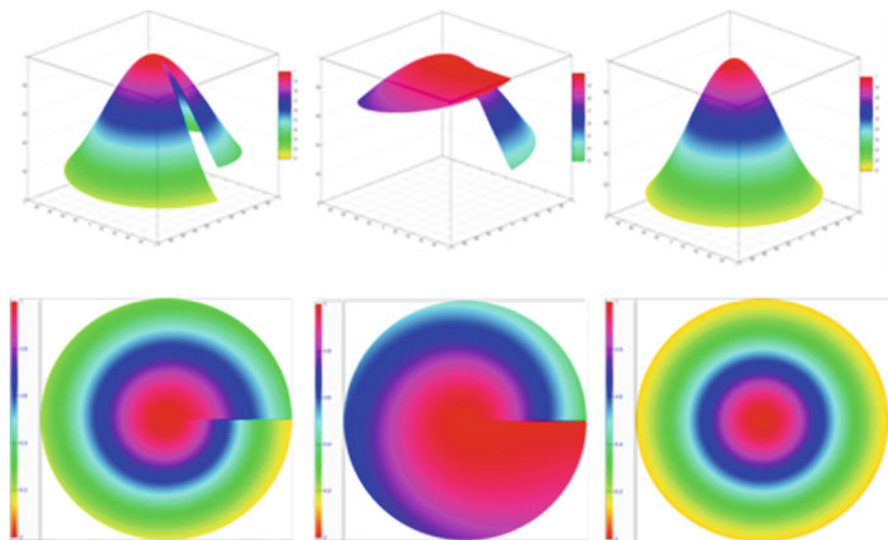
Fig. 8.21 Tuning the half-width of a Gaussian apodizer by the use of a pair of asymmetric masks that have helical amplitude variations

$$T(\rho; \beta) = T_1 \left(\rho, \varphi + \frac{\beta}{2} \right) T_2 \left(\rho, \varphi - \frac{\beta}{2} \right)$$

$$= exp \left\{ -\frac{\beta}{4\pi} R(\rho) \right\} circ \left(\frac{\rho}{\Omega} \right). \tag{8.49}$$

From Eq. (8.49) it is clear that the overall amplitude transmittance does not longer depend on the angular variable φ. That is, the overall amplitude transmittance has radial symmetry. Furthermore, the half-width of the radially symmetric, hyper Gaussian masks can be controlled by changing the rotation angle β. This general result is illustrated for the particular case of $n = 2$, in Fig. 8.21.

Along the first line, of Fig. 8.21, we show the 3-D amplitude distributions of the transmittances in Eqs. (8.47), (8.48) and (8.49) respectively. Along the second line, of Fig. 8.21, we show the amplitude variations as 2-D color encoded pictures. It is interesting to note that the product of the asymmetrical masks in the first and second columns, of Fig. 8.21, generates the symmetrical masks shown at the third column of Fig. 8.21.

Finally, we emphasize on the many possibilities of this procedure by using the illustrations in Fig. 8.22. Along the first line we display the 1-D amplitude profiles of a sub Gaussian mask, $n = 1.5$, a Gaussian mask, $n = 2$, and super Gaussian mask, $n = 8$. The amplitude variations of these amplitude masks are shown as 2-D pictures along the second line of Fig. 8.22. Along the third line, of the same figure, we display 3-D curves.
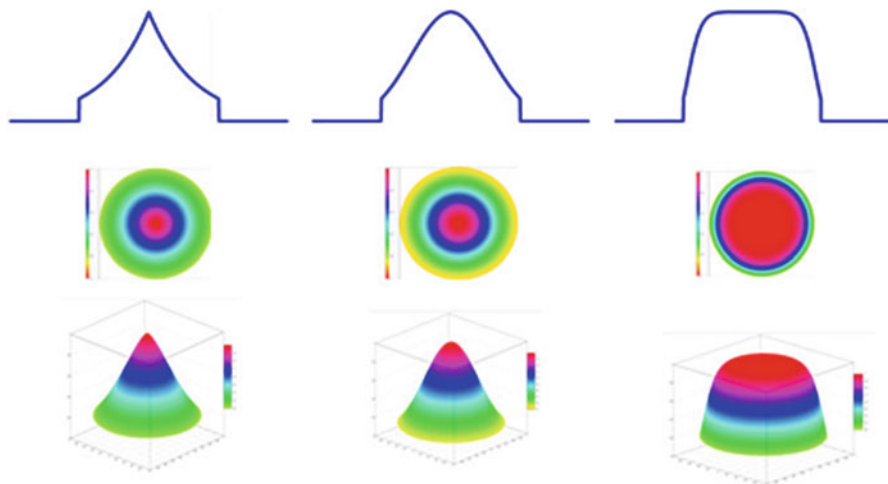
Fig. 8.22 Radially symmetric hyper Gaussian apodizer with tunable half-widths, which were generated by using a pair of masks that have helical amplitude variations

It is apparent from Eq. (8.49) and from Figs. 8.21 and 8.22 that by using a proper pair of masks, which have helical amplitude variations, one can control the half-width of a rather large set of hyper Gaussian masks. Of course, in principle one can extend the previous results to other types of apodizers.

8.5 Final Remarks

We have indicated that one can employ a rather simply optical processor for visualizing, as a 2-D picture, the evolution of a 2-D scalar wave; as is predicted by Helmholtz equation. For this type of application, one needs to use a very narrow slit that follows a semicircle over an otherwise opaque mask.

Then, we have noted that within the paraxial regime, Helmholtz equation has a different expression. Hence, for visualizing the evolution of the point spread function with focus error, one needs to use a very narrow slit that follows now a parabolic curve.

The above results were extended for visualizing the influence that the optical path difference (of certain phase mask) has over the point spread function of an optical system. We have discussed the use of another optical processor for obtaining displays that describe the impact of the optical path difference over the modulation transfer function.

Then, we have discussed the use of anamorphic processors for visualizing the generation of the ambiguity function of a 1-D pupil mask. We have related this method with the visualization of the optical transfer function with variable focus

errors. When analyzing nonconventional devices using the ambiguity function, it is convenient to take into account the results obtained using the narrow slits.

Next, we have noted that the mathematical tools employed for describing the ambiguity function have a physical counterpart when using two refractive elements forming a pair, for implementing varifocal lenses; here denoted as Alvarez-Lohmann lenses. We have shown that the Alvarez-Lohmann lenses have an equivalent, when setting Gaussian apodizers with variable half-width.

We have indicated that the use of a pair of refractive elements, for controlling the optical power of a lens, leads to optical elements with helical phase variations. We have shown that one can control the optical path difference of a wide range of radial focalizers, if one uses a pair of refractive elements that have both helical phase variations and radial phase variations. To this end, one introduces an in-plane rotation between the refractive elements of the pair.

Finally, based on the previous results, we have discussed the use of two masks that have helical and radial amplitude variations for setting a large set of hyper Gaussian apodizers, with tunable half-width. Again for this application, one needs to introduce an in-plane rotation between the amplitude elements of the pair.

References

1. Jacquinot, P.: Apodization, Appendix E, in concepts of classical optics, John Strong, pp. 410–418. W. H. Freeman, San Francisco (1958)
2. Marechal, A., Françon, M.: Diffraction Structure Des Images, pp. 152–155. Masson, Paris (1970)
3. Papoulis, A.: Systems and Transforms with Applications in Optics, pp. 442–444. McGraw-Hill, New York (1968)
4. Steel, W.H.: Interferometry, pp. 23, 234, 248–249. Cambridge University Press, Cambridge (1983)
5. Goodman, J.W.: Introduction to Fourier Optics, pp. 151–154. McGraw-Hill, New York (1996)
6. Ojeda-Castañeda, J., Berriel-Valdos, L.R., Montes E.: Bessel annular apodizers: imaging characteristics. Appl. Opt. **26**(10), 2770–2772 (1987)
7. McCutchen, C.W.: Generalized aperture and three-dimensional diffraction image. J. Opt. Soc. Am. **54**(2), 240–244 (1964)
8. Ojeda-Castañeda, J., Berriel-Valdos, L.R.: Arbitrarily high focal depth with finite apertures. Opt. Lett. **13**(3), 183–185 (1988)
9. Ojeda-Castañeda, J., Andres, P., Diaz, A.: Strehl ratio with low sensitivity to spherical aberration. J. Opt. Soc. Am. A **5**(8), 1233–1236 (1988)
10. Ojeda-Castañeda, J., Tepichin, E., Pons, A.: Apodization of annular apertures: Strehl ratio. Appl. Opt. **27**(24), 5140–5145 (1988)
11. Mino, M., Okano, Y.: Improvement in the OTF of a defocused optical system through the use of shaded apertures. Appl. Opt. **10**(10), 2219 (1971)
12. Hauesler, G.: A method to increase the depth of focus by two step image processing. Opt. Commun. **6**(1), 38–42 (1972)
13. Chung, C.S., Hopkins, H.H.: Influence of nonuniform amplitude on the optical transfer function. Appl. Opt. **28**(6), 90–91 (1989)

14. Ojeda-Castañeda, J., Yépez-Vidal, E., Gómez-Sarabia, C.M.: Multiple-frame photography for extended depth of field. Appl. Opt. **52**(10), D84–D90 (2013)
15. Lohmann, A.W., Ojeda-Castañeda, J., Serrano-Heredia, A.: Trading dimensionality in signal processing. Opt. Laser Technol. **28**(2), 101–107 (1996)
16. Ojeda-Castañeda, J., Lohmann, A.W.: Young's experiment in signal synthesis, Chapter 14, Trends in Optic, Anna Consortini Editor, pp. 263–280. Academic Press, San Diego (1996)
17. Lohmann, A.W., Ojeda-Castañeda, J., Frausto, C.: Optical simulation of free-space propagation. Opt. Commun. **157**(1–6), 7–12 (1998)
18. Ojeda-Castañeda, J., Castro, A.: Simultaneous Cartesian coordinate display of defocused optical transfer functions. Opt. Lett. **23**(13), 1049–1051 (1998)
19. Woodward, P.M.: Radar ambiguity analysis, Technical Note No. 731. Royal Radar Establishment, London (1967)
20. Papoulis, A.: Ambiguity function in Fourier optics. J. Opt. Soc. Am. **64**(6), 779–788 (1974)
21. Guigay, J.P.: The ambiguity function in diffraction and isoplanatic imaging by partially coherent beams. Opt. Commun. 26(2), 136–138 (1978)
22. Marks, R.J., Walkup, J.K., Krile, T.F.: Ambiguity function display: an improved coherent processor. Appl. Opt. **16**(3), 746–750 (1977)
23. Brenner, K.-H., Lohmann, A.W., Ojeda-Castañeda, J.: The ambiguity function as a polar display of the OTF. Opt. Commun. **44**(5), 323–326 (1983)
24. Ojeda- Castañeda, J., Berriel-Valdos, L.R., Montes, E.: Ambiguity function as a design tool for high focal depth. Appl. Opt. **27**(4), 790–795 (1988)
25. Ojeda-Castañeda, J., Noyola-Isgleas, A.: High focal depth by apodization and digital restoration. Appl. Opt. **27**(12), 2583–2586 (1988)
26. Dowski, E.R., Cathey, T.W.: Extended depth of field through wave-front coding. Appl. Opt. **34**(11), 1859–1865 (1995)
27. Cook, C. E., Bernfeld, M.: Radar Signals: An Introduction to Theory and Applications, pp. 59–108. Arctech House, Norwood (1993)
28. George, N., Chi, W.: Extended depth of field using a Logarithmic asphere. J. Opt. Pure Appl. **5,** s157–s163 (2003)
29. Muyo, G., Harvey, A.R.: Decomposition of the optical transfer function: wavefront coding imaging systems. Opt. Lett. **30**(20), 2715–2717 (2005)
30. Sauceda-Carvajal, A., Ojeda-Castañeda, J.: High focal depth with fractional-power wave fronts. Opt. Lett. **29**(6), 560–562 (2004)
31. Castro, A., Ojeda-Castañeda, J.: Asymmetric phase masks for extended depth of field. Appl. Opt. **43**(17), 3474–3479 (2004)
32. Ojeda-Castañeda, J.: Focus error operator and related special functions. J. Opt. Soc. Am. **73**(8), 1042–1047 (1983)
33. Ojeda-Castañeda, J., Boivin, A.: The influence of wave aberrations: an operator approach. Can. J. Phys. **63**(2), 250–253 (1985)
34. Ojeda-Castañeda, J., Noyola-Isgleas, A.: Differential operator for scalar wave propagation. J. Opt. Soc. Am. A **5**(10), 1605–1609 (1988)
35. Ojeda-Castañeda, J., Berriel-Valdos, L.R., Montes, E.: Ambiguity function as a design tool for high focal depth. Appl. Opt. **27**(4), 790–795 (1988)
36. Marks, R.J. II, Walkup, J.K., Krile, T.F.: Ambiguity function display: an improved coherent processor. Appl. Opt. **16**(3), 746–750 (1977)
37. Castro, A., Ojeda-Castañeda, J., Lohmann, A.W.: Bow-tie effect: differential operator. Appl. Opt. **45**(30), 7878–7884 (2006)
38. Ojeda-Castañeda, J., Yépez-Vidal, E., García-Almanza, E.: Complex amplitude filters for extended depth of field. Photonics Lett. Pol. **2,** 162–164 (2010)
39. Ojeda-Castañeda J., Ledesma S. and Gomez-Sarabia C. M., Hyper Gaussian Windows with fractional wavefronts. Photonics Lett. Pol. **5**(1), 23–25 (2013)
40. Brenner, N., Rader, C.: IEEE Acoustics. Speech Signal Process. **24,** 264–266 (1976)
41. Plummer, W.T., Baker, J.G., van Tassell, J.: Photographic optical systems with nonrotational aspheric surfaces. Appl. Opt. **38**(16), 3572–2592 (1999)

42. Kitajima, I.: "Improvement in lenses". British Patent 250, 268 (July 29, 1926)
43. Lohmann, A.W.: Lente a focale variabili. Italian Patent 727, 848 (June 19, 1964)
44. Lohmann, A.W.: Improvements relating to lenses and to variable optical lens systems formed for such a lens. Patent Specification 998,191, London (1965)
45. Lohmann, A.W.: A new class of varifocal lenses. Appl. Opt. **9**(7), 1669–1671 (1970)
46. Alvarez, L.W.: Two-element variable-power spherical lens. US Patent 3, 305, 294 (December 3, 1964)
47. Alvarez, L.W., Humphrey, W.H.: Variable power lens and system. US Patent 3, 507, 565 (April 21, 1970)
48. Ojeda-Castañeda, J., Landgrave, J.E.A., Gómez-Sarabia, C.M.: The use of conjugate phase plates in the analysis of the frequency response of optical systems designed for an extended depth of field. Appl. Opt. **47**(22), E99–E105 (2008)
49. Ojeda-Castañeda, J., Aguilera Gómez, E., Plascencia Mora, H., Torres Cisneros, M., Ledesma Orozco, E.R., León Martínez, A., Pacheco Santamaría, J.S., Martínez Castro, J.G.: Carlos Salas Segoviano R., U. S. Patent 8, 159, 573B2 (April 17, 2012)
50. Ojeda-Castañeda, J., Gómez-Sarabia, C.M.: Key concepts for extending the depth of field with high resolution. Opt. Pura Apl. **45**(4) 449–459 (2012)
51. Ojeda-Castañeda, J., Yépez-Vidal, E., García-Almanza, E., Gómez-Sarabia, C.M.: "Tunable Gaussian mask for extending the depth of field". Photonics Lett. Pol. **4**(3), 115–117 (2012)
52. Lohmann, A.W., Paris, D.P.: "Variable Fresnel Zone Pattern" Appl. Opt. **6**(9), 1567–1570 (1967)
53. Burch, J.M., Williams, D.C.: Varifocal moiré zone plates for straightness measurement. Appl. Opt. **16**(9), 2445–2450 (1977)
54. Bernet, S., Jesacher, A., Fuerhapter, S., Maurer, C., Ritsch-Marte, M.: "Quantitative imaging of complex samples by spiral phase contrast microscopy". Opt. Express **14**(9) 3792–3805 (2006)
55. Jesacher, A., Fürhapter, S., Bernet, S., Ritsch-Marte, M.: "Spiral interferogram analysis". J. Opt. Soc. Am. A **23**(6) 1400–1409 (2006)
56. Bernet, S., Ritsch-Marte, M.: "Optical device with a pair of diffractive optical elements". US Patent 0134869 A1 (June 3, 2010)
57. Ojeda-Castañeda, J., Ledesma, S., Gomez-Sarabia, C.M.: Tunable apodizers and tunable focalizers using helical pairs. Photonics Lett. Pol. **5**(1), 20–22 (2013)
58. Ojeda-Castañeda, J., Gomez-Sarabia, C.M., Ledesma, S.: Tunable focalizers: axicons, lenses and axilenses, Tribute to H. John Caulfield, SPIE Proceedings 8833, 88330601–88330606 (2013)
59. Bryngdahl, O.: Radial- and circular-fringe interferograms. J. Opt. Soc. Am. **63**(9), 1098–1104 (1973)
60. Ojeda-Castañeda, J., Ledesma, S., Gomez-Sarabia, C.M.: Hyper Gaussian Windows with fractional wavefronts. Photonics Lett. Pol. **5**(1), 23–25 (2013)
61. Ojeda-Castañeda, J., Ledesma, S., Gomez-Sarabia, C.M.: Helical apodizers for tunable hyper Gaussian masks, Novel Optical System Design and Optimization XVI, SPIE Proceedings 8842, 88420N-1-88420N-6 (2013)

Chapter 9
Description of the Dynamics of Charged Particles in Electric Fields: An Approach Using Fractional Calculus

F. Gómez-Aguilar and E. Alvarado-Méndez

Abstract The Free Electron Lasers (FEL) uses a beam of electrons accelerated to relativistic velocities as the active medium to laser generation; these electrons are bound to atoms, but move freely in a magnetic field. The efficiency of FEL depends on several parameters such as relaxation time, longitudinal effects and transverse variations of the optical field. Moreover, the electron dynamics in a magnetic field undulator serves as a means of radiation source for coupling to the electric field. The transverse motion of the electrons leads to either a gain or loss energy from or to the field; this depends on the position of the particle regarding the phase of the external radiation field. On the other hand, optical tweezers are noninvasive tools that use a laser beam to generate powerful forces enough to manipulate microscopic matter by using electric and magnetic fields. In this work, we described the fractional dynamics of charged particles in electric fields to know their displacement. Fractional Newton's second law is considered and the order of the fractional differential equation is $0 < \gamma \leq 1$. We use the Laplace transform of the fractional derivative in Caputo sense. Dissipative effects are observed in the study cases of the particle dynamics due to the order of the derivative, and the standard electrodynamics is recovered by taking the limit when $\gamma = 1$.

9.1 Introduction

Radiation-matter interaction has been the foundation of a wide diversity of linear and non linear optical phenomena. Recently, new technologies are based on the use of ultrashort pulses where attoseconds lasers are used to understand physical and

F. G.-Aguilar (✉)
Centro Nacional de Investigación y Desarrollo Tecnológico, Tecnológico Nacional de México.
Interior Internado Palmira S/N, Col. Palmira, C.P. 62490,Cuernavaca, Morelos, México
e-mail: jgomez@cenidet.edu.mx

E. A.-Méndez
Departamento de Ingeniería Electrónica, División de Ingenierías Campus Irapuato Salamanca, Universidad de Guanajuato, Carretera Salamanca-Valle de Santiago, km 3.5+1.8 km, Comunidad de Palo Blanco, Salamanca, GTO, México
e-mail: ealvarad@ugto.mx

chemical processes. These technologies have had an impact on electric films such as photonic crystals, and quantum wells. Free electron lasers (FEL) are suitable for these types of studies due to their properties of coherent emission of electromagnetic radiation. By changing electrons energy, FEL reach high power and they are easily tunable [1, 2]. The physical principle of FEL is found on the use of a beam of electrons accelerated to relative velocities, as an active means, to generate the laser. Since the electrons are not connected to atoms, they can generate electromagnetic radiation in any spectrum wavelength. Electrons relaxation time has been widely researched and modeled. It affects the energy of pulse laser in materials such as photonic crystals, dielectrics, conductors and magnetics [3]. One of the applications of this process is to produce diffraction limit structures whose refraction index is different from the sample.

The efficiency of FEL depends on several parameters such as relaxation time, longitudinal effects and transverse variations of the optical field. Moreover, the electron dynamics in a magnetic field undulator serves as a means of radiation source for coupling to the electric field. The transverse motion of the electrons leads to either a gain or loss energy from or to the field, depending on the position of the particle regarding the phase of the external radiation field [4].

Fractional calculus (FC) involves derivatives and integrals of non-integer order. Integer order derivatives give a direct physical explanation (i.e. velocity, acceleration, etc.); however, it is not easy to make an interpretation of non-integer order derivatives. In many applications FC provide more accurate models of the physical systems than ordinary calculus do. Mathematical and physical considerations in favor of using models based on derivatives of non-integer order are given in (see references [5–23]).

The Lagrangian and Hamiltonian formulation of dynamics of electromagnetic fields using fractional calculus has been reported in [24–29]. Fractional derivatives are an excellent instrument to describe memory and hereditary properties of different materials and processes [30]. This is the main advantage of FC in comparison with the classical integer-order models, in which such effects are neglected. FC has been applied to calculate temporal relaxation of FEL. One interesting result is that temporal relaxation is given by a linear combination of Mittag-Leffler functions [31]. Kkulish in [32] measured changes in the reflectivity on thin films by heating with pulsed lasers. In the same work, the reflectivity changes were related to the corresponding variations of the surface temperature by applying fractional diffusion.

The authors in [33] present light scattering intensity fluctuation in dusty plasma; they considered the scattered electric field as a stationary stochastic process. The FC is used to model the fractional kinetic for polydisperse particles and show that the correlation based on fractional Ornstein–Uhlenbeck process may provide a novel insight into the complex transport behaviors in dusty plasma. An optical tweezer is a scientific instrument that uses a laser beam to provide an attractive or repulsive force to hold and physically move microscopic dielectric objects. Micromanipulation of biologic particles such as biomolecules, cells, ADN, can be performed using electric and magnetic fields. Recently kinetic equations with partial fractional derivatives were applied in the description of anomalous diffusion and relaxation phenomena, some examples include motions under the influence of optical tweezers, reactions

in complex systems [34–36]. Granek investigated the relaxation and autocorrelation function of a particle attached to a membrane under the combined influence of an external potential. The Mittag-Leffler function is used to explain the relaxation behavior. This model was proved by using optical tweezers [37]. Recently, in [38] has been proposed a systematic way to construct fractional differential equations for physical systems. The method consists in dimensional analysis of the ordinary derivative operator.

In this work, we propose an alternative procedure for constructing fractional differential equations, in particular, the fractional dynamics of charged particles in electric fields. Three cases are considered: electric field constant, ramp and harmonic. The order of the fractional differential equation is $0 < Y \leq 1$.

9.2 Fractional Calculus

Several definitions exist about fractional order derivative, including: Grünwald-Letnikov, Riemann-Liouville, Riesz and Caputo [1–3]. In Caputo case, the initial conditions for the fractional differential equations have a physical interpretation. Due to the impact on physics and engineering we use Caputo Fractional Derivative (CFD) as a function of time, $f(t)$, and is defined as follows [3]

$$
{}_o^C D_t^\gamma f(t) = \frac{1}{\Gamma(n - \gamma)} \int_0^t \frac{f^{(n)}(\tau)}{(t - \tau)^{\gamma - n + 1}} d\tau,
\tag{9.1}
$$

where $n = 1, 2, \ldots, \varepsilon\ N$ and $n - 1 < Y \leq n$. We consider the case $n = 1$, i.e., in the integrand there is only first derivative. In this case, $0 < Y \leq 1$, is the order of the fractional derivative.

The Caputo derivative operator satisfies the following properties

$$
{}_o^C D_t^\gamma [f(t) + g(t)] = {}_o^C D_t^\gamma f(t) + {}_o^C D_t^\gamma g(t),
$$

$$
{}_o^C D_t^\gamma c = 0
\tag{9.2}
$$

where c is constant.

Laplace transform to CFD gives [3]

$$
L\left[{}_o^C D_t^\gamma f(t) \right] = S^\gamma F(s) - \sum_{k=0}^{m-1} S^{\gamma - k - 1} f^{(k)}(0).
\tag{9.3}
$$

The Mittag-Leffler function arises as the solution of fractional differential equations. This function has caused extensive interest among physicists due to its vast potential of applications, by describing realistic physical systems with memory and delay, is defined as

$$
E_a(t) = \sum_{m=0}^{\infty} \frac{t^m}{\Gamma(am + 1)}, (a > 0),
\tag{9.4}
$$

where Γ is the gamma function. When $a = 1$, from Eq. (9.4), we have

$$E_1(t) = \sum_{m=0}^{\infty} \frac{t^m}{\Gamma(m+1)} = \sum_{m=0}^{\infty} \frac{t^m}{m!} = e^t. \tag{9.5}$$

The Mittag-Leffler function includes the exponential function as a special case.

9.3 Procedure for Constructing Fractional Differential Equations

We propose replace the time derivative operator d/dt by a new fractional operator d^γ/dt^γ (γ represents the order of the derivative). The proposed alternative is introducing an additional parameter σ that must have dimension of seconds to be consistent with the dimension of the ordinary derivative operator. Thus, we replace the ordinary time derivative operator by the fractional one as

$$\frac{d}{dt} \rightarrow \frac{d^\gamma}{dt^\gamma}, 0 < \gamma \leq 1 \tag{9.6}$$

From a physical standard point, Eq. (9.6) is not correct. The time derivative operator d/dt has dimension of inverse seconds s^{-1}, while the fractional time derivative operator d^γ/dt^γ has $s^{-\gamma}$. To be consistent with the temporal dimensionality we propose a new parameter σ in the following way

$$\left[\frac{1}{\sigma^{1-\gamma}} \frac{d^\gamma}{dt^\gamma} \right] = \frac{1}{s}, 0 < \gamma \leq 1 \tag{9.7}$$

where γ is an arbitrary parameter which represents the order of the derivative. In the case $\gamma = 1$ the Eq. (9.7) becomes an ordinary derivative operator d/dt. In this way Eq. (9.7) is dimensionally consistent if and only if the new parameter σ, has dimension of time $[\sigma] = $ s. Now, it is called the cosmic time [40], and it is a non-local time. Another physical and geometrical interpretation of the fractional operators is given in [41].

$$\frac{d}{dt} \rightarrow \frac{1}{\sigma^{1-\gamma}} \frac{d^\gamma}{dt^\gamma}, n - 1 < \gamma \leq n \tag{9.8}$$

The Eq. (9.8) is a temporal derivative in the usual sense because its dimension is s^{-1}. The parameter σ (auxiliary parameter) represents the fractional time components, and shows an intermediate behavior between a conservative and dissipative system.

In this work, we study the case where a particle is launched within an electric field. The motion and trajectory of a particle will be calculated when

a. The electric field is constant.
b. The electric field is linear (ramp).
c. The electric field is harmonic.

9.4 Constant Electric Field

For the first case, we can consider motion of charged particles in a uniform electric field $\vec{E} = E_y \hat{a}_y$. Using the fractional Newton second law, we have

$$_0^c D_t^\gamma \, p_{\gamma,y}(t) = \sigma^{1-\gamma} q E_y, \tag{9.9}$$

Applying Laplace transform to Eq. (9.9) we have

$$s^\gamma P_y(s) - s^{\gamma-1} p_y(0) - \sigma^{1-\gamma} q E_y \left(\frac{1}{s}\right) = 0 \tag{9.10}$$

if $p_y(0) = 0$

$$P_y(s) = \frac{\sigma^{1-\gamma} q E_y}{s^{1+\gamma}} \tag{9.11}$$

Applying inverse Laplace transform we have

$$p_{\gamma,y}(t) = q E_y \sigma^{1-\gamma} \left(\frac{t^\gamma}{\Gamma(\gamma+1)}\right), \quad 0 < \gamma \le 1 \tag{9.12}$$

if $Y = 1$, we can show that

$$p(t) = q E_y t, \tag{9.13}$$

considering $p(t) = m(dy/dt)$, applying Caputo definition and substituting in Eq. (9.12) gives

$$_0^c D_t^\gamma \, y_\gamma(t) = \frac{q E_y \sigma^{2(1-\gamma)}}{m} \left(\frac{t^\gamma}{\Gamma(\gamma+1)}\right) \tag{9.14}$$

Applying Laplace transform and considering that $y(0) = 0$, we have

$$Y_\gamma(s) = \frac{q E_y \sigma^{2(1-\gamma)}}{m} \left(\frac{1}{s^{2\gamma+1}}\right) \tag{9.15}$$

Applying inverse Laplace transform to Eq. (9.15) becomes

$$y_\gamma(t) = \frac{q E_y \sigma^{2(1-\gamma)}}{m} \frac{t^{2\gamma}}{\Gamma(2\gamma+1)}, \quad 0 < \gamma \le 1, \tag{9.16}$$

if $Y = 1$, we can show that

$$y(t) = \frac{q E_y}{m} \frac{t^2}{\Gamma(3)} = \frac{q E_y}{2m} t^2, \tag{9.17}$$

The Eq. (9.17) corresponds to classic electrodynamics case. Since the charged particle moves at nearly speed of light, we contemplate relativistic conditions to determine the constant $\sigma = 1/$. From the Planck relation

$$E = h\nu \tag{9.18}$$

We considered the relativistic frequency

$$\nu = \frac{m_0 c^2}{h\sqrt{1 - \frac{v_0^2}{c^2}}} \left[\frac{1}{\sqrt{1 - \frac{v_0^2}{c^2}}} - 1 \right],\qquad\qquad (9.19)$$

Then the parameter σ is

$$\sigma = \frac{1}{\nu} = \frac{h}{m_0 c^2} \left[\frac{1 - \frac{v_0^2}{c^2}}{1 - \sqrt{1 - \frac{v_0^2}{c^2}}} \right],\qquad\qquad (9.20)$$

In consequence, the Eq. (9.16) can be written as

$$y_\gamma(t) = \frac{qE_y\sigma^{2(1-\gamma)}}{m_0} \frac{t^{2\gamma}}{\Gamma(2\gamma + 1)} \sqrt{1 - \frac{v_0^2}{c^2}}, \qquad 0 < \gamma \le 1 .\qquad (9.21)$$

where σ is given by the Eq. (9.20). The Eq. (9.21) describes the trajectory of the particle in the external electric field.

Considering the values of $v_0 = (0.98c)m/s$; $q = 1.602 \times 10^{-19}C$; $m_0 = 9.11 \times 10^{-31}Kg$; $c = 3 \times 10^8 m/s$; Planck constant, $h = 6.62606896 \times 10^{34}Js$; and $E_y = 500 KV/m$. The trajectory of the particle in a constant electric field is showed in Fig. 9.1. The value $\gamma = 1$ corresponds to enter order derivative. For this case, the dynamics that the particle undergoes is parabolic. However, for $0 < \gamma < 0.998$, the trajectory decreases when x is incremented and is not a parabolic trajectory.

9.5   Ramp Electric Field

For the second case we consider the motion of the charged particle in a ramp electric field with the form, $\vec{E} = E_y t \hat{a}_y$. In differential form, the dynamical behavior of the particle is given by,

$$\frac{dx}{dt} = v_{ox},\qquad\qquad (9.22)$$

and

$$\frac{dy}{dt} = \frac{qE_0}{m}t,\qquad\qquad (9.23)$$

In other words, the particle is launched in x-axis direction with constant initial velocity; nonetheless, it is accelerated in y-axis direction due to external electric field. The corresponding fractional equation with initial condition $x(0)=0$ for Eq. (9.22) is

$$x(t) = v_{0x}\sigma^{1-\gamma} \left(\frac{t^\gamma}{\Gamma(1 + \gamma)} \right) ,\qquad 0 < \gamma \le 1.\qquad (9.24)$$
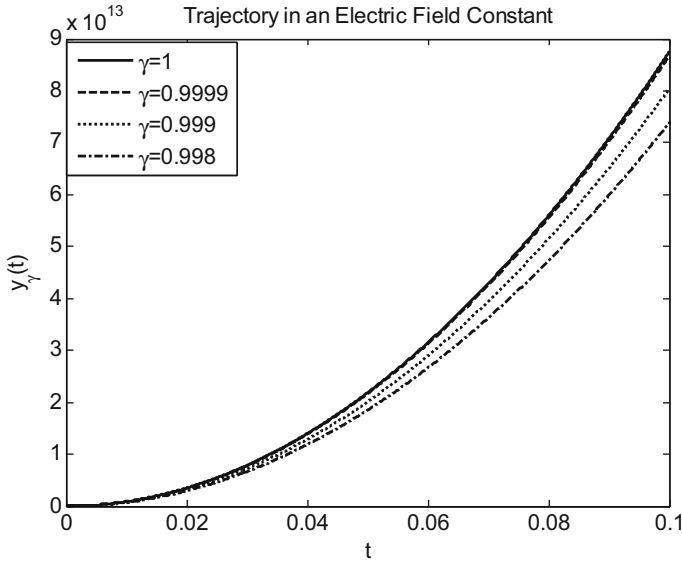
Fig. 9.1 Trajectory in a constant electric field for different values of γ

if $Y = 1$, we can show that

$$x(t) = v_{0x}t. \tag{9.25}$$

For the case Eq. (9.23) the fractional equation with the condition $x(0) = 0$ may be written as

$$y(t) = \left(\frac{qE_o}{m}\right)\sigma^{2(1-\gamma)}\left(\frac{t^{1+2\gamma}}{\Gamma(2+2\gamma)}\right), \qquad 0 < \gamma \leq 1, \tag{9.26}$$

In the particular case with $Y = 1$ we obtain y-axis component of the trajectory

$$y(t) = \left(\frac{qE_o}{m}\right)\left(\frac{t^3}{6}\right). \tag{9.27}$$

The Eq. (9.27) corresponds to the classic case. The full solution is

$$r_\gamma(t) = v_{0x}\sigma^{1-\gamma}\left(\frac{t^\gamma}{\Gamma(1+\gamma)}\right)\hat{a}_x$$

$$+ \left(\frac{qE_o}{m}\right)\sigma^{2(1-\gamma)}\left(\frac{t^{1+2\gamma}}{\Gamma(2+2\gamma)}\right)\hat{a}_y, \qquad 0 < \gamma \leq 1. \tag{9.28}$$

where σ is given by Eq. (9.20).

Considering the next values, initial velocity $v_0 = (0.98c)m/s$; $q = 1.602 \times 10^{-19}C$; $m_0 = 9.11 \times 10^{-31}Kg$; $c = 3 \times 10^8m/s$; the Planck constant, $h = 6.62606896 \times 10^{34}Js$; and electric field of $E_y = 500KV/m$, the Fig. 9.2 shows the trajectory of the particle in an electric field ramp.
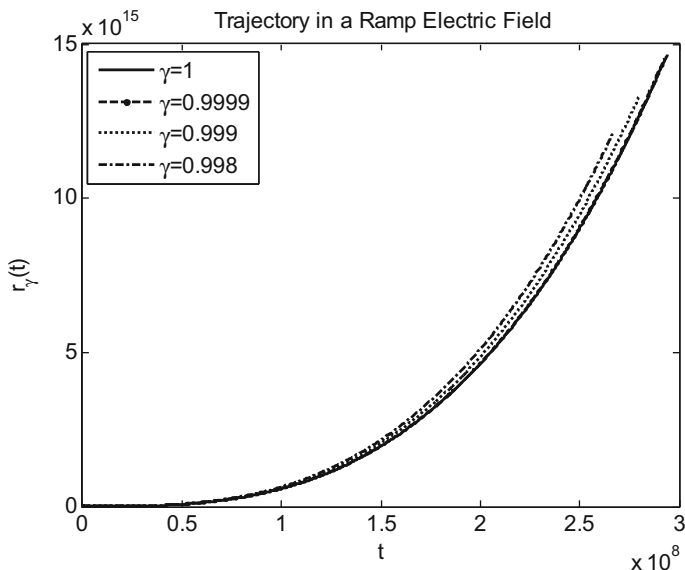
Fig. 9.2 Trajectory of the particle charged launched in a ramp electric field for different values of Y

9.6 Harmonic Electric Field

Other very interesting case is when a charged particle is launched in a harmonic electric field with the form $\overrightarrow{E} = E_y \sin(\omega t)\hat{a}_y$. We applied the second Newton law anew in the following equation

$$\frac{dp_x}{dt}\hat{a}_x + \frac{dp_y}{dt}\hat{a}_y = qE_0 sin(\omega t)\,\hat{a}_y, \tag{9.29}$$

for $\hat{a}_x$ we have

$$\frac{dx}{dt} = v_{ox}, \tag{9.30}$$

the corresponding fractional equation with $x(0) = 0$ for Eq. (9.30) is

$$x(t) = v_{0x}\sigma^{1-\gamma}\left(\frac{t^\gamma}{\Gamma(1+\gamma)}\right), \qquad 0 < \gamma \le 1. \tag{9.31}$$

if $Y = 1$, we can show that

$$x(t) = v_{0x}t. \tag{9.32}$$

For $\hat{a}_y$ we have

$$\frac{dp_y}{dt} = qE_0 sin(\omega t), \tag{9.33}$$

the corresponding fractional equation with initial condition $y(0) = 0$ for Eq. (9.33) is

$$P_y(s) = (q E_o \sigma^{1-\gamma}) \frac{\omega}{s^\gamma (\omega^2 + s^2)}, \tag{9.34}$$

If $p_y(t) = m(dy/dt)$, applying Laplace transform with zero initial conditions becomes

$$Y(s) = \frac{\sigma^{1-\gamma}}{m} \frac{P_y(s)}{s^\gamma}, \tag{9.35}$$

substituting the Eq. (9.34) in Eq. (9.35) we have

$$Y(s) = \left(\frac{q E_0 \sigma^{2(1-\gamma)}}{m} \right) \frac{\omega}{s^{2\gamma} (\omega^2 + s^2)}, \tag{9.36}$$

the fractional form of the equation corresponding to Eq. (9.36) is

$$y(t) = \left(\frac{q E_0 \sigma^{2(1-\gamma)}}{m} \right) \left(\frac{1}{\omega} \cdot \frac{t^{2\gamma-1}}{\Gamma(2\gamma)} + \frac{\omega}{\omega^{2\gamma+1}} sin(\omega t - \pi \gamma) \right), \tag{9.37}$$

if $\gamma = 1$, is easy to show that

$$y(t) = \left(\frac{q E_0}{m} \right) \left(\frac{t}{\omega} + \frac{1}{\omega^2} sin(\omega t - \pi) \right), \tag{9.38}$$

where $sin(\omega t - \pi \gamma) = -sin(\omega t)$ we have

$$y(t) = \left(\frac{q E_0}{m} \right) \left(\frac{t}{\omega} - \frac{1}{\omega^2} sin(\omega t) \right). \tag{9.39}$$

The Eq. (9.39) corresponds to the classic case. The full solution is

$$r_\gamma(t) = v_{0x} \sigma^{1-\gamma} \left(\frac{t^\gamma}{\Gamma(1+\gamma)} \right) \hat{a}_x + \left(\frac{q E_0 \sigma^{2(1-\gamma)}}{m} \right)$$
$$\left(\frac{1}{\omega} \cdot \frac{t^{2(\gamma-1)}}{\Gamma(2\gamma)} + \frac{\omega}{\omega^{2(\gamma-1)}} sen(\omega t - \pi \gamma) \right) \hat{a}_y, \quad 0 < \gamma \leq 1. \tag{9.40}$$

where σ is given by Eq. (9.20).

We suppose that $v_0 = (0.98c)m/s$; $q = 1.602 \times 10^{-19}C$; $m_0 = 9.11 \times 10^{-31} Kg$; $c = 3 \times 10^8 m/s$; Planck constant, $h = 6.62606896 \times 10^{34} Js$; $f = 60 Hz$; $\omega = 2\pi f$ and $E_y = 500 KV/m$. The Fig. 9.3 shows the trajectory of the particle in a harmonic electric. We can see that for $0 < x < 0.5x10^7$, and $0 < \gamma < 0.998$, the particle trajectory has small oscillations and they are very close. However, when x grows, the trajectory oscillations are increased, and we can see small differences. First, the periodicity of the trajectory breaks up, and second, the amplitude decreases.
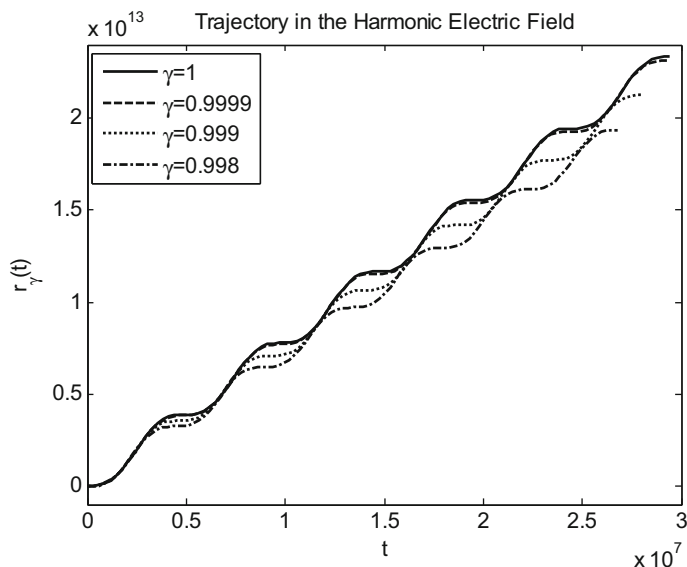
Fig. 9.3 Trajectory of the particle charged into the harmonic electric field for different values of Y

9.7 Conclusions

Fractional calculus is a very useful tool in the description of the evolution of systems with memory, which typically are dissipative in complex systems. In this work, we have proposed a new fractional differential equation of order $0 < Y \leq 1$ to describe the fractional dynamics of charged particles in electric fields. We analyzed three different cases: constant, ramp and harmonic electric fields. We have used the idea suggested in [38] to construct fractional differential equations.

As it was expected, the net force of the particle immersed in the constant electric field is only due to electric force. The particle describes a parabolic path due to the constant force exerted on it. Thus, the particle shows a uniformly accelerated movement. For the second case where the particle enters a ramp electric field, the force exerted on the particle is increasing; consequently, the acceleration of the particle will also increase over time in a proportional factor to t^3. In the harmonic field case, the electric field begins to accelerate the particle in the positive sense and alternates his polarity along the field, causing changes in its direction. This effect arises due to the sum of a linear function of t and a *sin* function. The electron seems to be braked due to dissipative effects present in the field; as a result, it shows phenomena that are not considered in the classical model. In all cases, particle dynamics changes due to the order derivative.

Since the particle travels at nearly speed of light, the parameter σ (auxiliary parameter) was related to Plank's equation for Energy $E = h\upsilon$ and relativistic equations for mass and kinetic energy.

Some possible applications of our results are in tweezers optics. Micromanipulation of biologic particles such as biomolecules, cells, ADN, can be performed using electric and magnetic fields. In 1969 Arthur Ashkin at Bell Laboratories realized that the pressure from an intense laser was sufficient to manipulate dielectric particles [39], demonstrating levitation by balancing radiation pressure with gravity. The basis for a dielectric trapping force originates in the polarizability of a particle in an electromagnetic field. A best control of biological particle can be obtained if the trajectory is known, and our mathematical model can predict the trajectory.

The fractional dynamics of charged particles in magnetic fields will be considered in future works.

References

1. Brau, C.A.: Free-electron lasers. Science. **239**, 1115–1121 (1988)
2. Freund, H.P., Antonsen, T.M.: Principles of Free-Electron Lasers, 2nd edn. Chapman & Hall, London (1996)
3. Tsakiris, G.D., Eidmann, K., Meyer-ter-Vehn, J., Krausz, F.: Route to intense single attosecond pulses. New J. Phys. **8**(19) (2006)
4. Colson, W.B. Electron dynamics in free electron laser resonator modes. Appl. Phys. B. **29** 101–109 (1982)
5. Oldham, K.B., Spanier, J.: The Fractional Calculus. Academic Press, New York (1974)
6. Samko, S.G., Kilbas, A.A., Marichev, O.I.: Fractional Integrals and Derivatives, Theory and Applications. Gordon and Breach Science Publishers, Langhorne (1993)
7. Podlubny, I.: Fractional Differential Equations. Academic Press, New York (1999)
8. Baleanu, D.: Fractional Calculus Models and Numerical Methods. World Scientific, Singapore (2012)
9. Monje, C.A., Chen, Y.Q., Vinagre, B.M., Xue, D., Feliu, V.: Fractional-order systems and controls, series: advances in Industrial control. Springer (2010)
10. Caponetto, R., Dongola, G., Fortuna, L., Petrás, I.: Fractional Order Systems: Modeling and Control Applications. World Scientific, Singapore (2010)
11. Baleanu, D., Günvenc, Z.B., Tenreiro, M.J.A. (eds.): New Trends in Nanotechnology and Fractional Calculus Applications. Springer (2010)
12. Baleanu, D., Diethelm, K., Scalas, E., Trujillo, J.J.: Fractional Calculus Models and Numerical Methods. Series on Complexity, Nonlinearity and Chaos. World Scientific, Singapore (2012)
13. Baleanu, D., Golmankhaneh, A.K., Golmankhaneh, A.K., Nigmatullin, R.R.: Newtonian law with memory. Nonlinear Dyn. **60**(1–2), 81–86 (Springer) (2010)
14. Guía, M., Gómez, F., Rosales, J.: Analysis on the time and frequency domain for the RC electric circuit of fractional order. Cent. Eur. J. Phys. **11**(10), 1366–1371 (2013) (Springer)
15. Hilfer, R.: Fractional diffusion based on Riemann-Liouville fractional derivatives. J. Phys. Chem. **104**, 3914–3917 (2000)
16. Gómez, F., Rosales, J., Guía M.: RLC electrical circuit of non-integer order. Cent. Eur. J. Phys. **11**(10), 1361–1365 (2013) (Springer)
17. Metzler, R., Klafter, J.: The Restaurant at the end of random walk: recent development in description of anomalous transport by fractional dynamics. J. Phys. **A37**, R161–R208 (2004)
18. Agrawal, O.P.: A general formulation and solution scheme for fractional optimal control problems. In: Duarte, M., Tenreiro-Machado, J.A., (eds.) Special issue of fractional order

derivatives and their applications. Nonlinear Dyn. **38**(1–2), 323–337. Berlin: Springer-Verlag (2004)

19. Hilfer, R. (ed.): Applications of Fractional Calculus in Physics. World Scientific, Singapore (2000)
20. West, B.J., Bologna, M., Grigolini, P.: Physics of Fractional Operators. Springer, Berlin (2003)
21. Magin, R.L.: Fractional Calculus in Bioengineering. Begell House, Roddin (2006)
22. Caputo, M., Mainardi, F.: A new dissipation model based on memory mechanism. Pure Appl. Geophys. **91**, 134–147. (1971)
23. Gómez, F., Bernal, J., Rosales, J., Córdova, T.: Modeling and simulation of equivalent circuits in description of biological systems—a fractional calculus approach. J. Electr. Bioimpedance. **3**, 2–11 (2012)
24. Riewe, F.: Nonconservative lagrangian and hamiltonian mechanics. Phys. Rev E. **53**, 1890–1899 (1996)
25. Herzallah, M.A.E., Muslih, S.I., Baleanu, D., Rabei, E.M.: Hamilton-Jacobi and fractional like action with time scaling. Nonlinear Dyn. **66**(4), 549–555 (Springer) (2011)
26. Golmankhaneh, A.K., Yengejeh, A.M., Baleanu, D.: On the fractional Hamilton and Lagrange mechanics. Int. J. Theor Phys. **51**(9) 2909–2916 (2012)
27. Golmankhaneh, A.K.: Investigations in Dynamics: With Focus on Fractional Dynamics. LAP (Lambert Academic publishing), Saarbrucken (2012)
28. Muslih, S.I., Saddallah, M., Baleanu, D., Rabei, E.: Lagrangian formulation of Maxwell's field in fractional D dimensional space-time. Romanian J. Phys. **55**(7–8) 659–663 (2010)
29. Baleanu, D., Muslih, S.I., Rabei, E.M.: On fractional Euler-Lagrange and Hamilton equations and the fractional generalization of total time derivative. Nonlinear Dyn. **53**(1–2) 67–74 Springer (2008)
30. Uchaikin, V.: Fractional calculus. Edit. Artishok. In Russian, (2008).
31. Preda, L., Mihailescu, M., Preda, A.: U. P. B. Sci. Bull. Series **71**(4) 11–20 (2009)
32. Kkulish, V.V., Llage, J.L., Komarov, P.L., Raad, P.E.: A fractional-diffusion theory for calculating thermal properties of thin films from surface transient thermoreflectance measurements. J. heat Transf. **123**(6).1133–1138 (2001)
33. Muniandy, S.V., Chew, W.X., Wong C.S.: Fractional dynamics in the light scattering intensity fluctuation in dusty plasma. Phys. Plasmas. **18**(1), 013701-1,013701-8 (2011)
34. Metzler, R., Klafter, J.: J. Phys. A: Math. Gen. 37R161, (2004).
35. Schumer, R., Benson, D.A., Meerschaert, M.M., Wheatcraft, S.W.: Eulerian derivation of the fractional advection-dispersion equation. J. Contam. Hydrol. **48**(1–2), 69–88 (2001)
36. Berkowitz, B., Klafter, J., Metzler, R., Scher, H.: Water Resour. Res. **38,** 1191 (2002)
37. Granek, R., Klafter, J.: Anomalous motion of membranes under a localized external potential. Europhys. Lett. **56**, 15 (2001)
38. Gómez-Aguilar, J.F., Rosales-García, J.J., Bernal-Alvarado, J.J., Córdova-Fraga, T.: Fractional mechanical oscillators. Rev. Mex. Fís. **58**, 348–352 (2012)
39. Ashkin, A.: Acceleration and trapping of particles by radiation pressure. Phys. Rev. Lett. 24, 156–159 (1970)

Chapter 10
Sub- and Nanosecond Pulsed Lasers Applied to the Generation of Broad Spectrum in Standard and Microstructured Optical Fibers

Julián M. Estudillo-Ayala, Roberto Rojas-Laguna, Juan C. Hernández Garcia, Daniel Jauregui-Vazquez and Juan M. Sierra Hernandez

Abstract This chapter provides an experimental and theoretical overview of pulsed lasers applications focused on obtaining supercontinuum light source. Particular attention is paid to the supercontinuum generation with short piece of conventional and microstructured fiber. An investigation in the regime of long pulses is performed through pumping sources with pulse duration of 700 ps and 6 ns, showing that it is possible to obtain this kind of source in an economical way by using a microchip laser and a few meters of standard fiber, and achieve spectral broadening comparable with that one using a femtosecond laser. In this chapter the nonlinear effects in short lengths of optical fibers are analyzed, starting with modulation instability, stimulated Raman scattering, and stimulated Brillouin scattering. The interaction of these effects for obtaining supercontinuum light source is shown. It also shown that using a Nd:YAG laser with pulse duration of 6 ns and a repetition rate of 50 Hz to pump two joined photonic crystal fibers with different microstructure and dispersion is possible to obtain a spectral broadening with a greater flatness. Finally the spectral evolution of pumping pulses is presented for different input intensities and different lengths of standard and microstructured fibers.

10.1 Introduction

The Supercontinuum generation (SG) and spectral broadening is an inherent feature of nonlinear optic. This phenomenon was first observed for the first time in 1970 by Alfano and Shapiro in bulk borosilicate glass [1]. Thanks to the invention and production of photonic crystal fibers (PCFs), the SG experiencing a great boom in many areas of research such as sensors, nonlinear optics, spectroscopy, optical coherence tomography, pulse compression, telecommunication, wavelength tunable source [2–6], and many other topics. Supercontinuum generation involves a series

J. M. E.-Ayala (✉) · R. R.-Laguna · D. J.-Vazquez · J. M. S. Hernandez · J. C. H. Garcia
Cuerpo Académico de Optoelectrónica, DICIS Universidad de Guanajuato,
Guanajuato, Mexico
e-mail: julian@ugto.mx

of nonlinear phenomena, such as four wave mixing (FWM), modulation instability (MI), self-phase and cross-phase modulation (SPM and XPM), Stimulated Raman (SRS), Stimulated Brillouin Scatering (SBS) and the formation of higher-order solitons, as presented in several publications [7–9]. Two nonlinear effects SRS and SBS, through which the optical field transfers part of its energy to the nonlinear medium, are related to vibrational excitation modes of silica. The difference between the two phenomena is that optical phonons participate in SRS while acoustic phonons participate in SBS. In the case of SRS a photon of the incident field is annihilated to create a phonon and a photon at lower frequency, corresponding to larger wavelength. The pump characteristics associated with nonlinear effects that result in SG are the pulse width, pump power, and dispersion parameter of the group velocity. When pumping is generated in the continuous-wave (CW), picosecond and nanosecond regimes, the spectral broadening is generated mainly by MI for anomalous dispersion.

Nonlinear effects are vital for multiple applications, mainly telecommunications, sensors [3], coherent optical tomography [4] and supercontinuum spectrum generation. Among one of most successful applications of these effects is broadband supercontinuum generation. The PCFs brought new opportunities to build novel types of supercontinuum sources with improved energy conversion efficiency and with low threshold power. These fibers offer an isolated core that allows strongly localizing a propagating mode in a limited area of few square microns over a distance of tens of meters. Another alternative to SC generation is based on SMF-28 fiber. More recently presented different designs have been using dispersion shifted fiber (DSF) pumped by a Q-switched microchip laser emitting sub-nanosecond pulses. Other authors have achieved SC using highly nonlinear fiber (HNLF) and dispersion-shifted fibers. By the production of new types of optical fibers such as photonic crystal fiber (PCF) a high-cost technology and expensive laboratory equipment are required. The supercontinuum generation through a standard fiber is a topic that has not been analyzed in detail, however, the development of devices capable of providing the power required to induce nonlinear phenomena in telecom fibers allow researching supercontinuum generation in this fiber. The progress in the field of supercontinuum generation is due to large measure to remarkable advancement in the features provided by new pumping sources, features such as: spectral width and level of power supplied, which can found in a microchip laser of ps regime.

10.1.1 Modulation Instability and Stimulated Raman Scattering in Short Lengths of Optical Fibers

Modulation instability can be interpreted as a four waves mixing (FWM) between Fourier components and intense continuous wave or quasi-continuous wave, derivate from the noise, inside a spectral region where phase matching exists [10]. The change in phase produced by the dispersion, can be compensated by self-phase modulation (SPM) and cross-phase modulation (XPM) only in group velocity dispersion (GVD) anomalous region; while in normal region, phase conditions can be satisfied by vectorial differences presented in every polarization state or fiber modes [10, 11].

Other nonlinear fiber optics effects are related to the vibration excitation modes of a propagating medium and are known as Stimulated Ramman Scattering (SRS) and Stimulated Brillouin Scattering (SBS). Quantum-mechanically the SRS consist in a phenomena when incident light beam photons are dispersed by silica molecules, by that suffer a frequency shifting, obtaining two new photons with different frequencies: one with lower value than the original optic radiation named Stokes frequency and other higher named anti-Stokes frequency [10]. There are a wide range of theoretical [12, 13] and experimental studies on MI and SRS in both normal- and anomalous-dispersion regimes which mostly was done using fibers of several meters [12–20].

10.2 Theoretical Model

The propagation of pulses in optical fibers is described by the NLSE

$$i\frac{dQ}{dZ} - \frac{\beta_2}{2}\frac{d^2Q}{dt^2} + \gamma|Q|^2Q = 0 \qquad (10.1)$$

Here Z and t denote the distance and retarded time (in the frame traveling at the group-velocity) coordinates; β_2 and γ are the group-velocity dispersion and the nonlinear coefficient, and Q is the field envelope. In dimensionless units, and in the normal dispersion regime (i.e., $\beta_2 > 0$), Eq. (10.1) reads as:

$$i\frac{dq}{dZ} - \beta_2\frac{d^2q}{dT^2} + |q|^2q = 0 \qquad (10.2)$$

where $T = t/t_0$, $Z = z\gamma P_0 = z/L_{NL}$, $\beta^2 = \beta_2/(T_0^2\gamma P_0) \equiv L_{NL}/L_D$, where L_{NL} and L_D are the nonlinear and dispersion lengths, respectively, $q = Q/\sqrt{P_0}$, t_0 is the initial pulse width, and P_0 is the peak power.

Depending on the initial width t_0 and the peak power P_0 of the incident pulse, either dispersive or nonlinear effects may dominate along the fiber. The dispersion length L_D and the nonlinear length L_{NL} provide the length scales over which dispersive or nonlinear effects become important for pulse evolution.

In order to study the solution stability against perturbation, a small perturbation is introduced into Eq. (10.2), which gives:

$$i\frac{dq}{dZ} - \beta^2\frac{d^2q}{dT^2} + |q|^2q(a + a^*) = 0 \qquad (10.3)$$

This linear equation can be solved easily in the frequency domain. However, because of the a^* term, the Fourier components at frequencies Ω and $-\Omega$ are coupled. Thus, the solution is considered in the form

$$a(z, T) = a_1\exp(i(Kz - \Omega T)) + a_2\exp(-i(Kz - \Omega T)) \qquad (10.4)$$
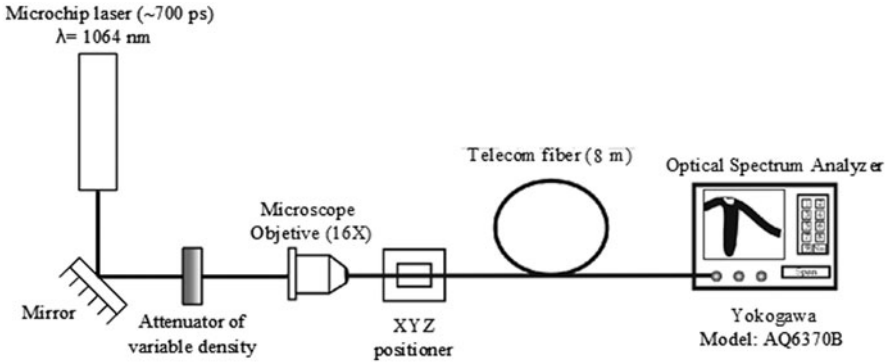
Fig. 10.1 Experimental setup for analysis between modulation instability and stimulated Raman scattering in short lengths of optical fibers

Where K and Ω are the wave number and the frequency of perturbation, respectively. Equations (10.3) and (10.4) provide a set of two homogeneous equations for a_1 y a_2. This set has a nontrivial solution only when K and Ω satisfy the following dispersion relation

$$K = \pm \frac{1}{2}\beta_2\Omega\left(\Omega^2 + \text{sgn}\,(\beta_2)\,\Omega_c^2\right)^{1/2} \tag{10.5}$$

Where $\text{sgn}\,(\beta_2) = \pm 1$ depending on the sign of β_2,

$$\Omega_c^2 = \frac{4\gamma P_0}{|\beta_2|} = \frac{4\gamma}{|\beta_2|\,L_{NL}} \tag{10.6}$$

The two terms in Eq. (10.4) represent two different frequency components, $\omega_0 + \Omega$ and $\omega_0 - \Omega$, that are presented simultaneously. These frequency components correspond to the two spectral sidebands that are generated when modulation instability occurs.

The dispersion relation (10.5) shows that steady-state stability depends critically on whether light experiences normal or anomalous GVD inside the fiber. In the case of normal GVD ($\beta_2 > 0$), the wave number K is real for all Ω, and the steady state is stable against small perturbations. By contrast, in the case of anomalous GVD ($\beta_2 < 0$), K becomes imaginary for $|\Omega| < \Omega_c$, and the perturbation $a(z, T)$ grows exponentially with z as seen from Eq. (10.4).

The experimental setup is illustrated in Fig. 10.1, in which a pulsed signal was used as a pump. The pulsed signal was provided by a microchip laser (Teem Photonics, MNP-08E) which is running at 1064 nm at 8.7 kHz repetition rate and 700 ps duration of the pump pulse. Two 8 m length fibers were used for the test, one of them is 1060XP fiber with a cut off wavelength at 980 nm and 5.8 μm core diameter. The other fiber was a communication standard single mode fiber (SMF-28) with 9-μm core diameter.

Increasing the lasers average power between 12 and 20.5 mW (Fig. 10.2) shows that similarity between generated spectra of the fibers is decreased. In this case two
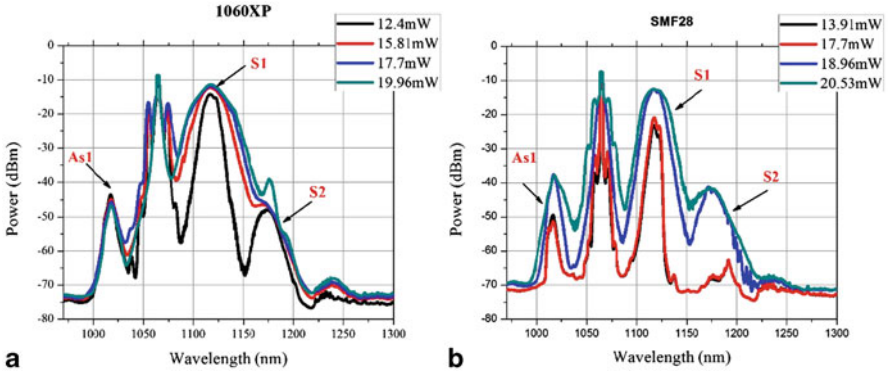
Fig. 10.2 Spectra outputs for the input beam intensities between 12 and 20.5 mW. **a** 1060XP fiber, and **b** communication fiber (SMF28)
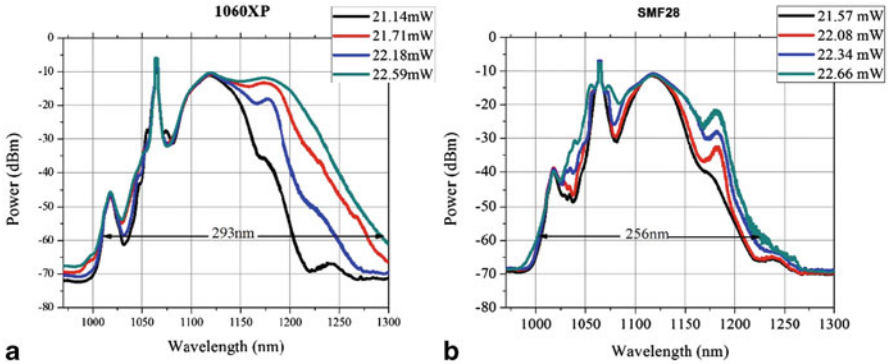
Fig. 10.3 Spectra outputs for the input beam intensities bigger than 21 mW. **a** 1060XP fiber, and **b** communication fiber (SMF28)

Stokes in both fibers are observable. However on 1060XP second Stokes formation (S2) is initiated with a pumping power of 12.4 mW, while on SMF28 S2 formation begins at 18.96 mW. Another important difference between both spectra is defined observing AS1, which reach a higher gain on the communication fiber with an amplitude of − 37.56 dBm, beating 1060XP fiber for almost 10 dBm. Also 1060Xp first Stokes presents a widening spectra wider than the other (enhanced by 31.97 nm).

Output spectra of both fibers with pump intensity higher than 21 mW are presented in Fig. 10.3. Differences are more notorious in this case. Raman amplification is most benefited on 1060XP with 263 nm range.
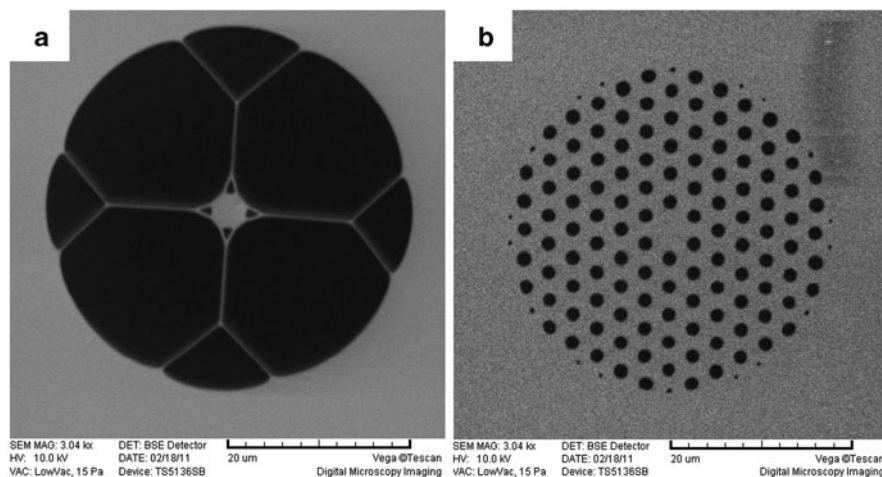
Fig. 10.4 Microscope image of cross section of microstructured PCFs used in the experimental setup. The PCF is denoted in this work by **a** PCF1, and **b** PCF2

10.2.1 Propagation of Q-Switch Laser Pulse in Two Different PCFs for Supercontinuum Spectrum Generation

In this section we show that in the nanosecond regime it is possible to obtain an improved supercontinuum spectrum which has a significantly larger bandwidth in comparison to others works presented up today. The supercontinuum spectrum is induced through two different photonic crystal fibers (PCF) having solid core. The different microstructures of the PCFs are used as means of propagation, while the pump is formed by pulsed Nd: YAG with output pulses of 6 ns and a central wavelength of 1064 nm. An important aspect is the optical scheme developed, which has the ability to have proper control over the power output to the output of the pump source, which allows to go step by step analyzing the evolution of supercontinuum spectra generated; the scheme also allows an adequate protection ot the PCsF used in the work, which can be damaged by high energy generated by the pulses from the laser. Another novelty is application of nanosecond pumping, as this regime has not been reported to study the evolution of the SG. Getting advantages of the type of the fiber used, the pulse width, control of the laser output power and wavelength of operation we can stimulate non-linear effects in a relatively simple and controlled manner.

PCFs have different structures in comparison to conventional optical fibers, their structures are based on a solid or hollow core surrounded by an array of air holes can be periodic or not periodic, which extends along the all length of the fiber as shown in Fig. 10.4. Profiles in Fig. 10.4 were obtained using an electronic microscope. The experimental setup used in this section is shown in Fig. 10.5. The scheme seeks to obtain the evolutions of the supercontinuum spectrum for each PCF shown in Fig. 10.4. Table 10.1 shows the physical parameters of PCFs. As a pumping source
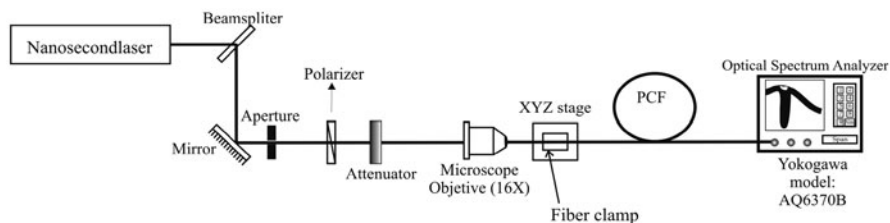
Fig. 10.5 Experimental scheme to study the evolution of the supercontinuum spectrum in the PCFs

Table 10.1 Table of physical parameters in the PCF used

PCF parameters	(PCF Fig. 10.4a)	(PCF Fig. 10.4b)
Core diameter	4.10 μm	4.51 μm
Pitch	5.91 μm	2.87 μm
Hollow diameter	7.28 μm (major) 0.23 μm (minor)	1.23 μm
Fiber diameter	116.21 μm	118.13 μm
Fiber length	5.97 m	1.87 m

to the input of the PCF we used a pulsed Q-Switch Nd: YAG laser, which has the following characteristics: a central wavelength of 1064 nm, a repetition rate of the oscillator of 50 Hz, pulses with constant duration of 6 ns, energy in the pulse of 180 mJ and the output the average optical power is $\sim$ 9 W.

In order to provide adequate control over the amount of energy present at the output of the laser a beam splitter is used to attenuate the laser energy, reducing output energy by a factor of 10. Therefore, the amount of energy used in the pilot scheme was 10 % of the original signal. An aperture pinhole allows increasing or decreasing the intensity at the input of the polarizer. The polarizer together with the attenuator varies the power at the fiber input allowing a working range between 0.15 and 1.86 mW in the case of PCF1 and PCF2. The process previously described is necessary because it is not possible to work with the total energy provided by the laser, in addition, if all the energy is used the tip of the PCF is damaged. Subsequently, the laser beam is incident on an opening used to increase or decrease the laser spot, allowing choosing the appropriate intensity to avoid damage to the PCF, this part is implemented with a first check on the input power to the fiber. A polarizer is inserted in the scheme in order to rotate the shaft from 0 to 360° and to be able to obtain variations on the beam power after passing through the opening of the pinhole (which provides a second control on the power supplied to the fiber input). The third power control is achieved by inserting an attenuator after the polarizer, allowing selecting the desired output power to the input of the PCF.

With the proposed scheme an average input power to the PCF in a range from 0.15 to 1.86 mW is possible to accept. After passing through the optical elements that provide power control, the beam enters a lens with a magnification of 16X in order to obtain a maximum coupling between the input beam and the PCF under
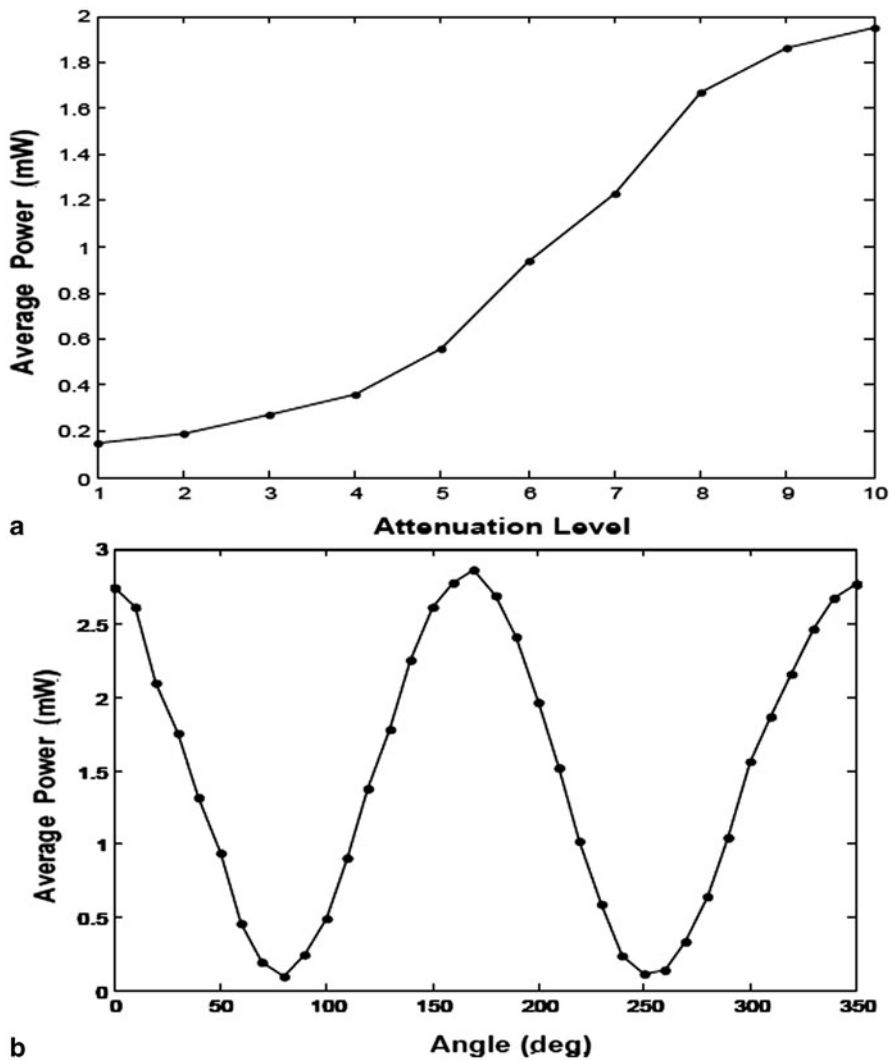
Fig. 10.6 Characteristic curves of the behavior of **a** attenuator, and **b** polarizer

test. A manual control XYZ base was used to hold the fiber for proper alignment with the input signal beam to propagate through the PCF and record the evolution of the spectrum of supercontinuum using an optical spectrum analyzer (OSA). In the experiments a fiber length of 5.91 m for PCF1 and 1.87 m for PCF2 is used. The scheme presented in Fig. 10.5 presents the optical elements needed to achieve the proper selection of input power into the PCF. The polarizer and the attenuator allow the passage of a beam that has a specific energy, which is related to the aperture size and the characteristic curves of the polarizer and attenuator are shown in Fig. 10.6.

The PCFs used are composed of silica as main element; estimating that the zero dispersion wavelengh is 1025 nm, which was calculated based on an empirical relation for the dispersion of PCFs [21].

10.3   Results and Discussions

The Fig. 10.4a shows a microstructure of PCF, in this case the hollow diameters are not equal as the microstucture is composed of three kinds of holes, the smaller ones have a diameter of 0.23 μm, the medium ones have a diameter of 2.16 μm and the larger ones have a diameter of 7.28 μm (see Table 10.1). These values were estimated on an image obtained through an electron microscope and based on the scale provided through the measuring element.

It is important to mention that this study has the objective to improve the super-continuum spectrum and investigate the evolution of the spectra in the nanosecond regime using a Nd:YAG laser delivering 6 ns pulses with a central wavelength of 1064 nm. The PCF spectra are compared with the final spectra obtained with the use of PCF1 and PCF2 at the same time in the experimental scheme of Fig. 10.5. As expected the final spectra obtained by each PCF is different due to the geometry of the micorstructures which is an essential part in the design of these kinds of fibers.

In this section the results of the supercontinuum spectra obtained for PCF1 are presented, the evolution is shown in Fig. 10.7. The figure shows the optical spectrum for different values of input power. The evolution begins showing only the spectrum of the pulse of the Nd:YAG laser which is centered at 1064 nm. With increasing power the spectrum widens due to nonlinear phenomena in the PCF, for low power values SPM is observed. Beyond ∼ 0.14 mW two lobes appear on each side of the main pulse spectrum which is the signature of modulation instability (MI). For higher power values phenomena like SRS and possibly FWM are generated and the spectrum continues widening until a broad supercontinuum spectrum is obtained for a power of ∼ 2.03 mW. The final spectrum obtained with the PCF1 is shown in Fig. 10.7f, where a wide spectrum between 600 and 1700 nm is observed. It has to be noted however that this spectrum does not present a good flatness, which is a disadvantage for some applications.

The results obtained for PCF2 are shown in Fig. 10.8. The optical spectrum show-ing the evolution again begins with the pulse spectrum of the Nd:YAG at 1064 nm. The spectrum broadens due to nonlinear phenomena in the PCF when input power is increased. However, in comparison to the spectrum of PCF1, the phenomenon of MI is not observed here. For higher powers the spectrum continues widening only to the long wavelength side, which indicates the interplay between SPM and GVD. The behavior of non-generation of short wavelength components indicates that FWM is not at play. The final spectrum obtained with the PCF2 is shown in Fig. 10.8f. A wide spectrum is shown between 930 and 1700 nm, in this case again the spectrum is not flat; moreover, shorter wavelengths are not observed. The process of devel-oping the SC source consisted in widening the spectrum of the pulsed pump source
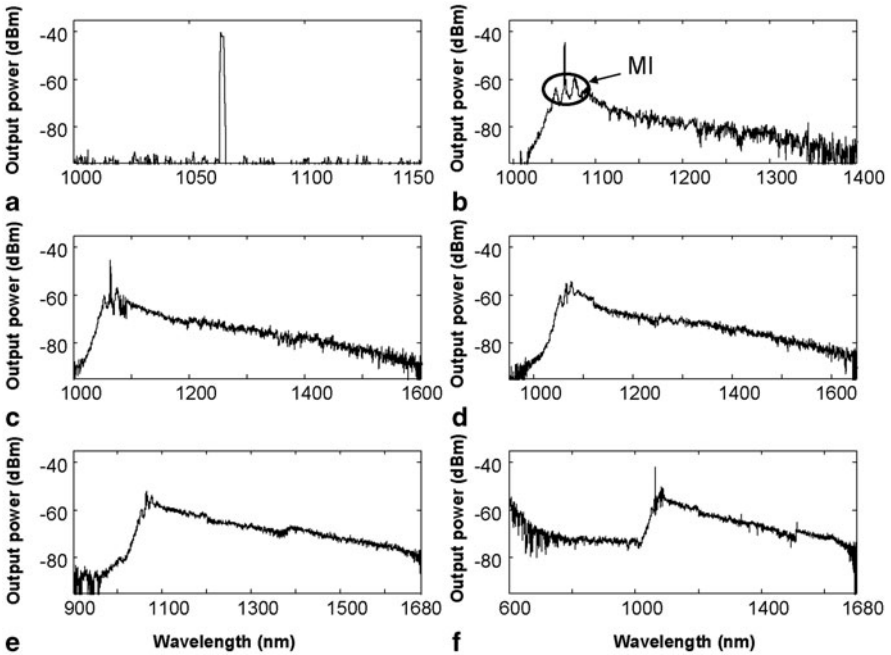
Fig. 10.7 Supercontinuum spectra of the PCF1 for input power values of **a** 0.15 mW, **b** 0.27 mW, **c** 0.36 mW, **d** 0.56 mW, **e** 1.23 mW, and **f** 1.86 mW

(Nd: YAG). This broadening was the result of a combination of different linear and nonlinear effects that occur under propagation of light inside the PCF. The input spectrum at low power is the reference signal to observe the evolution of SG by varying the input power. This shows the evolution of the spectrum of supercontinuum generated in the PCF discussed in the previous section, organized in such a way that shows the evolution of the laser pulses through the microstructure shown in Fig. 10.4a, while Fig. 10.7 shows the signal propagation within the microstructure presented in Fig. 10.4b. The spectra presented show the way in which the reference signal, undergoes a spectral broadening with increasing input power of the PCF, this widening is due to the nonlinearities present in the PCF and exploit the energy provided by pumping pulses.

Numerical studies presented in [14–16] mention that using pulses in the ns or even ps regime, or CW pump, the initial mechanism responsible for generating the pulse spectral broadening is the MI. As shown in Figs. 10.7b and 10.8b, as the input power into the PCF is increased, one can to see the MI, observing the characteristic lobes of the phenomenon being more prominent in the spectrum of Fig. 10.8. With increasing input power it is shown that the phenomenon of MI generates a break in very narrow pulses, thereby generating temporal solitons [22, 23], as shown in Figs. 10.7c and 10.8c. Subsequently, for higher power values the predominant phenomena were SRS and SPS, which can be appreciated by the transfer of energy to shorter frequencies
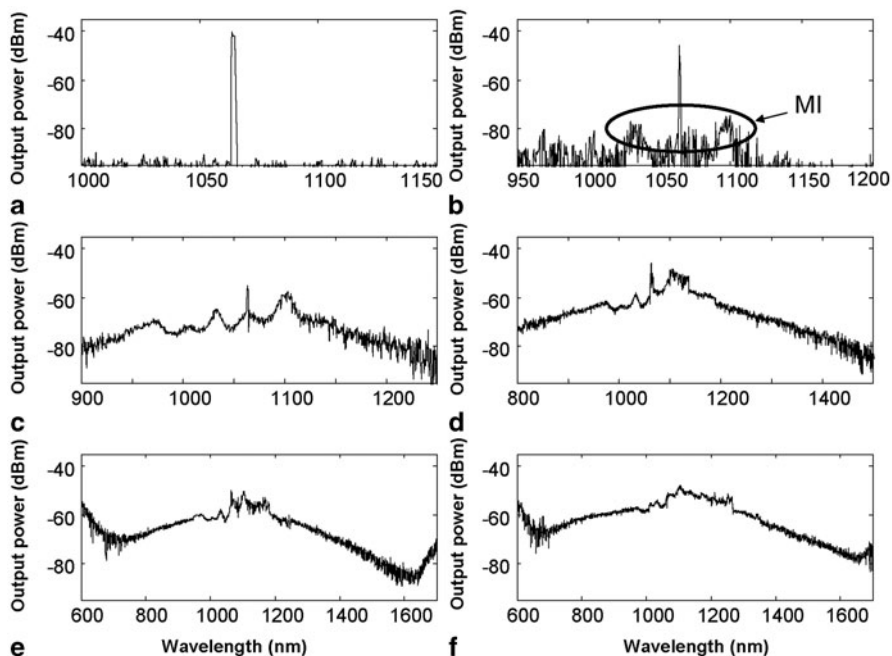
Fig. 10.8 Supercontinuum spectra of the PCF2 for input power values of **a** 0.15 mW, **b** 0.27 mW, **c** 0.36 mW, **d** 0.56 mW, **e** 1.23 mW, and **f** 1.86 mW

of the signal (Figs. 10.7d and 10.8d) [24]. At this point one can conclude that MI generates a reference pulse broadening and then this mechanism serves as a means to generate SPS and SRS. Another phenomenon that can be seen in the evolution of the spectrum is called FWM, in which the signal begins to spread to larger frequencies (Figs. 10.7e and 10.8e), this phenomenon may arise due to the power provided by the pump source used in the PCF. For average powers of around 1.86/2.03 mW, the final spectrum of SG is observed (Figs. 10.7f and 10.8f), and one can see a broad spectrum ranging from 980 to 1685 nm in the case of the first PCF (see Fig. 10.4a). The second spectrum (Fig. 10.8f) extends from 600 nm to beyond 1700 nm in the case of the second PCF (Fig. 10.4b). It is important to note the difference between the spectra generated for both PCF (differences are mainly due to the different microstructures of the fibers). Figure 10.7f shows an area which is predominantly made of low frequencies, while the spectrum of Fig. 10.8f presents symmetry that extends from high frequencies to low frequencies.

Significantly broad and flat supercontinuum spectrum generated in the ns regime through a PCF hybrid system is proposed experimentally. Awaiting the final spectrum showed a variety of advantages in comparison with other experimental results shown in recent works (focusing these in the flatness and broadband spectrum). It is possible supporting the experimental results through the estimation of dispersion (D) of PCF, in order to indicate the type of dispersion existing in the fibers and mention each of
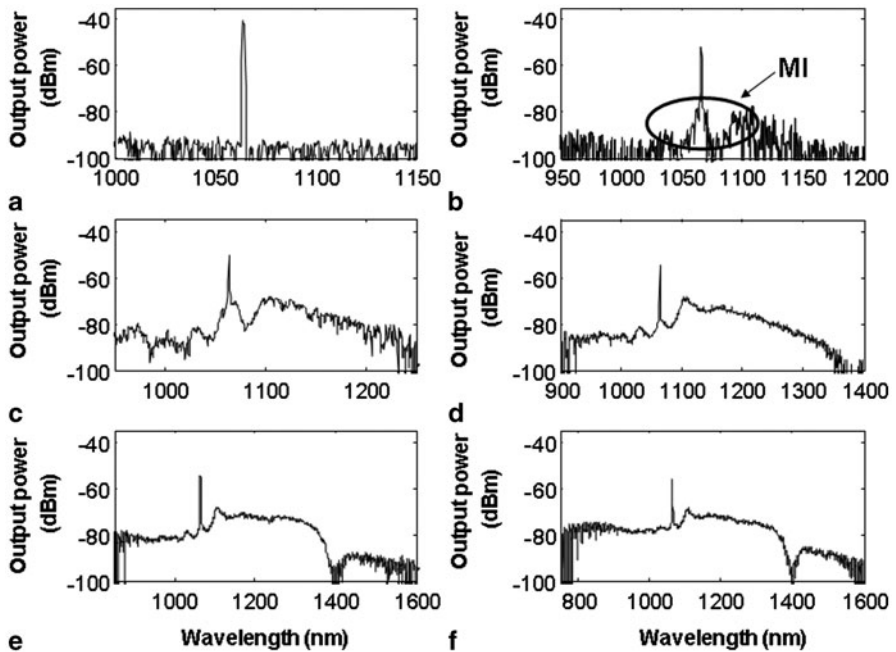
Fig. 10.9 Spectral evolution for the supercontinuum spectrum result of the PCF hybrid system proposed for **a** 0.15 mW, **b** 0.27 mW, **c** 0.36 mW, **d** 0.56 mW, **e** 1.23 mW, and **f** 1.86 mW

nonlinear phenomena generated on the spectral broadening (MI, SRS, FWM, SPM, XPM). The possibility to generate a final supercontinuum signal over 800 nm (full spectrum) with flatness better than three dB over two regions (790–1090 nm and 1150–1380 nm) is attributed to the peculiar properties of the PCF (see Fig. 10.8). An important conclusion is that using two consequent PCFs, it is possible extend and improve the flatness of generating supercontinuum.

Finally, analyzing the evolution of the spectra obtained in both PCF allowed to raise the issue of possible applications that can be given to the PCF in this paper. For this purpose there are proposals which are under discussion now and have begun to yield results. Such as the PCF fiber-optic tunable lasers able to be tuned to 3 different wavelengths, or an application is being studied in the field of temperature sensors and pressure gratings using electric arc in the analyzed PCF.

10.4 Conclusion

This chapter shows the developed supercontinuum source in which two different kinds of PCF are used. The evolution of the optical spectra is analyzed in the nanosecond regime using a Nd:YAG laser. The use of various microstructured fibers with

the purpose to improve the supercontinuum spectrum and to use this source in some applications of interest is possible. The optical arrangement developed in this work allowed an adequate control of the input power to the PCF under study and may show the evolution of the supercontinuum spectrum generated in two different microstructures of PCF. SG spectra were obtained using as the pump a Nd: YAG, which generates pulses of 6 ns duration (long pulse regime), using only a few mW of average power at the input of the fiber and exploiting the characteristics of input pulses. The spectra reported present an extension of ~ 710 nm for the PCF shown in Fig. 10.8f and greater than ~ 1100 nm for the microstructure presented in Fig. 10.9f. It was shown that pulses of 6 ns can be used to obtain supercontinuum generation and, therefore, a wide range of wavelengths. The development presented in this work is due to the SG is obtained more easily for the fs pulse regime and due to the lack of papers on experimental studies of SG in the ns regime. Ongoing work includes the development of possible applications of the PCF, according to the characteristics presented in the evolution of SG, now yielding applications in the field of tunable lasers, pressure and temperature sensors. The applications based on SC generation are of great importance in optical metrology, optical coherence, tomography and low noise sources for device characterization. Finally, the generation of SC in PCF for optical communication systems and wavelength tunable sources is another area of interest.

References

1. Alfano, R.R., Shapiro, S.L.: Emission in the region 4000–7000 Å via four-photon coupling in glass. Phys. Rev. Lett. **24**, 584–587 (1970)
2. Jáuregui-Vázquez, D., Estudillo-Ayala, J.M., Rojas-Laguna, R., Vargas-Rodríguez, E., Sierra-Hernández, J.M., Hernández-García, J.C., Mata-Chávez, R.I.: An all fiber intrinsic fabry-perot interferometer based on an air-microcavity. Sensors. **13**, 6355–6364 (2013). ISSN:1424–8220
3. Hartl, I., Li, X.D., Chudoba, C., Ghanta, R.K., Ko, T.H., Fujimoto, J.G., Ranka, J.K., Windeler, R.S.: Ultrahighresolution optical coherence tomography using continuum generation in an air-silica microstructure optical fiber. Opt. Lett. **26**, 608–610 (2001)
4. Sanders, S.T.: Wavelength-agile fiber laser using group-velocity dispersion of pulsed supercontinua and application to broadband absorption spectroscopy. Appl. Phys. B Lasers Opt. **75**, 799–802 (2002)
5. Smirnov, S.V., Ania-Castanon, J.D., Ellingham, T.J., Kobtsev, S.M., Kukarin, S., Turitsyn, S.K.: Optical spectral broadening and supercotinuum generation in telecom applications. Opt. Fiber Technol. **12**, 122–147 (2006)
6. Théberge, F., Aközbek, N., Liu, W., Becker, A., Chin, S.L.: Tunable ultrashort laser pulses generated through filamentation in gase. Phys. Rev. Lett. **97**, 023904(1) (2006)
7. Hernandez-Garcia, J.C., Estudillo-Ayala, J.M., Mata-Chavez, R.I., Pottiez, O., Rojas-Laguna, R., Alvarado-Mendez, E.: Experimental study on a broad and flat supercontinuum spectrum generated through a system of two PCFs. Laser Phy. Lett. **10**(7), 075101 (2013)
8. Vidne, Y., Rosenbluh, M.: Spatial modes in a PCF fiber generated continuum. Opt. Express. **13**, 9721 (2005)

9. Hernandez-Garcia, J.C., Pottiez, O., Estudillo-Ayala, J.M.: Supercontinuum generation in a standard fiber pumped by noise-like pulses from a figure-eight fiber laser. Laser Phy. **22**(1), 221–226 (2012)
10. Agrawal, G.P.: Nonlinear fiber optics, 3th edn. Academic, USA (2001)
11. Agrawal, G.P.: Modulation instabilty induced by cross-phase modulation. Phys. Rev. Lett. **59**(8), 880 (1987)
12. Weiping, H.: A coupled-mode analysis of modulation instability in optical fibers. IEEE J. Lightwave Technol. **10**(2), 156 (1992)
13. Chávez Boggio, J.M., Grosz, D.F., Fragnito, H.L.: Observation of modulation instability in the normal dispersion region over nonpolarization preserving fibers. Conference Proceedings - Lasers and Electro-Optics Society Annual Meeting-LEOS. IEEE. **1**, 242–243 (1999)
14. Cao, W.-h., Chan, K.-t.: Cross-phase modulation induced ultrashort pulse train generation from cw light in the normal-dispersion regime of optical fibers. Opt. Commun. **163**, 285 (1999)
15. Xu, W.-c., Zhang, S.-m., Chen, W.-c., Luo, A.-p.: Modulation instability of femtosecond pulses in dispersion-decreasing fibers. Opt. Commun. **199**, 355–360 (2001)
16. Pitois, S., Millot, G.: Experimental observation of a new modulational instability spectral window induced by fourth-order dispersion in a normally dispersive single-mode optical fiber. Opt. Commun. **226,** 415–422 (2003)
17. Zhang, S., Lu, F., Xu, W., Wang, J.: Phase modulation in decreasing dispersion fiber. Opt. Fiber Technol. **11**, 193–201 (2005)
18. Demircan, A., Bandelow, U.: Supercontinuum generation by the modulation instability. Opt. Commun. **244**, 181–185 (2005)
19. Zhong, X., Xiang, A.: Cross-phase modulation induced modulation instability in single-mode optical fibers with saturable nonlinearity. Opt. Fiber Technol. **13**, 271–279 (2007)
20. Gutiérrez, J.G., Vargas-Trevio, M., Romero-Salanzar, C., Hernández Flores, O.A., Rojas-Laguna, R., Estudillo-Ayala, J.M., Vargas Rodriguez, E.: Influencia de la inestabilidad modulacional en la generación de un espectro continuo en fibras ópticas con pulsos de nanosegundos. Rev. Mex. Fís. **55**(5), 359–366 (2009)
21. Hernandez-Garcia, J.C., Estudillo-Ayala, J.M., Mata-Chavez, R.I., Pottiez, O., Rojas-Laguna, R., Alvarado-Mendez, E.: Experimental study on a broad and flat supercontinuum spectrum generated through a system of two PCFs. Laser Phy. Lett. **10**(7), 075101 (2013)
22. Zhuan, W.Z., Huang, W.C., Chiang, P.Y., Su, K.W., Huang, K.F., Chen, Y.F.: Millijoule-level Yb-doped photonic crystal fiber laser passively Q-switched with AlGaInAs quantum wells. Opt. Express. **18**, 27910–27915 (2010)
23. Horowitz, M., Barad, Y., Silberberg, Y.: Noiselike pulses with a broadband spectrum generated from an erbium-doped fiber laser. Opt. Lett. **22**, 799–801 (1997)
24. Holzwarth, R., Udem, Th., Hansch, T.W., Knight, J.C., Wadsworth, W.J., Russell, P.St.J.: Optical Frequency Synthesizer for Precision Spectroscopy. Phys. Rev. Lett. **85**, 2264 (2000)

Chapter 11
Extremely High Power CO$_2$ Laser Beam Correction

Alexis Kudryashov, Alexander Alexandrov, Alexey Rukosuev and Vadim Samarkin

Abstract This paper presents the design of the closed loop adaptive system to measure and correct for the aberrations of CO$_2$ laser radiation. We considered two wavefront sensors—one sensor is based on commercially available IR camera while the second one—on the so-called thin film sensors. Also we present the design of two bimorph deformable mirrors to be used under high power laser radiation. We discuss both positive and negative attributes of these devices and the possibility to use them in the real laser high-power systems.

11.1 Introduction

It is very well known that the wavefront of the radiation of most of high power lasers is highly aberrated. This does not allow to obtain a good focus and high concentration of the energy of laser beam. The reason for the wavefront distortions are first of all thermally induced aberrations in active elements and also some residual aberrations of various optical elements. In general the initial quality of each optical element is high enough (P-V about λ/10) but the whole optical setup consists sometimes of tens of such elements that altogether introduce sufficiently large aberration. So, in order to improve the quality of the input laser beam first one needs to be able to measure it and after correct for them. If we talk about some solid state lasers that generate in the range of 400–1100 nm there is a huge variety of wavefront sensors, interferometers that could be used for this application. Also coating technique for mirrors is very well developed —one can get up to 99.98 % of reflectivity of the mirror. But as soon as we move to far infrared spectrum (10 μ radiation) the situation changes—there are almost no commercially available wavefront sensors that could be used in this range. On one hand it is understandable—there is a problem with a reliable infra red cameras (arrays of independent sensors) or single sensors. At the same time—most of industrial lasers and laser complexes are still based on high power CO$_2$ lasers with

A. Kudryashov (✉) · A. Alexandrov · A. Rukosuev · V. Samarkin
Adaptive Optics Lab, Moscow State Technical
University (MAMI), Moscow, Russia
e-mail: kud@activeoptics.ru

10.6 μ output! And this kind of radiation need to be evaluated, moreover, in the real time and also corrected! One of the first, and probably, the only work demonstrating the application of adaptive optics to correct for industrial CO_2 laser wavefront was published in 1995 [1].

This paper represents two types of Hartmann wavefront sensors— one—based on bolometer IR camera produced by INO, Canada. Another—is based on Russian technology of thin film deposition on Si substrates.

11.2 Hartmann Wavefront Sensor—General Remarks

Hardware and software of Hartmann sensor have some important advantages:

- Characterize response functions of bimorph mirror;
- Reconstruct wavefront and intensity distribution simultaneously;
- Possibility to measure both CW and pulse radiation and single shots;
- Ability to estimate a quality of laser radiation;
- Wide dynamic range;
- High precision;
- Fast measurements;
- Low sensitivity to mechanical noises and vibrations;
- Low-cost.

One of the demands of any optical system—is its reliability and ability to work not only in laboratory, but also in the real conditions, so that every student could use it and not break it. From this point of view Hartmann wavefront sensor is the most suitable one to be included in industrial laser [2]. These kinds of sensors are widely used by astronomers or in medical research but in fact very rarely were applied to control for laser beam. One of the shortcoming of existing wavefront sensors—is their relatively high price, that varies from 25,000 $ to 60,000 $ or even to 200,000 $ (it depends on the tasks and parameters of the system).

11.2.1 Some Theory

The wavefront measurements by Hartmann wavefront sensor (HS) are based on the measurements of a local slopes of a distorted wave front $\partial\varphi/\partial n$. So, the whole wavefront is divided in several subapertures by some set of diaphragms and the deviation of the spot from some reference position in each subaperture is measured. Figure 11.1 gives some idea about the work of the HS.

The centroid position (x, y) of a spot is calculated as

$$x = \sum_{i=1}^{m}\left(\sum_{j=1}^{n} i I_{ij}\right) \bigg/ \sum_{i=1}^{m}\left(\sum_{j=1}^{n} I_{ij}\right) \quad y = \sum_{i=1}^{m}\left(\sum_{j=1}^{n} j I_{ij}\right) \bigg/ \sum_{i=1}^{m}\left(\sum_{j=1}^{n} I_{ij}\right)$$

where i, j are pixels of some sensing square, I_{ij} –optical intensity distribution.
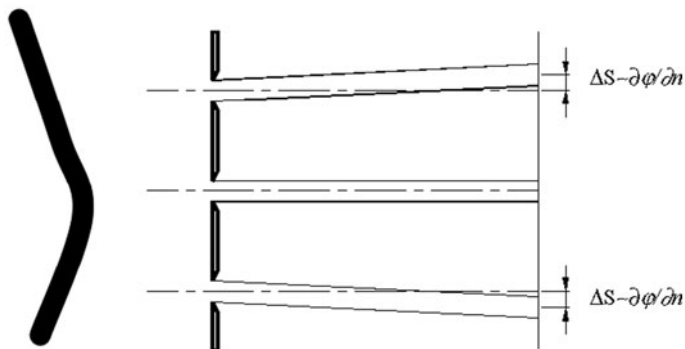
Fig. 11.1 Idea of Hartmann sensor

Fast Fourier transformation is applied to determine number of focal sports on hartmannogram N and the angle of hartmannogram alignment relative to the boundary of sensing matrix. The phase function with some accuracy could be presented as the superposition of M orthogonal functions:

$$\varphi(x, y) = \sum_{k=0}^{M} a_k F_k(x, y)$$

where x, y—coordinates of NX x NY spots, F_k- two-dimensional orthogonal function (Zernike polynomial, for example) and a_k–coefficients to be determined.

The local slope of the wavefront is obtained as:

$$S^x = \sum_{k=1}^{M} a_k \frac{\partial F_k}{\partial x}, S^y = \sum_{k=1}^{M} a_k \frac{\partial F_k}{\partial y}$$

Or in matrix form:

$$\vec{S} = A\vec{a}$$

where A- so-called gradient rectangular matrix with M columns and $2 \times N$ rows.

Therefore the coefficients a_k could be obtained by least-squares solution of $\min \| S - Aa \|^2$:

$\vec{a} = B \cdot \vec{S}$, where $B = (AA^t)^{-1} A^t$

Figure 11.2 gives the view of the standard image of the HS picture (hartmannogram) on the standard CCD camera

11.3 Computer Code

The developed algorithm was tested by modeling the distortions of the wavefront with low order aberrations (with the noise and rotation of the diaphragm array vs sensing matrix) of the hartmanogramms. The maximal time of complete processing

Fig. 11.2 Example of
hartmannogramme
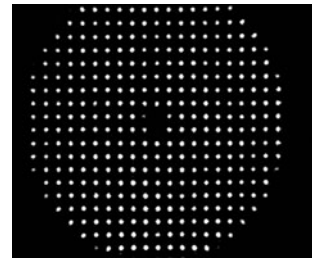
by optimum algorithm was about 2 ms. The obtained Zernike coefficient gave a good agreement with the predetermined (Fig. 11.2).

As a result of measurements we obtain: Peak-to-Valley (P-V) of wavefront and root-mean-square error (RMS); coefficients of wavefront aberrations in terms of Zernike polynomials expansion and terms of Seidel aberrations; 3D, 2D distributions of phase and intensity and also synthesized fringes for different beam shapes. As long as the phase $\varphi(x, y)$ and the amplitude of the beam intensity $I(x, y)$ were obtained, it was possible to calculate far field intensity distribution (Fig. 11.3). Beam quality M2 is obtained as ratio between the diameters of measured beam and Gaussian beam in a focus. Focal diameters are obtained by Fourier transform of initial beam and Gaussian beam, synthesized on the same aperture with the following calculation of second moments of intensity distribution. It should be noted that there is an important advantage of such M2 way of estimation compare to standard beam analyser. Hartmann sensor does not only estimate beam quality as number but also defines aberrations affected on it. At the same time Hartmann wavefront sensor can measure M2 only single mode laser beams [2].

Wavefront reconstruction for sure is associated with the accuracy of spots centers definition and dynamic range of phase measurements. These parameters depend on the distance between diaphragm array and sensing area and number of holes (pitch) on the beam aperture and wavelength of input radiation. Besides the measurements made by sensor are more precise, if we can define more precisely spots centers on discrete structure of sensing area, and therefore measure smaller spots displacements. Dynamic range has the opposite tendency: for its extension we have to choose diaphragm array with large pitch and smaller distance to sensing area. As far as our sensor specification, its accuracy is $\lambda/10$–$\lambda/100$ and dynamic range for tilts up to 100λ.

In this paper we present two types of Hartmann sensors—one based on IR commercial camera and another one—on thin film technology sensors.

11.4　Hartmann Sensor Based on IR Bolometer Camera

Picture of such sensor is presented on Fig. 11.4. To build wavefront sensor on the base of commercial IR camera has several advantages, such as compactness; convenience to use it for various applications; it is like standard video camera—"plug and
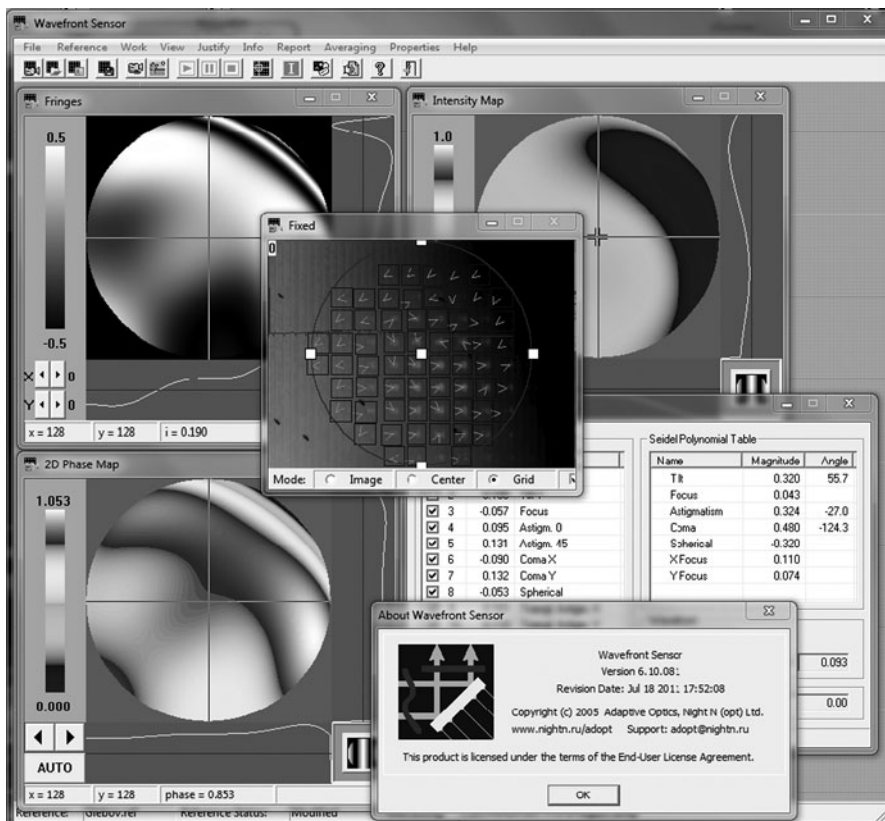
Fig. 11.3 Computer code realization—user interface

play"; possible high resolution. In our case we constructed this sensor based on INO (Canada) IR camera. Below we give the main parameters of the "bolometer" sensor.

- Sensor INO160—Microbolometer uncooled FPA bolometer; 160X120 pixels; 52 mm pitch
- Video Output—Gigabit Ethernet Link RJ-45 connector; 16 bit raw data; 8 bit corrected data
- Frame Rate—30 Hz (with extension to 60 Hz)
- Number of input diaphragms—16 × 16, 20 × 20
- Available Options—External trigger input (opto-isolated); TEC driver; Microshutter electronic driver; Serial interface; Thermistor interface (x2); Random access readout; Real time clock
- Overall Dimensions–65 mm(H) X 60 mm(W) X 105 mm(L)
- Weight∼ 230 g

This is a very convenient device, but it also has some disadvantages: all bolometer cameras are too sensitive to input radiation. And as soon as you want to use them

Fig. 11.4 Hartmann sensor
based on IR camera

to measure the radiation of some industrial lasers you need to be very careful not
to destroy the sensor and to provide a complicated set of filters. Another problem—
input window has a limited size. So, if the input high power laser beam has large
aperture a special telescope should be used to reduce the input beam size to fit the
sensing window.

11.5 Sensor Based on Thin Film Technology

Figure 11.5 presents the idea of Hartmann sensor based on thin film technology. It
consists of set of diaphragms and a sensing area—a number of quadrant thermo-
electric converters (TEC) made on thin film technology. Main advantage of such
wavefront sensor is it could be used with high CW power laser beams and plus
large aperture beams might be easily detected. Parameters of proposed sensor are
the following:

Wavelength of measurements, 4–12 μ;
Input beam size-ring Ø 160 x 80 mm;
Number of subapertures—72;
Range of measurements—50 μ;
Precision of measurements— < 0.6 μ;
Frame frequency—80 Hz;
Interfacing port—USB.

Figure 11.6 demonstrates the photo of Hartmann wavefront sensor to measure high
power laser beams.

As a thermo-electric converters we used the anisotropic quadrant elements shown
on Fig. 11.7.
Properties of converter:
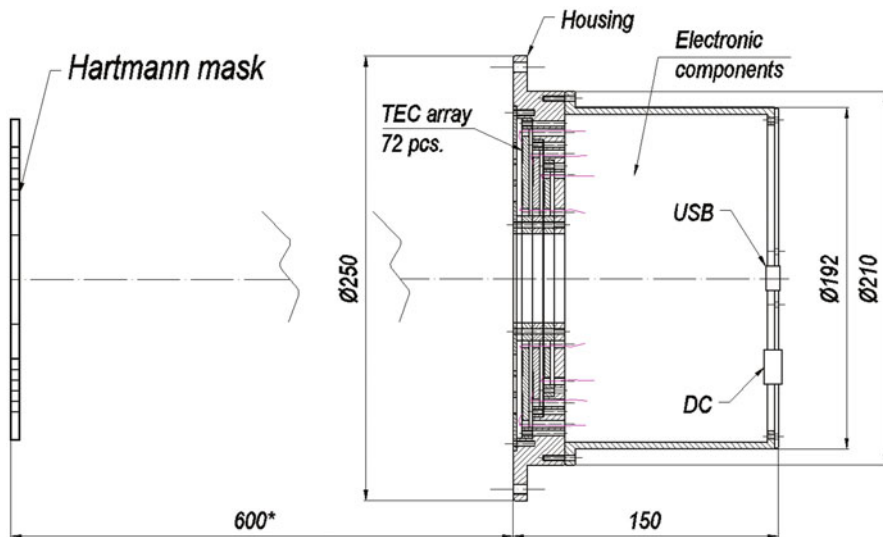
Fig. 11.5 Thing-film Hartmann sensor

Fig. 11.6 Photo of
Hartamann wavefront sensor
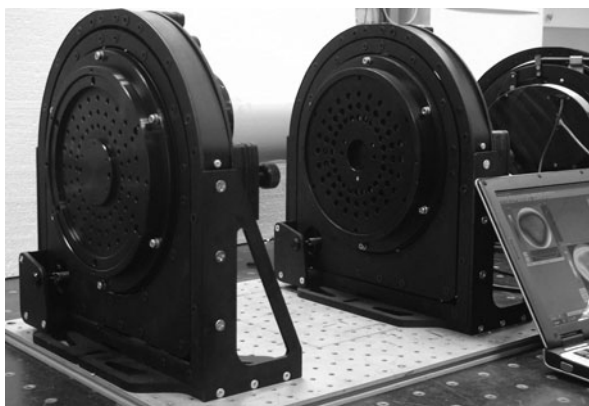
Material	Si
Thickness of layer	0.465 mm
Working wavelength	$\lambda = 4\text{--}12\,\mu$
Absorption for $\lambda = 10{,}6\,\mu$ and $\alpha = (0\text{--}13)^\circ$	$< 10\,\%$
Sensitivity for $\lambda = 10{,}6\,\mu$,	$> 0.5\,\text{mV/W}$
Response time	$< 10^{-3}\,\text{s}$
Resistance	$< 100\,\text{Om}$
Resistance of isolation	$> 10\,\text{kOm}$

It is interesting to point out that main disadvantages of this kind of sensors are
continuation of their advantages—they cannot measure small input beams and low
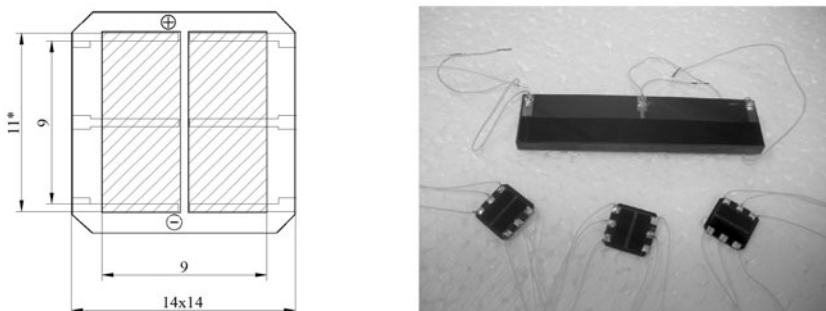
Fig. 11.7 Quadrant TECs

Table 11.1 Parameters of two types of water-cooled deformable mirrors.

Mirror with waffle cooling structure	Aperture	Up to 180 mm
	Mirror quality	1.2 μ
	Deformation range	40 μ
	Frequency bandwidth	800 Hz
	Reflecting coefficient	$> 98\,\%$ at $\lambda = 10.6\,\mu$
	Substrate material	Cooper
Mirror with "passive" cooling system	Aperture	Up to 80 mm
	Mirror quality	1 μ
	Deformation range	16 μ
	Frequency bandwidth	1500 Hz
	Reflecting coefficient	98.5 % at $\lambda = 10.6\,\mu$
	Substrate material	Silicon

CW power beams. At the same time—number of subapertures of such a sensors is also limited by its design. And they have a large size, so it is not very comfortable to install them.

11.6 Deformable Mirror

As a wavefront corrector we suggest to use a watercooled bimorph deformable mirror (Fig. 11.8) [3, 4]. Main advantage of the use of such type of correctors is that they almost perfectly fit the aberrations (mainly thermally induced) of laser beam that need to be compensated. We either use wafer type water cooling system (Fig. 11.8a) or so called passive cooling system (Fig. 11.8b). Main parameters of proposed deformable mirrors are presented in Table 11.1.
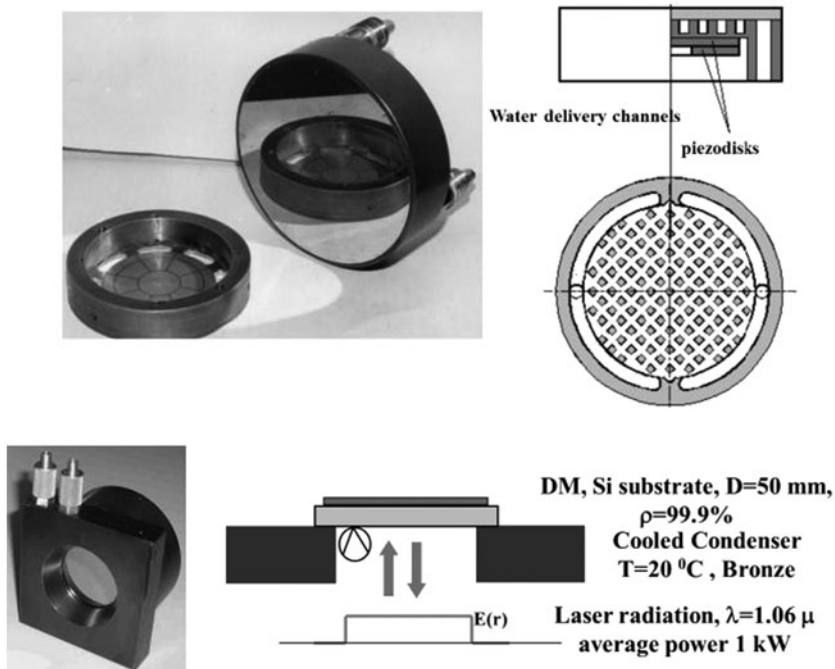
Fig. 11.8 Water-cooled deformable mirrors: top—waffle structure of cooling; bottom—"passive" cooling system

11.7 Conclusion

We demonstrated two types of wavefront sensors to measure the radiation of CO$_2$ lasers and two types of deformable mirrors to correct for high power CO$_2$ laser radiation. They both have advantages and problems. And only field of application determines which kind of mirror or sensor is the most appropriate.

References

1. Kudryashov, A.V., Samarkin, V.V.: Control of high power CO$_2$ laser beam by adaptive optical elements. Opt. Comm. **118**, 317–322 (1995)
2. Sheldakova, J.V., Kudryashov, A.V., Zavalova, V.Y., Cherezova, T.Y.: Beam quality measurements with Shack-Hartmann wavefront sensor and M2-sensor: comparison of two methods. Proc. SPIE. **6452**, 207 (2007)
3. Samarkin, V., Aleksandrov, A., Kudryashov, A.: Novel wavefront correctors based on bimorph elements. In: Restano, S.R., Teare, S.W. (ed.) Proc. 3rd Int. Workshop on Adaptive Optics for Industry and Medicine, 23–26 July 2001, Albuquerque, NM, USA, pp. 171–178, Starline Printing, Inc (2002)
4. Kudryashov, A.V., Samarkin, V.V.: Bimorph mirrors for correction and formation of laser beam. In: Love, G. (ed.) Proc. 2nd Int. Workshop on Adaptive Optics for Industry and Medicine, 12–16 July 1999, Durham, England, pp. 193–199, World Scientific (2000)

Chapter 12
Measurements of Intense and Wide-Aperture Laser Radiation Parameters with Thinwire Bolometers

S. V. Pogorelov

Abstract Measurement methods of parameters and characteristics of intense (up to several tens of kilowatts in continuous mode and up to several tens of kilojoules in pulse mode) and wide-aperture laser radiation with bolometric gauges have been considered. The bolometric gauges are able to work in wide spectral range, withstand high levels of laser power or pulse energy. The considered methods use bolometric grids, which are loop-through type gauges and consume a low part of laser radiation. The maximal size of input aperture of bolometric grids has no limitations. Non-linearities of bolometer transformation characteristics have been considered.

12.1 Introduction

Measurement of parameters and characteristics of intense (up to several tens of kilo-watts in continuous mode and up to several tens of kilojoules in pulse mode in single pulse) and wide-aperture laser radiation is a complex scientific and metrological problem. The measured parameters of laser radiation are power of continuous radiation, energy of single pulse, average power of modulated radiation, direction of linear polarization, parameters of elliptic polarization, coefficient of intensity distribution non-uniformity in beam section, coordinates of energy center, diameter of optic beam with the specified part of intensity. The characteristics of laser radiation are intensity and phase distributions in beam section, profile of intensity distribution along certain coordinate's directions in beam section.

Accurate measurements of laser power and beam focus position are important for laser materials processing: both are listed as process essential variables for quali-fication of welding procedures and should, therefore, be controlled within agreed tolerances.

Laser power can be measured using standard laser power meters; there are two main types: calorimeter and pyroelectric. And new kinds of detectors for measuring laser radiation have been proposed regularly [1]. Calorimeter power meters measure

S. V. Pogorelov (✉)
National University of Pharmacy, Kharkov, Ukraine
e-mail: svpog@yahoo.co.uk

laser power using a timed exposure. They display average power absorbed on a calibrated readout scale and can be used for measuring the average of either continuous or pulsed power output. They usually have a response time of up to several seconds.

Pyroelectric power meters are relatively fast but cannot be used to measure continuous laser power directly, since this type only responds to changes in incident energy. These are the preferred choice for measuring the output of pulsed lasers with repetition rates up to several 100 kHz.

Currently, there is a wide choice of commercially available laser power meters. Selection of a particular meter for a given application will depend on the spectral range, sensitivity or minimum required response, and damage threshold. To produce a reproducible and accurate measurement, all laser power meters should be regularly calibrated.

For infrared high-power laser radiation the classical measurement methods of considered parameters and characteristics [2–4] are practically hard to use since they are intended for low levels radiation intensity and have low sizes of input aperture. There are some difficulties with measurements of single pulses of laser radiation.

Matrices of photodiodes or pyroelectric elements are widely used in the visible, near and middle infrared ranges for measurements of laser radiation parameters [5]. These arrays gauges are able to measure laser radiation parameters with power 100 µW to 10 W and up to several tens of kilowatts with usage of attenuators. Input aperture sizes of the matrix vary from one to several tens of millimeters.

A thinwire lattice or single scanning bolometer is one of the laser radiation receivers to measure intense and wide-aperture laser radiation. The bolometric receivers can withstand high levels of measured densities of continuous power and single pulse energy, are able to work within wide spectral range, are loop-through gauges with a low coefficient of radiation absorption and have no restrictions on maximal size of input aperture. The damage possibility of receiving element (melting or break off) is the main weakness of the thinwire bolometers.

The principle of the thinwire bolometric gauges is based on the phenomena of electromagnetic radiation interaction with metallic cylinder with finite conductivity. A part of incident radiation on the bolometer is absorbed. Bolometer electric resistance changes as a result of bolometric cylinder heating (bolometric effect). The value of resistance change depends on temperature coefficient of resistance of cylinder material. It should be noted that main physical parameters of the bolometer depends on bolometer temperature which in turn leads to nonlinearity of bolometer transformation characteristic of laser radiation.

The parameters of interaction with radiation—factors of absorption efficiency (FAE) $q^{E/H}$ for E-polarized and H-polarized radiation and coefficient of dichroizm $K_D = \frac{q^H}{q^E}$ are used in bolometric effect. FAE of bolometer are equal to the appropriate absorption coefficients $A^{E/H}$ at geometric optic approximation when cylinder diameter d is much more longer than radiation wavelength λ. FAE of the bolometer depend on incident angle of radiation on the bolometer Θ, radiation wavelength λ, complex index of refraction $m = m^{/} - im^{//}$, where $m^{/}$ and $m^{//}$ are refraction index and absorption index of cylinder material, ratio of cylinder radius to radiation wavelength a/λ and cylinder elliptic degree in its cross-section.

The exact solution of the problem of the flat electromagnetic wave diffraction on an absorbing cylinder is well known [6]. There were some difficulties at the solution with Bessel and Henkel function calculation for high values of complex arguments of the functions which are determined with complex refraction index for the most of metal, radiation wavelength 10 μ and values $a/\lambda > 10$.

The gauges in the form of two practically identical bolometric grids made of thin metal fibers have been suggested to measure continuous power and single pulse energy of laser radiation [7, 8]. The grids are located close to each other, have constant period and fibers of two grids are located orthogonally to each other. The laser pulse duration at energy measurements have to be much shorter than heat-time constant of the bolometer. The increase of bolometer resistance under this condition is proportional to absorbed optical energy. The grids perform spatial integration of radiation intensity distribution in beam cross-section. 1 % integration error can be achieved for circular beam with uniform intensity distribution if beam is crossed with 10 grid fibers. The grid period have to be less than two root-mean-square radii of the beam for the case of Gauss distribution of power or energy in a laser beam cross-section.

12.2   Bolometer Transformation Characteristic

Let's consider a bolometer with length *2l* directed along an axis with origin of coordinates in the middle of the bolometer. The temperature increase distribution along the bolometer $T(x)$ relative to environment temperature T_0 is settled by the end of radiation pulse. The total increase of relative bolometer resistance in case of temperature resistance coefficient (TRC) of the bolometer determined with a polynomial of the second order is

$$\frac{\Delta R}{R_0} = (\alpha_0 + \alpha_1 \delta \overline{T})\overline{T}, \qquad (12.1)$$

where R_0—is initial bolometer resistance; $\alpha_0 = \alpha_0' + \alpha_1 T_0$ and α_1—are linear and square-law coefficients of bolometer TRC (α_0'—is bolometer TRC at $T_0 = 0°C$); $\overline{T} = \frac{1}{2l}\int_{-l}^{+l} T(x)dx$—is average temperature of the bolometer heating; $\frac{1}{2l}\int_{-l}^{+l} T^2(x)dx = \overline{T^2}$—is average square of bolometer heating temperature and $\overline{T^2} = \sigma_T^2 + \overline{T}^2 = (1 + \sigma_{T_0}^2)\overline{T}^2 = \delta\overline{T}^2$ (where σ_T and σ_{T_0}—are absolute and relative root-mean-square deviations (RMSD) of temperature from the mean value $\overline{T}$; $\delta = 1 + \sigma_{T_0}^2$—is introduced coefficient of temperature distribution non-uniformity along the bolometer. The relation (12.1) shows that temperature distribution non-uniformity increases the nonlinearity of the bolometer resistance increment in σ times.

One of the best materials for bolometer is platinum. It has high melting temperature 1769°C, is an anticorrosive and nonmagnetic material. The tabulated dependence of specific platinum resistance within temperature range 0. . . .1500°C has been taken

from [9] and has been approximated with polynomial of the second degree. As a result the coefficients $\alpha_0^/ = 3.978 \cdot 10^{-3} \text{deg}^{-1}$ with relative RMSD $\sigma_{\alpha_0^/} = 1 \cdot 10^{-4}$ and $\alpha_1 = -5.87 \cdot 10^{-7} \text{deg}^{-2}$ with relative RMSD $\sigma_{\alpha_1} = 5 \cdot 10^{-4}$ have been obtained.

The dependence of the platinum complex refraction index on radiation wavelength 10 μ within the specified temperature range has been estimated in classic optic approximation [10]. The necessary criterion of this approximation usage is relation between relaxation time of free electrons τ and period of electromagnetic field wave τ_u. The latter one τ_u has to be more than relaxation time of free electron τ. The relaxation time estimated with relations [11] is $\tau = 2.17 \cdot 10^{-14}$ s for $T_0 = 0°C$ and $\tau = 0.538 \cdot 10^{-14}$ s for $T_0 = 1000°C$ whereas $\tau_u = 3.53 \cdot 10^{-14}$ s. Thus the necessary criterion is satisfied. The platinum complex refraction index for fixed temperatures was determined and then temperature dependence of bolometer FAE with diameter 10 μ was estimated and approximated with least-square method as polynomial of the second degree

$$q^E(T) = q_0^{/E}(1 + q_1^/ \cdot T + q_2 \cdot T^2) \tag{12.2}$$

where $q_0^{/E} = 0.0377$; $q_1^/ = 1.38 \cdot 10^{-3} \text{deg}^{-1}$; $q_2 = -3.8 \cdot 10^{-7} \text{deg}^{-2}$ with relative RMSD $\sigma_{q_0^{/E}} = 0.012$; $\sigma_{q_1^/} = 0.029$ and $\sigma_{q_2} = 0.063$. The relative RMSD σ_{q^E} increases from 0.012 to 0.038 within temperature range from 0 to 1500°C.

Heat loses of the bolometer via heat-exchange with environment and via bolometer material heat-conductivity from its elementary part during optic pulse duration are insignificantly small and thus bolometer temperature increase distribution $T(x)$ is close to incident energy distribution $E(x)$.

The tabulated temperature dependence of specific heat-capacity of platinum from 0 to 1500°C has been taken from [12] and has been approximated with least-square method as polynomial of the second degree

$$c(T) = c_0^/ + c_1 T + c_2 T^2 \tag{12.3}$$

where $c_0^/ = 0.1321 \frac{J}{\text{deg}}$; $c_1 = 2.76 \cdot 10^{-5} \frac{J}{\text{deg}^2}$; $c_2 = 306 \cdot 10^{-9} \frac{J}{\text{deg}^3}$ with relative RMSD $\sigma_{c_0^/} = 0.0013$; $\sigma_{c_1} = 0.017$ and $\sigma_{c_2} = 0.82$. It is obtained that dependence $c(T)$ is too close to linear one.

The heat-balance equation for elementary part of the bolometer is

$$mc[T(x)]dT(x) = q[T(x)] \cdot E(x) \tag{12.4}$$

where m—is a linear bolometer mass; $E(x)$—is a linear incident energy on the bolometer. The averaged along the bolometer length Eq. (12.4) is :

$$\frac{c_0^/ + c_1\delta\overline{T}}{q_0^/ + q_1\delta\overline{T} + q_2(\delta\overline{T})^2}d(\delta\overline{T}) = d\left(\frac{\delta\overline{T}}{m}\right) \tag{12.5}$$

where $c_0^/ = c_0 + c_1 T_0$, T_0—is environment temperature; $q_0^/ = q_0 + q_1 T_0 + q_2 T_0^2$; $q_1 = q_1^/ - 2q_2 T_0$; $\delta = 1 + \sigma_{E_0}^2$—is coefficient of non-uniformity of incident energy distribution and σ_{E_0}—is its relative RMSD. The values σ_{T_0} and σ_{E_0} are very close. Let's

Table 12.1 Please insert missing text here

$T_0°C$	0	20	40
η_0, g/J	1.136	1.159	1.181
η_{0P}, cm/W	0.493	0.494	0.495
a_E, g/J	$1.367 \cdot 10^{-4}$	$1.361 \cdot 10^{-4}$	$1.354 \cdot 10^{-4}$
a_P, cm/W	$-6.3 \cdot 10^{-3}$	$-8.0 \cdot 10^{-3}$	$-9.6 \cdot 10^{-3}$
b_E, g^2/J^2	$-2.71 \cdot 10^{-8}$	$-2.76 \cdot 10^{-8}$	$-2.82 \cdot 10^{-8}$
b_P, cm^2/W^2	$-1.5 \cdot 10^{-3}$	$-1.4 \cdot 10^{-3}$	$-1.3 \cdot 10^{-3}$

introduce an effective temperature $T_e = \delta \overline{T}$ and effective linear incident energy $E_e = \delta \overline{E}$. The solution of the Eq. (12.5) with initial condition $E_e/m = 0$ and $T_e = 0$ is [13, 14]

$$\frac{E_e}{m} = \frac{1}{\sqrt{-\Delta}} \left(c_0' - c_1 \frac{q_1}{2q_2} \right) \ln \frac{(2q_2 T_e + q_1 - \sqrt{-\Delta})(q_1 + \sqrt{-\Delta})}{(2q_2 T_e + q_1 + \sqrt{-\Delta})(q_1 - \sqrt{-\Delta})} +$$
$$+ \frac{c_1}{2q_2} \ln \frac{q_0' + q_1 T_E + q_2 T_E^2}{q_0'}, \tag{12.6}$$

where $\Delta = 4q_2 q_0' - q_1^2 < 0$.

Dependencies $\frac{E_e}{m}$ on T_e for values T_e from 0 to 1500 °C have been estimated for environment temperatures $T_0 = 0°C$, 20°C and 40 °C. The relative RMSD of calculation $\frac{E_e}{m}$ is $\sigma_{E_0} = 0.013$.

The relative increase of bolometer resistance (12.1) may be set down as:

$$\frac{\Delta R}{R} = \eta_0 F \left(\frac{E_e}{m} \right) \frac{\overline{E}}{m}, \tag{12.7}$$

where $\eta_0 = \frac{\alpha_0 q_0}{c_0}$ and

$$F \left(\frac{E_e}{m} \right) = \frac{c_0}{q_0} \left(1 + \frac{\alpha_1}{\alpha_0} T_E \right) \frac{T_e}{E_e/m} = 1 + a_E \frac{E_e}{m} + b_E \left(\frac{E_e}{m} \right)^2. \tag{12.8}$$

The calculated values $F(E_e/m)$ have been approximated with least-square method as polynomial of the second degree and coefficients a_E and b_E have been estimated with relative RMSD $\sigma_{\eta_0} = 0.012$, $\sigma_{a_E} = 4 \cdot 10^{-3}$ and $\sigma_{b_E} = 7 \cdot 10^{-3}$. The received results are shown in the table 12.1.

Dependencies $F(E_e/m)$ on E_e/m are shown at Fig. 12.1 One can see that systematic error of transformation characteristic nonlinearity $\Theta = F(E_e/m) - 1$ can achieve $+18\%$. The initial transformation coefficient η_0 within the specified environment temperature range increases linearly by 4 %.

The bolometer transformation coefficient of continuous power ha been determined with TCR of platinum $\alpha(T)$, FAE $q(T)$ and with coefficient of heat exchange with
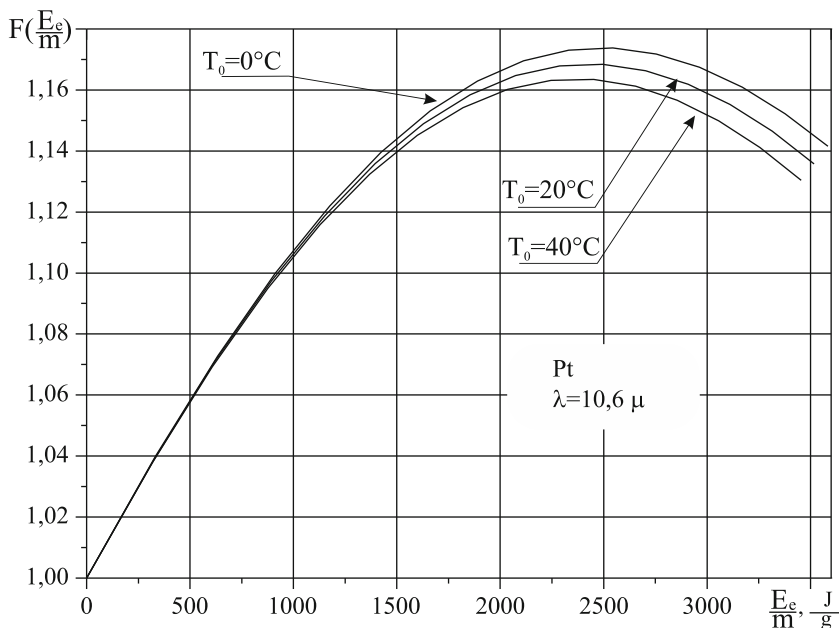
Fig. 12.1 Dependencies $F(E_e/m)$ on E_e/m

environment $\gamma(T)$. The solution of heat-balance equation for elementary part of the bolometer is

$$\gamma[T(x)]dT(x) = q[T(x)] \cdot dP(x), \tag{12.9}$$

where $P(x)$—is linear power and dependencies $q(T)$ and $\gamma(T)$ in the form of polynomial of the second degree has been obtained for averaged along the bolometer length Eq. (12.9) in the form of dependence of effective incident power $\overline{P}_e = \delta\overline{P}$ on effective heat temperature $T_e = \delta\overline{T}$ [15]. Using this solution the dependence of normalized transformation coefficient has been estimated with least-square method

$$F(\overline{P}_e) = 1 + a_P P_e + b_P P_e^2 \tag{12.10}$$

and equation of bolometer measurement is

$$\frac{\Delta R}{R_0} = \eta_{oP}(P_e)\overline{P}, \tag{12.11}$$

where $\eta_{oP} = \frac{\alpha_0 q_0}{\gamma_0}$—is an initial transformation coefficient of the bolometer

Coefficients for $\gamma(T)$ were determined in [16]. They have the values $\gamma = 2.93 \cdot 10^{-4}$ W/(cm $\cdot$ deg) with relative RMSD $\sigma_\gamma = 0.01$; $\gamma_1 = 3.6 \cdot 10^{-7}$ W/(cm $\cdot$ deg^2) with relative RMSD $\sigma_{\gamma_1} = 0.02$; $\gamma_2 = 0$. Relative RMSD of values in (12.11) are: $\sigma_{\eta_0 P} = 0.01$, $\sigma_{a_P} = 0.05$ and $\sigma_{b_P} = 0.06$ for different temperatures T_0.
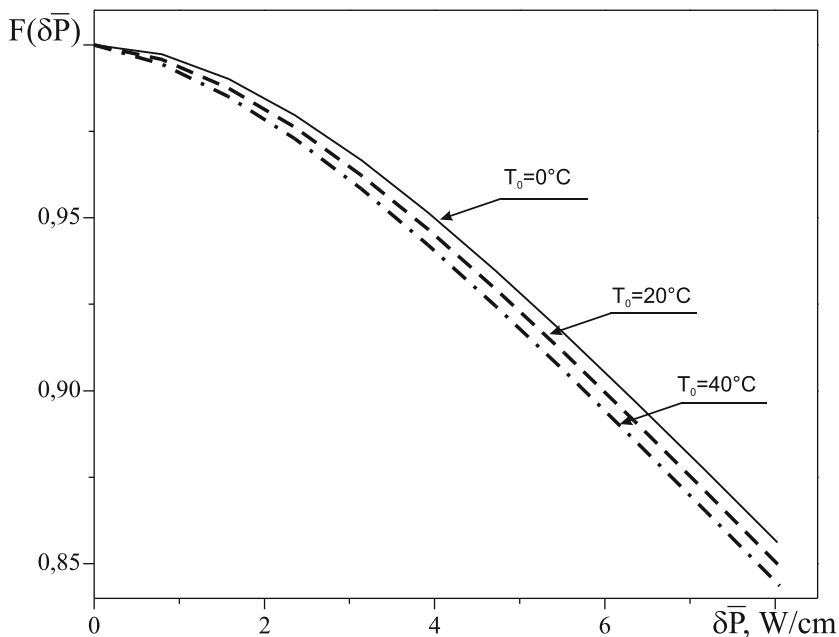
Fig. 12.2 Dependencies $F(P_e)$ on P_e

Dependencies $F(P_e)$ on P_e are shown at Fig. 12.2 One can see that systematic error of nonlinerity of bolometer transformation characteristic $\theta = F(P_e) - 1$ can achieve 15 %.

12.3 Measurements of Radiation Parameters with Bolometer in Linear Mode

The bolometer resistance increase in linear mode is proportional to absorbed radiation intensity.

One introduces a polarized coefficient of bolometer interaction with radiation. For linear polarization of radiation it is

$$k(\varphi) = \cos^2\varphi + K_D\sin^2\varphi, \tag{12.12}$$

where φ—is an angle between polarization direction and bolometer axis and $K_D = \frac{q^H}{q^E}$—is a coefficient of bolometer dichroism. For elliptic polarization of radiation the polarized coefficient of bolometer interaction with radiation is

$$k = K_D - (K_D - 1)\left(\xi_x^2\cos^2\psi + \xi_y^2\sin^2\psi + \xi_x\xi_y \sin 2\psi \cos\alpha\right), \tag{12.13}$$

where ψ—is an angle of bolometer direction in cross-section of radiation beam; ξ_x and ξ_y—are relative amplitudes of radiation field parallel and orthogonal to bolometer axis; α—is a phase shift between ξ_x and ξ_y.

The sum of polarization coefficients for two-grid bolometer with angles of its elements directions $\psi_1 = 0$ and $\psi_2 = \frac{\pi}{2}$ is $k_1 + k_2 = 1 + K_D$ either for linear, or elliptic polarization of radiation. The signal of the grid is a relative increase of it resistance under the radiation i.e.

$$U_i = \frac{\Delta R_i}{R_{io}} = \frac{e_i - e_{io}}{e_{io}},$$

where R_{io} and ΔR_i—are initial grid resistance and its increase; e_{io}—is direct voltage of electric shift on the bolometer, and e_i—is a maximal voltage at grid under radiation. The sum of grid signals U_1 and U_2 at radiation pulse energy measurement in accordance with (12.7) is

$$U_1 + U_2 = \frac{\Delta R_1}{R_{1o}} + \frac{\Delta R_{21}}{R_{2o}} = \frac{\alpha_0 q_0^E}{C_0}(1 + K_D)\frac{\bar{E}}{m}. \tag{12.14}$$

The total beam energy of laser radiation E is

$$E = S\frac{m}{d_\delta}\left(\frac{\bar{E}}{m}\right) = \frac{mlxnc_0}{d_\delta\alpha_0 q_0^E(1 + K_D)}\left(\frac{\Delta R_1}{R_{1o}} + \frac{\Delta R_2}{R_{2o}}\right), \tag{12.15}$$

where S—is an area of a single grid; d_δ—is a bolometer diameter.

The total power of continuous power of radiation P is

$$P = S\frac{\bar{P}}{d_\delta} = \frac{lxnc_0}{d_\delta\alpha_0 q_{0P}^E(1 + K_D)}\left(\frac{\Delta R_1}{R_{1o}} + \frac{\Delta R_2}{R_{2o}}\right). \tag{12.16}$$

The measuring error of q_0^E introduces the dominating contribution to cumulative error of energy and power measurements with usage of high-sensitive and low-inertia analog-to-digital convertor (ADC) for signal registration. In the work [17] it is shown that the relative RMSD of pulse energy is $\sigma_{E_0} = 0.2\%$ and relative RMSD of continuous power is $\sigma_{P_0} = 0.53\%$.

Spatial beam parameters are calculated with registered signals from grid elements $U_{i,j}$ which have coordinates x_i and y_i where $i, j = 1, \ldots n$.

The coordinates of beam energy center are

$$\bar{x} = \frac{1}{n}\sum_{i=1}^{n} x_i \frac{U_i}{\overline{U}_x}; \quad \bar{y} = \frac{1}{n}\sum_{j=1}^{n} y_i \frac{U_j}{\overline{U}_y}. \tag{12.17}$$

The root-mean-square radius along the X-coordinate is

$$r_x = \left[\frac{1}{n}\sum_{i=1}^{n}(x_i - \bar{x})^2\frac{U_i}{\overline{U}_x}\right]^{1/2}. \tag{12.18}$$

The root-mean-square radius along the Y-coordinate r_y can be found with the similar expression and mean root-mean-square radius of the beam is determined as a geometrical mean of values r_x and r_y:

$$r = (r_x \cdot r_y)^{1/2}. \tag{12.19}$$

The coefficients of distribution non-uniformity of radiation intensity along the coordinate axis are determined with a formula

$$\delta_{x,y} = \frac{1}{n} \sum_{i,j=1}^{n} \frac{U^2{}_{i,j}}{\overline{U}^2{}_{x,y}}, \tag{12.20}$$

and the coefficient of the whole beam is $\delta = \delta_x \cdot \delta_y$.

The generalized area of the beam is $S_0 = S/\delta$.

One has to draw up the dependence $F(x_k) = \sum_{i=1}^{K} \frac{U_i}{U_x}$ in order to estimate the beam diameter with specified part of radiation intensity. This dependence is analogous to of the accumulated distribution in the probability theory and it varies from 0 to 1.

Values of coordinates $x^/$ and $x^{//}$ are determined for given part of radiation intensity $p = 1 - \beta$ with relations $F(x^/) = \frac{\beta}{2}$ and $F(x^{//}) = 1 - \frac{\beta}{2}$.

The beam diameter along the X-coordinate is $d_x = x^{//} - x^/$. The beam diameter along the Y-coordinate is determined similarly for the same part of radiation intensity $d_y = y^{//} - y^/$. The total beam diameter is determined as mean-geometrical of values d_x and d_y, i.e. $d = (d_x d_y)^{1/2}$.

12.3.1 Estimation of Radiation Linear Polarization Direction

Parameters of linear polarization of laser radiation may be measured with two-grid bolometer [18–20]. Grid element direction angles are $\psi_1 = 0$ and $\psi_2 = \frac{\pi}{2}$. Normalized signals on a value proportional to total radiation intensity, which is a grid signals sum (12.16) are:

$$U_{in} = \frac{U_i}{\eta_0 \overline{E}/m} = (K_D + 1)\frac{U_i}{U_1 + U_2} = k_i, \; i = 1,2 \tag{12.21}$$

and they are equal to polarization coefficients of interaction k_i. Proceeding from the formula (12.12) one obtains the values of angles φ_{i_1,i_2} relative to both grids

$$\varphi_{i1,i2} = \psi_i \pm \left\{ \frac{1}{K_D - 1}\left[\left(K_D + 1\right)\frac{U_i}{U_1 + U_2} - 1 \right] \right\}^{1/2} \tag{12.22}$$

Two angles φ_{i_1,i_2} are obtained for each grids and an angle measurement ambiguity is eliminated with a coincidence of angles relative to grids in optical beam section.

Experimental measurements were carried out in the following way. The coefficient of dichroism K_D was measured for bolometers with diameter $10\,\mu$ beforehand. The grids can rotate with respect to direction of a linear polarization of radiation. Their signals were registered and the value K_D was estimated with the relation (12.21). The averaged value $K_D = 1.8285$ with relative RMSD $\sigma_{K_D} = 0.52 \cdot 10^{-2}$ was calculated from 20 measurements. Grid signals $U_1 = 0.1859$ and $U_2 = 0.2491$ were obtained for grid rotation angle of $30°$. The estimated with (12.22) angles are $\varphi_{11,12} = \pm 30.13°$ and $\varphi_{21,22} = +90 \pm 59.87°$. The measured value of the polarization angle is $\bar{\varphi} = \frac{1}{2}(\varphi_{12} + \varphi_{22}) = 30.13°$ and it well coincides with the fixed one. The estimation of errors showed that absolute RMSD of the measured angle of polarization direction is $\sigma_{\bar{\varphi}} = 0.23°$.

12.3.2 Estimation of Elliptic Polarization Parameters of Radiation

A three-grid bolometer with element direction angles $\psi_1 = 0$, $\psi_2 = +\frac{\pi}{3}$ and $\psi_3 = -\frac{\pi}{3}$ is used for measurements of elliptic polarization parameters of laser radiation [21, 22]. The sum of polarization coefficients (12.13) is

$$\sum_{i=1}^{3} k_i = 1.5(K_D + 1) \tag{12.23}$$

and it does not depend on radiation polarization state, and it is proportional to total radiation intensity. Grid normalized signals are

$$U_{in} = \frac{U_i}{\eta_0 \overline{E}/m} = 1.5\,(K_D + 1)\,\frac{U_i}{\sum_{i=1}^{3} U_i} = k_i, \quad i = 1, 2, 3 \tag{12.24}$$

and they are equal to polarization coefficients of grids interaction with radiation.

Values ξ_{xi}^2 and ξ_{yi}^2 of relative projections of radiation intensity on the axis of elements of i-th grid and perpendicular to it with origin of angle from this grid are estimated with (12.13)

$$\xi_{xi}^2 = \frac{K_D - U_i}{K_D - 1}; \quad \xi_{xi}^2 = \frac{U_i - 1}{K_D - 1}; \quad i = 1, 2, 3. \tag{12.25}$$

The angle φ of a major axis of the ellipse is a sum of degree of ellipse rotation with $\alpha = \frac{\pi}{2}$ and a supplementary rotation due to $\alpha \neq \frac{\pi}{2}$. It can be shown that the angle φ obeys the relation

$$tg2\varphi = \frac{A_{ij}\cos 2\varphi_i - \cos 2\varphi_j}{\sin 2\varphi_j - A_{ij}\sin 2\varphi_i}, \tag{12.26}$$

where

$$A_{ij} = \frac{\xi_{xj}^2 - \xi_{yj}^2}{\xi_{xi}^2 - \xi_{yi}^2}. \tag{12.27}$$

Relative intensity of radiation is related to relative square of ellipse axes of radiation ξ_η^2 and ξ_ζ^2 by the system of linear equations with two variables:

$$\xi_{xi}^2 = \xi_\eta^2 \sin^2(\varphi - \psi_i) + \xi_\eta^2 \cos^2(\varphi - \psi_i);$$
$$\xi_{x_i}^2 = \xi_\eta^2 \cos^2(\varphi - \psi_i) + \xi_\eta^2 \sin^2(\varphi - \psi_i), \quad i = 1, 2, 3 \qquad (12.28)$$

The solution of this system of equation gives values ξ_ζ^2 and ξ_η^2.

Experiments with bolometers with diameter $10\,\mu$ give the following results. Normalized signals are $U_{1n} = 1.6061$, $U_{2n} = 1.6136$ and $U_{3n} = 1.00018$ at the rotation of grids with respect to linear polarization direction of radiation by angle $60°$. Angles of the major axis direction of the ellipse turned out $\varphi_{12} = -59.70°$, $\varphi_{12} = -59.69°$ and $\varphi_{23} = -59.51°$. Calculations with formula (12.28) give the result: $\xi_{\eta_1}^2 = 0.0018$ and $\xi_{\xi_1}^2 = 1.0018$; $\xi_{\eta_2}^2 = 0.0023$ and $\xi_{\xi_2}^2 = 0.9975$; $\xi_{\eta_3}^2 = -0.0016$ and $\xi_{\xi_3}^2 = 0.9999$. Thus there is a case of ellipse degeneration into a line segment.

Averaged values are $\overline{\xi_\eta^2} = 0.0003$ and $\overline{\xi_\xi^2} = 0.9997$. The analysis of errors gives the absolute RMSD $\sigma_\varphi = 0.13°$ and absolute RMSD $\sigma_{\xi_\xi^2} = \sigma_{\xi_\eta^2} = 1.2 \cdot 10^{-2}$.

One can measure an angle of linear polarization direction with bolometer with three grids as well. The angle of radiation polarization direction is estimated with the same normalized grid signals

$$\varphi_{i1,i2} = \psi_i \pm \arcsin\left\{\frac{1}{K_D + 1}\left[1.5(K_D + 1)\frac{U_i}{\sum_{i=1}^3 U_i} - 1\right]\right\}^{1/2}, \quad i = 1, 2, 3.$$
$$(12.29)$$

Calculations give the following results: $\varphi_{12} = -59.77°$, $\varphi_{21} = -59.71°$ and $\varphi_{32} = -60.78°$. The averaged value of the angle is $\bar\varphi = -60.09°$. The absolute RMSD of measurement of angle φ is $\sigma_\varphi = 0.52°$.

12.4   Estimation of Polarization State and Energy Parameters of Laser Radiation in Nonlinear Mode

Three profiled grids are used to estimate polarization state of laser radiation [17]. One has to estimate a total pulse energy E and total power P of optic beam, polarization coefficients of interaction of grids with radiation k_i and coefficient of intensity distribution non-uniformity of radiation δ. After that the linearized grid signals U_i and polarization state of radiation are estimated.

We consider the method at continuous radiation with wavelength $10,6\,\mu$ with determined non-linearity of transformation characteristic of platinum bolometer with diameter $10\,\mu$. FAE of the bolometer for E- and H-polarized radiation $q^{E,H}(T)$ within temperature range $T = 0\ldots 1500\,°T$ and averaged coefficient $K_D = 1.381$ within the pointed temperature range with absolute RMSD $\sigma_{K_D} = 0.003$ have been calculated

with exact relations [12]. One has to solve the measurement equation to estimate linearized incident power P:

$$\sum_{i=1}^{3} U_i = \eta_{0P} \bar{P} \sum_{i=1}^{3} F_i(k_i \delta \bar{P}) k_i. \tag{12.30}$$

In this relation the $F_i(k_i \delta \bar{P})$—are normalized coefficients of bolometer transformation (12.10) and both k_i and δ depend on radiation intensity level. The equation is solved with step-by-step method. As the first approximation one considers that the bolometer runs in a linear mode. At this assumption the polarized coefficients of interaction are

$$k_i' = \frac{1.5(K_D + 1)}{1 + \frac{U_{i+1}}{U_i} + \frac{U_{i+2}}{U_i}}, \quad i = 1, 2, 3 \tag{12.31}$$

and coefficient of intensity distribution non-uniformity is

$$\delta = (\delta_1 \delta_2 \delta_3)^{2/3}, \tag{12.32}$$

where δ_i—is coefficient of non-uniformity distribution of i-th grid corresponding to relation (12.20).

The Eq. (12.30) becomes a form

$$M\left(\bar{P}\right) = -U_{\sum} + c\bar{P} + d\bar{P}^2 + f\bar{P}^3 = 0 \tag{12.33}$$

after substitution of relations $F_i(k_i \delta \bar{P})$, where

$$U_{\Sigma} = \frac{1}{\eta_{0P}} \sum_{i=1}^{3} U_i; \quad c = \sum_{i=1}^{3} U_{in}; \quad d = a_P \delta \sum_{i=1}^{3} U_{in}^2; \quad f = b_P \delta^2 \sum_{i=1}^{3} U_{in}^3, \tag{12.34}$$

and U_{in} are normalized grid signals (12.24). The Eq. (12.33) has only one real solution which determines the first approximation of $\bar{P}'$. The effective power $\delta\bar{P}'$ is estimated at the first approximation as well. Now corrections on systematic errors of values δ and k_i are introduced.

The second approximation of coefficients k_i'' is estimated with formula (12.31) but instead of the values U_i one uses values $F_i'(k_i' \delta\bar{P}') \cdot k_i'$. The dependencies of ratio k_i/k_i' on k_i' and $\delta\bar{P}'$ are shown at the Fig. 12.3. The factor for the second approximation of k_i'' is estimated with a curve on the graph. The similar curve for pulse energy measurements are shown at Fig. 12.4.

Dependencies of normalized on δ_0 coefficient of radiation intensity non-uniformity upon effective power or effective specific energy are shown at Fig. 12.5. These curves have been obtained with calculation at fixed Gaussian distribution of incident radiation with dependence on radiation intense. The curves allow to determine a systematic error at a second approximation of value δ''.
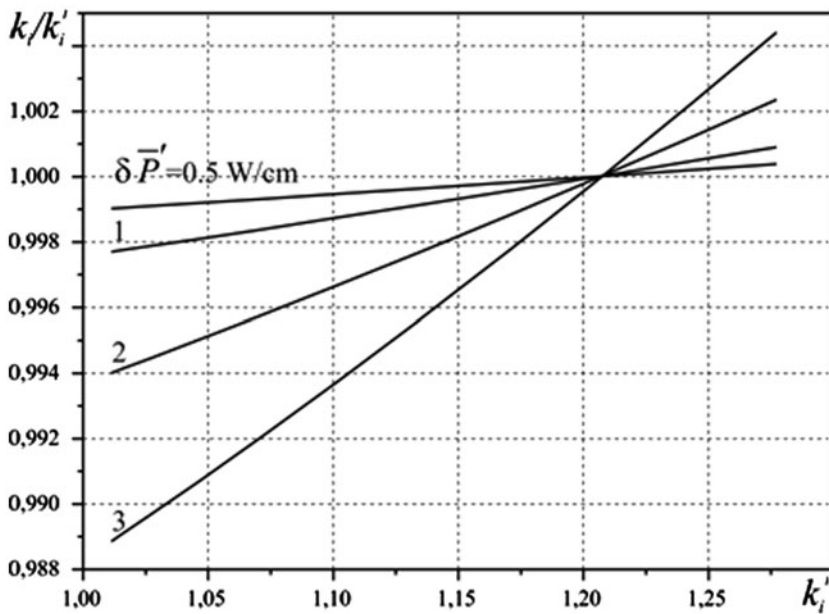
Fig. 12.3 Dependencies of ratio k_i/k_i' on k_i' and $\delta \overline{P}'$
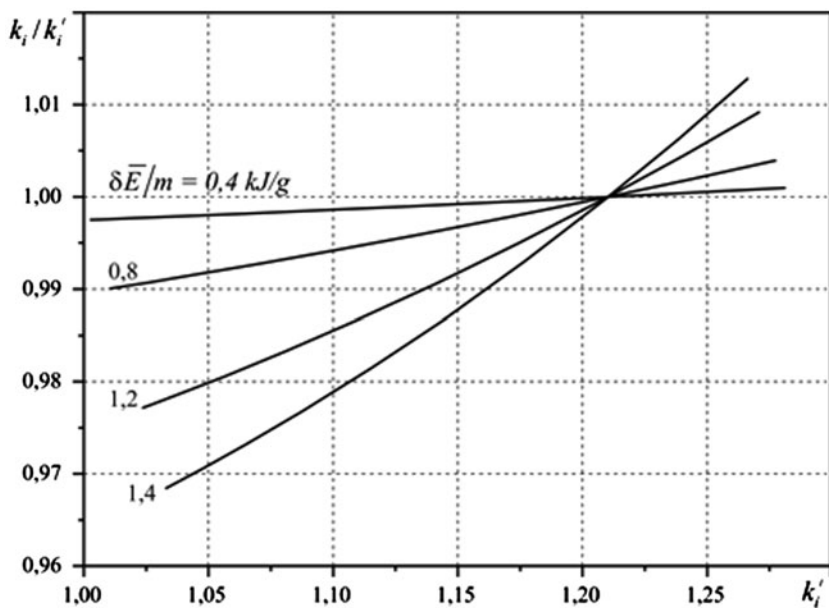
Fig. 12.4 Dependencies of ratio k_i/k_i' on k_i' and $\delta \overline{E}/m$
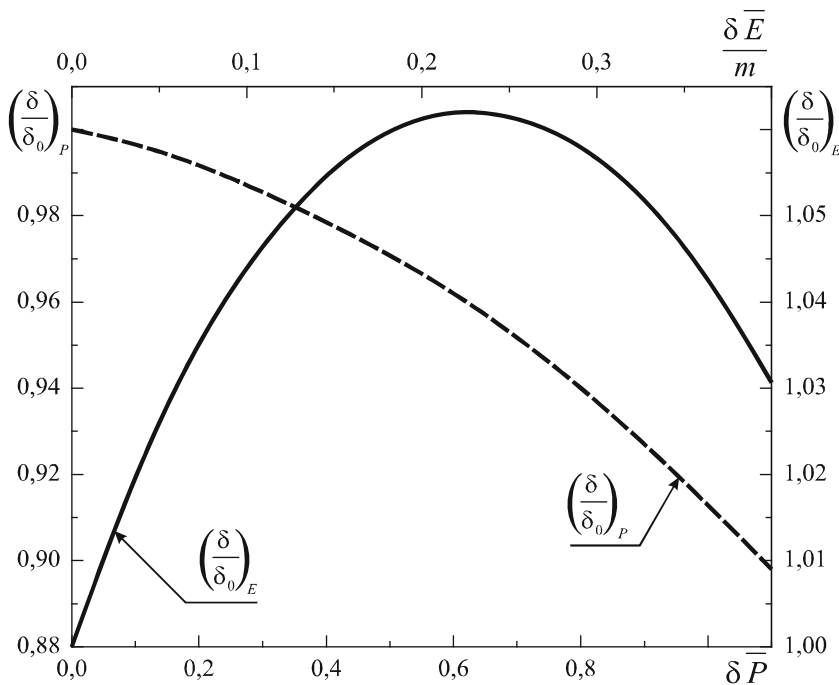
Fig. 12.5 Dependencies of coefficient of radiation intensity non-uniformity on effective power or effective specific energy

The Eq. (12.33) is solved with corrected values of coefficients c, d and f and after that the second approximation of $\overline{P}^{//}$ is estimated. The subsequent approximations one can carry out in the similar way until the admissible error of estimation of value $\overline{P}$ will be achieved. The total power of optic beam is

$$P = \frac{\overline{P}}{d_\delta} S. \tag{12.35}$$

One can use the two-grid bolometer working in the non-linear mode to measure pulse energy or continuous power. In this case the relations (12.31–12.35) should be applied where summation is carried out for two grid parameters only.

The same dependencies (Figs. 12.3, 12.4, and 12.5) as for three-grids bolometer are used to eliminate systematic errors of estimations of polarized coefficient of interaction k_i and coefficient of non-uniformity of intensity distribution δ.

Normalized transformation coefficients $F_i(k_i \delta \overline{P})$ and linearized signals of grids

$$U_i{}' = \frac{U_i}{F_i(k_i \delta \overline{P})}, \quad i = 1, 2, 3 \tag{12.36}$$

are estimated after determination of values k_i, δ and $\overline{P}$. Then polarization state of laser radiation is determined. The current technique allows to obtain the RMSD $\sigma_{U_i{}'} = 1.1 \cdot 10^{-3}$.

The suggested, grounded, experimental checked and constructed thin-wire bolometric gauges of intense and wide-aperture laser radiation are applied in scientific researches of powerful laser making and at realization of their radiation in various scientific and industrial applications.

References

1. Zhang, G.Y., Zheng, H.R., Zhang, X.Y., Gao, D.L., Zhang, P.X., Habermeier, H.U.: Time-integral type strongly correlated electronic thin-film laser energy meter. Appl. Phys. B. **108**, 649–655 (2012)
2. Lansberg, G.S.: Optika. Nauka Moscow (1976)
3. Ivanov, V.S., Zolotarevskiy, Yu.M., Kotyuk, A.F., Liberman, A.A., Sapritskiy, V.I., Stolyarevskiy, R.I., Ulakovskiy, M.V., Chupdakov, V.F.: Basis of Optic Radiometry. Physmatlit, Moscow (2003)
4. Grugoruk, V.I., Ivanisik, A.I., Korotkov, P.A.: Experimental Laser Optic. Kievskiy universitet, Kiev (2007)
5. Fang, H.-T., Huang, D.-S.: Extracting mode components in laser intensity distibution by independent component analysis. Appl. opt. **44**(18), 3646–3653 (2005).
6. Hulst, H. Light Scattering with Small Particles. Izd. Lit, Moskow (1961)
7. Kuzmichov, V.M., Pogorelov, S.V., Safronov, B.V., Balkashin, V.P., Priz, I.A., Kohns, P.: Thin-wire bolomer of laser pulse energy. Telecommun. Radioeng. **66**(9), 907–913 (2007)
8. Kuzmichov, V.M., Pogorelov, S.V., Pohil'ko, S.M., Kohns, P.: The method of absolute calibration of profile thin-wire bolometer for laser pulse energy measurements within long-wave range Patent of Ukraine 79796, 25 June 2007
9. Kikoin, I.K.: Table of Physical Values. Reference Book. Atomizdat, Moscow (1976).
10. Sokolov, A.V.: Optical Properties of Metals. Nauka, Moscow (1965)
11. Ditchburn, R.: Physical Optic. Nauka, Moscow (1965)
12. Zinov'ev, V.E.: Heat-Physical Properties of Metals Under High Temperatures. Metallurgiya, Moscow (1989)
13. Kuzmichov, V.M., Pogorelov, S.V.: Transformation of laser pulse energy with platinum thin-wire bolometer. Ukr. Metrol. J. **2**, 42–47 (2003)
14. Kuzmichov, V.M., Pogorelov, S.V.: Estimation of transformation characteristic of platinum bolometer for measurement of laser pulse energy. Meas. tech. **5**, 23–25 (2004)
15. Kuzmichov, V.M., Pogorelov, S.V., Kohns, P. Transformation of laser continuous power on wavelength 10,6 μ with platinum thin-wire bolometer. Ukr. Metrol J. **3**, 39–41 (2005)
16. Kuzmichov, V.M., Perepechay, M.P.: Low-inertia measurer of power of CO_2 laser. Quat novaja electronica **11**, 2407–2410 (1974)
17. Kuzmichov, V.M., Pogsssorelov, S.V., Kohns, P.: Measurement of power and pulse energy of laser radiation with three profile bolometric grids. Ukr. Metrol. J. **2**, 35–39 (2007)
18. Katrich, A.B., Kuzmichov, V.M.: Measurement of direction of polarization of electromagnetic radiation. Pulse photom. **5**, 129–131 (1978)
19. Kuzmichov, V.M., Kuzmichova, E.V.: Measurement of angle direction of linear polarization of laser radiation with non-linear thin-wire bolometers. Meas. Tech. **8**, 24–26 (1996)
20. Kuzmichov, V.M., Pogorelov, S.V., Safronov, B.V., Balkashin, V.P., Priz, I.A.: The method of measurement of linear polarization of laser radiation with two-grids bolometer. Patent of Ukraine 41595, 25 May 2009
21. Kuzmichov, V.M., Pogorelov, S.V., Safronov, B.V., Balkashin, V.P., Priz, I.A., Kohns, P.: The measurer of polarization of laser radiation. Patent of Ukraine 200805632, 10 Sept 2008
22. Kuzmichov, V.M., Pogorelov, S.V., Kohns, P.: Measurement of polarization state of laser radiation with three profile bolometric grids. Ukr. Metrol J. **3**, 38–42 (2007)

Chapter 13
Spectral and Lasing Characteristics of Some Red and Nir Laser Dyes in Silica Matrices

I. M. Pritula, O. N. Bezkrovnaya, V. M. Puzikov, V. V. Maslov, A. G. Plaksiy, A. V. Lopin and Yu. A. Gurkalenko

Abstract We synthesized a series of sol–gel silica matrices doped with laser dyes DCM, LK678, LD1, and LD2 which alcohol solutions have efficient lasing in the red spectral region and Rh800–in the near infrared (NIR) one. Absorption, fluorescence, and laser properties of the dyes in silica samples prepared by sol–gel process were investigated. It has found some peculiarities in preparation process of the laser matrices and in spectral characteristics of the dyes in these matrices.

13.1 Introduction

The lasers tuned in the red and the near infrared (NIR) regions of the spectrum and dyes-sensitizers for this spectral range are widely applied for diagnostics of different biological and medical objects. For instance, an oxazine dye [1] is used for early diagnostics of Alzheimer's disease. The urgency of laser sources for this region is due to the fact that the penetration depth of the radiation into living tissue for them is about a centimeter. Furthermore study of new photosensitizers with the silica coating for photodynamic therapy at infrared excitation [2] necessitates quest of new radiation sources.

Dye lasers developed specially may be used for this purpose. However, for many practical applications solid-state dye lasers are the most challenging because of they are not required bulky dye-flow systems, and no toxic and inflammable solvents [3]. Matrices prepared by the sol–gel process, polymeric ones or porous glasses are used in these lasers.

I. M. Pritula (✉) · O. N. Bezkrovnaya · V. M. Puzikov · A. G. Plaksiy · A. V. Lopin · Yu. A. Gurkalenko
Institute for Single Crystals, SSI "Institute for Single Crystals",
National Academy of Sciences of Ukraine, Kharkiv, Ukraine
e-mail: pritula@isc.kharkov.ua

V. V. Maslov
O. Ya. Usikov Institute for Radiophysics and Electronics,
National Academy of Sciences of Ukraine, Kharkiv, Ukraine

The matrices prepared with the sol–gel method have higher thermal conductivity and lower temperature coefficient of the change of the refractive index than polymeric ones [4]. In addition the photostability of Rhodamine 6G in sol–gel matrix by 2.7 times exceeds the same value for poly (methyl methacrylate) host media [3]. Moreover, the silica gel matrices have higher laser damage threshold as against the polymer media [3], due to higher thermal conductivity of silica gel than of polymer materials [4].

The sol–gel process may be considered a method for producing glass and ceramic materials from metallorganic precursors by low temperature polycondensation reactions. The process represents a powerful tool for making almost all kinds of transparent materials with interesting optical and photonic properties. The sol–gel technique is based on hydrolysis of liquid precursors and formation of colloidal sols. The precursors are usually organosilicates giving silicate sol–gel materials. These materials potentially combine the excellent optical properties of silica with the flexibility of incorporating organic moiety at the molecular level. Their potential photonic applications cover an enormous range, including passive and active waveguides, sensors, optical limiters and solid-state dye lasers [5, 6].

Though the first laser sol–gel matrices have been fabricated more than 20 years ago [7, 8] their upgrading and studying of their spectral and lasing properties are spreading at present, and new articles are routinely published in the known journals of optics, spectroscopy, and advanced functional materials.

13.2 Review of Sol–Gel Laser Materials

Gao et al. report [9] on the preparation of the TiO_2/ORMOSILs organic–inorganic hybrid planar waveguide films doped with dye—disperse red 13 (DR13) and the fabrication of the ridge waveguide structure based on the as-prepared hybrid films by combining a sol–gel process with a UV-cured imprint technique, which offers a promising fabrication method for obtaining a low loss waveguide in a cost-effective and efficient way, and the as-fabricated waveguides have a good third-order nonlinearity at the near ultraviolet region in the femtosecond domain, which has potential for integrated optics applications. The prepared planar waveguide film shows the photo-responsive properties of the trans–cis photoisomerization under the irradiation of the UV light, which indicates potential applications in the optical switching and storage. The results [9] indicate that the waveguides containing DR13 are expected to be potential candidates for photonic applications at the near ultraviolet region.

In [10], the laser dye PM567 was incorporated into various organically modified silicate gel glasses (ORMOSILs) derived by methyltriethoxysilane (MTES) and vinyltriethoxysilane (VTES) precursors mixed in various ratios. The laser performances of the PM567 doped into MTES–VTES-derived ORMOSILs including the laser slope efficiency, threshold and laser photostability together with its spectroscopic properties were investigated. It was found that in ORMOSILs derived by mixed precursors of MTES and VTES, the PM567 dopant demonstrated improved

fluorescent and laser performances. Blue-shifts of fluorescent peaks, extended fluorescent lifetime, improved laser efficiency and photostability of the PM567 dye doped into the ORMOSILs have been observed, which might related to the microstructures and micro-chemical environment of the dye in the ORMOSILs.

Lasio et al. [11] have explored the process of dimerization of rhodamine 6G (Rh6G) at high concentrations when it was incorporated in a solid state matrix and the dimer response to the photodegration process. Silica sol–gel films have been doped by the Rh6G with a concentration up to 10^{-1} M to form different species of dimers which coexist together with the monomer form. In particular, H-dimers not fluorescent and J-dimers fluorescent have been detected using UV–vis absorption spectra (H-type) and fluorescence ones (J-type). Fluorescence and UV absorption spectra have shown that both not-fluorescent H-dimers and fluorescent J-dimers together with the monomer form of the Rh6G are present in the matrix. Analysis of the absorption spectra has shown that the H-type dimers are more resistant to photodegradation with respect to the J-type dimers.

Secu et al. [12] have used sol–gel chemistry within the pores of a polycarbonate template membrane to prepare Eosin Y–SiO_2 hybrid luminescent micro-and nanorods. Structural and morphological characterization using scanning electron microscopy (SEM) and luminescence microscopy have shown the formation of rods with 200 nm and 1.2 μm diameter and about 30–40 μm length. Spectroscopic characterization has shown that the luminescence is due to Eosin-Y molecule in the xerogel porous network, surrounded by a solvation shell given mainly by the water.

Authors [13] have incorporated laser dye Rh6G into Zirconia-Glymo (Glymo-3-Glycidoxypropyltrimethoxysilane) glasses obtained by sol–gel method showed increased luminescence in presence of silver nanoparticles. The intensity enhancement of fluorescence by 225 % was obtained. That may be applied for construction of tunable lasers, active waveguides and luminescent solar concentrations. The authors have shown that the enhancement of fluorescence in this system is due to scattering of excited electrons of the silver plasmons.

But the previous effort of Levchenko et al. [14] to incorporate the gold nanoparticles into existing sol–gel matrices resulted of their agglomeration. The use of other matrices: gelatin, gelatin/sol–gel composite, polyvinyl pyrrolydon (PVP) is not practical as the gold nanoparticles degrade in these media. Nevertheless fluorescence enhancement of 74 % for Rhodamine B into a film of polyvinyl alcohol was achieved with the negatively charged gold nanoparticles.

Al Dwayyan et al. [15] have prepared Rh6G dye-silica core–shell nanoparticles by the controlled hydrolysis and condensation of single silica precursor tetraethylorthosilicate using the sol–gel method. Scanning electron microscopy, transmission electron microscopy and energy dispersive X-ray analysis reveal that dye molecules are entrapped in silica (SiO_2) shell resulting into core–shell particles of $\sim$ 30 nm diameter. These particles are also characterized by X-ray diffraction and Fourier transforms infrared spectroscopy. The results indicate that core–shell particles are all in spherical shape and have a narrow size distribution. The fluorescent and optical

properties of core–shell particles have been investigated using fluorescence and UV–Visible absorption spectra. The photoluminescence in solid or liquid medium occurs at the same wavelength. The SiO_2 shell restricts the leakage and photobleaching of dye efficiently. These core–shell nanoparticles are found to be highly luminescent and stable and can be employed without change in luminescence wavelength, in device fabrication.

A. K. Dikshit [16] has studied the optical and fluorescence properties, structure and morphology of silica nanoparticles bearing laser dye molecules are electrostatically attached with high refractive index organic dopant in acrylic optical preform rod. The photo physical fluorescence behavior of the laser dye molecules at the surface of different size and shape of silica nanoparticles has been explored. The interaction of laser dye-nanoparticles, nature of particles, and effect of various sizes and shapes of silica nanoparticles on fluorescence properties has been investigated. The developed optical preform has high potential for possible applications as bio-analysis sensor probe.

In [17] full-color emitting hybrid materials with covalently bridged dye have been synthesized. Especially, novel yellow and blue emitting hybrid materials are demonstrated in this report. The authors have confirmed that oligomer size siloxane structures are well formed in dye-bridged oligosiloxane via non-hydrolytic sol–gel reaction. In particular, white luminescence is obtained by controlling the ratio of *RGB* components using UV light source. Robust matrix consisted with siloxane network and covalently bridged structure lead the high thermal stability of dye molecules not to change the photoluminescence characteristics at 120°C for 200 h. The authors expect dye-bridged hybrid materials will provide a promising strategy to develop full-color display and white lighting technology.

Chen et al. [18] have prepared gel-glass dispersed liquid crystal (GDLC) thin films doped with laser dye Rh6G by sol–gel method and produced surface-relief structures which formed distributed feedback on this film by soft lithographic technology. Authors have obtained directional laser emission at low concentration of liquid crystals (LCs) entrapped in hybrid films and showed that the high concentration of LCs leads to the decrease in the DFB lasing intensity and to rise the random lasing. As a result authors demonstrated the synchronous excitation of a DFB lasing with random lasing and such type emission might be useful for medical diagnostics.

Wang et al. [19] demonstrated two kinds of near-infrared DFB lasing of Oxazine 725 dye in zirconia thin films and in silica bulks. They used intensity modulation and polarization modulation to generate the DFB laser emission. Wideband tuning of the output wavelength was achieved by varying the period of the modulation produced by a nanosecond Nd:YAG laser at 532 nm. Tuning ranges were 716–778 nm and 724–813 nm for the thin film lasers and the bulk lasers, respectively. The laser output showed different polarization characteristics and threshold energy variation when the feedback mechanism was changed from intensity modulation to polarization one.

Photochromic molecules which applied in a wide range, from optical memory media to optical switches and filters may be incorporated in the silica gel materials.

Authors [20] have successfully embedded a photochromic spirooxazine dye in sol–gel thin silica films functionalized with different amino groups. The resulting films show high transparency and exhibit a strong blue coloration upon irradiation with UV light. The incorporation of amino groups (–PrNH$_2$, –PrNMe$_2$ and –PhNH$_2$) in the ormosil network, result in an enhanced stabilization of the photochromic dye, due to the interaction of the amino groups with the OH groups on the surface of the pores and the embedded dye molecules. In this way, the highest photostability of the dye was achieved in matrices modified with –PhNH$_2$ groups, showing more than eight times higher photostability as compared with the dye embedded in unfunctionalized silica thin films.

For the purpose of minimizing aggregation effects in the luminescent silica xerogels [21] two classes of sol–gel derived mesoporous materials were explored as hosts for Rh6G laser dye. The first consists of pure (SiO$_2$) and phenyl-modified silica (Ph$_{0.17}$ SiO$_{1.915}$) xerogels, prepared via sol–gel reaction using an ionic liquid as catalytic agent. The second consists of mesoporous sodium aluminosilicate glasses with Si to Al ratio in the range of $6 \leq \text{Si/Al} \leq 9$. The dye dispersion in the silica xerogels results in high quantum yields (up to 87 %), which is attributed to the low concentrations of Si-OH groups, a well-known facilitator of Rh6G aggregation. Due to its lower polarity and higher chemical affinity to the dye molecules, the phenyl-modified host offers a more favorable environment for dispersion of higher dye concentrations, without compromising the quantum yield. The chief advantages of these particular matrices are their ability to host high concentrations of dye and their strong retention in the matrices by electrostatic Coulomb interactions, making them also interesting candidates for biological applications.

Thus the review mentioned above demonstrates topicality and practical necessity of the further exploration and development of the sol–gel-derived materials.

13.3   Experimental

For fabrication laser media based on SiO$_2$ matrices for the red and the NIR spectral regions we used laser dyes with high efficiency in alcohol solutions studied early [22, 23] and two standard laser dyes: DCM and Rhodamine 800 (Rh800) [24]. The spectral and laser characteristics of these matrices were studied. The influence of the molar ratio of the reaction components on the matrix transparency was investigated.

The silica gel were synthesized using tetraethoxy- and tetramethoxysilane (TEOS and TMOS respectively; Aldrich), additionally purified ethyl alcohol, formamide (FA) chemically pure, and twice distilled water, as well as laser dyes LD1 and LD2 (synthesized at the V. Karazin Kharkiv National University [22]), LK678 (synthesized at the D. Mendeleev Moscow Chemical Technology University [25]), DCM (Aldrich) and Rh800 (Aldrich). Presented below are the structural formulas of some dyes:

LD1

LD2

DCM
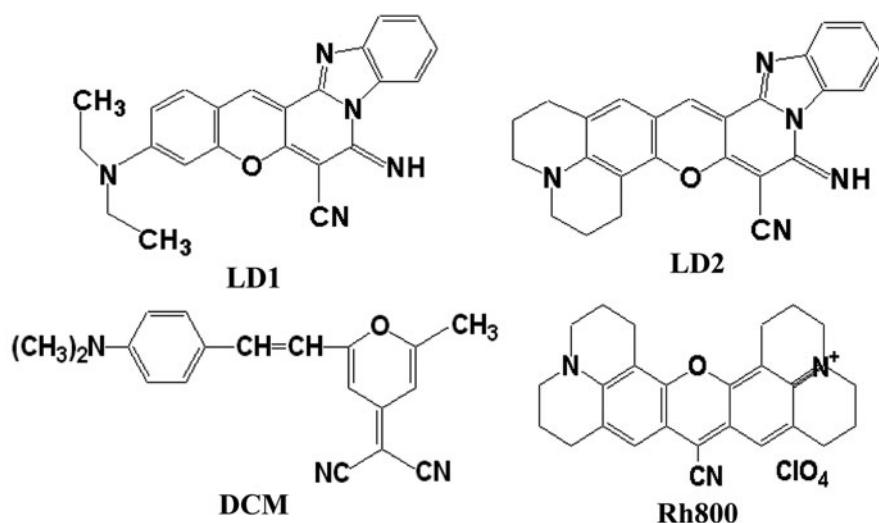
Rh800

SiO$_2$ matrices were synthesized using sol–gel method by the hydrolysis of TEOS (or TMOS) with addition of nitric acid as a reaction catalyst [26, 27]. The alcohol solutions of the dyes (LD1, LK678, Rh800 in ethanol; LD2 in ethanol with added 1 mM HNO$_3$; DCM in methanol) were introduced after 30 min. mixing of alkoxysilane in ethanol (or in methanol for the matrices based on TMOS). Then we added twice distilled water, FA as drying control chemical additive (DCCA). The resulting mixture was stirred during 2 h. and then pyridine was added to it. The synthesized sol was placed into plastic cuvette, hermetically sealed and stored till the gel was formed. Afterwards the plastic cuvette were opened and dried for 3–4 weeks at room temperature and 7–10 days at 60°C. The density of obtained SiO$_2$ matrices was 1.4–1.6 g cm^{-3}.

The absorption spectra of the samples were recorded by spectrophotometer Lambda 35 (Perkin–Elmer, USA). The measurement of the luminescence spectra were carried out by the fluorimeter FluoroMax-4 (Horiba Jobin Yuon, USA). The luminescence of the dyes was excited near their absorption band maxima.

The lasing characteristics of the sol–gel matrices were studied using the laser [28] with non-selective cavity (LNSC) formed by two dielectric wideband mirrors with the reflection coefficient R$_1 \approx 99$ %, R$_2 \approx 60$ %. The samples placed in a quartz cuvette containing immersion liquid (ethylene glycol) were put into the laser cavity. The excitation of the samples was performed on the transverse scheme by flashlamp-pumped dye laser (FLPDL) with the output energy ≤ 230 mJ, the pulse duration ~ 1.5 µs, and the spectrum half-width ~ 3 nm. Its radiation was focused on the cuvette by a cylindrical lens with F $= 110$ mm in a strip with height ~ 1 mm. The matrices with LD1, LD2, and DCM dyes were pumped by the FLPDL with ethanol solution of coumarin 314 at $\lambda_p = 507$ nm. Those with Rh800 were pumped by the FLPDL with ethanol solution of oxazine 17 at $\lambda_p = 667$ nm, and matrix with LK678–by the FLPDL with
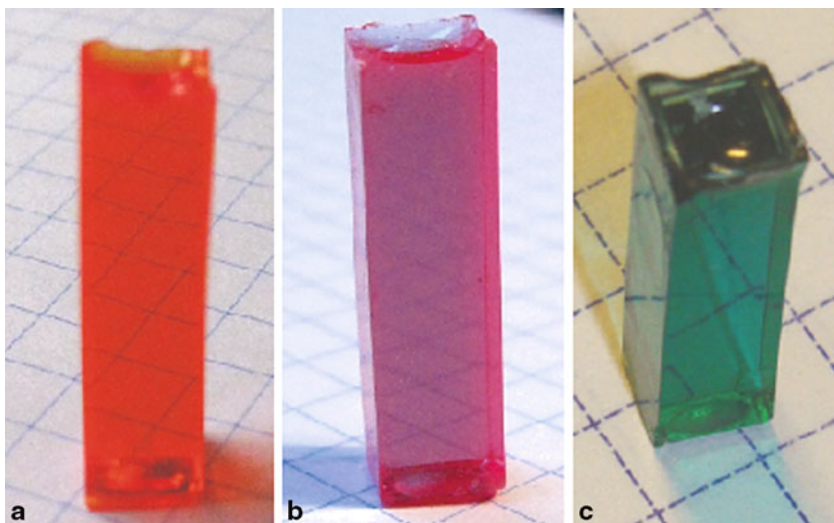
Fig. 13.1 SiO$_2$ matrices with the DCM (**a**), LK678 (**b**), and Rh800 (**c**) dyes; matrices were synthesized with FA

ethanol solution of Rhodamine 6G at $\lambda_p = 588$ nm. The output laser energy of the FLPDL and LNSC was measured by a device of IMO-2 type. The laser spectra were registered using a spectrograph based on UF-90 chamber with 1200 line/mm diffraction grating, and then photographed by an EOS 400D DIGITAL camera.

13.4   Results and Discussion

We synthesized transparent silica gel matrices with incorporated molecules of the mentioned laser dyes (Fig. 13.1).

The synthesis of SiO$_2$ matrices comprises the formation of the sol with subsequent aggregation of primary SiO$_2$ nanoparticles into spatial nets leading to gelation. The sol–gel transition is accompanied with the formation of the nanoparticles spatial structure which size may increase with time. The ageing and drying of the gel leads to the formation of amorphous xerogel with nanometric pores (5–20 nm) and 3–8 nm SiO$_2$ nanoparticles [29, 27]. In the process of ageing the solvent is removed from silica gels under the influence of capillary forces [29]. The dye molecules are incorporated in the pores of the three-dimensional SiO$_2$ xerogel network. The gelation process is influenced by the DCCA [29, 27] (in our case—FA). In the samples prepared with FA the rate of the solidification and drying was by several times higher than for ones without FA.

There was established an essential influence of micro-environment on the spectral properties of the dye molecules incorporated in the matrix. In the gel the absorption
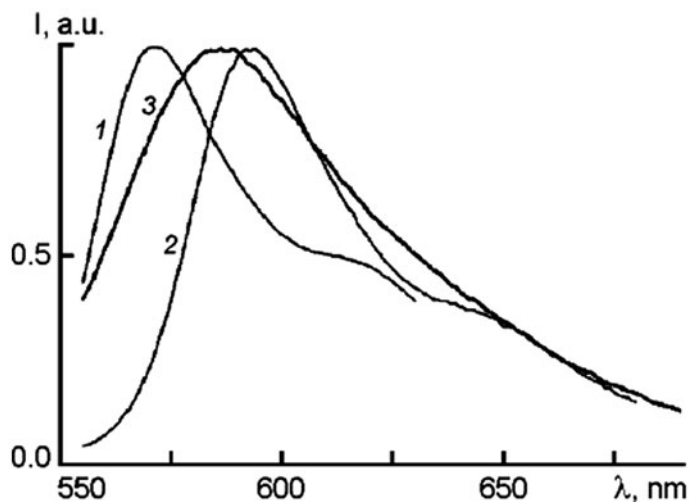
Fig. 13.2 Luminescence spectra of LD1 in: ethanol (*1*), ethanol + 0.44 mM HNO_3 (*2*), and SiO_2 matrix (*3*)

Table 13.1 Spectral characteristics of LD1 and LD2 dyes

Dye	Medium	C (HNO_3), mM	λ_a, nm	λ_l, nm
LD1	Ethanol	–	549	572
LD1	Ethanol	0.44	570	592
LD1	SiO_2-gel	1.33	564	586
LD1	SiO_2-matrix (60 °C)	–	566	582
LD2	Ethanol	–	567	586
LD2	SiO_2-gel	1.33	–	598
LD2	SiO_2-matrix (60 °C)	–	575	587

λ_a absorption maximum wavelength, λ_l luminescence maximum wavelength

and luminescence maxima of the LD1 dye correspond to 564 and 586 nm, respectively (Fig. 13.2, Table 13.1), but after drying of the matrix at 60°C the luminescence maximum was shifted to 582 nm.

The LD2 luminescence maximum was shifted from 598 nm (in the gel) to 592 nm and 587 nm while the sample was dried at 20 °C and 60 °C respectively (Fig. 13.3, Table 13.1).

The position of the absorption and luminescence maxima of the LD1 and LD2 dyes are caused by influence of solvation shell of the solvent molecules in the liquid-impregnated silica gel, and are prone to protonation in the presence of acid. In the process of drying the solvent and water are practically removed from the matrices and the dye molecules enter the silica gel pores. Moreover, is obvious that the molecules
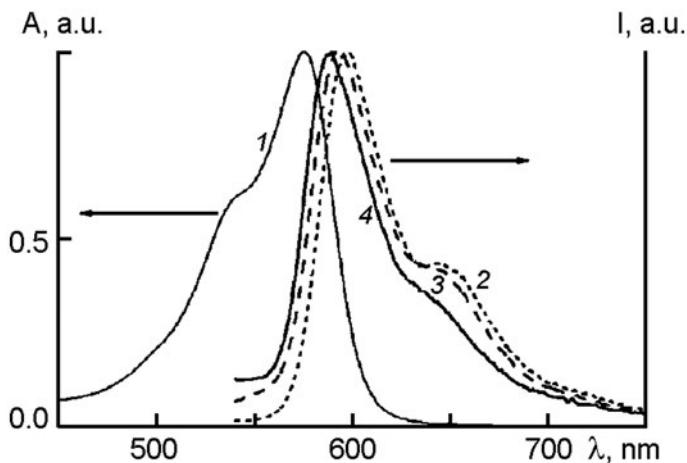
Fig. 13.3 Absorption (*1*) and luminescence (*2–4*) spectra of LD2 (0.35 mM LD2/1 M TEOS) in: SiO$_2$ matrix: gel (*2*), xerogel dried at 20°C (*3*), and 60°C (*4*)

of LD1 and LD2 dyes undergo partial deprotonation while interacting with the surface of the SiO$_2$ nanoparticles which form the silica gel skeleton.

As we have established, the process of drying is accompanied with bleaching of LD1 and LD2 in SiO$_2$ matrices. The observed effect seems to be caused by protonation of nitrogen in the 7th position of benzopyran base of the dyes. It is more noticeable for LD1 in which diethylaminogroup in this position may leave the plane of the molecular skeleton at the protonation, in the issue the probability of $S_1 \rightarrow S_2$ radiative transition is sharply diminished [22] and luminescence is quenched. Therefore, while fabricating the active media on the base of silica matrices we added pyridine to reduce the acidity in sol synthesis process. However, we did not manage to obtain lasing of the matrices with the LD1 and LD2 because of their essential bleaching.

We observed the complete bleaching of the LK687 dye at the matrix synthesis and low luminescence intensity of DCM in the matrices when not using pyridine. In this case the last do not lasing.

The laser radiation of SiO$_2$ matrices activated with DCM and LK678 dyes was obtained (Fig. 13.4, 13.5) when at their synthesis a small dose of pyridine was added for reducing the acidity of the medium. In the process of this synthesis we used both TEOS and TMOS. We founded that the matrices with these dyes are more transparent when TMOS is used as a precursor compared with TEOS.

On the TMOS matrices doped with the LK678 dye we obtained effective laser radiation at central wavelength $\lambda_{las} = 654$ nm with half-width of spectrum band— 4 nm (Fig. 13.5a, 13.5b). The dependence of output laser energy of this matrix on normalized pump energy (the last is normalized to the threshold pump energy $E_{th} \sim 70$ mJ) is depicted in Fig. 13.5c. It is necessary to note that for this matrix ($C_{LK678} = 1.08$ mM) under pumping energy ~ 200 mJ output laser energy was by 1.5 higher than for matrix doped with 1.9 mM Rh6G.
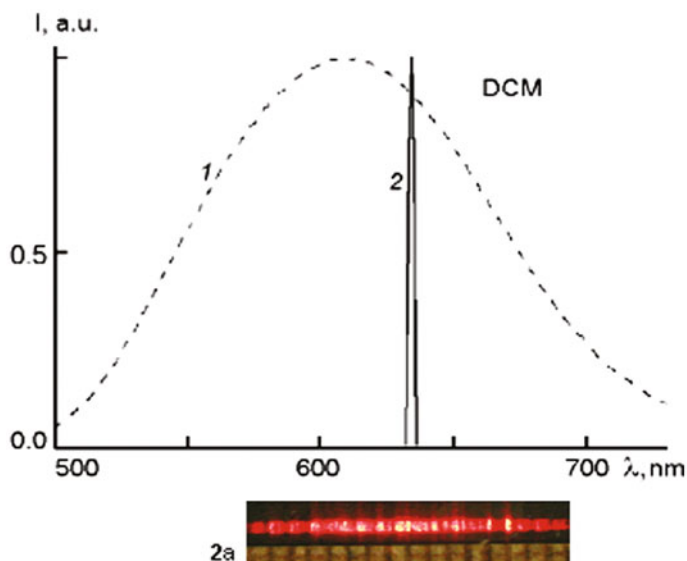
Fig. 13.4 Luminescence (*1*) and laser emission (*2*, *2a*) spectra of DCM in SiO$_2$ matrices. The reciprocal dispersion for lasing spectrogram (*2a*) is $\sim$ 6.2 Å/mm

Our studies of influence of the molar ratio of water and formamide—n (H$_2$O/FA) on transparency of the silica matrices have enabled to fabricate those activated with Rh800 and obtain laser emission on them in the NIR spectral range. We synthesized these matrices at n (H$_2$O/FA) = 8.8 and here pyridine was not used.

Spectral characteristics of Rh800 dye in different media are shown in Fig. 13.6. The absorption and luminescence spectra of it in SiO$_2$ matrix are shifted to long-wavelength side relative to ethanol solution. This shift indicates that the intermolecular interactions of the dye molecule with micro-environment in the matrix become stronger then in the alcohol solution. The laser emission maximum of Rh800 in SiO$_2$ matrix is at 747 nm, the halfwidth of the laser spectrum is 4 nm (Fig. 13.6).

The main spectral parameters of the DCM, LK678, and Rh800 dyes in studied media are presented in Table 13.2 (λ_{las}—central laser wavelength, $\Delta\lambda_{las}$—half-width of laser spectrum.). One can see that the Stokes shift $\Delta\nu^{St}$ between the absorption and luminescence maxima of DCM in solvents is more about by an order than ones for LK678 and Rh800. As a result the lasing of the last was at the long-wavelength wing of the luminescence spectrum but DCM laser emission was near its maximum.

The measured laser emission divergence of the matrix doped with the LK678 dye was about 2.5 mrad, the full width of the spectrum band at level—8 nm, and its maximum—λ_{las} = 654 nm. The value of laser radiation divergence for the matrix corresponding to the values characteristic of the alcohol solutions of the dyes testifies that the optical quality of the matrix is high enough. This fact is also confirmed by the character of the laser emission spectrogram (Fig. 13.5b). The latter has an explicitly pronounced line structure typical for dye lasers with wide-band nonselective resonator and several inner reflective surfaces.
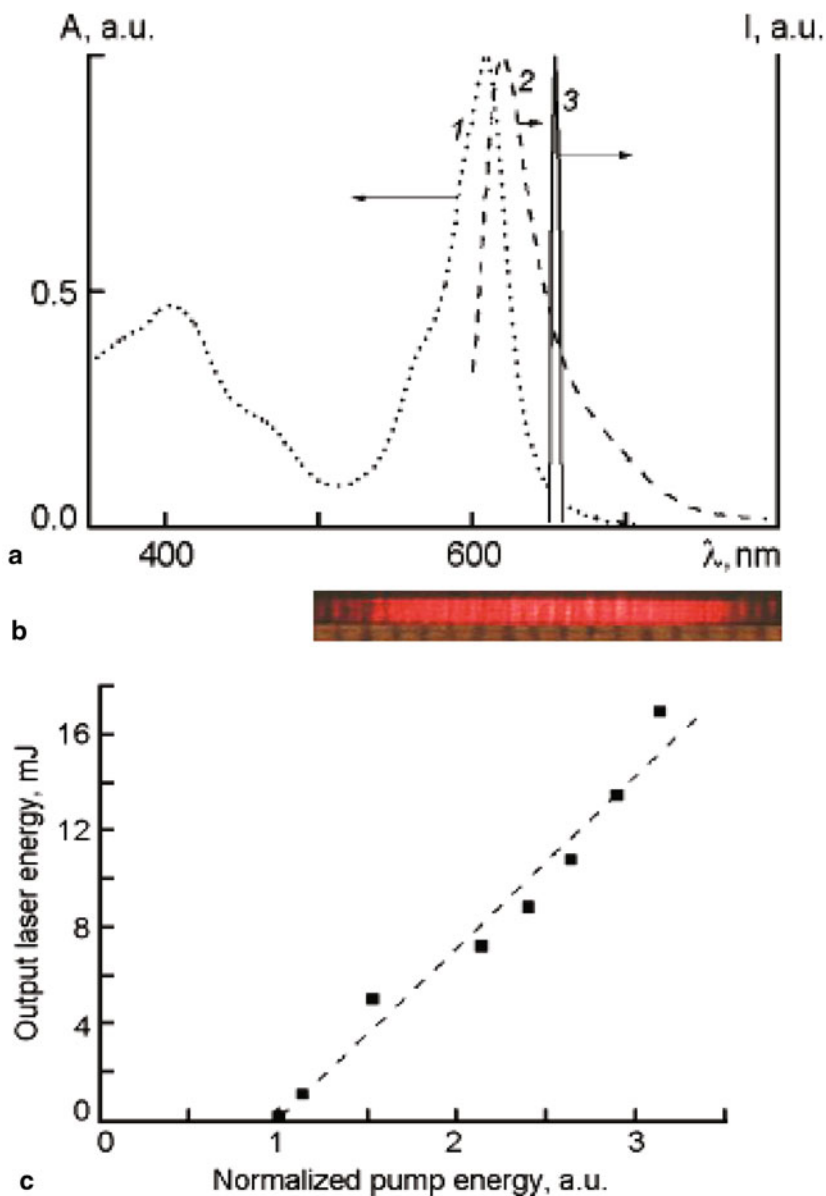
Fig. 13.5 Characteristics of the LK678 dye in SiO2 matrices. **a** Absorption (*1*), luminescence (*2*) and laser emission (*3*) spectra. **b** Lasing spectrogram (the reciprocal dispersion of spectrograph ~ 6.2 Å/mm). **c** Dependence of the output laser energy on the pumping one (λp = 588 nm)
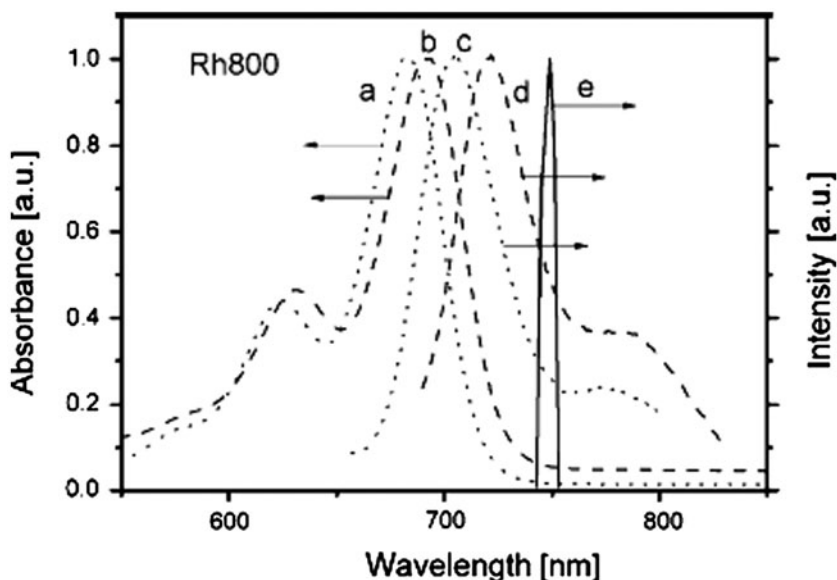
Fig. 13.6 Absorption (*a*, *b*) and luminescence (*c*, *d*) spectra of Rh800 in ethanol solution (*a*, *c*), in SiO$_2$ matrices (*b*, *d*), and laser spectrum of 1.1 9 mM Rh800 in SiO$_2$ matrix (*e*)

Table 13.2 Spectral parameters of the dyes

Dye	Medium	λ_a, nm	λ_l, nm	$\Delta\nu^{St}$, cm^{-1}	$\lambda_{las} \pm \Delta\lambda_{las}$, nm
DCM	Acetonitrile	463	622	5500	632 ± 6
DCM	Methanol	472	630	5280	635 ± 4
DCM	SiO$_2$ matrix		610		634 ± 2
LK678	Methanol	609	626	450	650 ± 10
LK678	SiO$_2$ matrix	608	620	320	654 ± 4
Rh800	Ethanol	683	705	460	725 ± 3
Rh800	SiO$_2$ matrix	690	720	600	747 ± 4

The laser spectra of the LK678 and Rh800 dyes in SiO$_2$ matrix were located at the long-wavelength slope of the luminescence band because of strong overlapping of the absorption and luminescence spectra and as a result the self-absorption in the active medium.

It is necessary to note that the lasing spectrograms with an explicitly pronounced line structure shown in Fig. 13.4 and Fig. 13.5 are typical and for all other lasing matrices. This points to the fact that for these matrices the lifetime of photons in the laser cavity is sufficient for forming the high-quality laser emission.

13.5   Conclusions

Silica matrices activated with series of laser dyes for 600–750 nm spectral range of lasing were synthesized and their spectral characteristics were determined. The necessity to employ acidity reduction additive in sol–gel process for some of the dyes was shown. For the matrices synthesized on the basis of TMOS with pyridine as such adding and doped with DCM and LK678 dyes there was obtained laser emission, whereas for those with LD1 and LD2 it was not achieved because of their essential bleaching in xerogel, connected probably with protonation of the nitrogen in 7th position of their benzopyran basis. The output laser energy of LK678 dye in the matrix was by 1.5 higher than of Rh6G at the equal conditions. A well-defined structure of the lasing spectra of the matrices at microsecond pumping testifies to their relatively high optical quality.

References

1. Hintersteiner M, Enz A., Frey P., et al.: In vivo detection of amyloid-β deposits by near-infrared imaging using an oxazine-derivative probe. Nat. Biotechnol. **23**(5), 577–583 (2005)
2. Zhang P., Steelant W., Kumar M., Scholfield M.: Versatile photosensitizers for photodynamic therapy at infrared excitation. J. Am. Chem. Soc. **129**(15), 4526–4527 (2007)
3. Rahn M.D., King T.A.: Comparison of laser performance of dye molecules in sol–gel, polycom, ormosil, and poly (methyl methacrylate) host media. Appl. Opt. **34**(36), 8260–8271 (1995)
4. Koechner W.: Solid-state laser engineering, 4th edn. Springer-Verlag, Berlin, pp. 400–403 (1996)
5. Gvishi R., Narang U., Ruland G., Kumar.N., Prasad P.N.: Novel, organically doped, sol–gel-derived materials for photonics: multiphasic nanostructured composite monoliths and optical fibers. Appl. Organometall. Chem. **11**, 107–127 (1997)
6. Reisfeld R., Weiss A., Saraidarov T., Yariv E., Ishchenko A.A.: Solid-state lasers based on inorganic–organic hybrid materials obtained by combined sol–gel polymer technology. Polym. Adv. Technol. **15**(6), 291–301 (2004)
7. Altstuler G.B., Bakhanov V.A., Dulneva E.G., et al.: Laser on silica gel activated with the dye. Optik. i Spektrosk. **62**(6), 1201–1203 (1987)
8. Reisfeld R., Seybold G.: Stable solid-state tunable lasers in the visible. J. Luminesc. **48**, **49**, 898–900 (1991)
9. Gao T., Que W., Zhang X., Chen J.: Fabrication and optical properties of sol–gel derived organic–inorganic photosensitive ridge waveguide structure doped with disperse red13. Opt. Commun. **305**, 255–259 (2013)
10. Liao Z., Zhou Yu., Yang Yu., Cui Yu., Qian G.: Fluorescent and laser properties of pyrromethene 567 (PM567) doped into multi-precursors derived gel glasses. J. Sol-Gel Sci. Technol. **67**(3), 480–485 (2013)
11. Lasio B., Malfatti L., Innocenzi P.: Photodegradation of rhodamine 6G dimers in silica sol–gel films. J. Photochem. Photobiol. A: Chem. **272**, 93–98 (2013)
12. Secu M., Secu C.E., Sima M., et al.: Luminescent EosinY–SiO$_2$ hybrid nano and microrods prepared by sol–gel template method. J. Luminesc. **143**, 89–92 (2013)
13. Reisfeld R., Levchenko V., Saraidarov T., et al.: Fluorescence intensification of Rhodamine 6G in Zirconia-Glymo glasses. Opt. Mater. **34**(12), 2021–2024 (2012)
14. Levchenko V., Grouchko M., Magdassi S., et al.: Enhancement of luminescence of Rhodamine B by gold nano-particles in thin films on glass for active optical materials applications. Opt. Mater. **34**(2), 360–364 (2011)

15. Al Dwayyan A.S., Qaid S.M.H., Khan M.A.M., Al Salhi M.S.: Structural and spectral investigations of Rhodamine (Rh6G) dye-silica core–shell nanoparticles. Opt. Mater. **34**(5), 761–768 (2012)
16. Dikshit A.K., Development of laser dye-doped silica nanoparticles embedded optical preform for bio-analysis. Opt. Mater. **34**(10), 1054–1061 (2012)
17. Kwak S.-Y., Yang S.C., Kim N.R., et al.: Sol–gel derived dye-bridged hybrid materials for white luminescence. J. Sol-Gel Sci. Technol. **65**(1), pp. 46–51 (2012)
18. Chen L., Gao F., Liu C., et al.: Distributed feedback leaky laser emission from dye doped gel-glass dispersed liquid crystal thin film patterned by soft lithography. Opt. Mater. **34**(1), 189–193 (2011)
19. Wang J., Dong H., Fan J., et al.: Near-infrared distributed feedback solgel lasers by intensity modulation and polarization modulation. Appl. Opt. **50**(33), 6248–6258 (2011)
20. Pardo R., Zayat M., Levy D.: Stability against photodegradation of a photochromic spirooxazine dye embedded in amino-functionalized sol–gel hybrid coatings. J. Sol-Gel Sci. Technol. **63**(3), 400–407 (2012)
21. de Queiroz T.B., Botelho M.B.S., De Boni L., Eckert H., et al.: Strategies for reducing dye aggregation in luminescent host-guest systems: Rhodamine 6G incorporated in new mesoporous sol-gel hosts. J. Appl. Phys. **113**, 113508 (2013)
22. Maslov V.V., Dzyubenko M.I., Kovalenko S.N., Nikitchenko V.M., Novikov A.I.: New efficient dyes for the red part of the lasing spectrum. Sov. J. Quantum Electron. **17**(8) 998–1001 (1987)
23. Maslov V.V.: Spectral and fluorescence characteristics of laser dyes for 650–800 nm range. Funct. Mater. **13**(3) 419–422 (2006)
24. Brackmann U.: Laser Dyes, 3rd edn. Lambda Physik AG, Goettingen (2000)
25. Stepanov B.I., Bychkov N.N., Nikiforov V.G., et al.: New generation of dyes for 660–860 nm spectral region for flashlamp-pumped lasers. Lett. Sov. J. Technic. Phys. **14**(7), 650–653 (1988) (in Russian)
26. Salin F., Le Saux G., Georges P., Brun A.: Efficient tunable solid-state laser near 630 nm using sulforhodamine 640-doped silica gel. Opt. Lett. **14**(15), 785–787 (1989)
27. Bezkrovnaya O.N., Pritula I.M., Maslov V.V., et al.: Luminescent properties of rhodamine 6G dye in silica sol-gel matrices. Funct. Mater. **17**(4), 433–437 (2010)
28. Dzyubenko M.I., Maslov V.V., Pelipenko V.P., Shevchenko V.V., Kupko E.A.: Laser tunable source for the red and near UV regions of the spectrum. J. Appl. Spectrosc. **71**(3), 435–440 (2004)
29. Khimich N.N.: Synthesis of silica gels and organic–inorganic hybrids on their base. Glass. Phys. Chem. **30**(5), 430–442 (2004)

Chapter 14
Interpretation of the Time Delay in the Ionization of Coulomb Systems by Attosecond Laser Pulses

Vladislav V. Serov, Vladimir L. Derbov and Tatyana A. Sergeeva

Abstract After a brief overview of attosecond pulse measurement techniques, we consider the time delay of electron detachment from a Coulomb center in the process of ionization. It is shown that the attosecond streaking, mostly used in time delay measurements, can be formally described by placing a virtual detector of the arrival time delay at a certain distance from the center of the system. This approach allows derivation of a simple formula for Coulomb-laser coupling that perfectly agrees with the results of numerical solution of the time-dependent Schrödinger equation.

14.1 Introduction

In 2012 a special issue of *Journal of Physics B* [1] was devoted to a remarkable event in the history of modern optics and atomic physics—the 10th anniversary of experimental generation of attosecond pulses [2, 3]. As summarized in [1], since the appearance of attosecond light sources the attosecond science has become an active research field. Detailed studies of ultrafast phenomena in atoms and molecules have been performed, especially in the time domain. Direct measurements of ultrafast characteristic times in atoms and molecules, e.g., Auger decay time and autoionization lifetime, have been carried out. The molecular tomography method allowed the reconstruction of molecular orbital wave function. Ultrafast phenomena in condensed matter and in nanostructures have been also studied.

This chapter is devoted to quantum mechanics of electrons ejected in the course of photoionization of atoms by attosecond light pulses rather than to attosecond optics itself. The motivation is that the attosecond pulse measurement actually means monitoring the motion of the ejected electrons with super-high temporal resolution. An exhaustive quantum mechanical picture is necessary to extract the light pulse duration, amplitude and shape from the measurements performed with the ionization electrons. On the other hand, if this picture is known, attosecond pulses become a powerful tool for tracing the real-time electron dynamics in atoms and molecules.

V. V. Serov (✉) · V. L. Derbov · T. A. Sergeeva
Department of Physics, Saratov State University, 83 Astrakhanskaya, 410012 Saratov, Russia
e-mail: derbovvl@gmail.com

Particularly, the attosecond optical technique can provide refined information on the temporal dynamics of the ionization process.

While the femtosecond time scale is characteristic for dynamics of nuclei in molecules, the time periods of a few attoseconds are typical for the time scale of the processes that occur with the valence electrons or even the electrons of the inner atomic shells [4]. Attosecond pulse generation is implemented using nonlinear optical phenomena, among which the high harmonic generation (HHG) theoretically studied [5, 6] long before the experimental observations [2, 3] is of the most current practical importance. The idea of this method is very simple. When a femtosecond pulse of ultra-high intensity interacts with matter, only the central part of the pulse provides the field strength sufficient for HHG, so that the arising HHG pulse appears to have much shorter duration and much higher frequency than the exciting one—the higher the frequency (the harmonic number), the shorter the duration. Typically, the pulses generated using this approach lie in the XUV spectral region. Alternative potential approaches include the use of stimulated Raman scattering [7].

During decades of early development of the picture of light-matter interaction was imagined as a sequence of instantaneous transitions ("quantum jumps") between the electronic eigenstates of the target. In the attosecond time scale each transition of the electron from one state to another appears to be a continuous time-resolved evolution of the appropriate electron wave packet rather than a "jump". One of the urgent problems arising in the theory of ionization of atoms by attosecond radiation pulses is the interpretation of time delay that occurs in the ionization of atomic and molecular systems, characterized by the Coulomb potential, which is the main subject of this Chapter.

At present all experimental studies of ultrafast processes that occur in atoms and molecules affected by ultrashort laser pulses are based on the pump-probe scheme. Usually the role of a probing pulse is played by the infrared laser pulse, while the pumping pulse is a XUV one having the duration of a few tens or hundreds of attoseconds, obtained by means of HHG from the radiation of the same infrared laser. Thus, the pumping and the probing pulses are mutually coherent, and one can provide an arbitrary phase difference between them using common optical techniques. Originally, the pump-probe schemes with ionization of atoms by a UV pulse were used to control the parameters of attosecond UV pulses themselves. In the process of ionization of the atom by the attosecond pulse an electron wave packet is generated with the central energy and the shape is varied by the probing infrared radiation [8]. However, high-precision assignment of phases of the probe and pump radiation in combination with the methods improving the shape and reducing the duration of UV pulses allow the measurement of fine delay effects related to the ionization process itself.

In the experiments based on the pump-probe scheme the system is ionized by the XUV field. The probing near IR (NIR) field, acting simultaneously, modulates the momentum distribution of the ejected electrons (the electron spectrogram) depending on the time delay between the XUV and NIR pulses. This dependence is just what is actually measured. The methods commonly used differ in how the desired information is encoded in the spectrogram and how it can be extracted from it.

The simultaneous pump-probe schemes can be divided into two types: those using pumping pulse trains and those using a single pumping pulse (Fig. 14.1). The first type

is represented by the method referred to as Reconstruction of Attosecond Beating by
Interference of Two-photon Transitions, or Reconstruction of Attosecond harmonic
Burst By Interference in Two-photon Transitions (RABITT) [10].

The train of symmetric XUV pulses, generated via the HHG from the IR radiation
having the frequency ω_{IR}, contains only odd harmonics, and acting on the atoms gives
rise to characteristic "banded" energy spectrum of the electrons, ejected as a result
of ionization (Fig. 14.2). The peaks of this spectrum correspond to the energies
$(2q + 1)\hbar\omega_{IR} - I$ (I is the ionization potential and q is an integer). If in addition
to the XUV radiation the electron is subject to the original IR radiation, then, due
via a two-photon process the electron can acquire the energy $2q\hbar\omega_{IR} - I$. This can
be implemented in two ways: either the electron first absorbs a XUV photon with
the energy $(2q - 1)\hbar\omega_{IR}$ and then absorbs one more IR photon with the energy
$\hbar\omega_{IR}$, or first the XUV photon with the energy $(2q + 1)\hbar\omega_{IR}$ is absorbed, and then
under the action of the IR radiation the stimulated emission of the IR photon with
the energy $\hbar\omega_{IR}$ takes place. The finite probability of detecting an electron with the
energy $2q\hbar\omega_{IR} - I$ is a result of interference of these two processes, and the phase
acquired in each of them is composed of the optical phase difference between the
XUV and IR waves, the phase of the ionization amplitude, and the phase of the
transition amplitude between the electron continuum states. The probability reaches
its maximum when the path time difference between the XUV and IR waves differs
by an integer number of IR optical periods from the finite-difference derivative of
the sum of phases of the ionization amplitude and the continuum-continuum on the
grid with the mesh $2\omega_{IR}$.
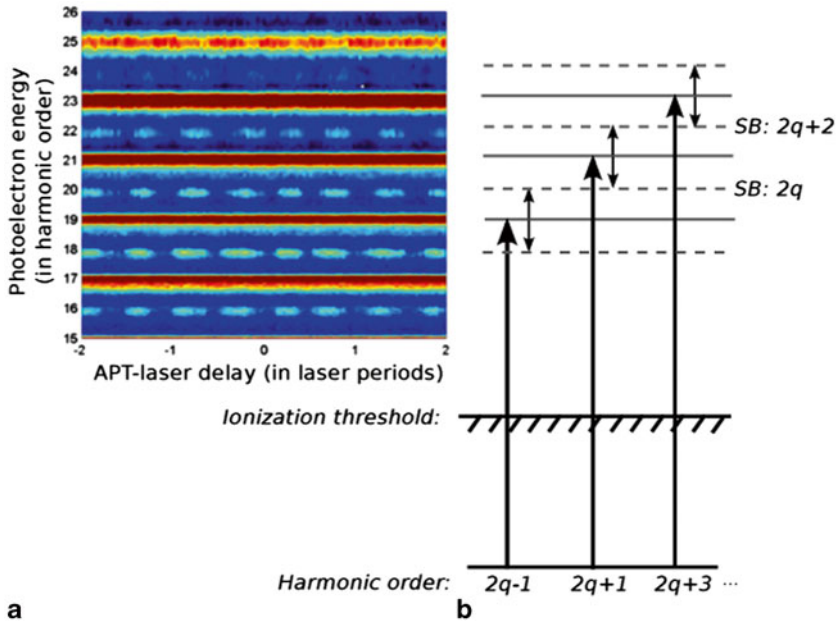
Fig. 14.2 RABITT method: **a** Photoelectron spectrogram over photon energy and delay between the attosecond pulse train and the IR field. The offset in the modulation of the sidebands contains information about the attosecond pulses and the ionization process. **b** Schematic energy diagram of transitions that yield the same final energy in sideband $2q$. (Reproduced from [9])

The basic idea for RABITT was published by Veniard et al. in 1996 [11]; it was applied for the first proof of attosecond time structure in pulse trains by Paul et al. [2]. The name RABITT was invented by H. Muller [10].

A number of methods were developed for providing desired information in the case of single (isolated) attosecond pulses. Thus, in the method of attosecond streaking [12] an atom is simultaneously affected by the extreme ultraviolet (XUV) ionizing pulse with the duration of about 100 attoseconds and the auxiliary variable field in the form of a femtosecond IR laser pulse. The latter inflects the momentum of the ejected electron, depending upon the time of ejection, which makes it possible to measure in such a way the ejection delay (Fig. 14.3).

The original proposal for the attosecond streak camera was by Constant et al. (1997) [14]. There it was suggested to use circularly polarized laser fields and observe the angular distribution of the XUV photoelectrons. The quantum theory was published in 2002 by Kitzler et al. [15] and Itatani et al., who invented its present name [12].

The theoretical concept of time delay in quantum mechanical scattering has a much longer history than the attosecond facilities that recently turned its measurement into a practically solvable problem. The concept arises in a more general wave-physical context in relation with the definition of a wave packet arrival time. A perfect historical survey of time delay theory can be found in the review paper [16]. The concept of
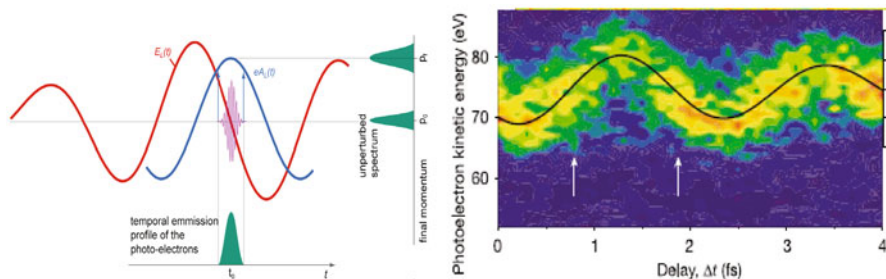
Fig. 14.3 Schematic representation (*left*) and photoelectron spectrogram (*right*), illustrating the method of attosecond streaking. (Reproduced from [13])

time delay was introduced by Eisenbud [17] and Wigner [18], in the context of s-wave quantum scattering. Their derivation was based on the group velocity of spherical wave packets, i.e., on following the 'peak' of a wave packet. Instead of tracing the scattered wave packet by its peak, it was proposed by Brenig and Haag [19] to evaluate the expectation value of the radial coordinate outside the range of the interaction. Smith [20] proposed an alternative approach based on the concept of the dwell time of a particle in a given spatial region and in the stationary scattering case rederived the Eisenbud–Wigner time delay as a difference between interacting and free dwell times.

Each of the above treatments has its unsatisfactory features [21]. The peak definition by stationary phase fails in the case of strong reshaping of the packet by dispersion, the asymptotic behavior of $\langle r \rangle$ applies only for times much larger than the spreading time of the wave packet, which is unrealistic in usual scattering experiments. The dwell time was originally derived under the restrictive assumption of stationary scattering. These drawbacks can be avoided within the frameworks of a general time-dependent approach, based on average wave packet dwell time [16].

The necessity of extracting time delays from the experimental data of such methods as RABBIT or attosecond streaking gave rise to new problems in theoretical calculations and interpretation of the results. At first the strong field approximation (SFA) was used ([22], see also the review [23]). From this approximation a simple relation follows, namely, the time shift of the streaking diagram with respect to the IR field phase coincides with the Wigner time. Later it was understood that this approximation is invalid because of the so called Coulomb-laser coupling (CLC) [24]. The attempts to calculate CLC were made using the eikonal approximation [25, 26], Monte Carlo simulation, and direct solution of time-dependent Schrödinger equation (TDSE) [27]. A semi-empirical formula obtained by fitting the results of the TDSE numerical solution is presented in [26]. It was also shown [8] that the time delay obtained from the attosecond streaking data coincides with that measured using RABITT.

In spite of this impressive theoretical progress, serious disagreements still exist between the experimentally measured and theoretically calculated data on ionization time delays in inert gases neon [29] and argon [30]. To explain this difference various

theoretical approaches are used that take the electron-electron correlations into account [31, 32]. The similarity of theoretical results to the experimental ones, attained in [32], allows a conclusion that at least in the argon atom the above discrepancy between theory and experiment is explained by the presence of multiple resonances due to electron-electron correlations.

The Chapter is organized as follows. In Sect 14.2 the general problem of choosing the reference point for the time delay in the case of Coulomb field is discussed. In Sect 14.3 we demonstrate that the known method of attosecond streaking is equivalent to a device, located at a certain distance from the center and detecting the delay of the electron arrival, and that the Coulomb-laser coupling, arising in the theory of the attosecond streaking, appears to be a consequence of the Coulomb advance of the electron arrival at this virtual device.

Below we use the atomic units of measurement, unless otherwise noted.

14.2 Ionization Time Delay Definition and Theory

In the framework of quantum mechanics the behavior of a system, ionized by an external laser field, is described by the wave function. After the finish of the external action it can be presented in the form

$$\psi(\mathbf{r}, t) = \int f(\mathbf{k})\varphi_{\mathbf{k}}^{(-)}(\mathbf{r})e^{-i\frac{k^2}{2}t}d\mathbf{k}, \tag{14.1}$$

where $f(k)$ is the ionization probability amplitude, $\varphi_{\mathbf{k}}^{(-)}(r)$ is the wave function of the continuous spectrum, describing the free particle with the momentum $\mathbf{k}$ at the infinitely large distance.

14.2.1 Short-Range Potential

If the potential of interaction of the particle with the center is short-range, then $\varphi_{\mathbf{k}}^{(-)}(r \to \infty) = (2\pi)^{-3/2} \exp(ikr)$. Using the known relation

$$\lim_{r \to \infty} e^{ikr\mathbf{n}\mathbf{n}'} = \frac{2\pi}{ikr} \left[e^{ikr}\delta(\mathbf{n} - \mathbf{n}') - e^{-ikr}\delta(\mathbf{n} + \mathbf{n}') \right], \tag{14.2}$$

where $\delta(\mathbf{n} + \mathbf{n}')$ is a delta function, we obtain that for $r \to \infty$ the wave function can be expressed as

$$\psi(\mathbf{r}, t) \sim \int_0^\infty |f(k\mathbf{n})|e^{iS_+}dk - \int_0^\infty |f(-k\mathbf{n})|e^{iS_-}dk. \tag{14.3}$$

Here the phases of the integrands are expressed as

$$S_\pm = \pm kr + \delta(\pm k\mathbf{n}) - \frac{k^2}{2}t,$$

where $\delta(\mathbf{k}) = \arg f(\mathbf{k})$ is the phase of the ionization complex amplitude. In the limit $t \to \infty$ the major contribution to the integrals is introduced by the vicinity of the stationary points $k_0 = k_0(\mathbf{r}, t)$, in which the derivative of the integrand phase is equal to zero,

$$\frac{dS_{\pm}}{dk}\bigg|_{k_0} = \pm r + \frac{\partial \delta(\pm k\mathbf{n})}{\partial k}\bigg|_{k_0} - k_0 t = 0,$$

since far from the points k_0 the integrands are fast-oscillating. For $k \geq 0$ only S_+ possesses an extremum, so that only the first term in Eq. (14.3) contributes to the wave function, and

$$\psi(\mathbf{r}, t) \sim f(k_0\mathbf{n})e^{ik_0 r - i\frac{k_0^2}{2}t}.$$

This fact can be interpreted as follows. At the point $\mathbf{r} = r\mathbf{n}$ at the moment of time

$$t = \frac{r}{k} + \frac{1}{k}\frac{\partial \delta(\mathbf{k})}{\partial k} \tag{14.4}$$

one can detect the particle having the momentum $\mathbf{k} = k\mathbf{n}$ with the maximal probability. Since the ratio r/k is the time, required for the arrival at the point $\mathbf{r}$ of the particle that left the center $r = 0$ at the time $t = 0$ and moved with the uniform velocity k, the expression

$$t_W = \frac{1}{k}\frac{\partial \delta(\mathbf{k})}{\partial k} = \frac{\partial \delta}{\partial E}(\mathbf{k}) \tag{14.5}$$

has the physical meaning of the time delay of the particle arrival at the distance r from the center with respect to that in the case of uniform rectilinear motion. Note that the condition that the particle should be ejected directly from the center is not necessary, because if the particle has the impact parameter b (which in the case of free motion is the minimal distance between the particle and the origin), then $\lim_{t\to\infty}(r/k) = \lim_{t\to\infty}\sqrt{b^2 + (kt)^2}/k = t$. The interpretation of the energy derivative of the phase as the time delay was first proposed by Eisenbud [17] and Wigner [18] (see also [20]). Winger [18] has shown that if a particle falls from infinity, then after passing the center of a short-range potential the delay with respect to the motion in free space equals to $2t_W$. In the same paper he has shown that if the potential is attractive, then $t_W > 0$ only for near-resonance energy (i.e., when the particle is captured into a quasistationary state for a long time). For the rest values of energy $(-r_{pot}/k) \leq t_W \leq 0$ (where r_{pot} is the potential action radius), i.e., corresponds to the expected from the point of view of classical physics. For brevity below we will refer the energy derivative of the phase, t_W, as Wigner time delay.

One more important note should be made before proceeding further. If the external impact on the system is weak, so that one can calculate the ionization amplitude using the first-order perturbation theory as follows

$$f(\mathbf{k}) = \langle \mathbf{k}|\hat{w}|i\rangle, \tag{14.6}$$

where $|i\rangle$ the wave function of the initial state of the system, $|\mathbf{k}\rangle \equiv \varphi_{\mathbf{k}}^{(-)}(\mathbf{r})$ is the wave function of the final state, describing the free electron with the momentum $\mathbf{k}$ at the infinity, $\hat{w}$ is the operator of external perturbation.

As it is known, for a centrosymmetric system the wave function is representable is the form of expansion

$$\varphi_{\mathbf{k}}^{(-)}(\mathbf{r}) = 4\pi \sum_{\ell m} i^{\ell} e^{-i\delta_{\ell}(k)} Y_{\ell m}^{*}(k) Y_{\ell m}(\widehat{r}) R_{k\ell}(r), \tag{14.7}$$

where $R_{k\ell}(r \to \infty) = \frac{1}{kr} \sin(kr - \pi\ell/2 + \delta_{\ell})$ is the radial wave function of the partial spherical wave, δ_{ℓ} is the phase of the spherical wave. In this case the amplitude is expressed as

$$f(\mathbf{k}) = \sum_{\ell m} A_{\ell m}(k) i^{-\ell} e^{i\delta_{\ell}(k)} Y_{\ell m}(k). \tag{14.8}$$

If the transition amplitude $A_{\ell m} = 4\pi \langle R_{k\ell} Y_{\ell m} | \hat{w} | i \rangle$ differs from zero for only one ℓ, then, obviously, the Wigner time delay depends only on the corresponding partial phase

$$t_W = \frac{d\delta_{\ell}}{dE}. \tag{14.9}$$

In other words, if in a one-center system the transition occurs into a state with fixed angular momentum, then the Wigner time delay appears to be completely determined by the energy and the quantum number of the squared angular momentum, and is by no means related to the initial state and the particular form of the perturbation potential.

14.2.2 Coulomb Potential

If the potential is not short-range and tends to a Coulomb one, Z/r, at large distances, then the asymptotic form of the wave function becomes essentially different, since the phase in Eq. (14.3) contains the term logarithmic in r, taking the form

$$S_+ = kr + \frac{Z}{k} \ln 2kr + \delta(k\mathbf{n}) - \frac{k^2}{2}t. \tag{14.10}$$

The stationary point will be now determined by the solution of the equation

$$\frac{dS_+}{dk} = r - \frac{Z}{k^2} \ln 2kr + \frac{Z}{k^2} + \frac{d\delta}{dk} - kt = 0. \tag{14.11}$$

Herefrom it is apparent that the time of arrival of the electron, having the momentum k, at the point at the distance r from the Coulomb center with the charge Z is equal to

$$t(r) = \frac{r}{k} - \frac{Z}{k^3} \ln 2kr + \frac{Z}{k^3} + t_W. \tag{14.12}$$

As it has been already mentioned, in systems with short-range potentials the Wigner time delay has simple physical meaning, namely, it is the delay of arrival of the particle, ejected from the force center, as compared to the case of rectilinear and uniform motion. In order to understand the physical meaning of Wigner time delay in the case of Coulomb field, the comparison should be made with a certain classical motion in Coulomb field. The most rational choice is the motion of a particle with zero angular momentum, starting from the center $r = 0$ at the moment of time $t = 0$. The law of such motion can be obtained from the known general law of a particle motion with arbitrary angular momentum [33]. However, it is simpler to use the known general formula for the law of a one-dimensional motion,

$$t_C(r) = \int_0^r \frac{dr}{p(r)}, \tag{14.13}$$

where $p(r) = \sqrt{k^2 + 2Z/r}$ is the momentum of the particle at the distance r from the center. Performing the integration, we get

$$t_C(r) = \frac{p(r)r}{k^2} + \frac{Z}{k^3} \ln \frac{p(r)/k - 1}{p(r)/k + 1}. \tag{14.14}$$

The asymptotic form of this law is

$$t_C(r \to \infty) = \frac{r}{k} - \frac{Z}{k^3} \ln \frac{2k^2 r}{Z} + \frac{Z}{k^3}. \tag{14.15}$$

Let us introduce the notion of the delay of a "quantum" particle moving in the asymptotic Coulomb field with respect to a classical particle with the angular momentum $\ell = 0$, ejected from the center at the time moment $t = 0$:

$$t_0 = \lim_{r \to \infty} [t(r) - t_C(r)]. \tag{14.16}$$

From Eqs. (14.12) and (14.15) it is clear that the ejection delay relates to Wigner time delay as

$$t_0 = t_W + \frac{Z}{k^3} \ln \frac{k}{Z}. \tag{14.17}$$

Figure 14.4a a shows the Wigner time delays for the continuum of a hydrogen atom at different values of the angular momentum ℓ, multiplied by k^3 for clearness. It is seen that at small energies $t_W \to -\frac{Z}{k^3} \ln \frac{k}{Z}$ for all values of ℓ. In Fig. 14.1, b the delays t_0 are shown. For $k \to 0$ they tend to infinity, but not as $-\frac{Z}{k^3} \ln \frac{k}{Z}$, but much slower, namely, as $1/k^2$. Besides, $t_0 > 0$ for all E values and grows with increasing ℓ. This can be interpreted as follows. The centrifugal potential can be considered as a short-range repulsive one, and the particle motion through it results in the delay with respect to the motion in the pure Coulomb field.

Let us also consider the time delay for the particle, arriving at the detector located at the distance r from the center, in comparison with the case of uniform and rectilinear motion,

$$t_D(r) = t_0 + t_C(r) - \frac{r}{k} \simeq t_0 - \frac{Z}{k^3} \ln \frac{2k^2 r}{Z} + \frac{Z}{k^3}. \tag{14.18}$$
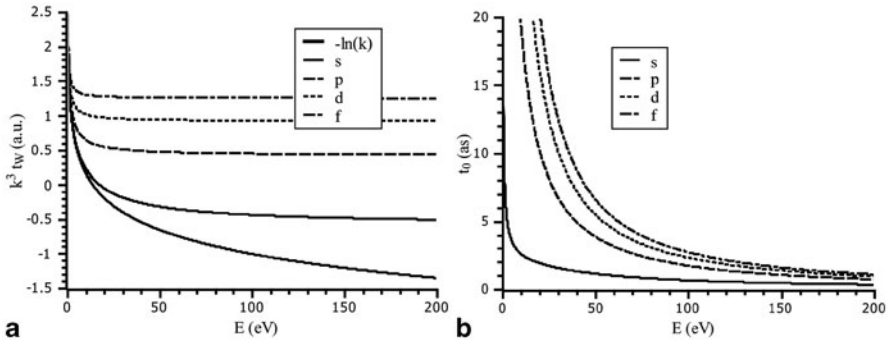
Fig. 14.4 Dependence of the time delay upon the energy of the ejected electron for a hydrogen atom: **a** Wigner time delay. **b** The ejection delay. (Eq. 14.17)

Obviously, at large r, when the logarithmic term, describing the Coulomb advance

$$t_{CA}(r) = t_C(r) - \frac{r}{k} \simeq -\frac{Z}{k^3}\left[\ln\frac{2k^2 r}{Z} - 1\right],\qquad(14.19)$$

becomes dominant, the time delay will be negative.

14.3 Physical Meaning of Coulomb-Laser Coupling in Attosecond Streaking

14.3.1 Attosecond Streaking Theory

Apparently, the above speculations of a detector, providing direct measurement of the particle arrival delay, concern rather a gedanken experiment rather than a real one. The latter implies the assessment of delays by virtue of certain indirect approaches. It is interesting to correlate the above discussion with these real measurements. In the present Section we demonstrate that the correction to the attosecond streaking time delay measurement, referred to as Coulomb-laser coupling [24], in fact is nothing but the Coulomb advance $t_{CA}(r)$, accumulated by the moment of essential variation of the laser field strength. This actually means that the attosecond streaking approach is exactly equivalent to a virtual detector, placed at a fixed distance from the center and measuring the time delay (14.18) of the particle arrival.

So let us proceed to the derivation of the basic equations of the underlying theory of the streaking camera technique. Let the electron be subject to an auxiliary probing electric field having the strength $\mathcal{E}(t)$. The potential energy of the electron in such field is

$$V(r, t) = \mathcal{E}(t) \cdot r.\qquad(14.20)$$

The detection of electrons is usually implemented in the direction of the polarization vector of the probing field, since in such geometry of the experiment the auxiliary

field does deflect the electron trajectory. Since during the action of the probing field the electron has enough time to move away from the center to a distance large compared to the atomic radius, the angular motion can be neglected. Thus, we arrive at a one-dimensional problem of a motion of an electron in the potential

$$V(r,t) = \mathcal{E}(t)r. \tag{14.21}$$

Stepwise Probing Field We start from the case hardly implementable experimentally, but more transparent for theoretical consideration, namely, the constant field, suddenly switched off at the time T:

$$\mathcal{E}(t) = \begin{cases} \mathcal{E}_0, & t < T; \\ 0, & t > T. \end{cases} \tag{14.22}$$

We also assume the strength of the field $\mathcal{E}_0$ to be very small. Note, that although the practical detection of the momentum increment requires rather strong streaking fields, no fundamental limitations follow from this requirement. The attosecond streaking works by virtue of the first-order effect surviving even for an infinitesimally weak "probing" field, so the assumption of the smallness of the $\mathcal{E}_0$ magnitude does not restrict the generality of our consideration. At the time τ the atom is affected by an ultrashort pulse of XUV radiation. The pulse causes the ejection of an electron having the energy E, equal to the difference between the mean energy of the XUV photon ω_0 and the ionization potential I. Before the change of the auxiliary IR field the energy is obviously conserved, the conservation law having the form $E = p^2(t)/2 + \mathcal{E}_0 r(t)$. This allows the assessment of the additional momentum, acquired before the field switching off: $\Delta p = -\mathcal{E}_0(T)/p(T)$. If in this formula we assume $r(T) \simeq r^{(0)}(T - \tau)$ and $p^{(0)}(T - \tau)$, i.e., instead of the exact position and momentum we use their values for a particle that appeared in the center at the time τ and moves in the absence of the auxiliary IR field, then only the second-order terms in $\mathcal{E}_0$ will be changed. In the first-order approximation with respect to $\mathcal{E}_0$ we obtain

$$\Delta p = -\mathcal{E}_0 \frac{r^{(0)}(T - \tau)}{p^{(0)}(T - \tau)}. \tag{14.23}$$

Both in systems with short-range potential and in Coulomb systems it is possible to assume that $p^{(0)}(T - \tau) \approx k$ at sufficiently large $T - \tau$. For systems with short-range potential $r^{(0)}(T - \tau) \approx k(T - \tau - t_W)$ and, correspondingly,

$$\Delta p = -\mathcal{E}_0(T - \tau - t_W). \tag{14.24}$$

Thus, in the plot of the dependence $\Delta p(\tau)$ the time of ejection will manifest itself as a horizontal shift of the plot with respect to the straight line $-\mathcal{E}_0(T - \tau)$. In systems with Coulomb potential $r^{(0)}(T - \tau) \approx k(T - \tau - t_D)[r^{(0)}(T - \tau)]\}$. Since t_D(see Eq. (14.18)) logarithmically depends upon the distance, one can use $t_D[r^{(0)}(T - \tau)] \approx t_D[(T - \tau)]\}$, which yields

$$\Delta p = -\mathcal{E}_0 \{T - \tau - t_D[k(T - \tau)]\}. \tag{14.25}$$

Thus, the attosecond streaking works as a detector, located at the distance $r_{eff} = k(T - \tau)$ from the point of free particle escape. An essential feature of the approach leading to this conclusion is that although the particle changes its velocity during the entire period of the IR field action, starting the acceleration directly after the transition to the unbound state, the energy conservation law allows the expression of this change in terms of the particle behavior far from the center, so that the unknown details of the particle behavior near the center become unimportant. It may be said that until the field is switched on, the variation of the momentum is a dynamical variable that takes the fixed value only at the time moment when the field is switched off.

Smoothly varying probing field Now let us consider the probing field strength $\mathcal{E}(t)$ smoothly varying with time. The temporal behavior of the particle total energy obeys the equation $\frac{dE}{dt}(t) = \frac{\partial U}{\partial t}(r(t), t)$. From this equation it is easy to derive the correction to the particle energy within the first-order approximation with respect to $\mathcal{E}(t)$

$$\frac{d(\Delta E)}{dt} = \frac{d\mathcal{E}}{dt}(t)r^{(0)}(t - \tau).$$

On the other hand, if the natural condition $\mathcal{E}(t \to \infty) = 0$ holds, then $\Delta E(t \to \infty) = k\Delta p$, where $k = \sqrt{2E}$, E being the energy averaged over the wave packet. Then the increment of the momentum is expressed as

$$\Delta p = \int_\tau^\infty \frac{d\mathcal{E}}{dt} \frac{r^{(0)}(t - \tau)}{k} dt. \tag{14.26}$$

The distance $r^{(0)}(t - \tau)$ between the center and the particle is small at small $t = \tau$. With time the distance $r^{(0)}$ unlimitedly grows, therefore, at $t = \tau$ the integrand may be expected to contribute to the integral insignificantly. However, the subject of our interest is just the contribution to $r^{(0)}(t-\tau)$ from the shift that does not grow with time. Hence, for sure we assume that $\frac{d\mathcal{E}}{dt}(t \to \tau) \to 0$. Below we will demonstrate that this assumption does not impede the applicability of the approach to realistic dependences $\mathcal{E}(t)$. Since in this case $r^{(0)}(t-\tau)$ does not contribute to the integral at small $t = \tau$, for short-range potentials we again can use the approximation $r^{(0)}(t-\tau) \simeq k(t-\tau-t_w)$. Integrating by parts and using the inverse Taylor expansion, we get

$$\Delta p = \int_z^\infty \frac{d\mathcal{E}}{dt}(t)(t - \tau - t_w)dt = \mathcal{E}(\tau)t_w - \int_x^\infty \mathcal{E}(t)dt.$$
$$= -\mathcal{A}(\tau) - \frac{d\mathcal{A}}{dt}(\tau)t_W \simeq -\mathcal{A}(\tau + t_w). \tag{14.27}$$

Here we introduce the vector potential $\mathcal{A}(t)$, related to the probing field strength as $\mathcal{E}(\tau) = -\frac{d\mathcal{A}}{dt}(\tau)$, so that

$$\mathcal{A}(\tau) = \int_\tau^\infty \mathcal{E}(t)dt. \tag{14.28}$$

Thus we arrive at the fundamental expression in the conventional streaking formalism [11]. In correspondence with it, the plot of the momentum of the registered electron versus time mimics the plot of the vector potential $\mathcal{A}(t)$ with the horizontal shift, equal to the Wigner time delay.

14.3.2   Coulomb-Laser Coupling

In a system with Coulomb potential, assuming again that $\frac{d\mathcal{E}}{dt}(t \to \tau) \to 0$ to avoid the necessity to know the particle trajectory near the center, we can use the approximation $r^{(0)}(t - \tau) \simeq k(t - \tau - t_D[k(t - \tau)])\}$. Integrating by parts and using the fact that $t_D(r) = t_0 + t_{CA}(r)$ and $t_{CA}(0) = 0$, we get

$$\Delta p = \int_\tau^\infty \frac{d\mathcal{E}}{dt}(t)\{t - \tau - t_D[k(t - \tau)]\}\, dt \simeq -\mathcal{A}(\tau + t_0) + \Delta p_{CL}. \quad (14.29)$$

Here the notation is introduced

$$\Delta p_{CL} = -\int_\tau^\infty \frac{d\mathcal{E}}{dt}(t)t_{CA}[k(t - \tau)]dt =$$

$$= -\mathcal{E}(\tau)t_{CA}(0) + \int_\tau^\infty \mathcal{E}(t)\frac{dt_{CA}[k(t - \tau)]}{dt}dt =$$

$$= \int_0^\infty \mathcal{E}(t + \tau)\left[\frac{1}{p^{(0)}(kt)} - \frac{1}{k}\right]kdt. \quad (14.30)$$

The change of the momentum Δp_{CL}, arising under the joint action of Coulomb and laser probing field, is usually referred to as Coulomb–laser coupling [24–26]. However, it is easily seen that if one substitutes the step function (14.22) for the field strength in Eq. (14.30), then Eq. (14.30) with the use of Eq. (14.13) yields $\Delta p_{CL} = \mathcal{E}_0 t_{CA}[k(T - \tau)]$, as a result of which Eq. (14.29) turns into Eq. (14.25). That is, the correction Δp_{CL} is connected with the Coulomb advance $t_{CA}(r_{eff})$ of the particle arrival at the point separated by the distance $r_{eff} = k(T - \tau)$ from the center, which, in turn, represents the distance, that the particle can reach before the moment of the strong variation of the probing field. For a periodic probing field with the frequency ω the characteristic time of the field variation has the order $\sim 1/\omega$, that yields an estimate $r_{eff} \sim k/\omega$. Let the probing radiation pulse have the form $\mathcal{E}(t) = \mathcal{E}_0(t)\sin(\omega t)$, where $\mathcal{E}_0(t)$ is a slowly varying envelope function. Using the expression for the sinus of a sum, and assuming the integrand in Eq. (14.30) to decrease much faster, than the variation of $\mathcal{E}_0(t)$, so that the approximation $\mathcal{E}_0(\tau + t) \approx \mathcal{E}_0(\tau)$ is valid, we obtain from Eq. (14.30) the following expression:

$$\Delta p_{ct} = \frac{\mathcal{E}_0(\tau)}{\omega}\sin(\omega\tau)I_{\cos}(a) + \frac{\mathcal{E}_0(\tau)}{\omega}\cos(\omega\tau)I_{\sin}(a). \quad (14.31)$$

Here we use the notation

$$I_{\cos}(a)\int_0^\infty \cos(t)\left[\frac{1}{\sqrt{1 + 2a/t}} - 1\right]dt; \quad (14.32)$$

$$I_{\sin}(a) = \int_0^\infty \sin(t)\left[\frac{1}{\sqrt{1 + 2a/t}} - 1\right]dt, \quad (14.33)$$

where the parameter a is defined as

$$a = \frac{Z\omega}{k^3}. \tag{14.34}$$

It should be noted that that Eq. (14.31) may be considered as the result of splitting of the IR field strength $\mathcal{E}(t)$ into two terms, $\mathcal{E}(t) = \mathcal{E}_1(t) + \mathcal{E}_{\Pi}(t)$, where the first term $\mathcal{E}_1(t) = \mathcal{E}(\tau) \sin [\omega (t - \tau)]$ (that yields the first term in Eq. (14.31)), satisfies the condition $\frac{d\mathcal{E}_1}{dt}(t = \tau) = 0$, which we use to avoid the dependence of the final result on the details of the particle behavior in the vicinity of the center. Under the condition $a \ll 1$ the integrals have simple expressions

$$I_{\cos}(a) \approx -a \left[\ln \frac{2}{a} - 1 - \gamma \right] - \frac{3\pi}{4} a^2, \tag{14.35}$$

$$I_{\sin}(a) \approx -\frac{\pi}{2} a + \frac{3}{2} a^2 \left[\ln \frac{2}{a} - \frac{1}{6} - \gamma \right], \tag{14.36}$$

where $\gamma = 0.57721 \dots$ is the Euler constant. If the variation of the envelope function $\mathcal{E}_0(t)$ during the period $T_{IR} = 2\pi /\omega$ is small and $\mathcal{E}_0(t \to \infty) = 0$, then the vector potential might be approximately expressed as $\mathcal{A}(t) \approx \frac{\mathcal{E}_0(t)}{\omega} \cos \omega t$. With this fact taken into account, Eq. (14.31) can be rewritten as

$$\Delta p_{CL} = -\frac{d\mathcal{A}}{dt} t_{C\mathcal{A}}(r_{eff}) - \mathcal{A}(\tau)\alpha, \tag{14.37}$$

where

$$r_{eff} = \frac{k}{\omega} \exp \left[-\gamma + \frac{3\pi}{4} a \right], \tag{14.38}$$

is the effective radius and

$$\alpha = -I_{\sin}(a) = \frac{\pi}{2} a - \frac{3}{2} a^2 \left[\ln \frac{2}{a} - \frac{1}{6} - \gamma \right]. \tag{14.39}$$

Finally, the increment of the momentum is expressed as

$$\Delta p = -(1 + \alpha)\mathcal{A}(\tau + t_S), \tag{14.40}$$

where

$$t_s = \frac{t_D(r_{eff})}{1 + \alpha} \tag{14.41}$$

is the time shift. We recall that $t_D(r_{eff})$ arises from the first term in Eq. (14.31) and the increment of the amplitude of pulse variation α appears from the second one. The Eq. (14.31) follows from the decomposition of the periodic field oscillation into two components, one of them being constant at the ionization time moment τ and the other one changing at this moment. Summarizing these facts, we can conclude,
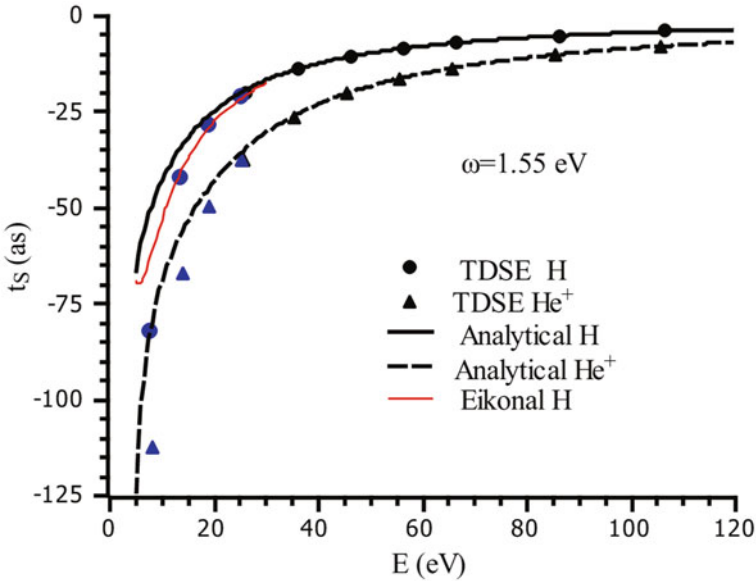
Fig. 14.5 Dependence of t_s upon the energy of the ejected electron with the angular momentum $\ell = 1$ for the ionization of a hydrogen atom (*solid line*) and a helium ion He$^+$ (*dashed line*). The frequency of the IR field is $\omega = 1.55\,\text{eV}$

that, in full analogy with the above model example of a stepwise field, the time delay $t_D(r_{eff})$ is recorded at the moment of the field switch-off, and (r_{eff}) is the distance reached by the particle at this moment. The field component, changing at the moment of ionization, gives rise to a distortion of this picture, increasing the momentum variation, synchronous with the vector potential of the external field. Against the background of this increased "swing" of the momentum the observed time delay t_S is reduced.

Figure 14.5 shows the results calculated analytically using Eqs. (14.41), (14.38), (14.39), and (14.34) (lines); for comparison the results of solving the time-dependent Schrödinger equation for an atom in the field of a femtosecond IR laser pulse (points) from [27] (black points) and our calculations (blue points) are shown, as well as the result of the eikonal approximation [26].

It is seen that the simple analytical expression (14.41) provides complete agreement with the results [27] and [34], obtained from the numerical solution of time-dependent Schrödinger equation for an electron affected by the ion field and the field of an IR probing laser pulse.

Let us explicitly express the time shift in terms of the Wigner time

$$t_S = t_W + t_{CLC}, \tag{14.42}$$

where the additive part of the contribution from the Coulomb-laser coupling to the observed time shift is

$$t_{CLC} = -\alpha(\omega Z/k^3)t_W - \frac{1}{1+\alpha(\omega Z/k^3)} \frac{Z}{k^3} \left[\ln \frac{2k^2}{\omega} - 1 - \gamma + \frac{3\pi}{4} \frac{\omega Z}{k^3} \right].$$

(14.43)

Using the eikonal approximation, the authors of [26] also derived an analytical expression for t_{IR}. Although the dominant term in this expression, logarithmically depending upon $1/\omega$, is analogous to the dominant term in our Eq. (14.43), the minor terms are not similar. At $k \to \infty$ the formula from [26] differs from our one by $2\gamma/k^3$. We were basing on the interpretation of attosecond streaking as an equivalent of a virtual detector placed at the large distance r_{eff} from the center, which allows considering only the classical behavior of the electron far from the nucleus. The Coulomb-laser coupling in this interpretation is a record of the Coulomb advance of the particle arrival at the point r_{eff}.

In the limit $\omega \to 0$ our formula (14.43) takes the form

$$t_{CLS} = -\frac{Z}{k^3} \left[\ln \frac{2k^2}{\omega} - 1 - \gamma \right] = -\frac{Z}{k^3} \left[\ln 1.12 \frac{k^2}{\omega} - 1 \right]$$

(14.44)

that corresponds to $r_{eff} = 0.56k/\omega$. The empirical formula derived by R. Pazourek et al. [28]

$$t_{CLS} = -\frac{Z}{k^3} \left[\ln 1.16 \frac{k^2}{\omega} - 1 \right].$$

(14.45)

corresponds to $r_{eff} = 0.58k/\omega$.

14.4 Conclusion

It is demonstrated that the known method of attosecond streaking is equivalent to a device, placed at a certain distance from the center and recording the delay of the electron arrival. We show that the laser-Coulomb coupling, arising in the theory of attosecond streaking, is related to the Coulomb advance of the particle arrival at this virtual detector. The advantages of our consideration are the clear interpretation of time delays in the case of Coulomb potential and the derivation of a simple analytical formula for ionization time delay. The fact that in our approach only the information on remote behavior of the electron is used opens the possibility for further generalization of the theory for the case of multiple ionization of atomic and molecular systems.

References

 1. Kienberger, R., Chang, Z., Nam, C.H.: 10th anniversary of attosecond pulses. J. Phys. B: At. Mol. Opt. Phys. **45**, 070201 (2012)
 2. Paul, P.M., Toma, E.S., Breger, P., Mullot, G., Auge, F., et al.: Observation of a train of attosecond pulses from high harmonic generation. Science. **292**, 1689–1692 (2001)
 3. Hentschel, M., Kienberger, R., Spielmann, C., Reider, G.A., Milosevic, N., et al.: Attosecond metrology. Nature. **414**, 509–513 (2001)
 4. Corkum, P.B., Ivanov, M.Y., Wright, J.S.: Subfemtosecond processes in strong laser fields. Annu. Rev. Phys. Chem. **48**, 387–406 (1997)
 5. Corkum, P. B.: Plasma perspective on strong-field multiphoton ionization. Phys. Rev. Lett. **71**, 1994–1997 (1993)
 6. Lewenstein, M., Balcou, P., Ivanov, M.Y., L'Huillier, A., Corkum, P.B.: Theory of high-harmonic generation by low-frequency laser fields. Phys. Rev. A. **49**, 2117–2132 (1994)
 7. Prokopovich, I.P., Khrushchinskii, A.A.: Highly efficient generation of attosecond pulses in coherent stimulated Raman self-scattering of intense femtosecond laser pulses. Laser Phys. **7**(2), 305–308 (1997)
 8. Dahlström, J.M., Guénot, D., Klünder, K., Gisselbrecht, M., Mauritsson, J., L'Huillier, A., Maquet, A., Taïeb, R.: Theory of attosecond delays in laser-assisted photoionization. Chem. Phys. **414**(12), 53–64 (2013)
 9. Dahlström, J.M., L'Huillier, A., Maquet, A.: Introduction to attosecond time-delays in photoionization. J. Phys. B. **45**, 183001 (2012)
10. Muller, H.G.: Reconstruction of attosecond harmonic beating by interference of two-photon transitions. Appl. Phys. B. **74**(1), Supplement, s17–s21 (2002)
11. Véniard, V., Taïeb, R., Maquet, A.: Phase dependence of $(N+1)$-color $(N>1)$ IR-UV photoionization of atoms with higher harmonics. Phys. Rev. A. **54**, 721–728 (1996)
12. Itatani, J., Quere, F., Yudin, G.L., Ivanov, M.Yu., Krausz, F., Corkum, P.B.: Attosecond streak camera. Phys. Rev. Lett. **88**, 173903 (2002)
13. Kienberger, R., Goulielmakis, E., Uiberacker, M., Baltuska, A., Yakovlev, V., Bammer, F., Scrinzi, A., Westerwalbesloh, T., Kleineberg, U., Heinzmann, U., Drescher, M., Krausz, F.: Atomic transient recorder. Nature. **427**, 817–821 (2004)
14. Constant, E., Taranukhin, V.D., Stolow, A., Corkum, P.B:. Methods for the measurement of the duration of high-harmonic pulses. Phys. Rev. A. **56**, 3870–3878 (1997)
15. Kitzler, M., Milosevic, N., Scrinzi, A., Krausz, F., Brabec, T.: Quantum theory of attosecond XUV pulse measurement by laser dressed photoionization. Phys. Rev. Lett. **88**, 173904 (2002)
16. De Carvalho, C.A.A., Nussenzveig, H.M.: Time delay. Phys. Rep. **364** 83–174 (2002)
17. Eisenbud, L.: Messiah, Quantum Mechanics. Ph. D. Dissertation (Princeton University, 1948), unpublished (pdf file available on-line); the result is also derived in A. (New York, Wiley, 1963), Eq. X.66
18. Wigner, E.P.: Lower limit for the energy derivative of the scattering phase shift. Phys. Rev. **98**, 145–147 (1955)
19. Brenig, W., Haag, R.: Allgemeine Quantentheorie der Stossprozesse. Fortschr. Phys. **7**, 183–190 (1959)
20. Smith, F.T.: Lifetime matrix in collision theory. Phys. Rev. **118**(1), 349–356 (1960)
21. Nussenzveig, H.M.: Time delay in quantum scattering. Phys. Rev. D. **6**(6), 1534–1542 (1972)
22. Ivanov, M.Yu., Smirnova, O., Spanner, M.: Anatomy of strong field ionization. J. Mod. Opt. **52**, 165–184 (2005)
23. Scrinzi, A., Ivanov, M. Yu., Kienberger, R., Villeneuve, D.M.: Attosecond physics. J. Phys. B: At. Mol. Opt. Phys. **39**, R1–R37 (2006)
24. Smirnova, O., Mouritzen, A.S., Patchkovskii, S., Ivanov, M.Yu.: Coulomb–laser coupling in laser-assisted photoionization and molecular tomography. J. Phys. B: At. Mol. Opt. Phys. **40**, F197–F206 (2007)
25. Zhang, C-H., Thumm, U.: Electron-ion interaction effects in attosecond time-resolved photoelectron spectra. Phys. Rev. A. **82**, 043405 (2010)

26. Smirnova, O., Ivanov, M.Yu.: How accurate is the attosecond streak camera? Phys. Rev. Lett. **107**, 213605 (2011)
27. Nagele, S., Pazourek, R., Feist, J., Doblhoff-Dier, K., Lemell, C., Tökési, K., Burgdörfer, J.: Time-resolved photoemission by attosecond streaking: extraction of time information. J. Phys. B: At. Mol. Opt. Phys. **44**, 081001 (2011)
28. Pazourek, R., Nagele, S., Burgdörfer, J.: Time-resolved photoemission on the attosecond scale: opportunities and challenges. Faraday Discuss. **163**, 353–376 (2013)
29. Schultze, M., Fieß, M., Karpowicz, N., Gagnon, J., Korbman, M., Hofstetter, M., Neppl, S., Cavalieri, A.L., Komninos, Y., Mercouris, Th., Nicolaides, C.A., Pazourek, R., Nagele, S., Feist, J., Burgdörfer, J., Azzeer, A.M., Ernstorfer, R., Kienberger, R., Kleineberg, U., Goulielmakis, E., Krausz, F., Yakovlev, V.S.: Delay in photoemission. Science. **328**, 1658–1662 (2010)
30. Guénot, D., Klünder, K., Arnold, C.L., Kroon, D., Dahlström, J.M., Miranda, M., Fordell, T., Gisselbrecht, M., Johnsson, P., Mauritsson, J., Lindroth, E., Maquet, A., Taïeb, R., L'Huillier, A., Kheifets, A. S.: Photoemission time-delay measurements and calculations close to the 3s ionization minimum in Ar. Phys. Rev. A. **85**, 053424 (2012)
31. Nagele, S., Pazourek, R., Feist, J., Burgdörfer, J.: Time shifts in photoemission from a fully correlated two-electron model system. Phys. Rev. A. **85**, 033401 (2012)
32. Carette, T., Dahlström, J.M., Argenti, L., Lindroth, E.: Multiconfigurational Hartree–Fock close-coupling ansatz: application to the argon photoionization cross section and delays. Phys. Rev. A. **87**, 023420 (2013)
33. Landau, L.D., Lifshitz, E.M.: Mechanics. (Vol 1 of A course of theoretical physics. Pergamon, Oxford (1969)
34. Klünder, K., Dahlström, J. M., Gisselbrecht, M., Fordell, T., Swoboda, M., Guénot, D., Johnsson, P., Caillat, J., Mauritsson, J., Maquet, A., Taïeb R., L'Huillier, A.: Probing single-photon ionization on the attosecond time scale. Phys. Rev. Lett. **106**, 143002 (2011)

Index